

**Structural and Optical Properties in Lanthanide
(Ln³⁺= Er³⁺/Yb³⁺/Ho³⁺) Doped Bi_{0.5}Na_{0.5}TiO₃ Ceramics**

**A Thesis Submitted
In Partial Fulfilment of the Requirements
for the Degree of
DOCTOR OF PHILOSOPHY
by
MEGHA NARWAN
(2K19/PHDAP/14)**

Under the Joint- Supervision of

**Dr. RENUKA BOKOLIA
Assistant Professor**

**Dr. RICHA SHARMA
Assistant Professor**



Department of Applied Physics

**DELHI TECHNOLOGICAL UNIVERSITY
(Formerly Delhi College of Engineering)
Shahbad Daulatpur, Main Bawan Road, Delhi-110042, India
January , 2026**

© DELHI TECHNOLOGICAL UNIVERSITY-2026
ALL RIGHTS RESERVED

*Dedicated to My
Family and my
Supervisor*

ACKNOWLEDGEMENT

First and foremost, I am deeply grateful to God for providing me with the strength, patience, and perseverance needed to complete these years of rigorous research. I sincerely dedicate this acknowledgement as a token of appreciation to all who have guided, encouraged, and supported me throughout this journey.

I sincerely thank my supervisors, **Dr. Renuka Bokolia & Dr. Richa Sharma**, for their excellent mentorship and invaluable, continuous support, which helped me navigate the complex aspects of this research. I am deeply appreciative of their insightful advice, constructive feedback, and constant encouragement, which have all contributed to the successful completion of my thesis. Their mentorship not only enriched my academic development but also taught me invaluable lessons that extend beyond the realm of research. I am truly fortunate to have had the privilege to work under her guidance, and I will carry forward the lessons she has imparted with immense respect and gratitude. For all of this and more, I am sincerely thankful and will always remain deeply indebted to them.

My sincere thanks also go to **Prof. Prateek Sharma**, Hon'ble Vice-Chancellor, DTU, for providing a marvellous research environment and ample research facilities to conduct this research. I extend my sincere gratitude to **Prof. Rinku Sharma**, Dean (Academic-PG), DTU, and **Prof. Vinod. Singh**, Former Head of the Department of Applied Physics, DTU, along with all the faculty and staff members, for their support and cooperation throughout my research journey.

I would like to express my heartfelt thanks to **Dr. Manoj Verma** for his valuable help in completing my PhD work. I am immensely grateful to my seniors, **Dr. Ankita Banwal**, **Dr. Bhavya Kumar** and **Dr. Km. Komal** who stood by me unwaveringly, serving as pillars of support through every high and low. Their support and companionship have undoubtedly left a lasting impression on me, for which I am immensely thankful. I am grateful to my dear friends **Dr. Shilpa Rana**, **Dr. Naima Tyagi**, **Dr. Sheetal Kumari**, **Dr. Sunil Kumar** **Mr. Hemant Arora**, **Dr. Priyanka**, **Mr. Aman**, **Ms. Anshul** **Mr. Surya**, **Mr. Ravindra**, **Mr. Alok**, **Mr. Praveen**, **Ms. Ankita Dahiya** **Mr. Dibyajyoti** for their enthusiasm, fresh perspectives, and

willingness to assist whenever needed. Your energy and curiosity have been a wonderful source of motivation.

I would like to express my deepest gratitude to my husband, **Mr. Kushank**, for his unwavering support, understanding, and encouragement throughout this long and challenging journey. His patience and faith in me have been a constant source of strength. I am also thankful to my son and daughter, **Kushagra, Dhanishka** whose love, smiles, and presence brought joy and motivation during the most demanding times of my research. Their unconditional support has been invaluable in helping me reach this milestone.

I am profoundly grateful to my father, **Mr. B. Raj Narwan**, and my mother, **Mrs. Usha Rani**, who mean the world to me and have always given me the freedom to follow my path. I deeply admire them for their selfless love, care, sacrifices, and unwavering support in shaping my life. I also extend my sincere gratitude to my brother, **Mr. Madhur and sister -in-law Mrs. Komal**, for their belief in me, their unwavering support and their constant kindness and understanding. They have always encouraged me to think beyond the ordinary and strive for excellence, pushing me to step outside my comfort zone and explore new horizons. Their infectious laughter and light-hearted presence have been a source of comfort, brightening my challenging Ph.D. journey and offering moments of joy and innocence. I dedicate this achievement to their boundless encouragement and love.

Lastly, I want to acknowledge the tiniest, most joyful members of my family, **Nimish and Dhanishka**. Though too young to understand what a thesis is, their innocent laughter, playful chaos, and unconditional affection brought balance and light to even the most stressful days. Thank you for being a source of pure happiness throughout this journey.

Megha Narwan

Date:



DELHI TECHNOLOGICAL UNIVERSITY

(Govt. of National Capital Territory of Delhi)

Shahbad Daulatpur, Bawana Road, Delhi-110042

CANDIDATE'S DECLARATION

I, **Mrs. Megha Narwan (2k19/PHDAP/14)**, hereby declare that the work which is being presented in the thesis entitled **Structural and Optical Properties in Lanthanide ($Ln^{3+} = Er^{3+}/Yb^{3+}/Ho^{3+}$) Doped $Bi_{0.5}Na_{0.5}TiO_3$ Ceramic** in partial fulfilment of the requirements for the Doctor of Philosophy degree, submitted in the **Department of Applied Physics**, Delhi Technological University is an authentic record of my own work carried out during the period from **August 2019 to July 2025** under the supervision of **Dr. Renuka Bokolia & Dr. Richa Sharma, Department of Applied Physics, Delhi Technological University**. The matter presented in the thesis has not been submitted by me for the award of any degree of this or any other institute.

Megha Narwan

Reg No: 2k19/PHDAP/14

This is to certify that the student has incorporated all the corrections suggested by the examiner in the thesis and the statement made by the candidate is correct to the best of our knowledge.

Dr. Renuka Bokolia

(Assistant Professor)

Dr. Richa Sharma

(Assistant Professor)

(Signature of External Examiner)



DELHI TECHNOLOGICAL UNIVERSITY

(Govt. of National Capital Territory of Delhi)

Shahbad Daulatpur, Bawana Road, Delhi-110042

CERTIFICATE BY THE SUPERVISORS

Certified that **Mrs. Megha Narwan (2K19/PHDAP/14)** has carried out her work presented in this thesis entitled "**Structural and Optical Properties in Lanthanide ($\text{Ln}^{3+} = \text{Er}^{3+}/\text{Yb}^{3+}/\text{Ho}^{3+}$) Doped $\text{Bi}_{0.5}\text{Na}_{0.5}\text{TiO}_3$ Ceramics**" for the award of **Doctor of Philosophy** from Department of Applied Physics, Delhi Technological University, Delhi, under my supervision. The thesis embodies results of original work and studies are carried out by the student herself and the contents of the thesis do not form the basis for the award of any other degree to the candidate or to anybody else from this or any other University/ Institution.

Dr. Renuka Bokolia
(Assistant Professor)
Department of Applied Physics
Delhi Technological University

Dr. Richa Sharma
(Assistant Professor)
Department of Applied Physics
Delhi Technological University

Prof. Vinod Singh
Professor,
Head of Department of Applied Physics
Delhi Technological University

Date:

ABSTRACT

Structural and Optical Properties in Lanthanide (Ln³⁺ = Er³⁺/Yb³⁺/Ho³⁺) Doped Bi_{0.5}Na_{0.5}TiO₃ Ceramics

The development of lead-free ferroelectric materials has gained considerable attention due to their potential in energy storage, sensing, and optoelectronic applications. Among them, bismuth sodium titanate ($\text{Bi}_{0.5}\text{Na}_{0.5}\text{TiO}_3$, BNT) is a promising candidate owing to its favorable ferroelectric and structural properties. The functional performance of BNT can be significantly tailored through rare-earth doping, which modifies its electrical, luminescent, and sensing characteristics.

This thesis outlines the effect of Er^{3+} substituted bismuth sodium titanate ceramics with the chemical composition $\text{Bi}_{0.5-x}\text{Er}_x\text{Na}_{0.5}\text{TiO}_3$ ($x = 0.00, 0.01, 0.02, 0.03, 0.04$, and 0.05) were synthesized using conventional solid-state technique. The influence of Er^{3+} ions on structural, optical, ferroelectric, and temperature sensing properties have been investigated. The prepared ceramic powders were initially heated at a calcination temperature 850°C to form single phase $\text{Bi}_{0.5-x}\text{Er}_x\text{Na}_{0.5}\text{TiO}_3$ and finally sintered at temperature 1050°C . Formation of pure phase composition with rhombohedral crystal structure is confirmed through X-ray diffraction studies. The typical FTIR bands near $540, 860, 910\text{ cm}^{-1}$ confirmed the presence of Ti–O stretching of octahedral groups in the perovskite structure. The decent squared shaped saturated P-E hysteresis are obtained under an electric field of $60 \leq E \leq 70\text{ kV/cm}$, and the loops become slimmer at higher Er^{3+} concentrations ($x = 0.04$). The efficiency of energy storage density increases with Er^{3+} doping and an improved recoverable energy storage ($W_r = 2.73\text{ J/cm}^3$) and a higher efficiency ($\eta = 70.77\%$) are obtained for Er content, $x = 0.04$. The photoluminescence spectra were recorded at two excitation wavelengths (488 nm and 980 nm). Two distinct green emission bands (529 nm and 550 nm) and one weak red emission band (670 nm) were observed at both excitation wavelengths. Increasing Er^{3+} content beyond ($x > 0.03$) leads to significant quenching of light emission due to cross relaxation process and non- radiative relaxations. The pump power dependency revealed that two photons were involved in the light upconversion process. The time-

resolved fluorescence spectroscopy confirmed the decrease in lifetime with increasing Er^{3+} concentration. The absolute and relative sensitivity of the prepared ceramic at Er^{3+} concentration ($x = 0.03$) were found to be $0.47\% \text{ K}^{-1}$ at 523 K and $1.1\% \text{ K}^{-1}$ at 303 K , respectively. These optical and electrical properties open the possibility of realizing multifunctionality in the field of energy storage and opto- electronic applications.

In continuation, a series of $\text{Er}^{3+}/\text{Yb}^{3+}$ co-doped $\text{Bi}_{0.5-x-y}\text{Er}_x\text{Yb}_{y}\text{Na}_{0.5}\text{TiO}_3$ ferroelectric ceramic is prepared using traditional solid-state technique to investigate the structural, optical and sensing properties. The XRD analysis confirms the rhombohedral geometry and no extra peaks shows the solubility of the dopant ions. SEM images exhibited a dense micro structure with well-defined grain boundaries. The FTIR vibrational bands observed at 550cm^{-1} and 820cm^{-1} depict the typical characteristics of perovskite structure caused by the expansion of the octahedral group of $\text{Ti}-\text{O}$ bonds. The Tauc plot displays the energy band gaps (E_g) in a range of 2.93 eV to 2.88 eV as a function of the Yb^{3+} concentration. The photoluminescence spectra were measured at two wavelengths of excitation at 489 nm and 980 nm for all the BNT ceramic compositions. It has been observed that the two intense green bands and one visible red band appeared at 530 nm , 549 nm and 662 nm , respectively. The dependency of pump power on UCL spectra is observed with varying pump powers at 980 nm excitation. The two photons that are involved in the UCL process are confirmed by this investigation. The time-resolved fluorescence spectroscopy reveals that the efficiency in energy transfer between the dopant ions increased for all the co-doped BNT ceramic compositions. The absolute (Sab) and relative (Sr) sensitivity of BE3Y3 ceramic composition are $0.54\% \text{ K}^{-1}$ and $1.24\% \text{ K}^{-1}$ at 523 K and 303 K , respectively.

Further, the Ho^{3+} ions are systematically inserted on the A-site of $\text{Bi}_{0.5-x}\text{Ho}_x\text{Na}_{0.5}\text{TiO}_3$ lead-free ferroelectric ceramic via solid-state method. The x-ray diffraction spectra (XRD) shows the rhombohedral structure of $\text{Bi}_{0.5-x}\text{Ho}_x\text{Na}_{0.5}\text{TiO}_3$. Fourier transform infrared (FTIR) spectroscopy shows two vibrational bands at 537 cm^{-1} and 832 cm^{-1} , due to the stretching vibrations of $\text{Ti}-\text{O}$ bonds in the octahedral units of the perovskite structure. The diffuse reflectance spectra (DRS) showed three bands at 454 , 542 , and 646 nm transit from $^5\text{I}_8 \rightarrow ^5\text{G}_6$, $^5\text{I}_8 \rightarrow ^5\text{F}_4/ ^5\text{S}_2$, and $^5\text{I}_8 \rightarrow ^5\text{F}_5$, respectively. The band gap varies and maximum for 0.03 concentration due to the local structural instability within

the lattice by Ho^{3+} ions. The photoluminescence (PL) emission spectra are traced under 452 nm, and one intense green band at 548 nm and two at 655 (orange) and 750 nm (red) were observed. In upconversion luminescence (UCL) spectra, four emission wavelengths were obtained at 490, 525, 552, and 660 nm. The orange emission band is highly intense, whereas other color bands are relatively weak. Pump power dependence on UCL spectra is analyzed using concentration ($x = 0.03$). The decay profile for green and orange bands showed an average lifetime of 12.99 μs and 9.43 μs , respectively. The PE loops become slimmer, and P_r values decrease with increasing concentration. The energy storage efficiency ($\eta\%$) of the ceramic is increasing with dopant concentration and comes out to be 90 %. The maximum absolute and relative sensitivity observed for the BNT ($x = 0.03$) is 0.29 % K^{-1} and 0.22 % K^{-1} at 303 K, respectively. This study demonstrates the novel observation of orange emission in Ho^{3+} -doped $\text{Bi}_{0.5}\text{Na}_{0.5}\text{TiO}_3$ ceramics without any sensitizers which is not usual behavior as Ho^{3+} typically exhibits green or red emission. This unusual luminescence highlights distinct site symmetry and energy level interactions within the lead-free BNT matrix, validating the uniqueness of the work.

Lastly this study presents the application of BNT, the development and characterization of flexible piezoelectric nanocomposite films based on bismuth sodium titanate (BNT) embedded in a polyvinylidene fluoride (PVDF) matrix for efficient mechanical energy harvesting. BNT ceramic powder was synthesized via a conventional solid-state reaction route and subsequently incorporated into PVDF at varying concentrations (0 – 25wt% BNT) using a drop casting method. Structural analyses confirmed the successful formation of phase-pure rhombohedral BNT and enhancement of the electroactive β -phase in PVDF upon BNT addition. Morphological evaluation using FESEM revealed uniform dispersion of BNT up to 20wt% BNT, beyond which agglomeration was observed. FTIR and XRD studies substantiated the β -phase promotion in the composites, while polarization–electric field (P–E) loop measurements demonstrated improved ferroelectric behavior with increasing BNT content, peaking at 20wt% BNT. Notably, the piezoelectric voltage and current outputs were maximized at 20wt% BNT, registering 25V and 12 μA , respectively, under mechanical excitation. A practical demonstration using the composite film to power LEDs confirmed its potential as a

flexible nanogenerator. These findings highlight the suitability of BNT/PVDF composites as promising candidates for next-generation, lead-free, wearable energy harvesting devices.

In conclusion, Er^{3+} , $\text{Er}^{3+}/\text{Yb}^{3+}$ and Ho^{3+} -doped $\text{Bi}_{0.5}\text{Na}_{0.5}\text{TiO}_3$ ceramics were successfully synthesized and systematically examined for their structural, ferroelectric, luminescent, and sensing characteristics. The results confirmed phase-pure rhombohedral structures, enhanced energy storage efficiency, and notable upconversion emissions with composition-dependent behavior. Particularly, Er^{3+} and $\text{Er}^{3+}/\text{Yb}^{3+}$ co-doping improved energy storage and temperature sensitivity, while Ho^{3+} substitution revealed an unusual orange emission, underscoring unique site symmetry effects. Furthermore, extending the study to BNT/PVDF nanocomposites demonstrated their effectiveness as flexible, lead-free piezoelectric generators with promising output performance. Overall, these findings establish BNT-based materials as multifunctional candidates for future energy storage, optoelectronic, and wearable energy-harvesting applications.

LIST OF PUBLICATIONS

Publications in Peer-Reviewed Journals from This Thesis Work

1. **M. Narwan**, A. Banwal, R. Sharma, R. Bokolia, “Non-invasive thermal sensing and improved recoverable energy storage density of $\text{Bi}_{0.5}\text{Na}_{0.5}\text{TiO}_3$: Er^{3+} doped multifunctional ferroelectric ceramic”, in *Journal of Luminescence* [265](#), 2024, 120236. (I.F. 3.6)
2. **M. Narwan**, R. Sharma, R. Bokolia “Optical temperature sensing and upconversion luminescence in $\text{Er}^{3+}/\text{Yb}^{3+}$ co-doped BN ferroelectric ceramic” *Applied Physics A* 130, 2024 , 854. (I.F. 2.8)
3. **M. Narwan** , A. Banwal, B. Kumar, M. Verma, A. Shandilya, V.K. Rai, R. Sharma, R. Bokolia “ Ho^{3+} - driven novel orange emission and enhanced energy storage in lead-free $\text{Bi}_{0.5}\text{Na}_{0.5}\text{TiO}_3$ ceramics” *Ceramics International* (I.F. 5.6)
4. **M. Narwan**, S. Rana, B. Singh, M. Verma, M. Bala, R. Bokolia, “Fabrication of flexible Thin Film for Energy Harvesting application based on $\text{Bi}_{0.5}\text{Na}_{0.5}\text{TiO}_3$ Nano powders” *Ceramics International* (I.F. 5.6)

Publications in Peer-Reviewed Journals Other Than This Thesis Work

1. M. Varshney, S. Soni, A. Banwal, **M. Narwan**, M. Verma, R. Bokolia, “Effect of Er^{3+} ion incorporation on the structural, photoluminescence, and ferroelectric properties of KNN ceramic for optoelectronic applications”, *Applied Physics A* 130,2024, 267 (I.F. 2.8)
2. A. Basith, S. Singh, A. Banwal, **M. Narwan**, M. Verma, R. Bokolia “Regulating novel tunable green to red upconversion luminescence in $\text{Er}^{3+}/\text{Yb}^{3+}$ co-doped $\text{SrBi}_2\text{Nb}_2\text{O}_9$ ferroelectric ceramics” *Ceramic International* 50(2024) 52344-52355. (I.F 5.6)
3. V. Khare, D. Garg, S.P Singh, **M.Narwan**, M. Verma, R. Bokolia, “Multifunctional Er^{3+} -Doped $\text{SrBi}_2\text{Ta}_2\text{O}_9$ Ceramics: Optimized Energy Storage and Photoluminescence Properties for Advanced Electronic Applications” *Applied Physics A* (I.F. 2.8)

Research Work Presented at International Conferences

1. **M. Narwan**, R. Sharma, R Bokolia “**Fabrication and Characterization of Piezoelectric Composite of BNT/PVDF for energy harvesting applications**”, in 2nd International Analytical Conference & Exhibition, (IAC-2022), organized by Graphic Era University, Dehradun, India.
2. **M. Narwan**, R. Sharma, R Bokolia “**BNT/PVDF Flexible Composite Films for Energy Harvesting Application**” in International Conference on Nanotechnology for Sustainable Living and Environment (ICON NSLE-2022), organized by BITS Pilani, Rajasthan, India.
3. **M. Narwan**, R. Sharma, R Bokolia “**Enhanced output performance of a flexible piezoelectric energy harvester based on BNT/PVDF composite films**” in 1st International conference on Recent Trends in Physical, Chemical, Biological Nanosciences-2022 organized by Lal Bahadur Shastri College of Arts, Science and Commerce Satara, Maharashtra, India.
4. **M. Narwan**, A. Banwal, R. Bokolia “**Comparative study of structural, upconversion and ferroelectric properties in Er³⁺ doped and Er³⁺/Yb³⁺ co-doped BNT ceramic**” in International Conference on Atomic, Molecular, Material, Nano and optical Physics with Applications (ICAMNOP-2023) organized by Delhi Technological University, Delhi, India.
5. A. Basith, S. Singh, A. Banwal, **M. Narwan**, M. Verma, and R. Bokolia, “**Structural, photoluminescence, and ferroelectric behaviour of Er³⁺/Yb³⁺ co-doped SrBi₂Nb₂O₉ ferroelectric ceramic for multifunctional device**”, in International Conference on Atomic, Molecular, Material, Nano and optical Physics with Applications (ICAMNOP-2023) organized by Delhi Technological University, Delhi, India.

TABLE OF CONTENTS

	<i>Page No.</i>
<i>Acknowledgement</i>	<i>iii-iv</i>
<i>Candidate's Declaration</i>	<i>v</i>
<i>Certificate</i>	<i>vi</i>
<i>Abstract</i>	<i>vii-x</i>
<i>List of Publications</i>	<i>xi-xii</i>
<i>Table of Contents</i>	<i>xiii-xvii</i>
<i>List of Figures</i>	<i>xix-xxiii</i>
<i>List of Tables</i>	<i>xxiv</i>
<i>List of Abbreviations</i>	<i>xxv</i>
Chapter 1: Introduction	1-23
1.1 Luminescence	2
1.1.1 Jablonski Diagram for Fluorescence and Phosphorescence	4
1.1.2 Down-conversion and Upconversion Photoluminescence Processes	5
1.1.3 Upconversion Luminescence Mechanism	6
1.1.3.1 Excited State Absorption Process	7
1.1.3.2 Energy Transfer Process	7
1.1.3.3 Cooperative Process	9
1.1.3.4 Cross Relaxation Process	9
1.1.3.5 Photon Avalanche Process	10
1.2 Selection of Host Materials	11
1.2.1 Ferroelectric Host Material	12
1.3 Selection of Suitable Dopants	12
1.3.1 Lanthanide Dopants	13
1.3.2 Non-Lanthanide Dopants	17

	<i>Page No.</i>
1.4 Applications	17
1.5 Thesis Objectives	18
1.6 Thesis Organization	19
1.6.1 Overview of Thesis	21
1.7 References.....	22
Chapter 2: Synthesis and Characterization Details.....	24-45
2.1 Synthesis Process	25
2.1.1 Selection of Raw Materials	26
2.1.2 Stoichiometric Weighing of Raw Material	27
2.1.3 Mixing of Raw Material.....	27
2.1.4 Calcination of Mixed Raw Material Formation of Pellets.....	27
2.1.5 Formation of Pellets Sintering	28
2.1.6 Sintering.....	29
2.2 Experimental and Characterization Details	30
2.2.1 X-ray Diffraction (XRD)	30
2.2.2 Scanning Electron Microscopy (SEM)	33
2.2.3 Fourier Transform Infrared Spectroscopy (FTIR)	34
2.2.4 Diffuse Reflectance Spectroscopy	36
2.2.5 Photoluminescence Spectroscopy (PL).....	38
2.2.6 Upconversion Luminescence Spectroscopy	40
2.2.6.1 Time-Resolved Photoluminescence (TRPL)	41
2.2.6.2 Optical Temperature Sensing	41
2.2.7 P-E Hysteresis loop.....	42
2.3 Summary	43
2.4 References.....	44

Chapter 3: Upconversion Luminescence and Temperature Sensing Properties of Er³⁺ Doped Bi_{0.5}Na_{0.5}TiO₃ Ferroelectric Ceramic.....	46-71
3.1 Introduction.....	47
3.2 Synthesis and Characterization Details.....	49
3.3 Results and Discussion	51
3.3.1 Structural and Microstructural Analysis	51
3.3.2 Fourier Transform Infrared (FTIR) Spectroscopy	54
3.3.3 Diffuse Reflectance Spectroscopy for Band Gap Analysis	54
3.3.4 Ferroelectric Hysteresis Analysis and Energy Storage Density	56
3.3.5 Temperature Independent PL Spectra under 488 nm	58
3.3.6 Visible Light Upconversion Luminescence under 980 nm	59
3.3.7 Time Resolved Decay Time Measurement.....	61
3.3.8 Upconversion Luminescence with Varying Pump Power	62
3.3.9 Non-Intrusive Temperature Sensitivity.....	63
3.4 Summary.....	65
3.5 References.....	67
Chapter 4: Upconversion Luminescence and Temperature Sensing Properties of Er³⁺/Yb³⁺ Co-Doped Bi_{0.5}Na_{0.5}TiO₃ Ferroelectric Ceramic	72-97
4.1 Introduction.....	73
4.2 Synthesis and Characterization Details.....	75
4.3 Results and Discussion	77
4.3.1 Structural and Microstructural Analysis	77
4.3.2 FTIR Spectroscopy	80
4.3.3 Diffuse Reflectance Spectroscopy	80
4.3.4 Downshifting Photoluminescence Spectroscopy.....	82
4.3.5 Upconversion Luminescence (UCL) Spectroscopy.....	83
4.3.6 Time Decay Analysis.....	84

	<i>Page No.</i>
4.3.7 Pump Power Dependency	86
4.3.8 Optical temperature Sensitivity.....	87
4.4 Summary	89
4.5 References.....	91
Chapter 5: Upconversion Luminescence and Temperature Sensing Properties of Ho³⁺ Doped Bi_{0.5}Na_{0.5}TiO₃ Ferroelectric Ceramic	98-128
5.1 Introduction.....	99
5.2 Synthesis and Characterization Details.....	102
5.3 Results and Discussion	104
5.3.1 XRD and SEM	104
5.3.2 FTIR Spectroscopy	107
5.3.3 Diffuse Reflectance and Optical Band Gap	108
5.3.4 Photoluminescence Spectra	110
5.3.5 Upconversion Luminescence Spectra.....	111
5.3.6 Time Decay Measurement	113
5.3.7 Pump Power Analysis	114
5.3.8 Ferroelectric Curve and Energy Storage Density	115
5.3.9 Optical Temperature Sensing.....	117
5.4 Summary	119
5.5 References.....	121
Chapter 6: Flexible BNT-PVDF Thin Film with Tunable Composition for Energy Harvesting Application	121-156
6.1 Introduction.....	130
6.2 Experimental Details.....	133
6.2.1 Preparation of BNT Powder.....	133
6.2.2 Fabrication of PVDF -BNT Flexible Composite Films.....	134
6.2.3 Fabrication of a Piezoelectric Generator Based on BNT/PVDF Composite	135

	<i>Page No.</i>
6.2.4 Characterization	135
6.3 Analysis of Results	136
6.3.1 Study of Structural and Surface Morphological Properties of BNT Ceramic Powder.....	136
6.3.2 Investigation of the Structural Behaviour of PVDF and BNT/PVDF Composite Materials.....	137
6.3.3 Comparative Analysis of the Surface Morphological of BNT, PVDF and BNT/PVDF Films	139
6.3.4 Fourier Transform Infrared Spectral Analysis.....	140
6.3.5 Polarization Electric Field (P-E) Hysteresis Characterization.....	142
6.3.6 Piezoelectric Voltage Response of PVDF and BNT/PVDF Nanocomposite Films	144
6.3.7 Piezoelectric Current Output from PVDF and BNT/PVDF Nanocomposites	146
6.3.8 Validation of Output Characterization Using LED Illumination	148
6.4 Summary	149
6.5 References.....	150
Chapter 7: Conclusion, Future Scope, And Social Impact	157-163
7.1 Conclusion	158
7.2 Future Scope	161
7.3 Social Impact	162
Publication Papers	164-167

LIST OF FIGURES

<i>Figures</i>	<i>Page No.</i>
Figure 1.1 : Classification of luminescence	2
Figure 1.2 : Jablonski schematic representing fluorescence and phosphorescence processes	5
Figure 1.3 : Representation of Downconversion and upconversion luminescence	6
Figure 1.4 : Representation of the excited state absorption process	7
Figure 1.5 : Representation of the energy transfer process	8
Figure 1.6 : Representation of the Cooperative process	9
Figure 1.7 : Representation of the Cross-relaxation process	10
Figure 1.8 : Representation of the Photon avalanche process	11
Figure 1.9 : Types of energy level splitting due to various interaction within the host	15
Figure 1.10 : Flowchart for the organisation of the thesis	21
Figure 2.1 : Schematic representation of the steps involved in the synthesis of ceramic using solid state method	26
Figure 2.2 : High temperature muffle furnace for calcination of the prepared sample	28
Figure 2.3 : Hydraulic press and pelletizer for making pellets	29
Figure 2.4 : Steps involved during sintering process	30
Figure 2.5 : (a) Bragg's Diffraction representation from crystal planes	31
Figure 2.6 : Bruker D8 Advance X-ray diffractometer	33
Figure 2.7 : JEOL Japan Mode: JSM 6610LV Scanning Electron Microscope (SEM)	34
Figure 2.8 : Perkin Elmer's Frontier FTIR spectrometer	36
Figure 2.9 : Phenomenon of specular and diffuse reflectance	36
Figure 2.10 : Jasco V-770 Spectrophotometer	38
Figure 2.11 : Jasco Spectrophotometer Spectrofluorometer FP-8300	40
Figure 2.12 : Upconversion luminescence spectroscopy Horiba PTI Quanta Master equipped using 980 nm laser	41

<i>Figures</i>	<i>Page No.</i>
Figure 2.13 : Temperature-dependent sensing upconversion luminescence	42
Figure 2.14 : P-E Hysteresis Loop Tracer	43
Figure 3.1 : Pictorial depiction of synthesis process (solid-state method).....	50
Figure 3.2 : (a) XRD spectra of $\text{Bi}_{0.5-x}\text{Er}_x\text{Na}_{0.5}\text{TiO}_3$ ($x=0.00, 0.01, 0.02, 0.03, 0.04, 0.05$), (b) Peak shifting of (110) plane, (c) Profile fitting using Topaz software	52
Figure 3.3 : (a-f) SEM micrographs of $\text{Bi}_{0.5-x}\text{Er}_x\text{Na}_{0.5}\text{TiO}_3$ ($x=0.00, 0.01, 0.02, 0.03, 0.04, 0.05$). Inset: Histograms for grain size calculation.....	53
Figure 3.4 : FTIR Spectra of $\text{Bi}_{0.5-x}\text{Er}_x\text{Na}_{0.5}\text{TiO}_3$ ($x=0.00, 0.01, 0.02, 0.03, 0.04, 0.05$) ferroelectric ceramic	54
Figure 3.5 : (a) Diffuse reflectance spectra of $\text{Bi}_{0.5-x}\text{Er}_x\text{Na}_{0.5}\text{TiO}_3$ ($x=0.00, 0.03, 0.05$) (b-d) Energy band gap of $\text{Bi}_{0.5-x}\text{Er}_x\text{Na}_{0.5}\text{TiO}_3$ ($x=0.00, 0.03, 0.05$)	55
Figure 3.6 : PE loop of $\text{Bi}_{0.5-x}\text{Er}_x\text{Na}_{0.5}\text{TiO}_3$ ($x=0.00, 0.01, 0.02, 0.03, 0.04, 0.05$) at room temperature.....	57
Figure 3.7 : PL spectra of prepared $\text{Bi}_{0.5-x}\text{Er}_x\text{Na}_{0.5}\text{TiO}_3$ ($x=0.01, 0.02, 0.03, 0.04, 0.05$) under the excitation of 488 nm	58
Figure 3.8 : (a) UCL spectra of $\text{Bi}_{0.5-x}\text{Er}_x\text{Na}_{0.5}\text{TiO}_3$ ($x=0.01, 0.02, 0.03, 0.04, 0.05$) at 980 nm excitation, (b) UCL intensity as a function of Er^{3+} concentration, (c) Energy level diagram of Er^{3+} , (d) CIE plot of $\text{Bi}_{0.5-x}\text{Er}_x\text{Na}_{0.5}\text{TiO}_3$ ($x=0.01, 0.02, 0.03, 0.04, 0.05$)	60
Figure 3.9 : (a-e) Time decay analysis of $\text{Bi}_{0.5-x}\text{Er}_x\text{Na}_{0.5}\text{TiO}_3$ ($x=0.01, 0.02, 0.03, 0.04, 0.05$), (f) Variation of lifetime with Er^{3+} concentration.....	61
Figure 3.10 : Pump Power dependency on UCL spectra of $\text{Bi}_{0.5-x}\text{Er}_x\text{Na}_{0.5}\text{TiO}_3$ ($x=0.03$) ferroelectric ceramic.....	62
Figure 3.11 : (a) Temperature dependent UCL spectra, (b) Plot of LIR and temperature, (c) $\text{Ln}(\text{LIR})$ vs inverse temperature, (d) Plot of absolute (S_{ab}) and relative sensitivity (S_{rel})	64
Figure 3.12 : (a) Repeatability test varying between two temperatures (303K-523K), (b) Plot of δT vs temperature	65
Figure 4.1 : Pictorial depiction of synthesis process (solid-state method).....	76
Figure 4.2 : (a) XRD patterns showing rhombohedral symmetry in all BNT compositions (b) Peak shifting of (110) plane.....	78

<i>Figures</i>	<i>Page No.</i>
Figure 4.3 : SEM images of BNT compositions (a) BE0Y0 (b) BE3Y0 (c) BE3Y1 (d) BE3Y5 (e) BE3Y9 and (f) BE3Y11. Inset: Histograms for grain size calculation	79
Figure 4.4 : FTIR spectra of prepared BNT ceramic compositions	80
Figure 4.5 : (a) Diffuse reflectance spectra of all the prepared BNT ceramic compositions, the Energy band gap of (b) BE0Y0 (c) BE3Y0 (d) BE3Y3 (e) BE3Y7 and (f) BE3Y13	81
Figure 4.6 : Downshifting photoluminescence (a) excitation spectra (b) emission spectra of prepared BNT ceramic compositions.....	82
Figure 4.7 : (a) UCL spectra of Er^{3+} doped and series of $\text{Er}^{3+}/\text{Yb}^{3+}$ co-doped BNT ceramic compositions (b) UC emission versus dopant concentration (c) Energy level diagram showing possible pathways for UCL emission	84
Figure 4.8 : Time decay profile of BNT compositions (a) BE3Y0 (b) BE3Y1 (c) BE3Y3 (d) BE3Y5 (e) BE3Y7	85
Figure 4.9 : (a) Pump power dependency on UCL spectra of BE3Y3 ceramic compositions (b) Ln (intensity) versus Ln (power) plot	86
Figure 4.10 : (a) Temperature dependent UCL spectra (b) Plot of FIR and temperature (c) Ln (FIR) vs T^{-1} , (d) Plot of S_{ab} and S_r	88
Figure 4.10 : (e) Repeatability test between 303 K and 523 K (f) Plot of δT vs temperature.....	89
Figure 5.1 : Pictorial depiction of the synthesis process	103
Figure 5.2 : (a) XRD plot of undoped and Ho^{3+} doped BNT, (b) peak shifting of (110) plane, (c) profile fitting using topaz software.....	105
Figure 5.3 : (a-e) SEM of $\text{Bi}_{0.5-x}\text{Ho}_x\text{Na}_{0.5}\text{TiO}_3$ ($x = 0.00 - 0.07$). Inset: Histograms for grain size calculation (f) variation of an average size of particles with dopant concentrations.....	106
Figure 5.4 : (a) FTIR spectra of pure and Ho^{3+} doped BNT ferroelectric ceramic, (b) shift in the FTIR bands	108
Figure 5.5 : (a) DRS of pure and Ho^{3+} doped BNT, (b-e) energy band gap of $\text{Bi}_{0.5-x}\text{Ho}_x\text{Na}_{0.5}\text{TiO}_3$ ($x = 0.00, 0.01, 0.03, 0.05, 0.07$)	109
Figure 5.6 : (a) Excitation spectra of Ho^{3+} doped BNT at 550 nm emission wavelength, (b) emission spectra of Ho^{3+} doped BNT at 452 nm excitation wavelength, (c) CIE plot	110

<i>Figures</i>	<i>Page No.</i>
Figure 5.7 : (a) UCL spectra of Ho ³⁺ doped BNT ceramic at 550 nm emission wavelength, (b) comparison of UCL intensity of various Ho ³⁺ doped BNT ceramic, (c) energy levels of Ho ³⁺ ions for possible UC process, (d) CIE plot	112
Figure 5.8 : (a-e) Time decay of green band for Ho ³⁺ doped BNT ceramics	113
Figure 5.9 : (a-e) Time decay of orange band for Ho ³⁺ doped BNT ceramics	114
Figure 5.10 : Pump power dependency on UCL spectra and log-log plot (Inset)	115
Figure 5.11 : (a) PE loops for undoped and doped BNT, (b) variation of energy storage density parameters	116
Figure 5.12 : (a) Variation of UCL spectra with T, (b) FIR vs. temperature plot, (c) plot of Ln(FIR) against T ⁻¹ , (d) variation of S _{ab} and S _r with T	117
Figure 5.13 : (a) Repeatability test between 303K and 553K, (b) plot of δT vs temperature	119
Figure 6.1 : Schematic diagram outlining the preparation process of BNT ceramic	133
Figure 6.2 : Schematic diagram showing the preparation of flexible BNT/PVDF composite films.....	134
Figure 6.3 : A schematic illustration of the PEG device with its key component.....	135
Figure 6.4 : XRD plot representing the calcined BNT ceramic sample	136
Figure 6.5 : (a) Micrograph obtained by SEM illustrating the morphology of the calcined BNT ceramic powder (b) the corresponding size distribution of particles	137
Figure 6.6 : (a) XRD spectra of PVDF and PVDF composites films containing different amounts of BNT ceramic powder and (b) a magnified section of Fig. 6(a) with 2θ ranging from 12° to 22°	138
Figure 6.7 : (a-f) SEM micrographs images of surface structure of PVDF and BNT/PVDF composite films with varying content of BNT powder (5, 10, 15, 20 and 25 %) at a scale of 1 μ m	140
Figure 6.8 : FTIR spectra of pure PVDF and BNT/PVDF composite films containing varying amounts of BNT ceramic.....	141

<i>Figures</i>	<i>Page No.</i>
Figure 6.9 : P-E loops of pristine PVDF and composite films incorporating various concentrations of BNT ceramics in the PVDF matrix.....	143
Figure 6.10 : (a-f) Output voltage response of PVDF and BNT/PVDF Nanocomposite films at 7 Hz frequency.....	145
Figure 6.11 : Output Current obtained for PVDF and BNT/PVDF Nanocomposites Films at 7 Hz frequency	147
Figure 6.12 : (a) Output voltage and current measurements of PNG devices with different load resistance and (b) power measurement of PNG device with different load resistance	147
Figure 6.13 : A schematic showing the circuit diagram of PNG device used to illuminate the LEDs with photographic image of LEDs illumination.....	148

LIST OF TABLES

<i>Tables</i>	<i>Page No.</i>
Table 2.1 : Details of precursor powders used for preparing doped and undoped $\text{Bi}_{0.5}\text{Na}_{0.5}\text{TiO}_3$ ceramics.....	27
Table 3.1 : Lattice and fitting parameters of XRD pattern for $\text{Bi}_{0.5-x}\text{Er}_x\text{Na}_{0.5}\text{TiO}_3$ with different concentration	53
Table 3.2 : Hysteresis loop parameters ($2P_r$, $2E_c$) and energy storage density parameters (W , W_{rec} , η) estimated from the Rietveld refinement of XRD pattern for $\text{Bi}_{0.50-x}\text{Er}_x\text{Na}_{0.5}\text{TiO}_3$ with different concentration.....	57
Table 3.3 : Sensitivity parameters of various Er^{3+} doped ferroelectric ceramics	65
Table 4.1 : Coding of prepared undoped and doped BNT compositions.....	77
Table 4.2 : Lattice and refinement parameters for all the BNT ceramic compositions	79
Table 4.3 : Absolute sensitivity values of various Er/Yb co-doped ferroelectric ceramic	89
Table 5.1 : Parameters of XRD pattern for $\text{Bi}_{0.5-x}\text{Ho}_x\text{Na}_{0.5}\text{TiO}_3$ with different concentrations	107
Table 5.2 : Summary of PE loop parameters ($2P_r$, $2E_c$) and energy storage density parameters (W , W_{rec} , $\eta\%$).....	117
Table 6.1 : Remnant Polarization value of PVDF and its composite films with different concentrations of BNT	143
Table 6.2 : Value of Voltage vs Time with different concentrations.....	145
Table 6.3 : Tabulated Performance of Various Energy Harvesting Materials	145
Table 6.4 : Value of Current vs Time with different concentrations	147

LIST OF ABBREVIATIONS

Acronym	:	Meaning
BNT	:	Bismuth Sodium Titanate
DC	:	Downconversion
DRS	:	Diffuse Reflectance Spectroscopy
Er	:	Erbium
ESA	:	Excited State Absorption
ETU	:	Energy Transfer Upconversion
FIR	:	Fluorescence Intensity Ratio
FTIR	:	Fourier Transform Infrared Spectroscopy
Ho	:	Holmium
K–M	:	Kubelka–Munk
LIR	:	Luminescence Intensity Ratio
PDMS	:	Polydimethylsiloxane
P–E	:	Polarization–Electric Field
PL	:	Photoluminescence
PLE	:	Photoluminescence Excitation
PMT	:	Photomultiplier Tube
PVDF	:	Polyvinylidene Fluoride
RT	:	Room Temperature
SEM	:	Scanning Electron Microscopy
TCLs	:	Thermally Coupled Levels
TPU	:	Thermoplastic polyurethanes
UC	:	Upconversion
UV–Vis	:	Ultraviolet–Visible
XRD	:	X-ray Diffraction
Yb	:	Ytterbium

CHAPTER - 1

Introduction

- ❖ *This chapter provides an in-depth exploration of luminescence, beginning with its basic principles and various classifications. The discussion mainly focuses on the concept of photoluminescence, with particular emphasis on upconversion (UC) photoluminescence.*
- ❖ *The upconversion mechanisms and recent advancements in materials incorporating both lanthanide and non-lanthanide dopants. Furthermore, it examines the critical role of the host lattice, emphasizing its energy storage capabilities and performance characteristics when combined with various rare-earth ion dopants.*
- ❖ *This section analyses the optical temperature sensing methodology employing the fluorescence intensity ratio (FIR) approach and highlights the pivotal role of ferroelectric host materials doped with rare-earth ions in enhancing sensing performance.*

1.1 Luminescence

Luminescence is defined as the emission of light from a material upon excitation by energy sources other than thermal energy, such as electrical stimulation, chemical reactions, lattice vibrations, or mechanical pressure applied to a crystal structure. This phenomenon arises when a material absorbs energy and subsequently re-emits it in the form of light. The term *luminescence* typically refers to cold-body radiation, wherein absorbed energy is converted into light without significant heat generation. Luminescence is further classified based on the nature of the excitation source, as depicted in (Figure. 1.1). The fundamental principles underlying these classifications were first introduced by E. Wiedemann in 1888.

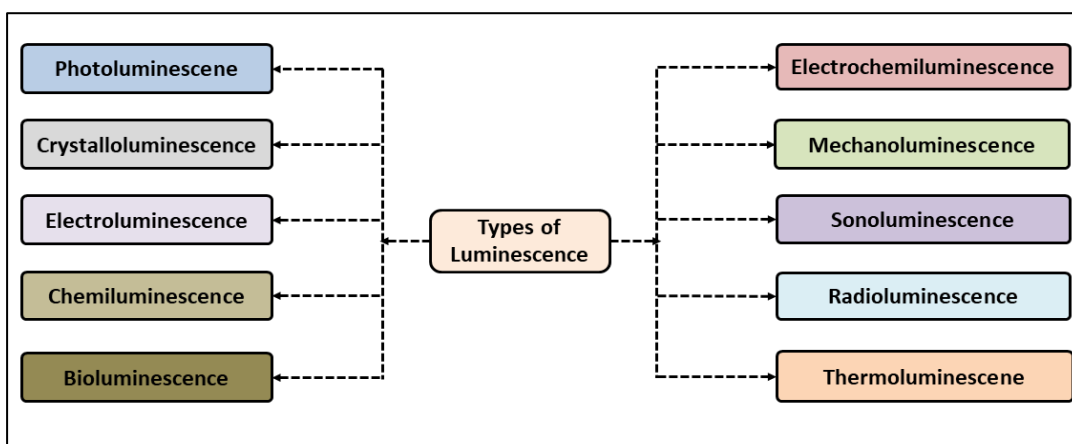


Figure 1.1: Classification of luminescence

Photoluminescence is the emission of light from a material after it absorbs photons. When the material absorbs light energy, its electrons move to higher energy states and then release photons as they return to their original levels. This process is widely used to study the electronic and optical properties of semiconductors, nanomaterials, and other luminescent substances.

Electroluminescence is the emission of light from a material when subjected to an electric field or current, without heat or chemical reactions. It occurs mainly in semiconductors and phosphors, where electron–hole recombination releases photons. The emitted light's color and intensity depend on the material's bandgap and applied voltage, making EL useful in LEDs, displays, and optoelectronic devices.

Bioluminescence is the natural emission of light by living organisms through biochemical reactions. It typically occurs when an enzyme reacts with a light-producing molecule called luciferin in the presence of oxygen, releasing visible light.

Mechanoluminescence is the emission of light from a material when it experiences mechanical action such as pressure, friction, or deformation. This effect occurs due to the release of trapped energy or charge carriers within the material's structure during mechanical stress. It is often used in sensors, stress analysis, and smart material applications.

Electrochemiluminescence is a light-emission process that occurs when electrochemically generated reactive species undergo electron transfer reactions near the electrode surface, leading to the formation of excited states that relax by photon emission. This technique combines the high sensitivity of luminescence with the controllability of electrochemical methods, making it highly useful in sensing, bioimaging, and analytical applications.

Sonoluminescence is the emission of light from a liquid medium when subjected to intense acoustic fields. It typically occurs when a sound wave of sufficiently high amplitude passes through a liquid, leading to the formation and oscillation of gas-filled microbubbles. During acoustic compression, these bubbles collapse rapidly and generate extremely high local temperatures and pressures within a very short duration, resulting in the release of light.

Radioluminescence is the emission of light from a material when it is exposed to ionizing radiation, such as alpha, beta, or gamma rays. The radiation excites atoms in the material, and as they return to their stable state, photons are released. This phenomenon is often used in watch dials, emergency signs, and radiation detection systems.

This thesis emphasizes the study of photoluminescence, and it is therefore necessary to describe its different forms in detail. Broadly, photoluminescence can be separated into two categories: fluorescence, which involves rapid radiative emission, and phosphorescence, which is characterized by a longer-lived emission process. Furthermore, depending on the way incident light is converted, photoluminescence is

generally classified into down-conversion, where higher-energy photons are converted into lower-energy emission, and up-conversion, in which lower-energy photons are combined to produce higher-energy emission.

1.1.1 Jablonski Diagram for Fluorescence and Phosphorescence

Figure 1.2 shows the Jablonski diagram, illustrating the mechanisms of fluorescence and phosphorescence. In this diagram, the singlet ground state is represented as S_0 , while S_1 and S_2 denote the excited singlet states.

When photons with an appropriate frequency strike a phosphorescent material, the material absorbs this energy. The first step in the diagram is the photon absorption by the molecule, indicated by an upward straight arrow. This absorption promotes an electron from the ground state to a higher electronic state, a process that takes place extremely quickly, within about 10^{-15} seconds.

Once the electron reaches the excited state, it becomes unstable and begins to lose energy through different mechanisms, including vibrational relaxation and non-radiative processes, shown as curved arrows between the vibrational energy levels in the diagram. In vibrational relaxation, the absorbed energy is transferred into vibrational motion, either within the same molecule or to nearby molecules, depending on the phase of the material. This energy dissipation happens very rapidly, typically within 10^{-4} to 10^{-8} seconds.

If the vibrational levels overlap significantly with the electronic states, the excited electron can undergo a transition between vibrational levels of different electronic states, a process known as internal conversion. This mechanism is similar to vibrational relaxation and occurs due to the interaction between vibrational and electronic energy states. However, because there is a relatively large energy gap between the ground state and the first excited state, the electron's return to the ground state through internal conversion is comparatively slow.

When the molecule returns from the excited singlet state (S_1) to the ground singlet state (S_0) while emitting light, the phenomenon is called fluorescence. This radiative decay typically occurs within picoseconds to nanoseconds (10^{-3} to 10^3 seconds) and is depicted by a straight downward arrow in the energy diagram connecting the electronic states.

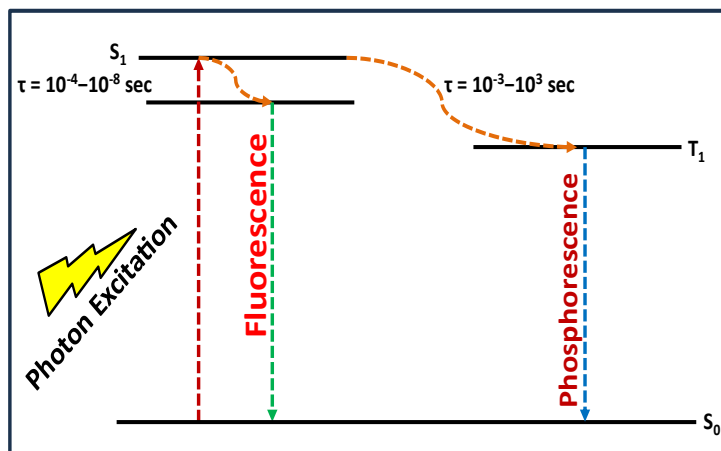


Figure 1.2: Jablonski schematic representing fluorescence and phosphorescence processes

1.1.2 Down-Conversion and Up-Conversion Photoluminescence Processes

Down-conversion refers to the process in which an absorbed photon of higher energy is transformed into one or more emitted photons of lower energy. In other words, the excitation occurs at shorter wavelengths (higher frequency), while the emission appears at longer wavelengths (lower frequency). This mechanism is particularly useful for improving the efficiency of optoelectronic devices, as it minimizes energy loss by converting high-energy radiation into the spectral region where the material or device has better response. In luminescent materials, down-conversion is often associated with rare-earth ions or other dopants that possess well-defined electronic transitions, enabling sharp emission lines with good stability. However up-conversion is a nonlinear optical process in which two or more low-energy photons are absorbed sequentially or simultaneously, resulting in the emission of a single photon with higher energy. Unlike down-conversion, the excitation occurs in the longer wavelength region, typically in the infrared, while the emitted light appears at shorter wavelengths, such as in the visible range. This phenomenon is commonly observed in materials doped with rare-earth ions, where intermediate energy levels facilitate the stepwise absorption of photons. Up-conversion has attracted considerable interest due to its potential applications in bio-imaging, solar energy conversion, security labelling, and photonic devices. **Figure 1.3** depicts the schematic diagram describing upconversion and Downconversion photoluminescence. This thesis mainly emphasizes upconversion luminescence (UCL); hence, the different mechanisms of UCL are outlined in the following section.

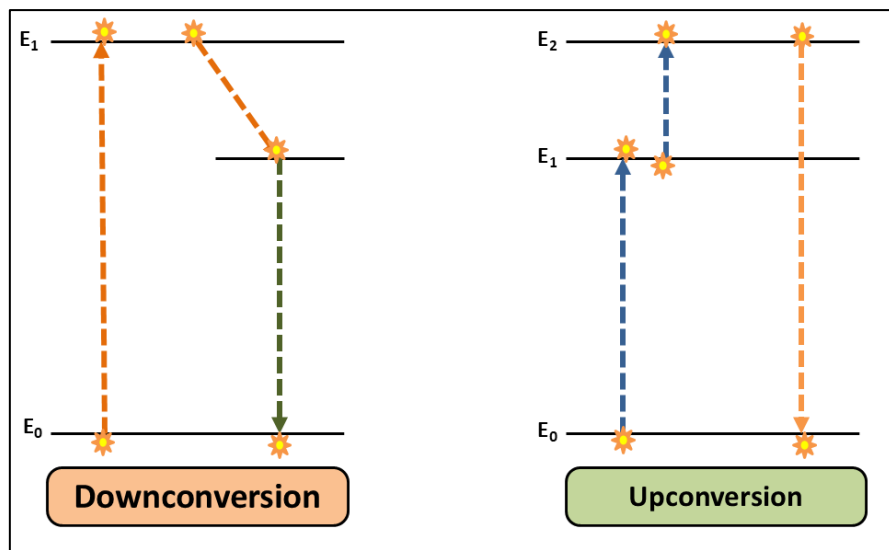


Figure 1.3: Representation of Downconversion and upconversion luminescence

1.1.3 Upconversion Luminescence Mechanism

Upconversion luminescence (UCL) is a process in which two or more photons of lower energy are absorbed successively and converted into the emission of a single photon of higher energy. This anti-Stokes type emission is characteristic of rare-earth-doped materials, where the presence of long-lived intermediate energy states allows stepwise excitation. As a result, incident near-infrared radiation can be converted into visible or even ultraviolet emission, making UCL fundamentally different from conventional Downconversion processes [1].

The main mechanisms responsible for UCL are excited state absorption (ESA), energy transfer upconversion (ETU), photon avalanche (PA), and cooperative sensitization (CS). In ESA, a single ion sequentially absorbs multiple photons, moving through intermediate states until it reaches a higher excited state, followed by radiative relaxation. ETU, which is the most efficient mechanism in many host lattices, involves interaction between sensitizer and activator ions; for example, Yb^{3+} ions absorb infrared photons and transfer the energy to Er^{3+} or Tm^{3+} ions, thereby promoting them to higher energy levels.

The effectiveness of these mechanisms strongly depends on factors such as dopant ion concentration, host lattice structure, phonon energy, and the excitation power density. Due to these unique properties, UCL has become highly significant in applications including optical imaging, solid-state lighting, laser technology, and solar energy conversion.

1.1.3.1 Excited State Absorption Process

The schematic diagram illustrates the Excited State Absorption (ESA) mechanism in a single ion system under near-infrared (NIR) excitation. The process begins when the ion, initially in the ground state energy level (E_1), absorbs an NIR photon and is excited to the metastable state (E_2). This primary excitation is known as Ground State Absorption (GSA) (Figure 1.4).

From the metastable state, the ion can absorb a second NIR photon, promoting it further to a higher excited energy level (E_3). This secondary absorption is referred to as Excited State Absorption (ESA). Once the ion reaches the higher excited state, it can relax radiatively back to a lower level, emitting a photon of higher energy than the incident excitation. This phenomenon is identified as upconversion (UC) emission, where the emitted photon lies in the visible region, even though the excitation occurs in the NIR region [2].

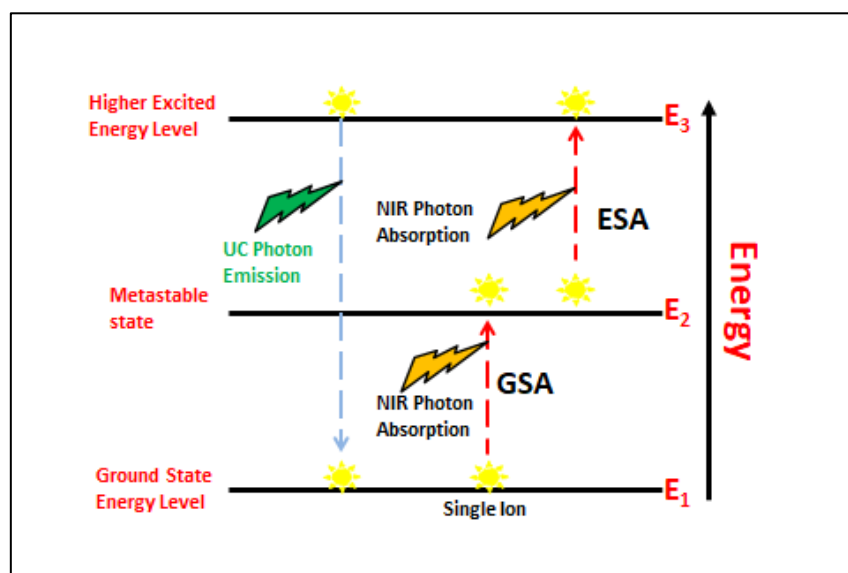


Figure 1.4: Representation of the excited state absorption process

1.1.3.2 Energy Transfer Process

The diagram represents the Energy Transfer Upconversion (ETU) process Figure 1.5, which involves two neighboring ions and is distinct from the single-ion Excited State Absorption (ESA) mechanism [3].

In this case, the first ion absorbs a near-infrared (NIR) photon through Ground State Absorption (GSA), leading to its excitation from the ground state energy level (E_1) to

the metastable state (E_2). Similarly, a second ion also undergoes GSA to reach its own metastable state. Once both ions are in the excited state, a non-radiative energy transfer interaction occurs between them. The excited first ion transfers part of its energy to the second ion, thereby promoting the second ion from the metastable level (E_2) to a higher excited state (E_3) [4].

As a result of this cooperative interaction, the second ion reaches an elevated energy state without directly absorbing a second photon, unlike in the ESA process. When this excited ion relaxes radiatively back to the lower levels, it emits a photon of higher energy compared to the excitation source. This phenomenon is observed as upconversion luminescence (UC emission) [5].

The ETU mechanism is particularly significant in lanthanide-doped systems because of the long-lived metastable states of rare-earth ions, which facilitate efficient energy exchange between neighboring ions. Compared with ESA, the ETU process often dominates in materials with high dopant concentrations, where the proximity of ions enhances interionic interactions [6].

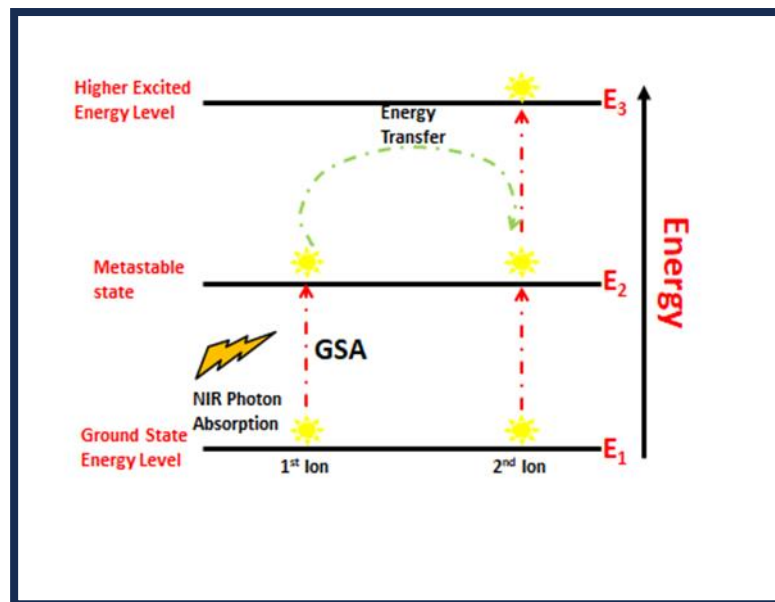


Figure 1.5: Representation of the energy transfer process

1.1.3.3 Cooperative Process

The cooperative energy transfer process involves three ion centers, where two ions (ion 1 and ion 3) are identical. As shown in **Figure 1.6**, upon absorption of excitation photons, both ion 1 and ion 3 are promoted to the metastable state (E_{1S}). These ions can then simultaneously and cooperatively interact with ion 2, transferring their absorbed energy to excite ion 2 from its ground state (E_{0A}) to a higher excited state (E_{1A}). The activator ion in the E_{1A} state subsequently relaxes back to the ground state (E_{0A}), releasing an upconverted photon. In this mechanism, ion 1 and ion 3 serve as sensitizers, absorbing energy from incoming NIR photons and delivering it to ion 2, which acts as the activator responsible for photon emission. Compared with excited state absorption (ESA) and energy transfer (ET), the cooperative process generally exhibits lower efficiency because it proceeds through a quasi-virtual pair level during the transition [7].

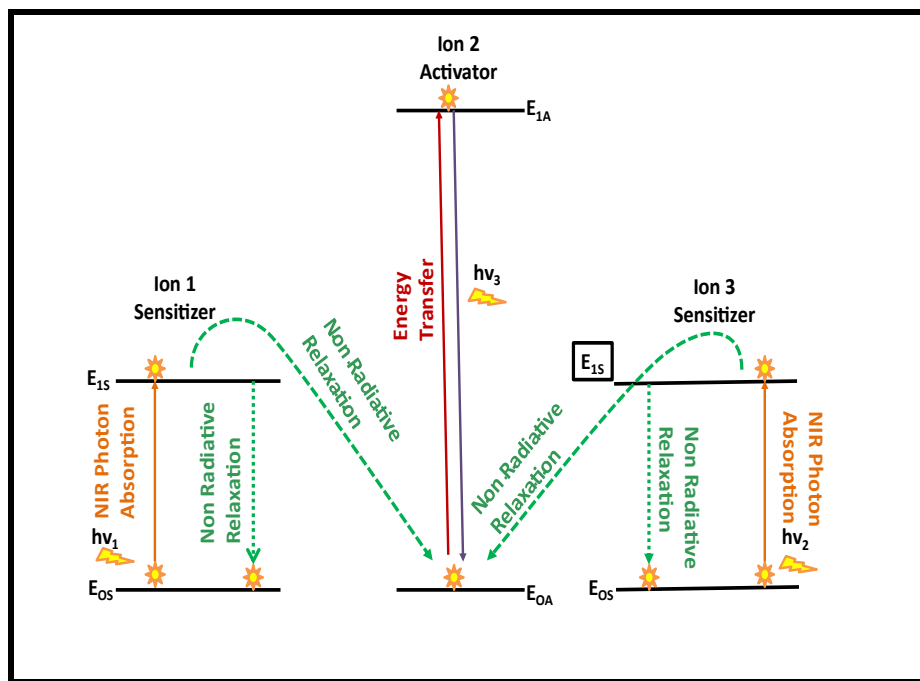


Figure 1.6: Representation of the Cooperative process

1.1.3.4 Cross Relaxation Process

Figure 1.7 illustrates the cross-relaxation (CR) process, in which Ion 1 transfers part of its energy to Ion 2 according to the cycle: E_2 (ion 1) + E_0 (ion 2) \rightarrow E_1 (ion 1) + E_1 (ion 2). The interacting ions may be identical or different, and in some cases, ion 2 can also exist in a higher excited state [6]. The efficiency of CR strongly depends on the dopant

concentration, as the interaction between neighbouring ions establishes the CR loop. This mechanism is a major cause of concentration quenching in luminescence. Nevertheless, cross-relaxation can be purposefully utilized to tune the color of upconversion emission or to trigger an intense photon avalanche process [7].

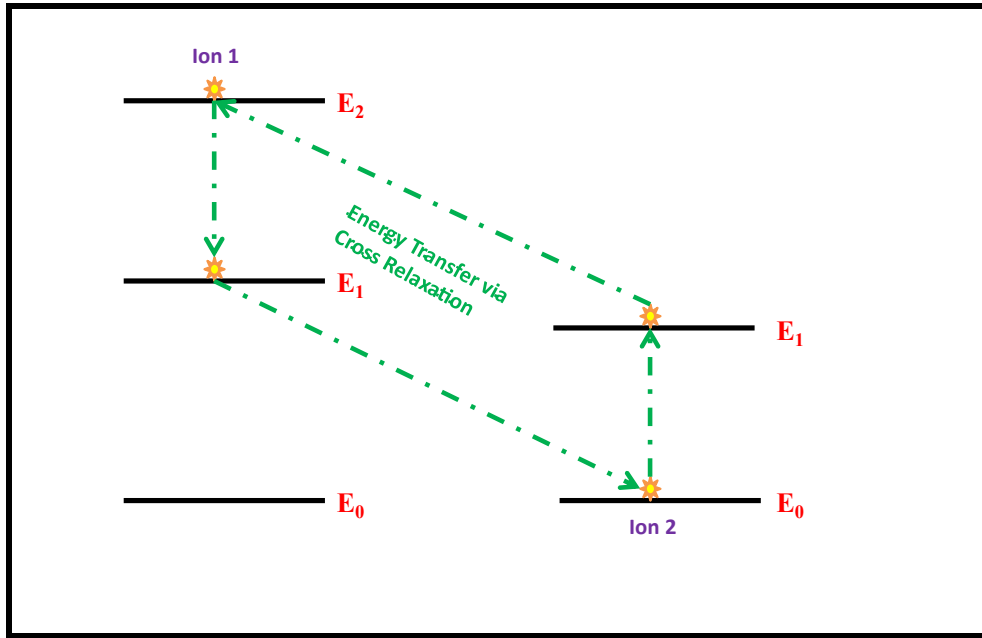


Figure 1.7: Representation of the Cross-relaxation process

1.1.3.5 Photon Avalanche Process

The schematic **Figure 1.8 illustrates** the Photon Avalanche (PA) process, a nonlinear upconversion mechanism involving multiple ions and strong interionic interactions. Unlike Excited State Absorption (ESA) or Energy Transfer Upconversion (ETU), the PA process relies on a feedback loop of excitation and relaxation steps that significantly amplify the upconversion luminescence.

Initially, the first ion is resonantly pumped from the metastable state (E_2) to the higher excited state (E_3) by absorption of a photon. From this elevated level, the ion can undergo avalanche emission, release a photon while simultaneously transfer energy through a cross-relaxation process to a neighbouring second ion. During cross-relaxation, the first ion relaxes back to the metastable state, while the second ion is promoted from its ground state (E_1) to the metastable state (E_2).

The second ion, now in the excited state, can again absorb a resonant photon, undergo further excitation, and repeat the same sequence of cross-relaxation and energy transfer. This cyclic interaction between ions creates a positive feedback loop, resulting in a rapid buildup of population in the excited state and the generation of strong upconversion (UC) emission.

The photon avalanche mechanism is particularly important at high excitation intensities, where the nonlinear response leads to a sharp increase in luminescence output. This process is advantageous in designing highly sensitive optical devices, sensors, and advanced photonic applications due to its strong signal amplification effect.

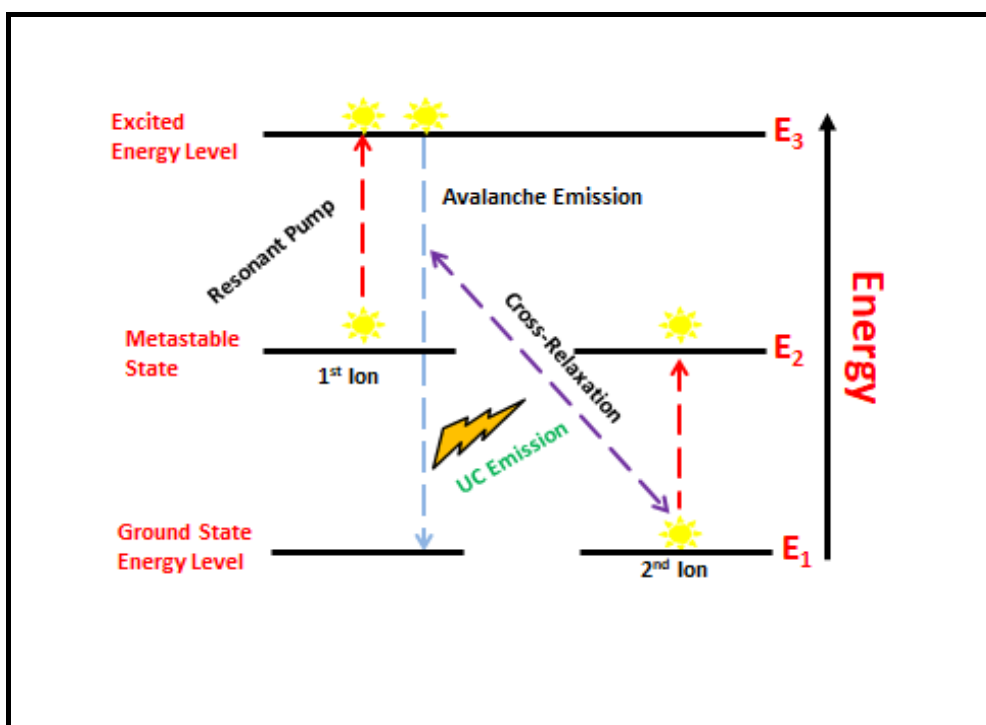


Figure 1.8: Representation of the Photon avalanche process

1.2 Selection of Host Materials

The host material provides the lattice framework that supports dopant ions and governs the luminescent properties of the system. Selecting an appropriate host is therefore a vital step in the development of advanced and efficient luminescent materials. Over the years, researchers have investigated a variety of inorganic hosts, including halides, oxides, silicates, nitrides, sulphides, and phosphates [10]. The performance of luminescent systems strongly depends on the host, making its careful selection essential

for achieving optimal emission characteristics. An ideal host is expected to exhibit a low cut-off phonon frequency, which reduces non-radiative losses and improves optical efficiency, while also maintaining properties such as high thermal and chemical stability, a wide transparency window, a relatively high refractive index, good solubility, and low toxicity [11]. Halides are of particular interest because of their low phonon energy, although their higher toxicity can be a drawback. Both conventional and more complex hosts are often employed to fine-tune the phonon environment and optimize luminescence performance.

1.2.1 Ferroelectric Host Materials

Ferroelectric host materials are an important class of functional oxides that exhibit spontaneous electric polarization, which can be reversed under the influence of an external electric field [12].

In the context of luminescence, ferroelectric hosts provide unique advantages. Their internal electric fields and high dielectric constants enhance the interaction between the dopant ions and the lattice, which can modify radiative transitions and influence the intensity and stability of emission. Moreover, the polar nature of these lattices facilitates better incorporation of rare-earth and transition metal ions, creating localized states that promote efficient luminescence. The presence of intrinsic defects, such as oxygen vacancies, further contributes to optical emission and broadens the spectral response.

Several perovskite oxides, such as barium titanate (BaTiO_3), lead zirconate titanate ($\text{Pb}(\text{Zr},\text{Ti})\text{O}_3$), bismuth sodium titanate ($\text{Bi}_{0.5}\text{Na}_{0.5}\text{TiO}_3$), and potassium niobate (KNbO_3), are widely studied as ferroelectric host matrices [13]. These materials are capable of sustaining strong polarization fields, which directly affect the energy transfer dynamics within the lattice. As a result, ferroelectric hosts serve as promising platforms for the development of advanced luminescent materials with potential applications in solid-state lighting, nonlinear optics, and optoelectronic devices [14].

1.3 Selection of Suitable Dopants

Inorganic upconversion phosphors are generally composed of a crystalline host material combined with dopant ions, most often lanthanides, introduced in small concentrations [15]. The dopant ions function as the main luminescent centers, while the host lattice

provides the structural framework that positions these centers in favorable sites. The exact spacing between rare-earth ions, along with their spatial distribution within the lattice, plays a decisive role in determining the efficiency and sensitivity of the luminescence process [16].

1.3.1 Lanthanide Dopants

The luminescence behavior observed in these systems arises primarily from the presence of lanthanide ions. To properly evaluate their performance, it is essential to understand the unique energy level structure of these elements. The rare-earth series belongs to the 6th period and 3rd group of the periodic table, covering atomic numbers 57 to 71. These elements possess a partially filled 4f shell, which is well shielded by the outer $5s^2$ and $5p^6$ orbitals [17]. Owing to this shielding effect, their energy levels remain largely unaffected by the surrounding environment and are relatively stable across different host lattices. In their neutral state, lanthanides have the electronic configuration $[Xe]5d6s^24f^n$ (where n ranges from 0 to 14), with the 4f orbitals filling progressively from lanthanum through lutetium. When incorporated into host matrices, the lanthanide ions are generally stabilized in the trivalent state, exhibiting the configuration $[Xe]4f^n$ [18].

The energy levels of a material are described in terms of its total spin angular momentum (S), total orbital angular momentum (L), and total angular momentum (J). Within the host lattice, these levels undergo splitting due to three primary types of interactions. The nature of these interactions, illustrated in **Fig. (1.11)**, is discussed in detail in the following sections:-

I. Electronic interaction: Electronic interaction arises from the Coulomb repulsion between electrons within the same ion. For lanthanide elements, this effect is especially important for the 4f electrons, which gradually fill as the series progresses. Since multiple electrons may occupy different 4f orbitals, their mutual repulsion leads to a splitting of energy levels. The resulting arrangement of electronic states is described by the total spin (S) and total orbital angular momentum (L), following Hund's rules. This interaction therefore determines the basic multiplet structure of the ion, which strongly influences its optical and

luminescent properties. The transition from the $4f^n$ to $4f^{n-1}5d$ configuration arises due to the involvement of the $4f^{n-1}$ and 5d electrons and is generally observed in divalent lanthanide ions. However, the energy gap between these levels is very large (greater than 10^4 cm $^{-1}$), which makes the likelihood of such transitions occurring extremely low [19-21].

II. **Coulombic interaction:** Coulombic interaction refers to the electrostatic force between charged particles. In the context of lanthanide ions, it describes the repulsion between electrons within the same ion or between neighbouring ions in a lattice. For electrons in partially filled 4f orbitals, this repulsion affects the relative energies of different electronic configurations, leading to a splitting of the multiplet states. The magnitude of this splitting depends on the number of electrons and their spatial arrangement within the orbitals [22].

This is the next strongest Coulombic interaction, which originates from the electrostatic repulsion between electrons occupying the 4f orbitals of lanthanide ions. This repulsion causes the energy levels of the free ion to split into multiple states, which are described by the ^{2S+1}L notation. Each of these split states has a degeneracy of $(2L+1)(2S+1)$. The splitting of the ^{2S+1}L levels is on the order of 10^4 cm $^{-1}$ and is particularly significant when compared to other types of interactions [23].

III. **Spin-orbit interaction:** Spin-orbit interaction refers to the coupling between an electron's spin angular momentum and its orbital angular momentum. In lanthanide ions, the 4f electrons are shielded by the outer $5s^2$ and $5p^6$ shells, which reduces—but does not eliminate—the strength of this interaction [24]. The spin-orbit effect causes each multiplet, determined by S and L, to split further into states characterized by the total angular momentum quantum number J. The magnitude of this splitting depends on the ion and increases with the number of 4f electrons. This interaction is particularly important because it gives rise to the sharp, well-defined emission lines observed in rare-earth doped materials [25].

According to the Russell-Saunders coupling scheme, the strong Coulombic interaction leads to the coupling of the total orbital angular momentum (L) and the total spin angular momentum (S) to form the total angular momentum (J) [26]. As a result of spin-orbit

interaction, the levels already split by Coulombic forces undergo further splitting into a set of $(2J+1)$ sub-levels. These states are represented as $^{2S+1}L_J$ levels. The magnitude of this splitting is approximately 10^3 cm^{-1} .

IV. Crystal field interaction: When lanthanide ions are introduced into a solid host matrix, their 4f orbitals experience the influence of the surrounding lattice ions. This is known as the crystal field interaction. Because the 4f electrons are shielded by outer orbitals, the crystal field effect is relatively weak compared to transition metals. Nevertheless, it lifts the degeneracy of J states and introduces further splitting, which can be observed as slight shifts or fine structures in absorption and emission spectra. The magnitude of this splitting depends on the symmetry and strength of the local environment within the host lattice.

The Stark splitting of the $^{2S+1}L_J$ levels is caused by the interaction between the ion and the surrounding crystal field, which further divides the energy manifolds. This crystal-field interaction alters the $(2J+1)$ degeneracy of the levels; for ions with an even number of electrons, the degeneracy is reduced to $(J+1/2)$. In contrast, for ions with an odd number of electrons, the degeneracy remains at $(2J+1)$, denoted as $^{2S+1}L_{J,\mu}$. In this case, the energy levels are typically split by approximately 10^2 cm^{-1} [27].

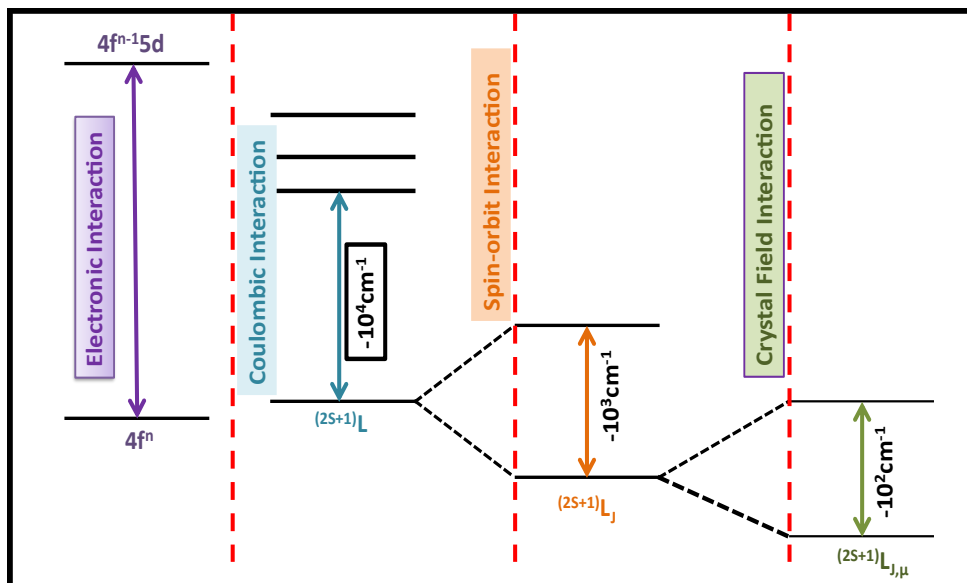


Figure 1.9: Types of energy level splitting due to various interaction within the host

The optical transitions exhibited by rare-earth ions are classified based on their outer electronic configurations:

- i. **f-f transition:** In rare-earth ions, f-f transitions occur between energy levels within the 4f shell. These transitions involve electrons moving from one 4f orbital to another, without leaving the 4f shell. Because the 4f electrons are well shielded by the outer 5s² and 5p⁶ orbitals, the energy levels involved in these transitions are minimally affected by the surrounding host lattice. As a result, f-f transitions produce sharp and well-defined absorption or emission lines, which are characteristic of the particular lanthanide ion.

Although these transitions are formally forbidden by the Laporte selection rule, they still occur with low probability due to mixing of 4f states with higher orbitals or because of asymmetric crystal-field effects. The narrow linewidths and high stability of f-f transitions make them particularly useful for applications in phosphors, lasers, and optical devices [28-29].

- ii. **f-d transition:** f-d transitions in rare-earth ions involve the excitation of an electron from a 4f orbital to a 5d orbital. Unlike f-f transitions, these transitions occur between different shells and are therefore allowed by selection rules, resulting in comparatively stronger absorption or emission bands. The 5d orbitals are less shielded than the 4f orbitals, so their energy levels are more sensitive to the surrounding crystal field of the host matrix. This sensitivity leads to broader absorption or emission bands and shifts in the transition energies depending on the local environment.

f-d transitions are typically observed in divalent or trivalent lanthanide ions and are important in applications such as phosphors, scintillators, and UV-visible optical materials, where strong and tunable emission is required [30].

- iii. **Charge transfer transition:** Charge-transfer transitions occur when an electron is transferred between the rare-earth ion and its surrounding ligands or host lattice. In most cases, this involves the movement of an electron from a ligand orbital, such as an oxygen 2p orbital, to an empty 4f or 5d orbital of the lanthanide ion, or vice versa. These transitions are typically allowed by selection rules and, as a result, exhibit much higher intensity than the intra configurational f-f transitions.

The energy of charge-transfer transitions depends strongly on the nature of the ligands and the crystal field environment, often resulting in broad absorption bands in the UV or visible region. These transitions play a key role in determining the optical and luminescent properties of lanthanide-doped materials and are particularly important in phosphors, scintillators, and other optoelectronic applications where efficient absorption and energy transfer are required [31].

1.3.2 Non-Lanthanide Dopants

Non-lanthanide dopants are elements other than rare-earth ions that can be incorporated into a host lattice to modify its optical, electrical, or structural properties. Their luminescence typically arises from d-d or charge-transfer transitions rather than shielded f-f transitions. Common examples include transition metal ions such as Mn^{2+} , Cr^{3+} , and Cu^{2+} , which are often used to tune emission wavelengths, enhance intensity, or improve energy transfer in phosphor and luminescent materials.

1.4 Applications

The unique optical response of rare-earth-doped ferroelectric ceramics, particularly their ability to exhibit upconversion luminescence (UCL), offers a wide spectrum of practical applications. Since BNT-based materials provide a stable perovskite host lattice with excellent ferroelectric properties, their UCL behavior can be effectively exploited in both fundamental research and applied technologies.

One of the most significant applications of UCL-active ceramics is in optical thermometry. The fluorescence intensity ratio (FIR) technique, which utilizes thermally coupled energy levels of dopant ions such as Er^{3+} or Ho^{3+} , enables precise, non-contact temperature sensing. In the case of BNT ceramics, the strong thermal stability of the lattice enhances the reliability of this method, making these materials suitable for sensing in microelectronics, harsh industrial environments, and biomedical systems.

In addition, biomedical imaging and therapy represent an important domain for UCL applications. Rare-earth-doped BNT ceramics excited under near-infrared light generate sharp emission bands with high photostability. Such features minimize background autofluorescence, allowing for high-contrast imaging and potential use in

targeted photodynamic therapy. Although polymer-based hosts are often employed in biomedical platforms, the incorporation of lead-free BNT ceramics offers a more environmentally benign alternative with added multifunctionality.

Another critical field is renewable energy harvesting. UCL materials can be integrated into photovoltaic devices to convert infrared light into visible emission, thereby extending the absorption range of solar cells. The combination of ferroelectric polarization in BNT with UCL activity provides a dual functionality: enhanced light management and efficient charge separation, both of which contribute to improved photovoltaic performance.

Furthermore, BNT-based UCL ceramics find relevance in optoelectronic and photonic devices. Their emission tunability, achieved by adjusting the concentration of rare-earth dopants, enables applications in solid-state lasers, display technologies, optical sensors, and data storage devices. The inherent ferroelectricity of the BNT matrix further adds multifunctional advantages, making them attractive for integrated electronic–photonic systems.

Finally, the distinct emission profiles of UCL-active ceramics are being exploited in security and anti-counterfeiting technologies. BNT-based phosphors, when excited by near-infrared radiation, produce characteristic emission colors that can serve as invisible markers or authentication labels.

1.5 Thesis Objectives

This thesis aims to achieve the following key objectives:

- Prepare the undoped $\text{Bi}_{0.5}\text{Na}_{0.5}\text{Ti}_2\text{O}_3$ ferroelectric ceramic by solid-state method and optimize its calcination and sintering temperature. Examine the formation of pure phase by X-ray diffraction spectra.
- Optimization of Er^{3+} content in $\text{Bi}_{0.5-x}\text{Er}_x\text{Na}_{0.5}\text{TiO}_3$ ceramic to study the luminescence properties. And also, to find the optimum content of Er^{3+} to cause a quenching effect.
- Study the optical temperature sensing up to wide temperature range and ferroelectric behaviour of Er^{3+} doped $\text{Bi}_{0.5-x}\text{Er}_x\text{Na}_{0.5}\text{TiO}_3$ ceramic at room temperature.

- Improve the upconversion luminescence intensity by co-doping $\text{Bi}_{0.5-x}y\text{Er}_x\text{Yb}_y\text{Na}_{0.5}\text{TiO}_3$ ferroelectric ceramic with varying Yb^{3+} and fixed optimized Er^{3+} content in the above host material.
- Determination of critical Yb^{3+} content in $\text{Er}^{3+}/\text{Yb}^{3+}$ co-doped $\text{Bi}_{0.5-x}y\text{Er}_x\text{Yb}_y\text{Na}_{0.5}\text{TiO}_3$ ceramic leads to a quenching effect.
- Study the effect of tuning Yb^{3+} content in optical temperature sensing of the $\text{Er}^{3+}/\text{Yb}^{3+}$ co-doped $\text{Bi}_{0.5-x}y\text{Er}_x\text{Yb}_y\text{Na}_{0.5}\text{TiO}_3$ ceramic in a wide temperature range.
- Synthesis of Ho^{3+} doped $\text{Bi}_{0.5-x}\text{Ho}_x\text{Na}_{0.5}\text{TiO}_3$ ferroelectric ceramic by solid-state method.
- The temperature-dependent upconversion luminescence of doped $\text{Bi}_{0.5-x}\text{Ho}_x\text{Na}_{0.5}\text{TiO}_3$ ferroelectric ceramic to study the optical temperature behaviour.
- Synthesis of BNT-PVDF thin film with different concentrations for energy harvesting applications.

1.6 Thesis Organization

Chapter 1 provides a comprehensive overview of different types of photoluminescence and their classification. It highlights the importance of selecting BNT ferroelectric materials as suitable host matrices. The role of rare-earth ions in upconversion luminescence is emphasized, and a brief overview is presented on the applications of upconversion luminescent materials across various fields. Additionally, this chapter outlines the main objectives of the thesis and provides a concise description of the overall thesis structure.

Chapter 2 describes the synthesis procedure and the characterization techniques employed in this work. The BNT ceramic was prepared using the solid-state reaction method. The chapter further details the methods used to analyze the synthesized ceramic. Structural characteristics were examined through X-ray diffraction (XRD), scanning electron microscopy (SEM), and Fourier-transform infrared spectroscopy (FTIR). The photoluminescence behavior was investigated using upconversion luminescence (UCL) spectra, pump power-dependent measurements, and time-resolved fluorescence spectroscopy. Temperature-dependent UCL studies were carried out using the fluorescence intensity ratio (FIR) method. In addition, the ferroelectric properties of the samples were evaluated from polarization-electric field (P-E) hysteresis loops.

Chapter 3 focuses on the preparation and characterization of Er^{3+} -doped $\text{Bi}_{0.5}\text{Na}_{0.5}\text{TiO}_3$ (BNT) ceramic composites. The structural features of the material were examined using X-ray diffraction (XRD) and scanning electron microscopy (SEM). Ferroelectric properties at room temperature were studied through polarization–electric field (P–E) hysteresis loop measurements. Upconversion luminescence (UCL) spectra, along with time-resolved photoluminescence, were recorded under 980 nm excitation. Furthermore, the temperature sensing characteristics of the optimized Er^{3+} -doped $\text{Bi}_{0.5}\text{Na}_{0.5}\text{TiO}_3$ (BNT) ferroelectric ceramic were investigated using the fluorescence intensity ratio (FIR) method.

Chapter 4 presents the preparation of $\text{Er}^{3+}/\text{Yb}^{3+}$ co-doped $\text{Bi}_{0.5}\text{Na}_{0.5}\text{TiO}_3$ ceramics, where the Er^{3+} concentration was kept at its optimized value while varying the Yb^{3+} content. Structural and microstructural features were examined through X-ray diffraction (XRD) and scanning electron microscopy (SEM), confirming the formation of a pure perovskite phase with a dense morphology. Fourier-transform infrared spectroscopy (FTIR) was employed to analyze the vibrational modes of the BNT lattice. Particular emphasis in this chapter is placed on the upconversion luminescence (UCL) behavior of the $\text{Er}^{3+}/\text{Yb}^{3+}$ co-doped $\text{Bi}_{0.5}\text{Na}_{0.5}\text{TiO}_3$ ceramic. The dependence of UCL spectra on pump power provided insight into the number of photons involved in the upconversion process, while time-resolved decay measurements were carried out for all co-doped samples under 980 nm excitation.

Chapter 5 investigates the synthesis of Ho^{3+} ions doped in $\text{Bi}_{0.5}\text{Na}_{0.5}\text{TiO}_3$ ceramics prepared by the solid-state method. Structural analysis confirmed the rhombohedral perovskite phase, while FTIR revealed Ti–O vibrational modes. Optical investigations showed absorption and emission transitions characteristic of Ho^{3+} , with an unusual dominant orange luminescence, alongside green and red bands. The optimized composition ($x = 0.03$) exhibited notable band gap variation, efficient upconversion behavior, and average lifetimes of $\sim 13 \mu\text{s}$ (green) and $\sim 9 \mu\text{s}$ (orange). Ferroelectric studies indicated reduced remnant polarization but enhanced energy storage efficiency, reaching 90%. Temperature-sensing performance was also significant, with maximum sensitivity observed at 303 K. The distinct orange emission without sensitizers highlights unique energy-level interactions in the $\text{Bi}_{0.5}\text{Na}_{0.5}\text{TiO}_3$ host, underlining the novelty of this work.

Chapter 6 explores the development of flexible piezoelectric nanocomposite films by incorporating bismuth sodium titanate (BNT) into a polyvinylidene fluoride (PVDF) matrix for mechanical energy harvesting. Structural and morphological studies confirmed the phase-pure nature of BNT, its uniform dispersion in PVDF, and the enhancement of the electroactive β -phase. The composites exhibited improved ferroelectric and piezoelectric responses, with optimal performance at 20 wt% BNT, delivering output voltages of 25 V and currents of 12 μ A. A practical test powering LEDs demonstrated the potential of these lead-free BNT/PVDF films for wearable energy-harvesting applications.

Chapter 7 provides an overall summary of the research findings and their broader significance in society. It outlines the key outcomes discussed in the preceding chapters and emphasizes their relevance. In addition, this chapter highlights the future scope of the work, suggesting possible directions for further studies and potential applications.

1.6.1 Overview of Thesis

The arrangement of the various thesis chapters is shown in a flowchart, which is illustrated in Fig. 1.10.

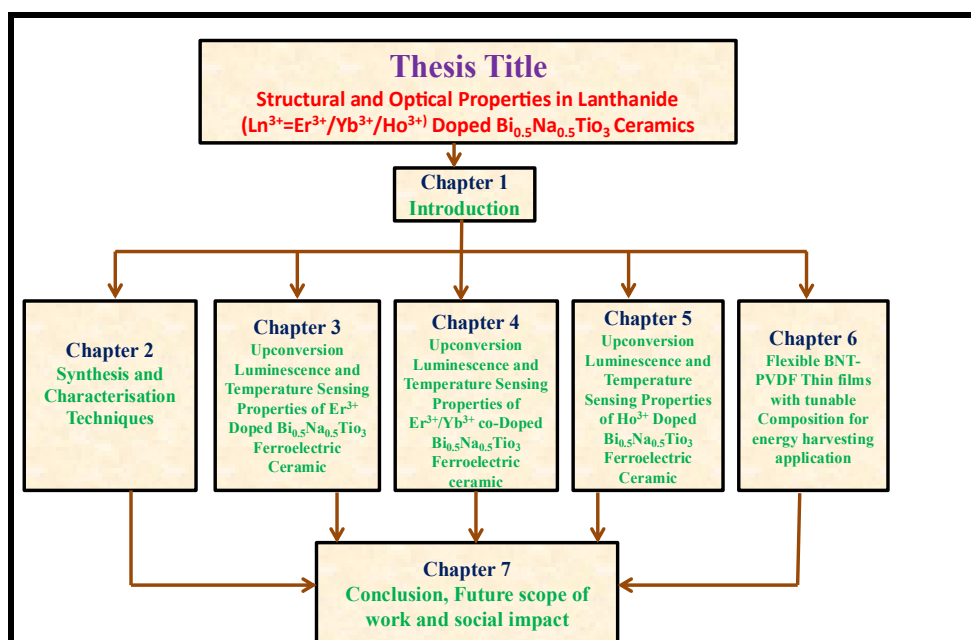


Figure 1.10: Flowchart for the organisation of the thesis

1.7 References

1. K. L. Reddy, R. Balaji, A. Kumar, and V. Krishnan, "Lanthanides doped near-infrared upconversion nanophosphors: Fundamental concepts, synthesis strategies and technological applications," *Small*, vol. 14, 1801304, 2018.
2. E. Hong, L. Liu, L. Bai, C. Xia, L. Gao, L. Zhang, and B. Wang, "Control synthesis, subtle surface modification of rare-earth doped upconversion nanoparticles and their application in cancer diagnosis and treatment," *Materials Science and Engineering C*, vol. 105, 110097, 2019.
3. H. Dong, L. D. Sun, and C. H. Yan, "Basic understanding of the lanthanides related upconversion emission," *Nanoscale*, vol. 5, pp. 5703–5714, 2013.
4. J. S. Chivian, W. E. Case, and D. D. Eden, "The photon avalanche: A new phenomenon in Pr^{3+} -based infrared quantum counters," *Applied Physics Letters*, vol. 35, 124, 125, 1979.
5. M. F. Joubert, "Photon avalanche upconversion in rare earth laser materials," *Optical Materials*, vol. 11, pp. 181–203, 1999.
6. T. Wei, C. Z. Zhao, Q. J. Zhou, Z. P. Li, Y. Q. Wang, and L. S. Zhang, "Bright green upconversion emission and enhanced ferroelectric polarization in $\text{Sr}_{1-1.5x}\text{Er}_x\text{Bi}_2\text{Nb}_2\text{O}_9$," *Optics Materials*, vol. 32, pp. 1209-1215, 2010.
7. A. Banwal and R. Bokolia, "Phase evolution and microstructure of $\text{BaBi}_2\text{Nb}_2\text{O}_9$ ferroelectric ceramics," *Materials Today: Proceedings*, vol. 46, part 20, pp. 10121-10124, 2021.
8. Z. Chen, X. Sheng, X. Li, P. Zheng, W. F. Bai, L. Li, F. Wen, W. Wu, L. Zheng, and J. Cui, "Enhanced piezoelectric properties and electrical resistivity in W/Cr co-doped $\text{CaBi}_2\text{Nb}_2\text{O}_9$ high-temperature piezoelectric ceramics," *Ceramics International*, vol. 45,no. 1, pp. 600-6011, 2019.
9. H. Zou, Y. Gu, J. Li, Q. Cao, C. Wang, and J. Zhou, "Photoluminescence, enhanced ferroelectric, and dielectric properties of Pr^{3+} -doped $\text{SrBi}_2\text{Nb}_2\text{O}_9$ multifunctional ceramics," *Materials Research Bulletin*, vol. 69, pp. 112-117, 2015.

10. X. Hui, D. Kang, H. Zou, Z. Li, Q. Cao, Y. Li, X. Wang, and Y. Yao, "A new multifunctional aurivillius oxide $Na_{0.5}Er_{0.5}Bi$: Up-conversion luminescent, ferroelectric and dielectric properties," *Ceramics International*, vol. 42, no. 14, pp. 15307-15312, 2016.
11. M. X. Façanha, J. P. C. do Nascimento, M. S. Silva, M. Filho, A. L. B. Marques, A.G. Pinheiro, and A. S. B. Sombra, "Up-conversion emission of Er^{3+} / Yb^{3+} co-doped $BaBi_2Nb_2O_9$ (BBN) phosphors," *Journal of Luminescence*, vol. 183, pp. 102–107, 2017.
12. Z. Zhang, J. Li, L. Liu, J. Sun, J. Hao, and W. Li, "Upconversion luminescence and electrical properties of (k, Er) co-modified $Na_{0.5}Bi_{4.5}Ti_4O_{15}$ high-temperature
13. T. Fu, X. Wang, H. Ye, Y. Ye, and H. Luo, "Up-conversion luminescence and temperature sensing properties of $CaBi_4Ti_4O_{15}:Tm^{3+}, Yb^{3+}$ Ceramics," *Journal of Electronic Materials*, vol. 49, pp. 5047–5052, 2020.
14. A. Banwal and R. Bokolia, "Thermometric sensing performance in erbium modified $SrBi_{2-x}Nb_2Er_xO_9$ ferroelectric ceramic for optoelectronic devices," *Ceramics International*, vol. 48, part 23, pp. 34408–34414, 2022.
15. Y. Zhang, Y. Wei, A. Zhang, R. Chu, G. Li, C. Zhang, and Z. Xu, "High electrical properties and good upconversion luminescence in $SrBi_{1.94-x}Er_{0.06}Yb_xNb_2O_9$ lead-free piezoelectric ceramics," *Journal of Alloys and Compounds*, vol. 923, 166432, 2022

CHAPTER – 2

Synthesis and Characterization Details

- ❖ *This chapter outlines the detailed procedure employed for preparing both pure and doped $Bi_{0.5}Na_{0.5}TiO_3$ ferroelectric ceramics through the conventional solid-state reaction technique.*
- ❖ *The experimental procedures adopted in this thesis are described, along with a brief explanation of the working principles and instruments involved.*
- ❖ *This chapter also covers various experimental techniques used to examine the structural, microstructural, and luminescent characteristics, along with methods employed to evaluate luminescence and ferroelectric behavior.*

2.1 Synthesis Process

Most bulk ceramics prepared from inorganic powders are commonly synthesized via the solid-state reaction route. This method is preferred due to its reproducibility, cost efficiency, and ability to produce large quantities of material with relative ease. In this process, precursor materials—typically oxides or carbonates—are subjected to high temperatures, where they undergo chemical reactions leading to the formation of the desired ceramic phase.

Under ambient conditions, these reactions generally do not occur. Instead, a minimum temperature equivalent to approximately two-thirds of the melting point of the least stable component is required to initiate the process. As the temperature rises, the reaction rate increases significantly due to enhanced atomic diffusion [1].

To overcome lattice energy barriers and allow for the migration of cations or anions into new lattice sites—an essential step for the continuation of the solid-state reaction temperatures in the range of 500 °C to 2000 °C are typically necessary. Although such reactions can be slow to complete, the kinetics can be improved by further elevating the temperature, which enhances ionic mobility.

Additionally, these reactions are usually carried out in the solid phase, as it is uncommon to heat the reactants to their melting points in ceramic synthesis.

The synthesis of $\text{Bi}_{0.5}\text{Na}_{0.5}\text{TiO}_3$ (BNT) ceramic was carried out via the conventional solid-state reaction technique. High-purity starting powders, procured from Sigma-Aldrich and Alfa Aesar, were accurately weighed in stoichiometric proportions and homogenized through ball milling in ethanol for a duration of 8 hours. The resulting mixture was then subjected to a calcination process at 850 °C for 3 hours to facilitate phase formation.

Following calcination, the powder was blended with 5 wt% polyvinyl alcohol (PVA) as a binder and pressed into circular pellets with a diameter of 10 mm. The green compacts were sintered using a two-step heating protocol in a high-temperature furnace. Initially, the samples were heated to 500 °C and held for 1 hour to ensure the complete removal of the organic binder. Subsequently, the temperature was elevated to 1050°C and maintained for 3 hours to achieve densification and final phase development. A

schematic representation of the synthesis procedure is provided in **Figure 2.1**. The powders were combined in the stoichiometric proportion according to the following synthesis reaction given by Eq. 2.1.

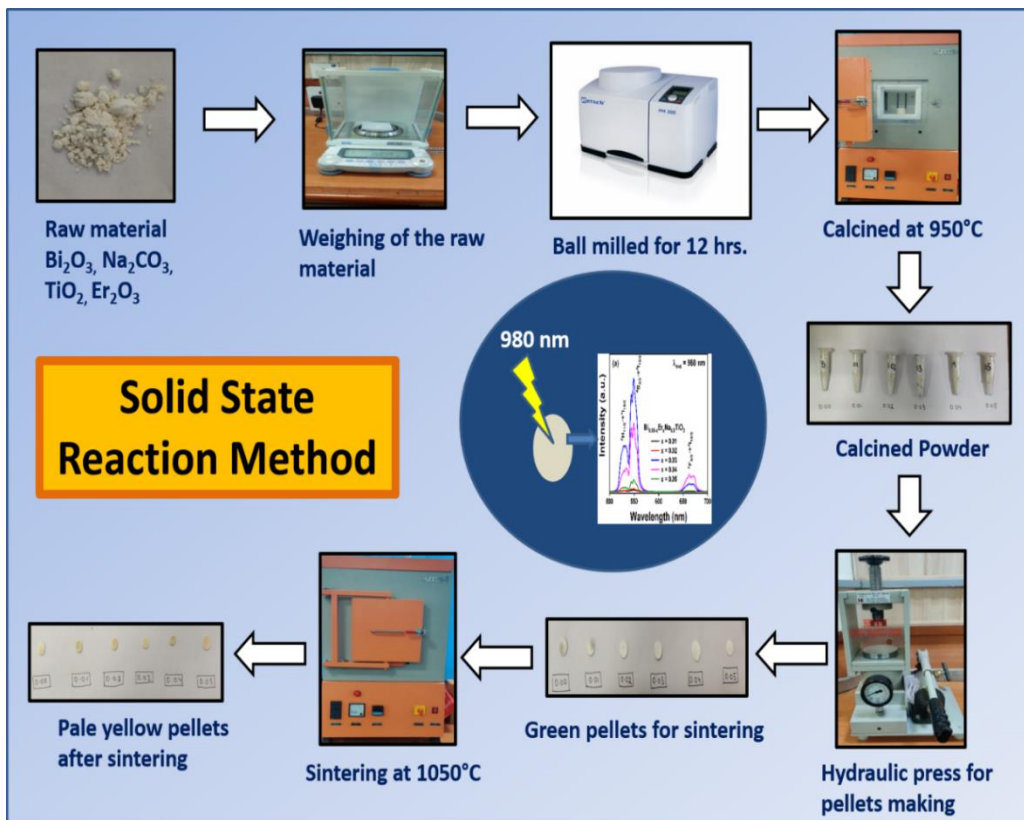


Figure 2.1: Schematic representation of the steps involved in the synthesis of ceramic using solid state method

2.1.1 Selection of Raw Materials

The solid-state reaction route predominantly employs inorganic oxides and carbonates as the primary source materials for the synthesis of ceramic systems. The raw materials selected for this process are of high analytical grade, characterized by exceptional purity and low moisture content to ensure reproducibility and phase stability during synthesis. To enhance the overall reactivity and minimize the possibility of particle agglomeration, the use of fine particle-sized powders is strongly recommended. Table 2.1 presents the list of precursor compounds utilized for the preparation of both undoped and doped $\text{Bi}_{0.5}\text{Na}_{0.5}\text{TiO}_3$ (BNT) compositions.

Table 2.1: Details of precursor powders used for preparing doped and undoped $\text{Bi}_{0.5}\text{Na}_{0.5}\text{TiO}_3$ ceramics

Precursors	Supplier	Purity (%)	Molecular weight (g/mol)	Density(g/cc)
Bi_2O_3	Alfa Aesar	99.00	465.96	8.90
Na_2CO_3	Sigma Aldrich	99.90	105.99	2.54
TiO_2	Sigma Aldrich	99.00	79.87	4.26
Er_2O_3	Alfa Aesar	99.99	382.56	8.64
Yb_2O_3	Sigma Aldrich	99.90	394.08	9.20
Ho_2O	SigmaAldrich	99.90	377.86	8.8

2.1.2 Stoichiometric Weighing of Raw Materials

The starting materials were chosen carefully, considering factors such as their chemical composition, purity, particle size, distribution, and reactivity. The required amounts of each component were then calculated according to the chemical formula and weighed precisely.

2.1.3 Mixing of Raw Materials

The accurately weighed chemicals were Ball milled with an acetone medium. This grinding process was done for 24 hrs until a fine, uniform powder was obtained. Ensuring homogeneity at this stage is essential for proper phase formation and to minimize porosity and particle agglomeration.

2.1.4 Calcination of Mixed Raw Materials

Calcination is a thermal treatment process applied to the prepared precursor powders to induce chemical reactions, remove volatile impurities, and promote the formation of the desired crystalline phase. The formation of the desired compound takes place as the individual components decompose and diffuse between the grains at temperatures below the melting points of the raw materials. After thoroughly mixing the precursor powders to achieve uniformity, they were subjected to heat treatment at 850 °C for 3 hours for calcination. A high-temperature muffle furnace was employed for this process, as shown in **Figure 2.2.**

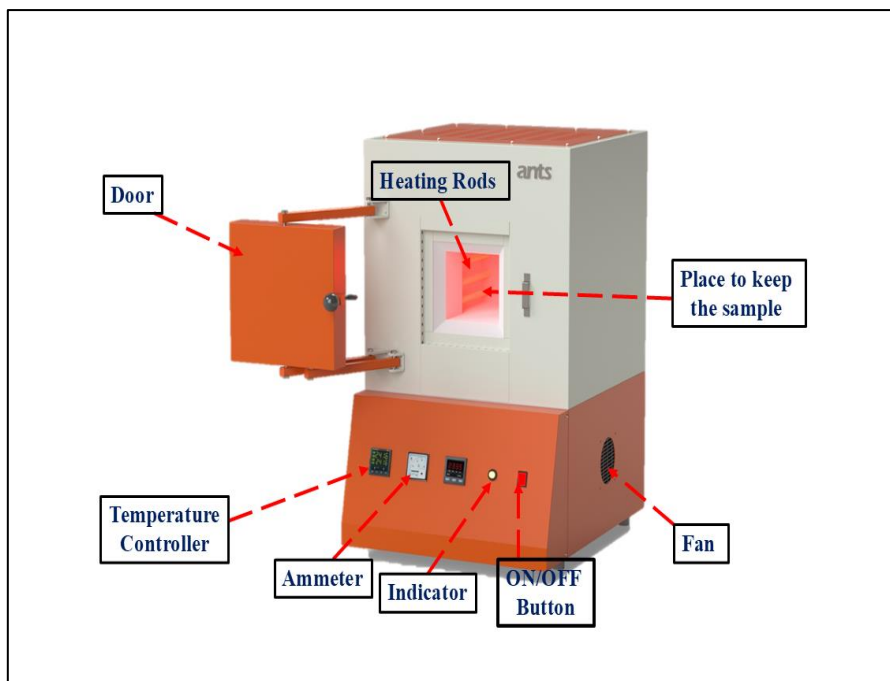


Figure 2.2: High temperature muffle furnace for calcination of the prepared sample

2.1.5 Formation of Pellets

Pellets from the calcined powder were prepared by incorporating polyvinyl alcohol (PVA) as a binder. The PVA solution was prepared by dissolving 5 g of PVA powder in 100 mL of distilled water. The water was heated, and the PVA powder was gradually added while stirring. Upon continued heating, the solution volume decreased to approximately half, and the mixture became viscous and sticky, indicating complete dissolution of PVA in water. The prepared PVA solution was then added dropwise to the calcined powder, and the mixture was thoroughly ground using a mortar and pestle. During this process, the powder gradually dried, yielding a fine, homogeneous calcined powder. This powder was subsequently placed into a die set to form circular pellets with a diameter of 10 mm and a thickness of 1 mm. The die set containing the powder was then subjected to compression using a manual hydraulic press at a pressure of 5 MPa, as illustrated in **Figure 2.3(a-b)**.

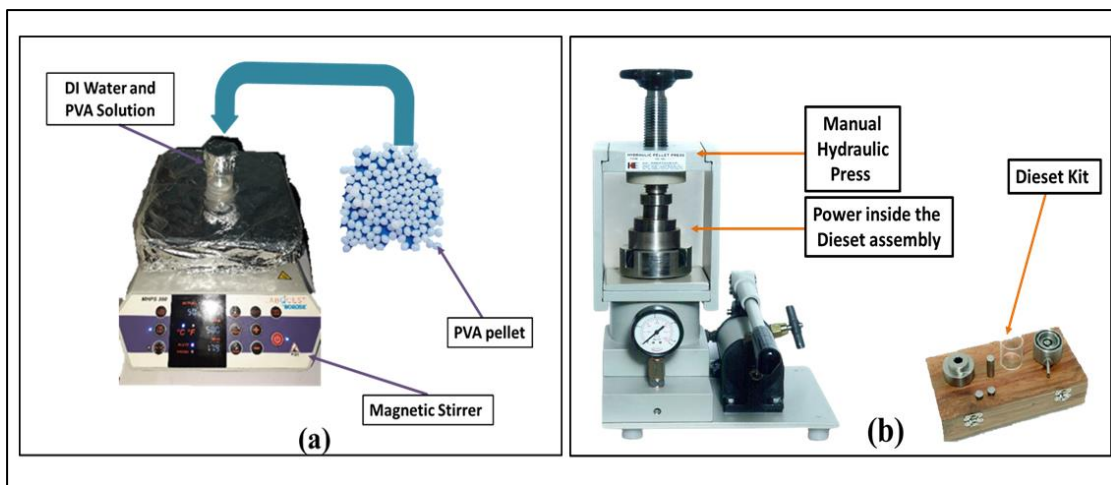


Figure 2.3: Hydraulic press and pelletizer for making pellets

2.1.6 Sintering

Sintering is a process in which a powdered material is exposed to elevated temperatures below its melting point, sufficient to promote bonding between particles. The applied heat enables particle movement, allowing them to merge with neighboring particles. This rearrangement reduces the total surface area of the particles, as they naturally seek a lower energy state. The decrease in surface area lowers the system's overall energy, which drives the formation of a denser ceramic structure during sintering. As the process progresses, the average grain size increases, which further reduces grain boundaries and the total surface area. This reduction in solid–gas interfaces contributes to the development of well-defined grains with distinct boundaries [2].

Prior to sintering, the material may contain internal strains resulting from grinding and shaping. During sintering, the high temperature facilitates atomic diffusion, which alleviates these strains. As the temperature rises, atoms move more freely, improving contact between grains. This increased interaction, particularly at grain surfaces, allows atoms to pack closely in all directions. This densification process produces a more compact and solid ceramic structure. In essence, sintering at elevated temperatures promotes atomic rearrangement, reduces internal stresses, and enhances the density and overall properties of the material [3].

The fabricated pellets were subjected to a two-step heat treatment at 1050 °C. In the first step, the temperature was gradually increased to 500 °C and held for 1 hour to

remove the PVA binder. In the subsequent step, the temperature was raised to 1050 °C and maintained for an additional 2 hours to complete the sintering of the pellets. **Figure 2.4** illustrates this sequential heat treatment process.

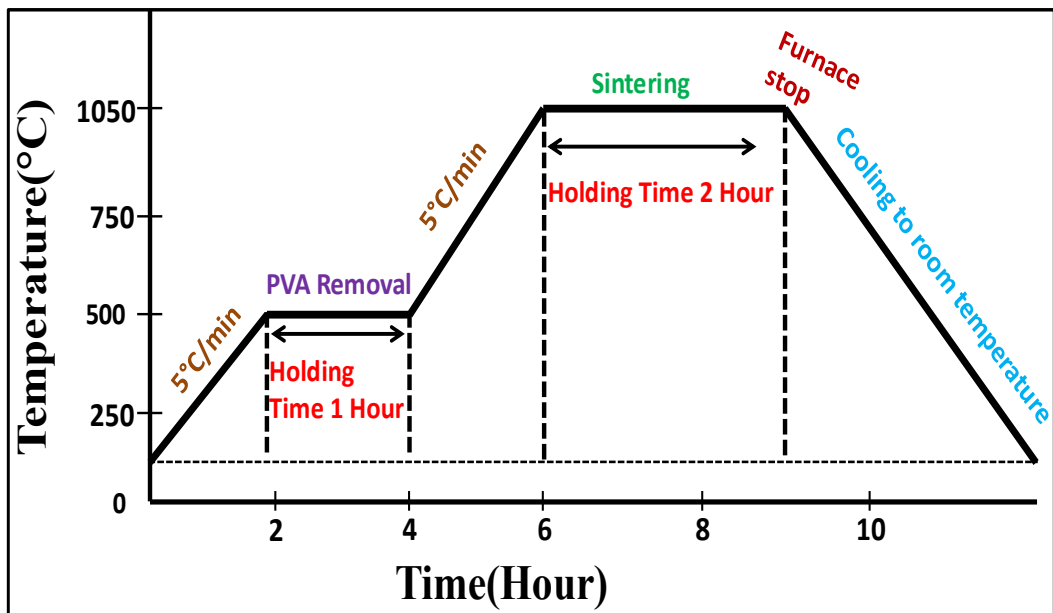


Figure 2.4: Steps involved during sintering process

2.2 Experimental and Characterization Details

A comprehensive characterization is necessary to evaluate the properties of the synthesized ceramic powder and to enhance its suitability for use as luminous materials in lighting applications. To achieve this, various standard analytical tools were employed to investigate their structural, morphological, and luminescent features. The subsequent sections of this chapter provide detailed explanations of the instruments and experimental techniques adopted for this study.

2.2.1 X-ray Diffraction (XRD)

In 1912, it was discovered that X-rays, when directed onto a solid material, generate an interference pattern through diffraction. This experiment not only confirmed the diffraction of X-rays but also provided evidence of their wave-like nature. Shortly thereafter, W. L. Bragg, extending the findings of Laue's work, recognized that the wavelength of X-rays is on the order of atomic dimensions—roughly a thousand times shorter than that of visible

light. Owing to this property, X-rays are able to interact with the periodic arrangement of atoms in a crystal lattice, making them an effective tool for probing structural details.

From his studies, Bragg proposed a mathematical relationship, now known as Bragg's law, which describes the condition for constructive interference. Constructive interference occurs when the difference in path length between incident and reflected X-rays is an integral multiple of the wavelength. When this condition is not satisfied, destructive interference results. The resulting diffraction pattern consists of peaks that correspond to reflections from different crystallographic planes, thereby revealing information about the internal arrangement of atoms in the material **Figure. 2.5**.

Bragg's equation can be expressed as Eq. 2.2.

$$2d \sin\theta = n\lambda \quad (2.2)$$

Here, d denotes the interplanar spacing, λ is the wavelength of the incident X-rays (commonly 1.54 Å), θ is the diffraction angle, and n is the order of reflection.

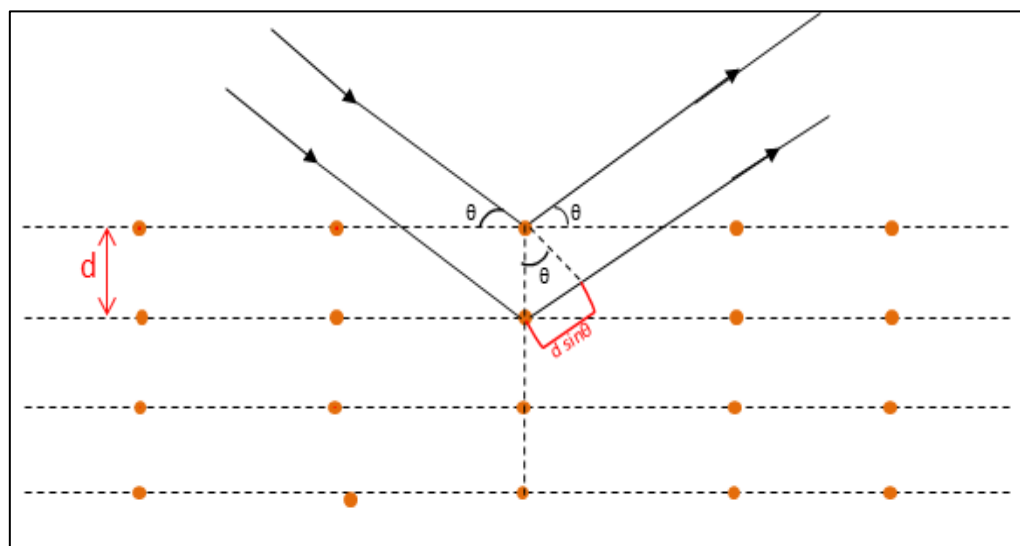


Figure 2.5: (a) Bragg's Diffraction representation from crystal planes

Bragg's equation provides a means to calculate the interplanar spacing (d) between atomic planes once the wavelength of the incident X-rays and the diffraction angle (θ) are known. By carefully adjusting the orientation of the crystal to satisfy Bragg's condition for different sets of planes, values of d for multiple planes can be

determined. This results in a series of diffraction patterns corresponding to various crystallographic orientations, which can then be used to deduce the unit cell dimensions and overall crystal structure. However, reorienting a single crystal for every reflection is impractical. To overcome this limitation, the powder diffraction method is widely adopted [4].

In this technique, the material is ground into a fine powder consisting of numerous tiny crystallites, each randomly oriented. When exposed to X-rays within an angular range (0° – 90°), the randomly oriented grains collectively satisfy Bragg's law for many planes, producing a diffraction pattern with peaks at different angles corresponding to distinct interplanar spacings. A goniometer is employed to rotate the X-ray source and detector over the angular range to record the intensity of diffracted beams.

In the present work, XRD measurements were carried out using a Bruker D8 Advance diffractometer equipped with a Cu-K α radiation source ($\lambda=1.5406$ Å) and a graphite monochromator, operating at 30 kV and 30 mA. The diffraction data were collected over the range of 15° – 60° , as illustrated in **Figure. 2.6**.

XRD is one of the most versatile and widely applied techniques for structural analysis. It allows the identification of crystalline phases, detection of secondary phases or impurities, determination of lattice parameters (a,b,ca, b, ca,b,c), estimation of unit cell volume, and evaluation of crystallite size. Furthermore, the presence of peak broadening in the diffraction pattern provides insight into the crystallinity of the sample, distinguishing between microcrystalline and nanocrystalline states [5].

This characterization is available within the Central facility (USIC) at University of Delhi (DU).



Figure 2.6: Bruker D8 Advance X-ray diffractometer

2.2.2 Scanning Electron Microscopy

A Scanning Electron Microscope (SEM) is an instrument used to examine material surfaces by scanning them with a finely focused beam of electrons. It provides detailed information about a sample's surface characteristics, including its topography, composition, and overall morphology. SEM is widely used to study both organic and inorganic materials across the nano- to microscale. It produces high-resolution images with magnifications reaching up to $30,000\times$, and in more advanced systems, up to $1,000,000\times$. When the electron beam interacts with atoms at different depths within the sample, it generates various signals such as secondary electrons, backscattered electrons, Auger electrons, and characteristic X-rays. Among these, secondary electrons—being highly sensitive to surface features—are primarily used for image

formation [6]. The resulting SEM images are useful for examining grain size distribution and surface morphology. However, a limitation of conventional SEM is its inability to clearly resolve grains smaller than approximately 50 nm, due to a resolution limit of around 10 nm. In the present work, the surface morphology and microstructural features of the sintered pellets at room temperature were examined through the Central Facility (USIC), University of Delhi, using a JEOL Japan Mode: JSM 6610LV Scanning Electron Microscope (SEM), as shown in **Figure. 2.7**.



Figure 2.7: JEOL Japan Mode: JSM 6610LV Scanning Electron Microscope (SEM)

2.2.3 Fourier Transform Infrared Spectroscopy (FTIR)

Fourier-transform infrared (FTIR) spectroscopy is commonly used to identify functional groups present in a compound. It is primarily applied to organic substances, and in certain cases, to inorganic compounds that contain functional groups. The name FTIR comes from the use of a Fourier transform, which is applied to the raw data to generate an interpretable spectrum. This technique is based on measuring the absorption

of infrared radiation by a sample and plotting it as a function of wavenumber. The resulting absorption bands or peaks are associated with specific molecular vibrations within the compound [7].

When infrared radiation interacts with a material, it causes the chemical bonds to vibrate at higher energy levels. The amount of radiation absorbed depends on the energy difference between the ground and excited vibrational states, and this absorption pattern reflects the molecular structure of the compound. For a molecule to be detected in an IR spectrum, a change in dipole moment must occur during vibration; molecules that do not undergo such a change will not show IR-active bands.

Infrared spectroscopy is typically divided into three regions: the near-infrared (4000–14,000 cm^{-1}), the mid-infrared (400–4000 cm^{-1}), and the far-infrared (50–400 cm^{-1}). Among these, the mid-infrared region is the most widely used in FTIR analysis, as the majority of organic and inorganic compounds exhibit characteristic vibrational absorption in this range. The vibrational modes of most chemically bonded atoms fall within this region.

An FTIR spectrometer is capable of rapid data acquisition and provides high-resolution spectra over a wide range, typically from 400 to 4000 cm^{-1} . The instrument operates using an interferometer, which modulates infrared radiation from a broadband IR source, while a detector records the intensity of the transmitted or reflected radiation. The detected signal is then processed through a Fourier transform to generate the final infrared spectrum. These spectra are generally presented as plots of percentage transmittance or absorbance versus wavenumber.

FTIR spectroscopy has several advantages, such as faster scanning speed compared to many dispersive techniques and the ability to analyze samples in solid, liquid, and gaseous states. The technique is based on the interactions between infrared radiation and the molecular bonds within a sample, allowing different chemical bonds to be identified according to their characteristic vibrations. In the present study, the FTIR spectrum was recorded using a PerkinElmer Fourier transform spectrometer in the range of 4000–400 cm^{-1} , the equipment was accessed in Department of Applied Physics, Delhi Technological University as shown in **Figure. 2.8**.



Figure. 2.8: Perkin Elmer's Frontier FTIR spectrometer

2.2.4 Diffuse Reflectance Spectroscopy (DRS)

Figure 2.9 shows the two ways in which light can be reflected when it makes contact with a material: specular and diffuse reflection. In the case of specular reflection, the light is reflected from the surface at an angle equal to the angle of incidence, which provides limited information about the internal properties of the material. Diffuse reflection, in contrast, occurs when the incoming light interacts with different physical and chemical features within the material's volume. As a result of this interaction, useful information can be obtained regarding the material's transmission, absorption, and scattering behavior.

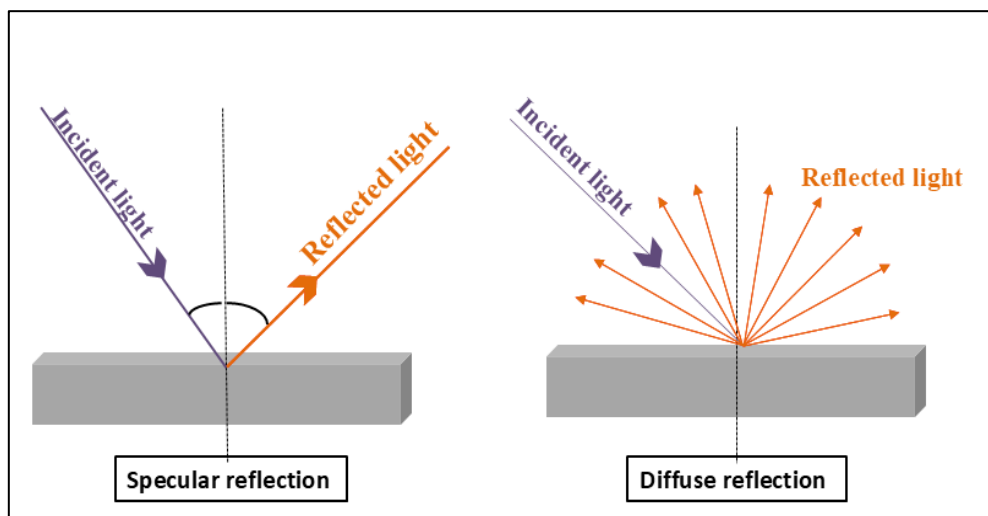


Figure 2.9: Phenomenon of specular and diffuse reflectance

As a result, UV–Vis diffuse reflectance spectroscopy (DRS) is commonly employed to examine the optical properties of solid materials. This technique measures the light that is scattered by the sample in multiple directions. DRS can provide both qualitative and quantitative information about a material. The spectrum, usually obtained in the visible or near-infrared region, contains valuable details related to the electronic and vibrational characteristics of the sample. Although reflectance measurements offer benefits such as higher sensitivity and a better signal-to-noise ratio when compared to transmission methods, they also introduce certain challenges. In particular, the resulting spectra tend to be more complex, making their interpretation and data collection more demanding [8].

In the present work, UV–Vis DRS instrument was used in the Department of Applied Physics, Delhi Technological University for analysis of the synthesized compounds was carried out using a Jasco UV-770 UV–Vis spectrophotometer, as shown in **Figure. 2.10**, operating over the wavelength range of 190–2700 nm. Barium sulphate (BaSO_4) was used as the reference material for baseline correction. Although the instrument is based on a single-monochromator configuration with a narrow spectral bandwidth, it provides a much higher energy throughput than a double-monochromator system. This leads to an enhanced signal-to-noise (S/N) ratio across the entire spectral range. The diffuse reflectance data were subsequently converted into absorption coefficient values at different wavelengths using Eq. 2.3.

$$F(R) = \frac{(1-R)^2}{2R} = \frac{k}{S} \quad 2.3$$

In this case, R denotes the reflectance of the sample, k represents the absorption coefficient, and $F(R)$ is the associated Kubelka–Munk (K–M) function. The forbidden band gap values were evaluated from Tauc plots using the relationship proposed by Tauc, as shown in Eq. 2.4.

$$(F(R)h\nu) = C(h\nu - E_g)^n \quad 2.4$$

In this equation, E_g refers to the band gap energy, $h\nu$ represents the photon energy, and C is a proportionality constant. The nature of the electronic transition is determined by the value of n , where $n = 1/2$ corresponds to a direct transition and $n = 2$ indicates an

indirect transition. The Tauc plot, which graphs $(\alpha h\nu)^2$ against $h\nu$, is used to determine the band gap energy from the point at which the extrapolated linear region of the absorption edge intersects the energy (x) axis [9].



Figure 2.10: Jasco V-770 Spectrophotometer

2.2.5 Photoluminescence Spectroscopy (PL):

Photoluminescence (PL) spectroscopy is widely used to study the optical and electrical behavior of solid-state materials, particularly in the field of optoelectronics. It is an important technique for investigating excitation and emission mechanisms within these materials. Photoluminescence refers to the spontaneous emission of light from a material after it has been optically excited. As a non-contact analytical method, PL provides valuable information about a material's electronic structure, including the presence and influence of dopants [10].

The photoluminescence process involves two main stages: excitation and emission. When a sample is exposed to light of a specific wavelength, its electrons absorb energy and move from a lower energy level (ground state) to a higher energy level (excited state). This initial step is known as photoluminescence excitation (PLE). After a short time, the excited electrons return to the ground state, releasing energy in the form of photons, which is referred to as photoluminescence or photo-emission.

To obtain the PL emission spectrum of a material, the excitation wavelength is kept constant while the emitted light is recorded using an emission monochromator. For recording the PLE spectrum, the emission wavelength is fixed, and the excitation monochromator is scanned to monitor the absorbed wavelengths [11].

Photoluminescence (PL) measurements of a sample can be performed using a spectrofluorometer. The main components of this instrument include a light source, wavelength selection units, a sample holder for illumination, detectors, and a system for recording corrected spectra. A 150 W xenon arc lamp is commonly used as a continuous excitation source for the down-conversion process. The emitted light is then directed toward a diamond-turned elliptical mirror, which focuses it onto the entrance slit of the excitation monochromator. A quartz window is placed between the lamp housing and the monochromator to allow proper heat dissipation and to protect the system in the event of lamp failure.

The instrument is composed of several essential components:

1. **Monochromators:** Two monochromators are used—one for excitation and one for emission—to achieve high spectral resolution across the entire range.
2. **Gratings:** Light is dispersed into its component wavelengths using gratings with 1200 lines/mm, which are coated with MgF_2 to prevent oxidation.
3. **Slits:** Slits positioned at the entrance and exit of the monochromators control the bandwidth of the incident light.
4. **Shutters:** Shutters are incorporated to protect the sample from photodegradation or bleaching caused by prolonged exposure to the light source.
5. **Sample compartment:** The light beam is directed onto the sample, and the emitted light is guided to the monochromator using optical fiber bundles.
6. **Detectors:** The system includes two detectors—a signal detector and a reference detector. The R928P photomultiplier tube (PMT) serves as the signal detector, while a UV-sensitive silicon photodiode functions as the reference detector, continuously monitoring lamp output.
7. **Computer control:** The spectrofluorometer is operated via computer software for fluorescence analysis. An example of this setup is the Jasco-8300 fluorescence spectrofluorometer, as shown in **Figure. 2.11**.

The PL instrument used is available in the Department of Applied Physics, Delhi Technological University.



Figure 2.11: Jasco Spectrophotometer Spectrofluorometer FP-8300

2.2.6 Upconversion Luminescence Spectroscopy

Up-conversion is a process in which low-energy photons are absorbed and then re-emitted as photons with higher energy. This effect is important for materials used in applications such as solid-state lighting, display technologies, and solar energy devices. In the case of phosphors excited with a 980 nm laser, near-infrared light is absorbed and subsequently converted into higher-energy photons, typically within the visible range [12]. The up-conversion (UC) emission spectra were recorded using a Horiba PTI QuantaMaster system equipped with a 980 nm laser, as shown in **Figure 2.12**.



Figure 2.12: Upconversion luminescence spectroscopy Horiba PTI Quanta Master equipped using 980 nm laser

2.2.6.1 Time-resolved photoluminescence (TRPL)

Time-resolved photoluminescence (TRPL) measures the emission of photons from a sample as a function of time following excitation by a light pulse. Upon excitation, the material emits photons while returning from the excited state to the ground state [13]. TRPL allows the determination of luminescence decay times, providing important information on processes such as recombination, energy transfer, and the lifetimes of excited states.

2.2.6.2 Optical Temperature Sensing

Optical temperature sensing operates on the principle that the optical properties of a material vary systematically with temperature. These variations may manifest as changes in absorption, transmission, reflection, refractive index, emission intensity, or luminescence lifetime. By monitoring one or more of these temperature-dependent optical parameters, the temperature of a system can be determined with high sensitivity and precision.

In a typical optical sensing configuration, light from a stable source (such as a laser or LED) is guided to the sensing region via an optical fiber or free-space optics. When the sensing material is exposed to temperature fluctuations, its interaction with the incident light is altered. This results in a measurable change in the output signal, such as a shift

in wavelength, a change in optical power, or variation in phase. These optical variations are then detected by a photodetector and processed to obtain the corresponding temperature values.

In luminescence-based optical thermometry, the sensing material is excited using a suitable wavelength, and it emits radiation whose intensity, spectral distribution, or decay time is temperature dependent. The temperature sensitivity arises due to thermally activated non-radiative transitions, commonly referred to as thermal quenching. As the temperature increases, the probability of non-radiative relaxation increases, leading to a reduction in emission intensity and lifetime. By calibrating these changes, accurate temperature measurements can be achieved **Figure 2.13** [14].

This instrument used for sensing is available in the IIT, Dhanbad.



Figure 2.13: Temperature-dependent sensing upconversion luminescence

2.2.7 P-E Hysteresis Loop

A P-E loop tracer is an instrument used to study the ferroelectric properties of a material by plotting the variation of polarization (P) with the applied electric field (E) **Figure 2.14**. When an electric field is applied, the dipoles inside the material align, causing an increase in polarization. After removing the field, some polarization remains, known as remanent polarization. On reversing the field, the polarization

becomes zero at a certain point called the coercive field, and then increases in the opposite direction. Repeating this cycle forms a hysteresis loop, which reveals important information about the material's switching behavior, energy loss, and domain dynamics. This technique is widely used to evaluate materials for applications in memories, sensors, and capacitors [15].

The P-E loop tracer employed in this study is available through the Department of Applied Physics of Delhi Technological University.



Figure 2.14: P-E Hysteresis Loop Tracer

2.3 Summary

In the following chapters, these different methods will be used to examine and evaluate the obtained results.

2.4 References

1. A. Gallegos-Melgar, D.G. Espinosa-Arbelaez, F.J. Flores-Ruiz, A. Lahmar, J.-L. Dellis, N. Lemée, F.J. Espinoza-Beltran and J. Munoz-Saldana, “Ferroelectric properties of manganese doped $(\text{Bi}_{1/2}\text{Na}_{1/2})\text{TiO}_3$ and $(\text{Bi}_{1/2}\text{Na}_{1/2})\text{TiO}_3\text{--BaTiO}_3$ epitaxial thin films”, *Appl. Surf. Sci.* 359 (2015) 923–930, doi.org/10.1016/j.apsusc.2015.09.175.
2. P. Julphunthong, T. Bongkarn, S. Maensiri, The effect of firing temperatures on phase formation, microstructure and via the combustion route, *Ceram. Int.* 41 (2015) S143–S151, <https://doi.org/10.1016/j.ceramint.2015.03.229>.
3. F. Li, J. Li, J. Zhai, B. Shen, S. Li, M. Zhou and H. Zeng, “Influence of structural evolution on electrocaloric effect in $\text{Bi}_{0.5}\text{Na}_{0.5}\text{TiO}_3\text{--SrTiO}_3$ ferroelectric ceramics”, *J. Appl. Phys.* 124 (2018) 164108, doi.org/10.1063/1.5050826.
4. D. Nawrocka, “Environmental supply chain management, ISO 14001 and RoHS. How are small companies in the electronics sector managing” *Corp. Soc. Responsib. Environ. Manag.* 15 (2008) 349–360, <https://doi.org/10.1002/csr.176>.
5. R.D. Shannon, Revised effective ionic radii and systematic studies of interatomic distances in halides and chalcogenides, *J. Acta Cryst. A*32 (2016) 751–767, <https://doi.org/10.1107/S0567739476001551>.
6. K. Akhtar, S. A. Khan, S. B. Khan, and A. M. Asiri, “Scanning electron microscopy: Principle and applications in nanomaterials characterization,” *Handbook of Materials Characterization*, pp. 113-145, 2018.
7. W. M. Doyle, “Principles and applications of Fourier transform infrared (FTIR) process analysis,” *Process Control and Quality*, vol. 2, pp. 11-41, 1992.
8. PA. Franco, P. Banerjee, P.L. Romanholo, Effect of composition induced transition in the optical band-gap, dielectric and magnetic properties of Gd doped $\text{Na}_{0.5}\text{Bi}_{0.5}\text{TiO}_3$ complex perovskite, *J. Alloys comppd.* 764 (2018) 122e127, <https://doi.org/10.1016/j.jallcom.2018.06.007>.
9. L.T.H. Thanh, N.B. Doan, N.Q. Dung, L.V. Cuong, L.H. Bac, N.A. Duc, P.Q.

Bao, D.D. Dung, Origin of room temperature ferromagnetism in Cr-doped lead-free ferroelectric $\text{Bi}_{0.5}\text{Na}_{0.5}\text{TiO}_3$ materials, *J. Electron. Mater.* 46 (2017) 3367–3372, <https://doi.org/10.1007/s11664-016-5248-0>

10. M. Bengisu, Production of Ceramic Bodies, *Engineering Ceramics, Engineering Materials*, Springer, Berlin, Heidelberg, 2001, https://doi.org/10.1007/978-3-662-04350-9_3.

11. Y. Zhang, T. Xu, H. Yu, R. Chu, G. Li, C. Zhang, Z. Xu, Sm-modified bismuth layerstructured $\text{SrBi}_2\text{Nb}_2\text{O}_9$ multifunctional ceramics with enhanced electrical properties and good photoluminescence properties, *Ceram. Int.* 48 (2022) <https://doi.org/10.1016/j.ceramint.2022.03.182>.

12. C. Liu, Q. Wang, X. Wu, B. Sa, H. Sun, L. Luo, C. Lin, X. Zheng, T. Lin, Z. Sun, “Boosting upconversion photoluminescence and multielectrical properties via Er Doping-Modulated vacancy control in $\text{Ba}_{0.85}\text{Ca}_{0.15}\text{Ti}_{0.9}\text{Zr}_{0.1}\text{O}_3$ ”, *ACS Omega* 4 (2019) 11004–1101, <https://doi.org/10.1021/acsomega.9b01391>.

13. Z. Guan, X. Li, R. Shen, Z. Tian, H. Yu, Y. Cao, Y. Wang, J. Zhang, S. Xu, B. Chen, Intense red up-conversion luminescence and temperature sensing property of $\text{Yb}^{3+}/\text{Er}^{3+}$ co-doped BaGd_2O_4 phosphors, *Spectrochim. Acta Mol. Biomol. Spectrosc.* 284 (2023), 121805 <https://doi.org/10.1016/j.saa.2022.121805>

14. R. Bokolia, O.P. Thakur, V.K. Rai, S.K. Sharma, K. Sreenivas, Dielectric, ferroelectric and photoluminescence properties of Er^{3+} doped $\text{Bi}_4\text{Ti}_3\text{O}_{12}$ ferroelectric ceramics, *Ceram. Int.* 41 (4) (2015) 6055–6066, <https://doi.org/10.1016/j.ceramint.2015.01.062>.

15. R. Bokolia, V.K. Rai, L. Chauhan, K. Sreenivas, Structural and light upconversion luminescence properties of Er^{3+} - Yb^{3+} - W^{6+} substituted $\text{Bi}_4\text{Ti}_3\text{O}_{12}$, *AIP Conf. Proc.* 1731 (2016) 4–7, <https://doi.org/10.1063/1.4948208>

CHAPTER – 3

Upconversion Luminescence and Temperature Sensing Properties of Er^{3+} Doped $Bi_{0.5}Na_{0.5}TiO_3$ Ferroelectric Ceramic

- ❖ This chapter presents a thorough analysis into the structural, optical, ferroelectric, and sensing properties of $Bi_{0.5-x}Er_xNa_{0.5}TiO_3$ ceramics synthesized through a conventional solid-state reaction route, with varying concentrations of Er^{3+} dopant.
- ❖ The upconversion (UC) luminescence of $Bi_{0.5-x}Er_xNa_{0.5}TiO_3$ compositions under 980 nm excitation at varying pump powers has been examined, along with their potential for luminescence-based temperature sensing.
- ❖ Under excitation wavelengths of 488 nm and 980 nm, two prominent green emissions are observed at approximately 530 nm and 550 nm, corresponding to the $^5H_{11/2} \rightarrow ^4I_{15/2}$, $^5S_{3/2} \rightarrow ^4I_{15/2}$ respectively, along with a weaker red emission around 660 nm attributed to the $^4F_{9/2} \rightarrow ^4I_{15/2}$ transition. The luminescence intensity increases with Er^{3+} content, reaching a maximum at a doping level of $x=0.03$.
- ❖ The efficiency of energy storage density increases with Er^{3+} doping and an improved recoverable energy storage ($Wr = 2.73 \text{ J/cm}^3$) and a higher efficiency ($\eta = 70.77\%$) are obtained for Er^{3+} content, $x = 0.03$.
- ❖ The absolute sensitivity measured for a wide temperature range (303 K to 523 K) and found to be 0.0047 K^{-1} at 523 K. The $Bi_{0.5-x}Er_xNa_{0.5}TiO_3$ ($x = 0.03$) ceramic has been observed to possess sensor capabilities, making it a promising material for potential applications in the field of optical temperature sensors.

The results reported in this chapter have been published in Megha et. al. in *Journal of Luminescence*

3.1 Introduction

In order to keep pace with the rapid progress of contemporary technology in the present era, it is essential to incorporate and analyze materials. Multifunctional materials have attracted significant attention lately due to their inherent versatility. When considering multifunctional applications, it is necessary to select dielectric and ferroelectric materials that demonstrate an ideal combination of down and upconversion emissions. With the increasing prominence of environmental issues, there is a pressing need to explore alternative lead-free piezoelectric materials. The challenge arises due to environmental issues which limits the use of lead-based materials [1, 2]. As a result, alternative lead-free ferroelectric materials based on $\text{Na}_{0.5}\text{Bi}_{0.5}\text{TiO}_3$ (NBT), $\text{K}_{0.5}\text{Na}_{0.5}\text{NbO}_3$ (KNN), and Bismuth layered ferroelectrics (BLSFs), etc. are being investigated to replace the current lead-containing materials [3-5]. Bismuth sodium titanate, $\text{Bi}_{0.5}\text{Na}_{0.5}\text{Ti}_{0.3}$ (abbreviated as BNT) is among the most widely used lead-free piezoelectric materials. BNT is an important member of classical electrical functional materials known for its notable characteristics, including a high dielectric constant and curie temperature, along with a relatively large remnant polarization [6]. Hence, the utilization of BNT can be extended to include multiple functionalities in the domains of luminescence and ferroelectricity. BNT ceramics exhibit a lowered vibrational energy, rendering them highly suitable for applications involving down conversion (PL) and upconversion (UC) luminescence. Numerous works confirmed the existence of ferroelectricity-enhanced function in rare-earth doped BNT ceramics [7]. The BNT material doped with rare earths (RE) exhibits exceptional photoluminescence characteristics. As an example, Wang et al. demonstrated that ceramics of Pr-doped BNT displayed a pronounced red emission. Similarly, Chen et al. reported that BNT ceramics doped with Er^{3+} exhibited notable upconversion emission in both green and red wavelengths under 980 nm excitation [8, 9]. Consequently, the investigation of the photo-luminescent characteristics of RE doped BNT material holds significant academic interest and relevance. In recent studies, it has been observed that the perovskite titanate doped with Er^{3+} exhibits notable green emission with a peak wavelength of approximately 550 nm, as well as red emission with a peak wavelength of around 660 nm [10-13]. The significance of incorporating RE ion-doped ferroelectric

host materials is heightened due to their possession of low phonon energy, capacity for crystal structure modifications through the introduction of dopants, and ability to enhance their functional piezoelectric properties alongside optical functionality. The erbium (Er^{3+}) ion is a crucial catalyst for upconversion luminescence, and has garnered considerable interest for its extensive utilisation in upconversion lasers. These lasers have the potential to induce robust up-conversion emission in BNT, thereby expanding its range of applications.

The literature review indicates that pure BNT exhibits notable characteristics such as a substantial coercive field, considerable dielectric losses, and elevated conductivity. These properties arise from the rapid generation of oxygen vacancies caused by Bi^{3+} volatilization. Extensive research has been conducted to enhance the piezoelectric, ferroelectric, and electrical properties of this material by exploring various BNT-based materials and synthesizing techniques, aiming to overcome the limitations and enhance its storage capacity [14]. In contrast, it has been concluded that the incorporation of rare-earth ions in BNT ceramics can enhance their performance. The rare-earth ions are responsible for the disturbance of the long-range ferroelectric order, which also serve as activators for the production of luminescent materials. The development of rare earth ion doped ferroelectrics has garnered significant scientific interest due to the widespread use of cost-effective laser diodes operating at wavelengths such as 980 nm and 800 nm along with their intriguing applications. These applications include next-generation lighting or displays, luminescent bioassays, UC lasers, solid-state NIR solar cells, etc. [15-18].

In the present work, efforts have been made to determine the influence of Er^{3+} substitution on the structural, microstructure, optical, ferroelectric and temperature sensing characteristics of BNT ceramics, which are analysed in detail. The selection of Er^{3+} is based on its distinctive characteristic of possessing a metastable energy level, specifically $^4\text{I}_{9/2}$ and $^4\text{I}_{11/2}$. These energy levels can be efficiently populated by a 980 nm laser source, making Er^{3+} suitable for upconversion luminescence. In contrast, trivalent erbium ions exhibit a highly stable oxidation state of 3+. Consequently, the substitution of Bi^{3+} ions in $\text{Bi}_{0.5-x}\text{Er}_x\text{Na}_{0.5}\text{TiO}_3$ ceramic is a straightforward process and its substitution with Er^{3+} is crucial due to significant

mismatch of the ionic radii at the A-site which induces structural distortion in the host matrix. The phase formation of Er^{3+} on BNT ceramics were examined through the utilisation of X-ray diffraction (XRD) analysis followed by FTIR analysis. To study the photoluminescence behaviours of Er^{3+} doped BNT ceramic a laser source of 980 nm excitation is used to collected emission spectra of the prepared ceramic. The pump power dependency on upconversion luminescence was also studied to examine the photons involved in the process. The time resolved photoluminescence spectroscopy was conducted at room temperature operating at wavelength of 980 nm. Furthermore, to quantify the P-E hysteresis loop of pure and Er^{3+} doped sintered BNT ceramics were traced at 30 Hz on Marine India Instrument (Model: 20PE1kHz 1N). This study aims to thoroughly explore the influence of varying concentrations of Er^{3+} on the ferroelectric, photoluminescence, energy storage density, and sensing properties of $\text{Bi}_{0.5-x}\text{Er}_x\text{Na}_{0.5}\text{TiO}_3$ ceramic. The objective is to assess the effectiveness and practicality of the prepared ceramic for its potential in energy storage devices and in the field of multifunctional optoelectronic devices.

3.2 Synthesis and Charactrization Details

The procurement of raw powders with a high level of purity was conducted through Sigma Aldrich. Lead free $\text{Bi}_{0.5-x}\text{Er}_x\text{Na}_{0.5}\text{TiO}_3$ ($x = 0.0 - 0.05$) ceramics were synthesized using Bi_2O_3 , Na_2CO_3 , TiO_2 and Er_2O_3 as initial precursors without any further purification. The synthesis procedure used is typical solid state reaction approach, as shown in **Figure 3.1**. The powders were combined in the stoichiometric proportion according to the following synthesis reaction given by Eq. (3.1).



Subsequently, the aforementioned powder underwent a comprehensive mixing process using a high energy ball mill, wherein zirconia balls were employed as the grinding medium. This procedure lasted for a duration of 12 hours, ensuring the complete homogenization of the precursors. Following this, the resulting mixture was then dried at 70°C in oven for 24h and finally, the dried powder was calcined for 3h in air at 850°C.

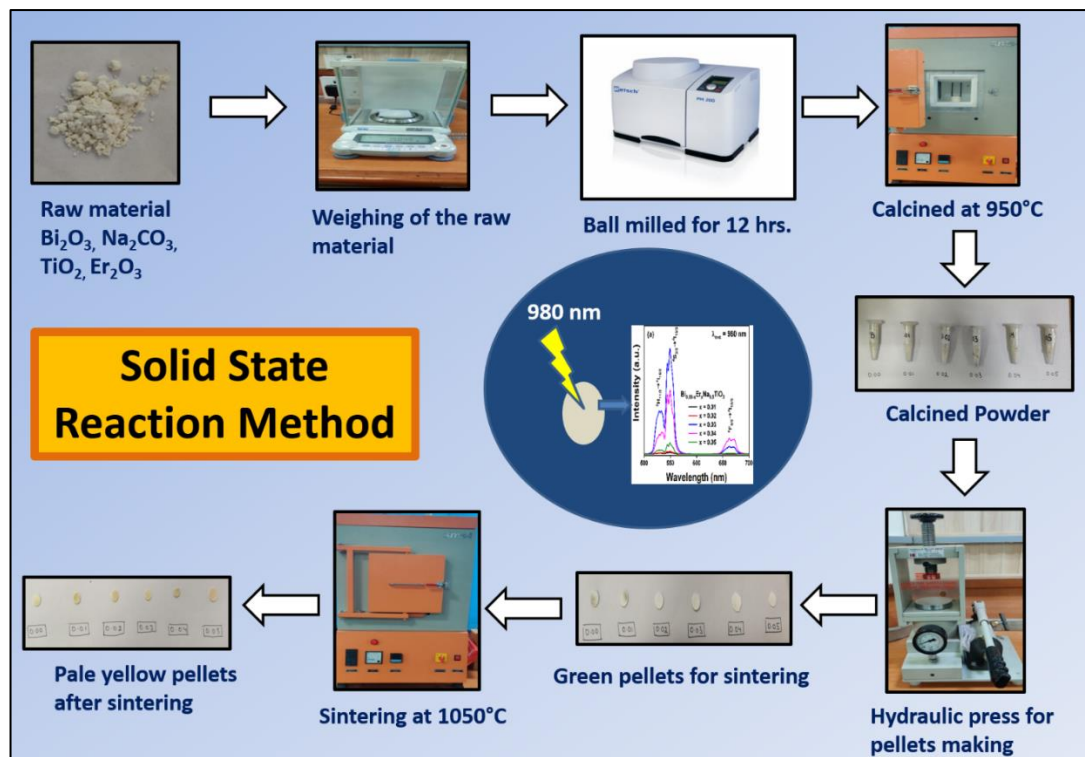


Figure 3.1: Pictorial depiction of synthesis process (solid-state method)

Subsequently, the aforementioned powder underwent a comprehensive mixing process using a high energy ball mill, wherein zirconia balls were employed as the grinding medium. This procedure lasted for a duration of 12 hours, ensuring the complete homogenization of the precursors. Following this, the resulting mixture was then dried at 70°C in oven for 24h and finally, the dried powder was calcined for 3h in air at 850°C . After calcination, the powder was combined with a solution of PVA binder. The resulting mixture was then uniaxially compressed at 50MPa into discs of 10mm diameter and 1mm thickness using a hydraulic press machine. Finally, the pressed pellets were sintered in air at a temperature of 1050°C for 3 hours.

X-ray powder Diffraction (XRD) equipped with $\text{Cu-K}\alpha$ radiation, $\lambda = 1.5406 \text{ \AA}$, (make: Bruker, Model: D8 Advance) was used to examine the phase purity and crystalline structure of the prepared ceramics sintered at 1050°C . The XRD patterns of the sintered $\text{Bi}_{0.5-x}\text{Er}_x\text{Na}_0.5\text{TiO}_3$ ($x = 0.0 - 0.05$) ceramics were acquired in the 2θ range of $10^\circ - 80^\circ$. Further, refinement was done through TOPAZ software to determine the refined unit cell parameters of the synthesized ceramics. Archimedes Principle was employed to measure the density of the sintered pellets. In addition to XRD, to analyse the formation

of perovskite structure, Fourier Transform Infrared (FTIR) Spectroscopy was done on finely crushed sintered powders using the Perkin Elmer spectrum-II instrument. For electrical measurement, silver paste was applied onto the sintered pellet was followed by firing the pellets at 500°C in a muffle furnace for 30 minutes. This firing procedure ensured the complete adherence of the silver paste to the pellets. The room temperature polarization (P) versus electric field (E) loops were traced at a 30 Hz frequency using a ferroelectric testing system produced by Marine India Electrical Ltd. The up-conversion luminescence spectra were recorded at room temperature using the HORIBA PTI Quanta-master instrument, with a continuous laser diode at an excitation wavelength of 980 nm. Time resolved fluorescence spectroscopy were conducted by a pulsed laser source having wavelength of 980 nm at room temperature. The emission spectra of photoluminescence (PL) were measured using a JASCO FP-8300 PC-spectrofluorophotometer equipped with a xenon arc lamp, with excitation at a wavelength of 488 nm. A cooled photo-multiplier tube was used to record the temperature dependent UC emission spectra for LIR analysis.

3.3 Results and Discussion

3.3.1 Structural and Microstructural Analysis

Figure 3.2(a) represents the room temperature X-Ray Diffraction (XRD) patterns of a series of modified $\text{Bi}_{0.5-x}\text{Er}_x\text{Na}_{0.5}\text{TiO}_3$ ($x = 0.00-0.05$) ceramic compositions synthesized via the solid-state reaction method and sintered at 1050°C for 4 hrs. The observed XRD pattern in the range from $2\theta = 20^\circ-80^\circ$, matches closely with the reported reference diffraction data with JCPDS #00-036-0340, suggesting formation of single phase of rhombohedral $\text{Bi}_{0.5-x}\text{Er}_x\text{Na}_{0.5}\text{TiO}_3$ ($x = 0.00 - 0.05$) with R3c space group for all the compositions [19]. Solubility and incorporation of Er^{3+} ions in the host lattice is confirmed through the absence of any traces of undesirable secondary phase. The acquired XRD data for all compositions were refined using TOPAZ software and is presented in **Figure 3.2(b)**. The calculated refined lattice parameters and profile parameters deduced from the profile fit of the calculated and observed XRD pattern are summarized in Table 1. The goodness of fit ($\chi \approx 1.5$) is close to 1, confirming the results obtained from the refinement are reliable and rational. **Figure 3.2(c)** shows the shifting of the most intense peak corresponding to the Bragg plane (110) towards

higher diffraction angles for all the compositions with respect to $\text{Bi}_{0.5}\text{Na}_{0.5}\text{TiO}_3$. This shifting indicates effective incorporation of smaller Er^{3+} ions (1.22 Å) in the host matrix $\text{Bi}_{0.5-x}\text{Er}_x\text{Na}_{0.5}\text{TiO}_3$ at the Bi^{3+} site (1.32 Å) [20]. A significant decrease in the lattice parameters (a, b and c) and unit cell volume with increasing Er^{3+} content in the $\text{Bi}_{0.5-x}\text{Er}_x\text{Na}_{0.5}\text{TiO}_3$ ($x = 0.00 - 0.05$) composition (Table 3.1) can be corroborated with contraction of unit cell caused by difference in the ionic radii of Bi^{3+} ions with smaller Er^{3+} ions. Further, it can be noticed from Table 3.1, the measured density (ρ) of sintered ceramics using Archimedes 'principle, has increased from 5.36 - 6.01 g/cm³ with increasing Er^{3+} content, which is greater than 99% of the reported theoretical density (5.99 g/cm³).

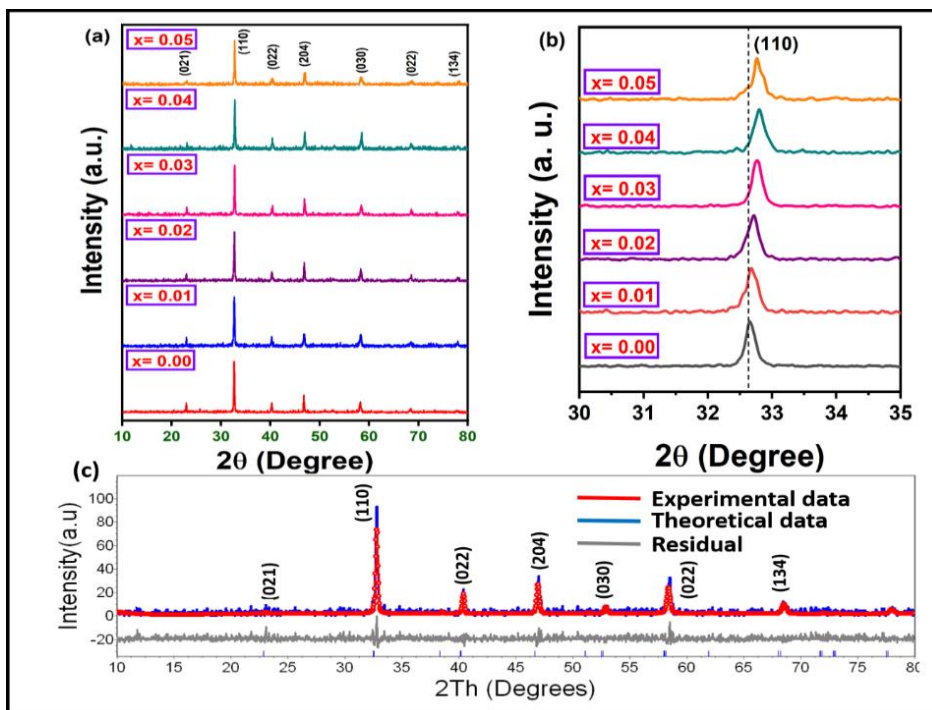


Figure 3.2: (a) XRD spectra of $\text{Bi}_{0.5-x}\text{Er}_x\text{Na}_{0.5}\text{TiO}_3$ ($x = 0.00, 0.01, 0.02, 0.03, 0.04, 0.05$), (b) Peak shifting of (110) plane, (c) Profile fitting using Topaz software

The microstructure and grain growth on the surface of sintered ceramics of Er^{3+} doped $\text{Bi}_{0.5-x}\text{Er}_x\text{Na}_{0.5}\text{TiO}_3$ were examined using surface electron microscopy as shown in **Figure 3.3(a-f)**. Microstructural details reveal non-uniform distribution of grain size. The average grain size for all the compositions were determined by Lorentz fit of the histogram plot obtained using Image software. It can be seen from the **Figure 3.3(a-f)**, compact microstructure with delineated grain boundaries along with reduced porosity are obtained with average grain size of $> 2\mu\text{m}$ for $x = 0.0$ composition. However, average grain size decreases with increasing Er

content in $\text{Bi}_{0.5-x}\text{Er}_x\text{Na}_{0.5}\text{TiO}_3$ for $x = 0.01$ to $x = 0.05$ in Table 3.1, which could be attributed to the variation in the electron charge density due to incorporation of Er^{3+} ions, which slows down the diffusion process and inhibits the grain growth mechanism [19].

Table 3.1: Lattice and fitting parameters of XRD pattern for $\text{Bi}_{0.5-x}\text{Er}_x\text{Na}_{0.5}\text{TiO}_3$ with different concentration

Lattice Parameters	$\text{Bi}_{0.5-x}\text{Er}_x\text{Na}_{0.5}\text{TiO}_3$					
	$x=0.00$	$x=0.01$	$x=0.02$	$x=0.03$	$x=0.04$	$x=0.05$
R_{wp}	24.35	20.26	11.83	12.01	9.08	9.53
R_{exp}	14.81	12.81	10.96	10.87	8.72	9.02
R_P	21.49	20.28	12.23	12.01	10.04	11.07
$\text{GoF}(\chi)$	1.64	1.58	1.08	1.10	1.04	1.00
a (Å)	5.4926	5.4812	5.4764	5.4648	5.4556	5.4360
b (Å)	5.4926	5.4812	5.4764	5.4648	5.4556	5.4360
c (Å)	13.4972	13.4818	13.4702	13.4643	13.3483	13.3289
V (Å ³)	352.6389	350.7760	349.8606	348.2274	344.0659	341.0889
Density (g/cm ³)	5.36879	5.85068	5.95810	6.01005	5.93988	5.98225
Grain Size (μm)	2.3246	1.4110	1.3747	1.3310	1.3002	1.2430

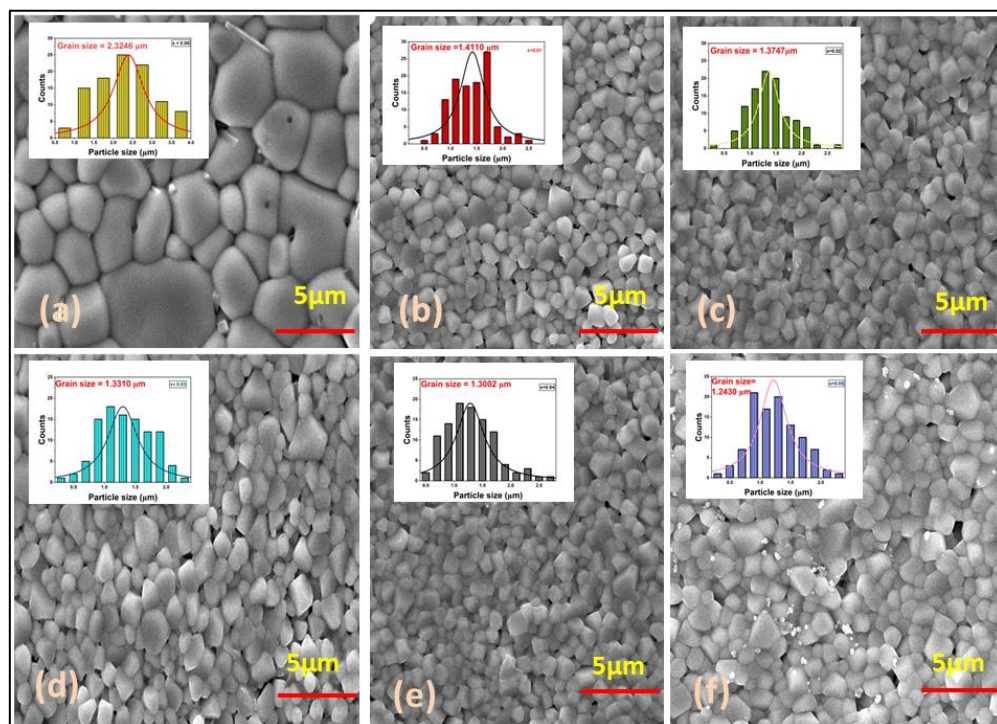


Figure 3.3: (a-f) SEM micrographs of $\text{Bi}_{0.5-x}\text{Er}_x\text{Na}_{0.5}\text{TiO}_3$ ($x = 0.00, 0.01, 0.02, 0.03, 0.04, 0.05$). Inset: Histograms for grain size calculation

3.3.2 Fourier Transform Infrared (FTIR) Spectroscopy Studies

Figure 3.4 displays the Fourier-transform infrared (FTIR) spectra of Er^{3+} doped $\text{Bi}_{0.5-x}\text{Er}_x\text{Na}_{0.5}\text{TiO}_3$ (BNT) samples, which were obtained at room temperature. The FTIR spectra were recorded within the wavenumber range of 400 to 1400 cm^{-1} . The vibrational bands detected at wavenumbers 534 and 820 cm^{-1} correspond to the intrinsic vibration band of BNT. The absorption bands observed in this study have been attributed to the stretching of Ti-O bonds within octahedral groups present in the perovskite structure [21]. The observed shift of the FTIR bands at 820 and 534 cm^{-1} towards lower wavenumbers can be attributed to the sensitivity of host materials to the presence of foreign ions within the host lattice [22, 23].

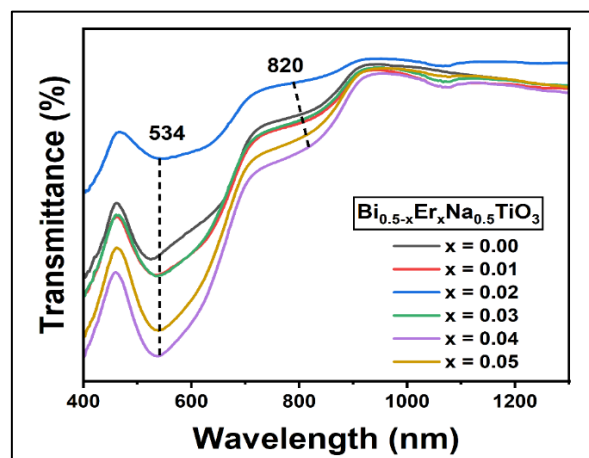


Figure 3.4: FTIR Spectra of $\text{Bi}_{0.5-x}\text{Er}_x\text{Na}_{0.5}\text{TiO}_3$ ($x=0.00, 0.01, 0.02, 0.03, 0.04, 0.05$) ferroelectric ceramic

3.3.3 Diffuse Reflectance Spectroscopy for band gap analysis

Reflectance spectra on sintered powders of Er^{3+} modified $\text{Bi}_{0.5-x}\text{Er}_x\text{Na}_{0.5}\text{TiO}_3$ ($x = 0.00 - 0.05$) ceramic compositions were recorded and are presented in **Figure 3.5(a)**. The absorption bands positioned at $\sim 384, 488, 522, 545, 653, 795, 975$ nm appears from the different energy levels of Er^{3+} ions and are represented as $^4\text{G}_{11/2}$, $^4\text{F}_{7/2}$, $^2\text{H}_{11/2}$, $^4\text{S}_{3/2}$, $^4\text{F}_{9/2}$, $^4\text{I}_{9/2}$ and $^4\text{I}_{11/2}$ respectively. The band gap energy (E_g in eV) of Er^{3+} doped $\text{Bi}_{0.5-x}\text{Er}_x\text{Na}_{0.5}\text{TiO}_3$ ceramic compositions are estimated using Kubelka-Munk (K-M) relation as expressed in the Eq. 3.2 [22]:

$$F(R) = \frac{(1-R)^2}{2R} = \frac{K}{S} \quad (3.2)$$

where, R stands for total reflectance of specimen, S for scattering coefficient, and K for absorption coefficient, $F(R)$ is known as the Kubelka-Munk (K-M) function. Further, for diffused scattered light, assuming S as constant with respect to wavelength, $F(R)$ can be associated with the tauc plot equation and represented by Eq. (3.3) [22]:

$$(F(R)hv) = B(hv - E_g)^n \quad (3.3)$$

where h is the Planck's constant, v is the vibrational frequency and B = constant of proportionality, E_g is the material's optical band gap and n denotes the nature of the electronic transition.

Figure 3.5 (b-d) shows the estimation of band gap values from the linear extrapolation in the $[F(R)hv]^2$ versus hv plot. The obtained values for the optical band gap of $\text{Bi}_{0.5-x}\text{Er}_x\text{Na}_{0.5}\text{TiO}_3$ ($E_g = 3.02\text{ eV}$) are in accordance with the reported literature [22]. The estimated value of band gap is found to decrease from 3.02 to 2.92 eV with an increase in Er^{3+} content from ($x = 0.01$ to 0.05). The observed variation in the optical band gap could be accredited to the local structural disorder in the lattice as well as the generated oxygen vacancies, which arises with the introduction of smaller Er^{3+} ions at the Bi^{3+} sites and affects the local electron density [22].

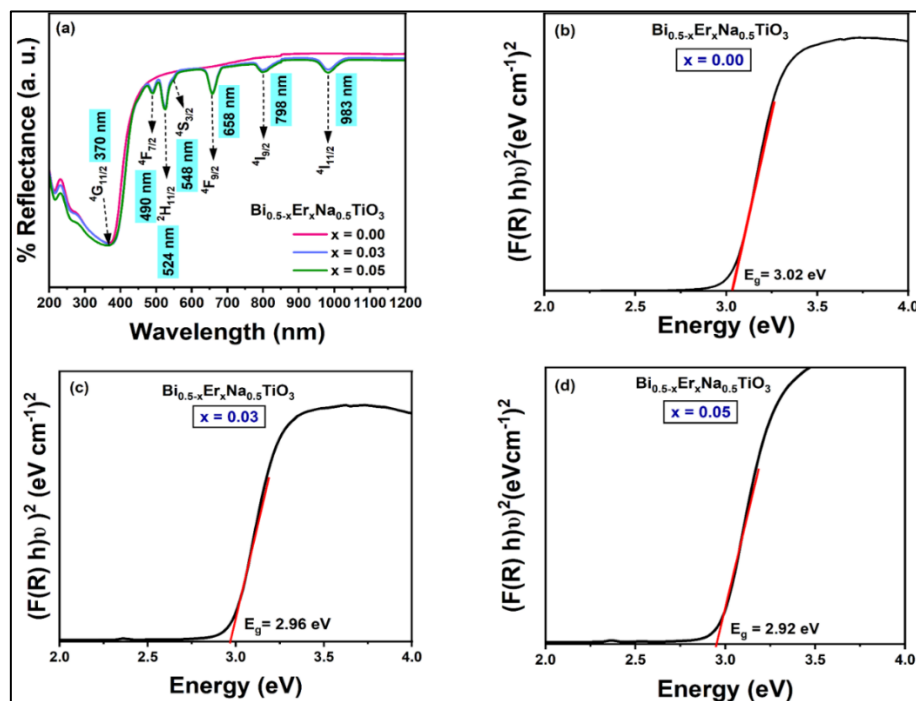


Figure 3.5: (a) Diffuse reflectance spectra of $\text{Bi}_{0.5-x}\text{Er}_x\text{Na}_{0.5}\text{TiO}_3$ ($x = 0.00, 0.03, 0.05$) (b-d) Energy band gap of $\text{Bi}_{0.5-x}\text{Er}_x\text{Na}_{0.5}\text{TiO}_3$ ($x = 0.00, 0.03$, and 0.05)

3.3.4 Ferroelectric Hysteresis Analysis and Energy Storage density

Figure 3.6 represents the plot of polarization against an applied electric field (P-E) hysteresis loops at room temperature (300K). The hysteresis loops of undoped and Er^{3+} doped BNT are traced at an applied frequency of 30 Hz under an external applied electric field of $E \leq 70 \text{ kV/cm}$. From **Figure. 3.6**, it can be seen that well shaped saturated P-E loops with remnant polarization ($2P_r$) = $137.06 \mu\text{C/cm}^2$ and coercive field ($2E_c$) = 88.48 kV/cm are obtained for the undoped polycrystalline $\text{Bi}_{0.5-x}\text{Er}_x\text{Na}_{0.5}\text{TiO}_3$ ($x = 0.0$) ceramic (Table 3.2). The values of the ferroelectric parameters (E_c and P_r) obtained in the present study are found to be in synchronization with the reported literature [26]. However, in the Er^{3+} modified $\text{Bi}_{0.50-x}\text{Er}_x\text{Na}_{0.5}\text{TiO}_3$ ($x = 0.01, 0.02, 0.03, 0.04, 0.05$) ceramic compositions, the remnant polarization decreases with an increase in Er^{3+} content and a similar trend is seen for the variation in coercive field. It is reported in the literature that the ferroelectric properties are influenced by compositional modifications, domain nucleation, processing conditions and inherent lattice defects causing cationic and oxygen vacancies [27]. The major cause of suppression in the ferroelectric properties could be attributed to the lattice defects or strain in the material composition due to volatilization of bismuth at high temperatures, resulting in the formation of oxygen vacancies. The oxygen vacancies exhibit high mobility and have a tendency to move towards the interfaces of domain walls or electrodes under the effect of an externally applied electric field. This phenomenon hinders the domain switching process and consequently leads to reduced P_r values.

The quality of PE loops is affected by the presence of stress within the lattice, changes in the chemical structure, or imperfections in the grain boundaries. The observed decrease in P_r and P_{\max} values with Er^{3+} substitution could be attributed to the decreasing grain size coupled with compositional disturbance caused by the incorporation of these rare earth ions of smaller radii in the host lattice and agree with other reported results in literature [28].

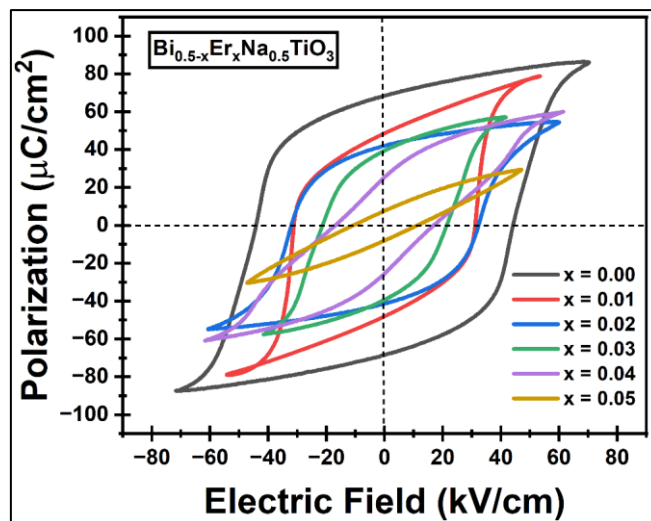


Figure 3.6: PE loop of $\text{Bi}_{0.5-x}\text{Er}_x\text{Na}_{0.5}\text{TiO}_3$ ($x=0.00, 0.01, 0.02, 0.03, 0.04, 0.05$) at room temperature

Table 3.2: Hysteresis loop parameters ($2P_r$, $2E_c$) and energy storage density parameters (W , W_{rec} , η) estimated from the Rietveld refinement of XRD pattern for $\text{Bi}_{0.50-x}\text{Er}_x\text{Na}_{0.5}\text{TiO}_3$ with different concentration

$\text{Bi}_{0.5-x}\text{Er}_x\text{Na}_{0.5}\text{TiO}_3$	$2P_r$ ($\mu\text{C}/\text{cm}^2$)	$2E_c$ (kV/cm)	W (J/cm^3)	W_{rec} (J/cm^3)	η (%)
$x = 0.00$	137.06	88.48	6.0179	2.9211	48.54
$x = 0.01$	96.24	62.94	4.230546	2.547846	60.22
$x = 0.02$	84.66	65.00	3.242354	1.309904	40.39
$x = 0.03$	77.06	43.98	2.368453	1.456968	61.51
$x = 0.04$	51.28	34.96	3.665171	2.594172	70.77
$x = 0.05$	16.42	22.48	1.393319	0.867962	62.29

The energy storage density of prepared $\text{Bi}_{0.5-x}\text{Er}_x\text{Na}_{0.5}\text{TiO}_3$ ceramic compositions is recorded in Table 3.2. The energy storage density (W), the recoverable energy storage density (W_r), and efficiency of energy storage density (η) is given by Eq. (3.4, 3.5, 3.6):

$$W = \int_0^{P_{max}} EdP \quad (3.4)$$

$$W_r = \int_{P_r}^{P_{max}} EdP \quad (3.5)$$

$$\eta = \frac{W_r}{W} \times 100\% \quad (3.6)$$

where P_{\max} is the maximum polarization of a particular concentration, P_r is the remnant polarization, and E is the applied electric field. The W_r of prepared ceramics showed improved results than the previously reported work of same host material [29]. The highest value of W_r for undoped BNT ceramic was found to be approximately 6.0179 J/cm^3 whereas for Er^{3+} doped BNT ceramic it is 2.5941 J/cm^3 . The energy storage density of BNT ceramic increases with increased Er^{3+} doping content (48.00 % to 70.77 %).

3.3.5 Temperature independent PL spectra under 488 nm

The temperature independent down conversion PL emission spectra of $\text{Bi}_{0.5-x}\text{Er}_x\text{Na}_{0.5}\text{TiO}_3$ with altering Er^{3+} concentrations under 488 nm excitation are shown in **Figure 3.7**. The intense green emission bands at 530 nm and 550 nm are attributed to the excited states $^2\text{H}_{11/2}$ and $^4\text{S}_{3/2}$ to the ground state $^4\text{I}_{15/2}$. The transition from $^4\text{F}_{9/2}$ to $^4\text{I}_{15/2}$ results in a weak red band at 660 nm. Also, it has been observed that the emission intensity degrades after the optimum Er^{3+} concentration ($x > 0.03$) as given in inset **Figure 3.7**. The results are consistent with upconversion luminescence spectra (discussed in Section 3.7). However, each emission band (530, 550, and 660 nm) under the excitation of 488 nm is less intense than that of the 980 nm excitation. This is because in the down conversion PL spectra (488 nm), the electrons undergo directly to $^4\text{F}_{9/2}$ energy level. The multiphonon relaxation at this level causes non-radiative transitions, which ultimately degrade the intensity of the emission band [30].

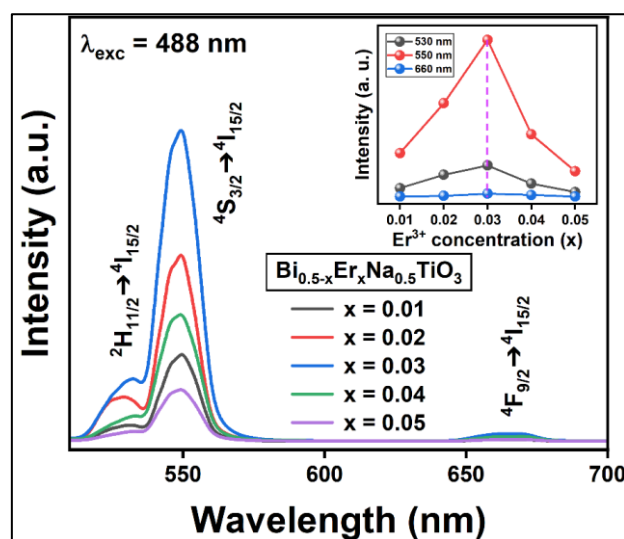


Figure 3.7: PL spectra of prepared $\text{Bi}_{0.5-x}\text{Er}_x\text{Na}_{0.5}\text{TiO}_3$ ($x=0.01, 0.02, 0.03, 0.04, 0.05$) under the excitation of 488 nm

3.3.6 Visible light upconversion luminescence under 980 nm

Figure 3.8(a) displays the light upconversion luminescence spectra of Er^{3+} doped $\text{Bi}_{0.5-x}\text{Er}_x\text{Na}_{0.5}\text{TiO}_3$ ceramic measured at an excitation wavelength of 980 nm. The emission spectra of Er^{3+} ions exhibit three distinct emission bands. The first two bands, which are characterized by two strong green emissions, are centered at peak positions of 530 and 550 nm. These emissions are attributed to the transitions from the $^2\text{H}_{11/2}$ and $^4\text{S}_{3/2}$ energy levels to the $^4\text{I}_{15/2}$ energy level. The second band, which is a weaker red emission, is observed at a wavelength of 670 nm. This emission is associated with the transition from the $^4\text{F}_{9/2}$ energy level to the $^4\text{I}_{15/2}$ energy level [31]. The emission intensity increases with an increase in concentration up to an optimum Er^{3+} concentration ($x < 0.03$), as shown in **Figure 3.8(b)**. This phenomenon is called concentration-quenching. In this scenario, the position of Er^{3+} ions become sufficiently close, facilitating energy exchange between them and leading to non-radiative transitions. The occurrence of non-radiative transitions leads to a reduction in the intensity of emission. The Blasse formula, as denoted by Eq. (3.7), can be utilized to assess the critical distance between Er ions [23]:

$$R_c \approx 2 \left[\frac{3V}{4\pi x_c Z} \right]^{\frac{1}{3}} \quad (3.7)$$

here, V is the unit cell volume and is equal to 351.0450, no. of host cations is denoted by $Z = 3$, and critical concentration $x_c = 0.03$. These parameters give R_c equal to 19.53 Å. In **Figure 3.8(c)**, the energy level of Er^{3+} is portrayed. The upconversion mechanism is commonly elucidated through the following processes: multiphonon relaxation (MPR), excited state absorption (ESA), ground state absorption (GSA), cross relaxation (CR), and energy transfer (ET). A photon with lower energy is stimulated by a laser emitting at a wavelength of 980 nm, it transitions to a higher energy level denoted as $^4\text{I}_{11/2}$ through a process called GSA.

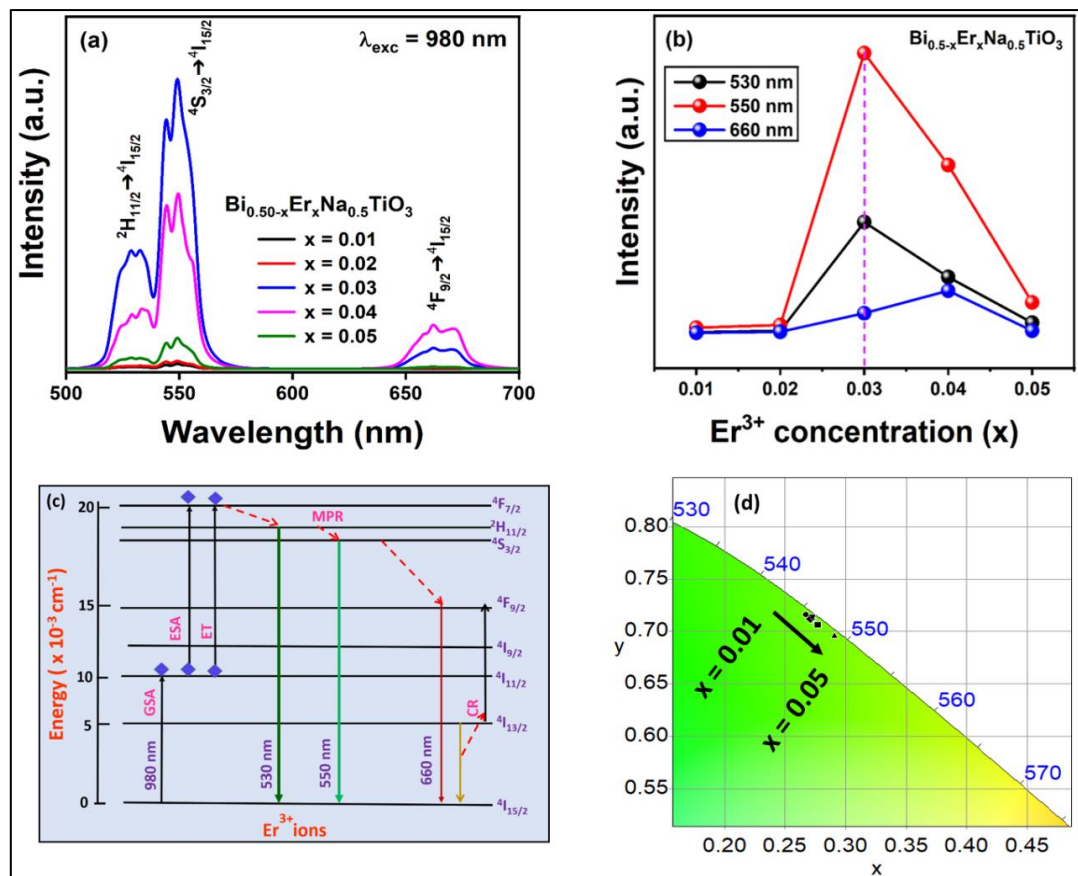


Figure 3.8: (a) UCL spectra of $\text{Bi}_{0.5-x}\text{Er}_x\text{Na}_{0.5}\text{TiO}_3$ ($x=0.01, 0.02, 0.03, 0.04, 0.05$) at 980 nm excitation, (b) UCL intensity as a function of Er^{3+} concentration, (c) Energy level diagram of Er^{3+} , (d) CIE plot of $\text{Bi}_{0.5-x}\text{Er}_x\text{Na}_{0.5}\text{TiO}_3$ ($x=0.01, 0.02, 0.03, 0.04, 0.05$)

From this level, the system undergoes the process of photon absorption through ESA, resulting in its transition to the ${}^4\text{F}_{7/2}$ energy level. Additionally, another photon was also transferred to this level by ET. The aforementioned processes resulted in the occupation of the higher energy level ${}^4\text{F}_{7/2}$. Non-radiative transitions occur from this particular energy level to lower energy levels ${}^2\text{I}_{11/2}$, ${}^4\text{S}_{3/2}$, and ${}^4\text{F}_{9/2}$. Ultimately, the electrons undergo a transition to the ground state from these particular energy levels, leading to the two distinct emission bands in the green region, specifically at wavelengths of approximately 530 nm and 550 nm. Additionally, there is a comparatively less intense emission band in the red region at 660 nm. The CIE plot of prepared ceramic is given in Figure 3.8(d). The XY coordinates are located in the green region and it has been observed that as the concentration of Er^{3+} increases, there is a noticeable shift towards a more pronounced green emission intensity.

3.3.7 Time resolved decay time measurements

Figure 3.9(a-e), illustrates the decay curve of the emission band at 550 nm, resulting from the excitation at 980 nm, via the transition $^4S_{3/2} \rightarrow ^4I_{15/2}$ for all the Er^{3+} doped BNT ceramics. The decay time is measured by fitting the curve using a tri-exponential function, given by Eq. (3.8):

$$I(t) = I_0 + A_1 \exp\left(-\frac{t}{\tau_1}\right) + A_2 \exp\left(-\frac{t}{\tau_2}\right) + A_3 \exp\left(-\frac{t}{\tau_3}\right) \quad (3.8)$$

where I_0 is the initial intensity when time, $t = 0$ sec, is $I(t)$ is the luminescence intensity at particular time t , A_1, A_2, A_3 are the fitting variables and τ is time decay at time t . The mean life time is evaluated by Eq. (9):

$$\langle \tau \rangle = \frac{A_1 \tau_1^2 + A_2 \tau_2^2 + A_3 \tau_3^2}{A_1 \tau_1 + A_2 \tau_2 + A_3 \tau_3} \quad (3.9)$$

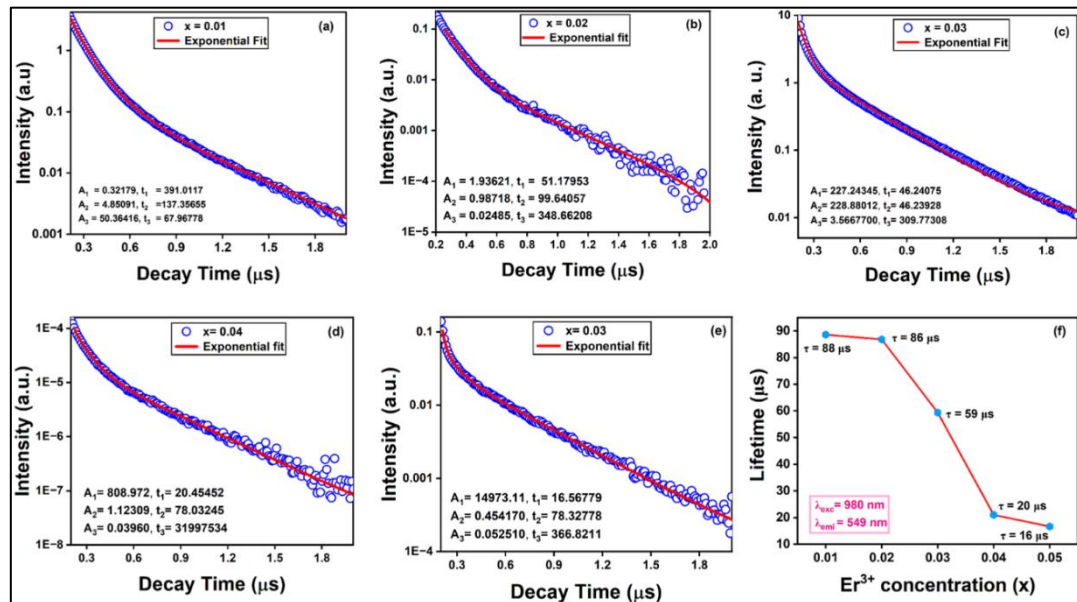


Figure 3.9: (a-e) Time decay analysis of $Bi_{0.5-x}Er_xNa_0.5TiO_3$ ($x=0.01, 0.02, 0.03, 0.04, 0.05$), (f) Variation of lifetime with Er^{3+} concentration

The photoluminescence lifetime of green emission of Er^{3+} doped $Bi_{0.5-x}Er_xNa_0.5TiO_3$ ceramic decreases from 88 μ s to 16 μ s as the Er^{3+} concentration increases as shown in **Figure 3.9(f)**. This decrease in lifetime values of prepared ceramic occurred because of the energy exchange between the Er^{3+} ions at higher doping concentrations, resulting in a non-radiative transition [32, 33].

3.3.8 Upconversion Luminescence with varying pump powers

The dependency of pump power on upconversion luminescence is an important study to determine the number of photons involved in the UC process. $\text{Bi}_{0.5-x}\text{Er}_x\text{Na}_{0.5}\text{TiO}_3$ ($x = 0.03$) is studied for upconversion luminescence spectra at various pump power spanning from 450 to 950 mW/cm^2 as shown in **Figure 3.10**. The intensity of upconversion luminescence seems to increase with increasing pump power. This can be verified from the Eq. (3.10):

$$I_{UCL} \propto P^n \quad (3.10)$$

where P is pumping power, n is the amount of photons needed in the up conversion process, and I_{UCL} is the UCL intensity. The log of intensity is plotted against the log of excitation pump power (inset of **Figure 3.10**).

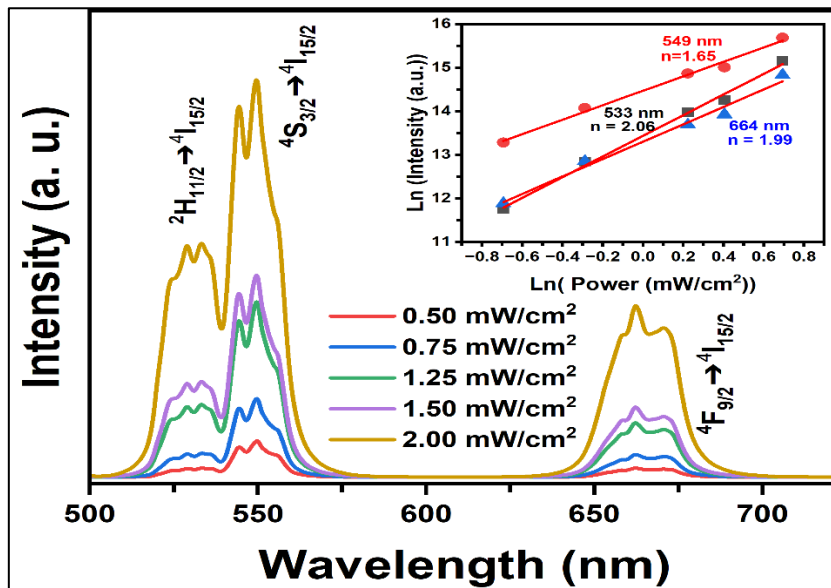


Figure 3.10: Pump Power dependency on UCL spectra of $\text{Bi}_{0.5-x}\text{Er}_x\text{Na}_{0.5}\text{TiO}_3$ ($x=0.03$) ferroelectric ceramic

The n value is evaluated for green and red emission bands from the slope of the logarithmic plot. The n value for two green bands and on red band are 2.36, 1.65, 1.99 respectively. This confirms the involvement of two photons in the UC emission intensity. The n value is approximated to the expected value of 2. This discrepancy is due to the influence of multiple mechanisms (non-radiative transitions, ET, ESA) in the emission spectra [34].

3.3.9 Non-Intrusive temperature sensitivity

The non-contact temperature sensing performance of $\text{Bi}_{0.5-x}\text{Er}_x\text{Na}_{0.5}\text{TiO}_3$ ($x = 0.03$) ceramic has been investigated by LIR (Luminescence intensity ratio) technique. This method compares the intensities of two thermocouple (TCLs) energy levels $^2\text{H}_{11/2}$ and $^4\text{S}_{3/2}$ with external temperatures. This approach has been extensively utilised for the examination of temperature sensitivity in various host materials doped with RE. The time-dependent upconversion luminescence spectra ranging from temperature 303K to 523K is represented in **Figure 3.11(a)**. The UCL intensity decreases with increasing temperature due to the result of thermal equilibrium in TCLs. The LIR can be expressed as the ratio of intensities of two green band emission through $^2\text{H}_{11/2} \rightarrow ^4\text{I}_{15/2}$ and $^4\text{S}_{3/2} \rightarrow ^4\text{I}_{11/2}$ and is given by Eq. (3.11) [35]:

$$LIR = \frac{I_H}{I_S} = C \exp\left(-\frac{\Delta E}{K_B T}\right) \quad (3.11)$$

where ΔE is the energy gap between two TCLs, C is the constant, I_H and I_S corresponds to green emission band intensities with emission wavelengths at 529 nm and 549 nm, respectively. The values of LIR vary from 0.28 to 1.19 in the temperature range 303K to 523K and are depicted in **Figure 3.11(b)**. To calculate the sensitivity of the ceramic the Eq. 3.12 can be expressed in the linear form as [33]:

$$\ln(LIR) = -\left(\frac{\Delta E}{K_B}\right)\left(\frac{1}{T}\right) + \ln C \quad (3.12)$$

The plot of $\ln(LIR)$ versus temperature inverse is displayed in **Figure 3.11(c)**. The slope gives $\Delta E/K_B$ value and intercept $\ln C$ as -1040.33 ± 16.19743 and 2.18446 ± 0.04097 , respectively. These parameters are used to calculate absolute (S_{ab}) and relative (S_{rel}) sensitivity of the ceramic demonstrated by Eq. 3.13, 3.14, respectively:

$$S_{ab} = \frac{d(LIR)}{dT} = \frac{d\left(C \exp\left(-\frac{\Delta E}{K_B T}\right)\right)}{dT} = C \exp\left(-\frac{\Delta E}{K_B T}\right) \left(\frac{\Delta E}{K_B T^2}\right) \quad (3.13)$$

$$S_{rel} = \frac{1}{LIR} * S_{ab} = \left(\frac{\Delta E}{K_B T^2}\right) \quad (3.14)$$

Figure 3.11(d) illustrates the graphical representation of S_{rel} and S_{ab} plotted against temperature. Between temperature 303-523 K, the absolute sensitivity of synthesized material ranges from $0.32\% \text{ K}^{-1}$ to $0.47\% \text{ K}^{-1}$. The largest value sensitivity is obtained 0.47

% K⁻¹ at 523 K. To ensure the success of sensor, temperature resolution and reproducibility of the sensor are important factors. The reproducibility test was conducted by repeatedly alternating between two temperatures, specifically 303 K and 523 K, as depicted in **Figure 3.12(a)**. The LIR values exhibit a small variance across the two temperatures. The calculation of reproducibility (R) and resolution (δT) is performed using the Eq. 3.15, 3.16, respectively:

$$R = 1 - \frac{(\Delta_m - \Delta_{sp})}{\Delta_{Av}} \quad (3.15)$$

$$\delta T = \frac{1}{S_r} \times \frac{\delta \Delta}{\Delta} \quad (3.16)$$

where Δ_{sp} and Δ_m are specific and mean values of LIR between temperature 303K to 523K and $\delta \Delta / \Delta$ represents the measure of precision of the instrument. **Figure 3.12(b)** represents, the temperature resolution increases 2.6 to 7.8 between temperatures 303K to 523K. Table 3.3 presents a comparative analysis of the sensitivity exhibited by various host materials doped with Er³⁺ ions. The Bi_{0.5-x}Er_xNa_{0.5}TiO₃ ($x = 0.03$) ceramic has been observed to possess sensor capabilities, making it a promising material for potential applications in the field of optical temperature sensors.

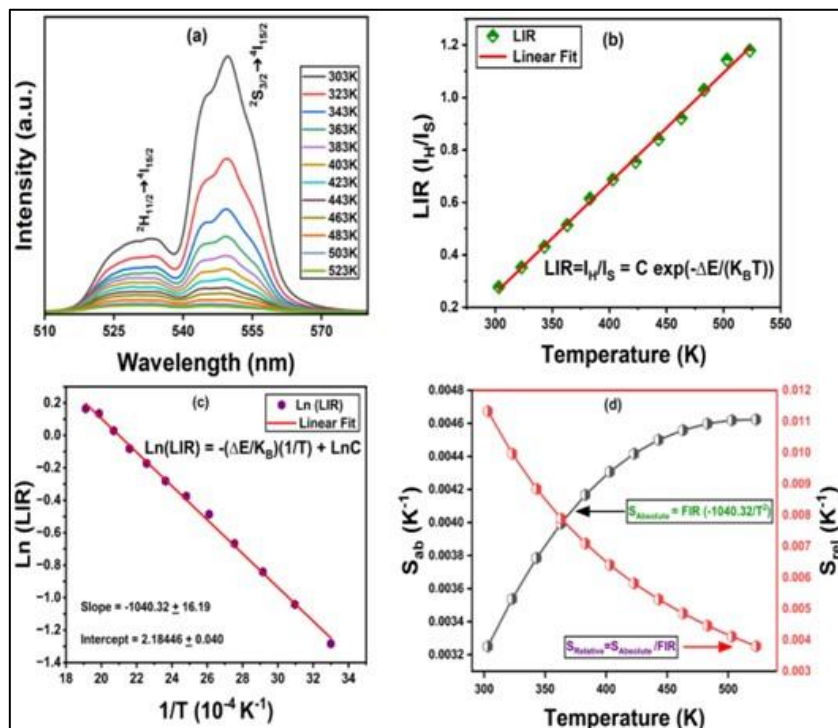
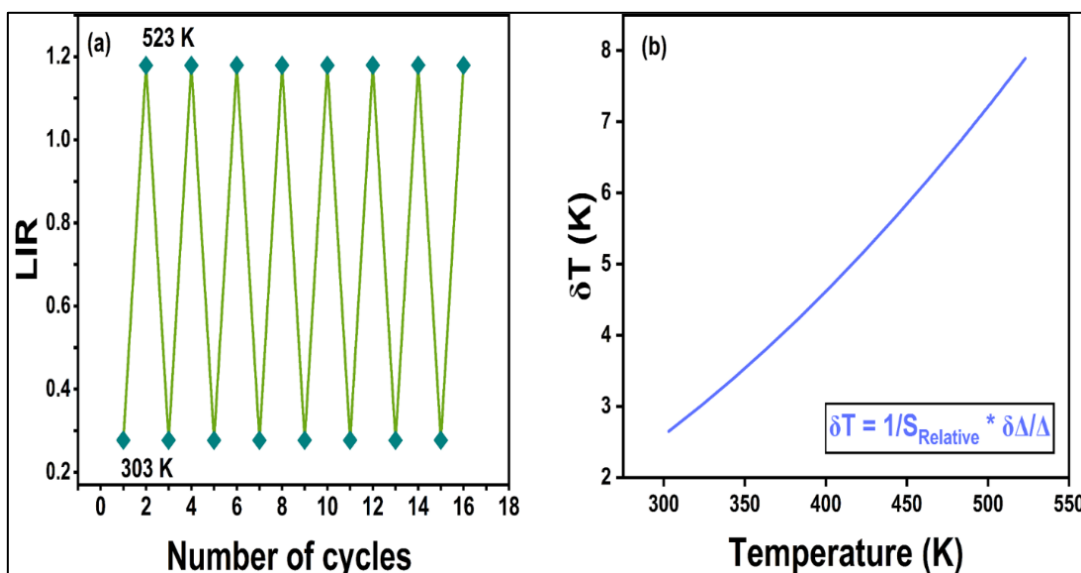


Figure 3.11: (a) Temperature dependent UCL spectra, (b) Plot of LIR and temperature, (c) Ln(LIR) vs inverse temperature, (d) Plot of absolute (S_{ab}) and relative sensitivity (S_{rel})

Table 3.3: Sensitivity parameters of various Er³⁺ doped ferroelectric ceramics

S. No.	Host material	Temp range (K)	Max sensitivity temp (K)	Max sensitivity (K ⁻¹)	Ref
1	NBT/BIT:Er	290-440	290	0.0020	[36]
2	NBT:Er	80-480	-	0.053	[37]
3	NBT:Er/Yb	163-613	-	0.0031	[38]
4	NBT :Er/Yb/Mo	173-553	493	0.0035	[39]
5	BBN:Er	300-623	483	0.00996	[33]
6	SBN:Er	303-443	443	0.0086	[23]
8	BNT/KNN:Er	-	425	0.002	[40]
9	BNT:Er	303-523	523	0.0047	This work

**Figure 3.12: (a) Repeatability test varying between two temperature (303K-523K), (b) Plot of δT vs temperature**

3.4 Summary

In summary, the present work shows that the pure $\text{Bi}_{0.5}\text{Na}_{0.5}\text{TiO}_3$ was synthesised by solid state method and incorporation of Er^{3+} with varying concentration ($x = 0.01, 0.02, 0.03, 0.04, 0.05$) was successfully done. The structural properties were thoroughly verified by X-Ray Diffraction and Rietveld refinement analysis. X-ray diffraction depicts the pure phase with no extra phases and complete solubility of Er^{3+} in the host

lattice. The shifting of peaks towards higher angles confirms by the decrement in cell volume parameters. The typical FTIR bands at 534 and 820 cm^{-1} confirms the stretching in Ti-O_3 . The decent squared shaped saturated P-E hysteresis are obtained under an electric field of $E \leq 70$ kV/cm , and the loops become slimmer at higher Er^{3+} concentrations (x . 0.04). The efficiency of energy storage density increases with Er^{3+} doping and an improved recoverable energy storage ($W_r = 2.594 \text{ J/cm}^3$) and a higher efficiency ($\eta = 70.77\%$) are obtained for Er content, $x = 0.04$. The two strong green emission spectra at 530 nm and 550 nm via transition $^5\text{S}_{3/2} \rightarrow ^4\text{I}_{15/2}$ and the weak red emission spectra at 660 nm by transition from $^4\text{F}_{9/2} \rightarrow ^4\text{I}_{15/2}$ under the excitation of 488 nm and 980 nm. The luminescence intensity increases upto optimum value of Er^{3+} ($x = 0.03$) concentration. The lifetime of green emission spectra of Er^{3+} ions decreases from $88\mu\text{s}$ to $16\mu\text{s}$ due to the non-radiative transition and cross relaxations of Er^{3+} ions. The variation in pump power of upconversion luminescence confirms involvement of two photons in the UC process. The energy band gap decreases gradually with the increase in dopant concentration. Well saturated P-E loops were obtained for all the concentrations of Er^{3+} and the shape of loop becomes slimmer at Er^{3+} content $x > 0.04$. The critical concentration ($x = 0.03$) is used for thermal sensing behaviour of $\text{Bi}_{0.5}\text{Er}_{1-x}\text{Na}_{0.5}\text{TiO}_3$ ceramic is evaluated in the temperature range 303 - 523 K. The absolute and relative sensitivity of the prepared ceramic obtained $0.47\% \text{ K}^{-1}$ at 523 K and $1.1\% \text{ K}^{-1}$ at 303 K, respectively. Therefore, we can conclude that by doping Er^{3+} in BNT based ceramics have a potential application in optoelectronic and energy storage multifunctional devices.

A detailed evaluation of the single Er^{3+} -doped $\text{Bi}_{0.5}\text{Na}_{0.5}\text{TiO}_3$ ceramic reveals certain limitations that need to be considered. While erbium incorporation improves upconversion luminescence and sensing performance, it simultaneously leads to a decline in ferroelectric behavior. To overcome this drawback, it becomes essential to investigate the combined influence of Yb^{3+} and Er^{3+} ions in BNT ceramics. In light of these findings, the study will proceed to investigate the co-doping of Yb^{3+} and Er^{3+} ions in BNT ceramics, which constitutes the main focus of the next chapter.

3.5 References

1. H. Katzke, M. Dietze, A. Lahmar, M. Es-Souni, N. Neumann, and S.-G. Lee, “Dielectric, ultraviolet/visible, and Raman spectroscopic investigations of the phase transition sequence in $0.71\text{Pb}(\text{Mg}_{1/3}\text{Nb}_{2/3})\text{O}_3\text{-}0.29\text{PbTiO}_3$ crystals”, *Phys. Rev. B*, 83 (2011) 174115, doi.org/10.1103/PhysRevB.83.174115.
2. D. Nawrocka, “Environmental supply chain management, ISO 14001 and RoHS. How are small companies in the electronics sector managing” *Corp. Soc. Responsib. Environ. Manag.* 15 (2008) 349–360, <https://doi.org/10.1002/csr.176>.
3. F. Li, J. Li, J. Zhai, B. Shen, S. Li, M. Zhou and H. Zeng, “Influence of structural evolution on electrocaloric effect in $\text{Bi}_{0.5}\text{Na}_{0.5}\text{TiO}_3\text{-SrTiO}_3$ ferroelectric ceramics”, *J. Appl. Phys.* 124 (2018) 164108, doi.org/10.1063/1.5050826.
4. A. Gallegos-Melgar, D.G. Espinosa-Arbelaez, F.J. Flores-Ruiz, A. Lahmar, J.-L. Dellis, N. Lemée, F.J. Espinoza-Beltran and J. Munoz-Saldana, “Ferroelectric properties of manganese doped $(\text{Bi}_{1/2}\text{Na}_{1/2})\text{TiO}_3$ and $(\text{Bi}_{1/2}\text{Na}_{1/2})\text{TiO}_3\text{-BaTiO}_3$ epitaxial thin films”, *Appl. Surf. Sci.* 359 (2015) 923–930, doi.org/10.1016/j.apsusc.2015.09.175.
5. S. Kumar and S. Singh, “Study of electrocaloric effect in lead-free $0.9\text{K}_{0.5}\text{Na}_{0.5}\text{NbO}_3\text{-}0.1\text{CaZrO}_3$ solid solution ceramics”, *J. Mater. Sci. Mater. Electron.* 30 (2019) 12924–12928, doi.org/10.1007/s10854-019-01654-w.
6. M. Benyoussef, M. Zannen, J. Belhadi, B. Manoun, J.L. Dellis, M. El Marssi and A. Lahmar, “Dielectric, ferroelectric, and energy storage properties in dysprosium doped sodium bismuth titanate ceramics”, *Ceram. Int.* 44 (2018) 19451–19460, doi.org/10.1016/j.ceramint.2018.07.182.
7. J. Sun, B. Fang, S. Zhang, Z. Chen, J. Ding, X. Zhao and H. Luo, “Upconversion and Downconversion luminescence properties of Er^{3+} doped NBT ceramics synthesized via Hydrothermalmethod” *Opt.Mater.* 69 (2017) 244-249 doi.org/10.1016/j.optmat.2017.04.048.

8. S. Chen, M. Wu, L. An, Y. Li and S. Wang, "Strong Green and Red Upconversion Emission in Er³⁺-Doped Na_{1/2}Bi_{1/2}TiO₃ Ceramics" J. Am. Ceram. Soc. 90 (2) (2007) 664–666 doi.org/10.1111/j.1551-2916.2006.01457.x.
9. H.Sun, D.Peng, X. Wang, M. Tang, Q. Zhang and X.Yao "Electrical and luminescence properties of Er –doped Bi_{0.5}Na_{0.5}TiO₃ " J.Appl.Lett. 110 (2011) 016102 -016105 doi.org/10.1016/j/mseb.2013.08.007.
10. P. Salas, R.Urby, L.A.Torre ,G.Rodriguez, ,M. Vega and C. Chavez " RE lectrical and luminescence properties of Er –doped Bi_{0.5}Na_{0.5}TiO₃ ceramics " Matter.Sci.Eng. B178 (2013) 1423-1429. Doi.org/10.1016/j.mseb.2013.08.007.
11. A. Banwal and R. Bokolia, "Efficient tunable temperature sensitivity in thermally coupled levels of Er³⁺/Yb³⁺ co-doped BaBi₂Nb₂O₉ ferroelectric ceramic," J. Lumin., vol. 263, no. May, p. 120071, 2023. doi: 10.1016/j.jlumin.2023.120071.
12. X. Wang, Q. Liu, Y. Bu,C.S. Liu,T. Liua and X Yan "Optical temperature sensing of rare-earth ion doped phosphors" R. Soc. Chem. v., 2015, 5, 86219 doi.org/10.1039/c5ra16986k.
13. P. Du, L. Luo, Y. Zhang and H. Chen "Electrical and luminescence properties of Er-doped Bi_{0.5}Na_{0.5}TiO₃" Mater. Sci. Eng. B 178, 18 (2013) 1219-1223 doi.org/10.1016/j.mseb.2013.08.007.
14. H. Sun, D. Peng, X. Wang, M. Tang, Q. Zhang and X. Yao, "Srrong red emiision (Bi_{0.5}Na_{0.5})TiO₃ ferroelctric ceramics"J. Appl. Lett. 110 (2011) 016102– 016105. doi.org/10.1063/1.3606425.
15. E. Heumann, S. Bär, K. Rademaker, G. Huber, S. Butterworth, A. Diening and W. Seelert, "Semiconductor-laser-pumped high-power upconversion laser", Appl. Phys. Lett. 88 (2006) 061108, doi.org/10.1063/1.2172293.
16. A. Demuro and I. Parker, "Optical single-channel recording: imaging Ca²⁺ flux through individual ion channels with high temporal and spatial resolution", J. Biomed. Opt. 10 (2005) 011002, doi.org/10.1117/1.1846074.
17. J. Milliez, A. Rapaport, M. Bass, A. Cassanho and H.P. Jenssen, "High-brightness white-light source based on up-conversion phosphors", J. Disp.

Technol. 2 (2006) 307–311, doi.org/10.1109/JDT.2006.879183.

18. A. Shalav, B.S. Richards, T. Trupke, K.W. Krämer and H.U. Güdel, “Application of NaYF₄: Er³⁺ up-converting phosphors for enhanced near-infrared silicon solar cell response”, *Appl. Phys. Lett.* 86 (2005) 013505, doi.org/10.1063/1.1844592.

19. R.Roy and A. Dutta “Microstructure correlated ion transport mechanism of sol-gel derived sodium bismuth titanate oxide ion conductors”, *Appl. Physics lett solid state sciences* 102 (2020) 106174 doi.org/10.1016/j.solidstatesciences.2020.106174.

20. Y.Q. Jia, “Crystal radii and effective ionic radii of the rare earth ions”, *J. Solid State Chem.* 95 (1991) 184–187, [https://doi.org/10.1016/0022-4596\(91\)90388-X](https://doi.org/10.1016/0022-4596(91)90388-X).

21. C.S. Devi, G.S. Kumar and G. Prasad, “Control of ferroelectric phase transition in nano particulate NBT-BT based ceramics”, *Mater. Sci. Eng. B Solid-State Mater. Adv. Technol.* 178 (2013) 283e292, doi.org/10.1016/j.mseb.2012.12.001.

22. A. Franco and P. Banerjee, P.L. Romanholo, “Effect of composition induced transition in the optical band-gap, dielectric and magnetic properties of Gd doped Na_{0.5}Bi_{0.5}TiO₃ complex perovskite”, *J. Alloys Compd.* 764 (2018) 122e127, <https://doi.org/10.1016/j.jallcom.2018.06.007>.

23. A.Banwal and R.Bokolia , “Thermometric sensing performance in Erbium modified SrBi_{2-x}Nb₂Er_xO₉ ferroelectcric ceramics for optoelectronics devices” *Ceram .Int* 48(2022) 34405-34414 doi.or/10/1016/j.ceramint.2022.08.019.

24. M. Muneeswaran, B.C. Choi, S.H. Chang and J.H. Jung, Effect of dysprosium doping on structural and vibrational properties of lead-free (Na_{0.7}K_{0.3})_{0.5}Bi_{0.5}TiO₃ ferroelectric ceramics, *Ceram. Int.* 43 (2017) 13696–13701, <https://doi.org/10.1016/j.ceramint.2017.07.081>.

25. W. Qiu and H.H. Hng, “Effects of dopants on the microstructure and properties of PZT ceramics”, *Mater. Chem. Phys.* 75 (2002) 151–156, [https://doi.org/10.1016/S0254-0584\(02\)00045-7](https://doi.org/10.1016/S0254-0584(02)00045-7).

26. N. udomkan, P. limsuwan and T. tunkasiri, “Effect of rare earth (RE = La, Nd, Ce and Gd) doping on the piezoelectric of PZT (52:48) ceramics”, *Int. J. Mod.*

Phys. B 26 (2007) 4549–4559, <https://doi.org/10.1142/S0217979207037909>.

27. J. Yin, Y. Zhang and X. Lv, et al., “Ultrahigh energy-storage potential under low electric field in bismuth sodium titanate-based perovskite ferroelectrics”, J. Mater. Chem. 6 (21) (2018) 9823–9832. doi.org/10.1039/C8TA00474A.

28. L.H. Luo, P. Du, W.P. Li, W.D. Tao and H.B. Chen, “Effects of Er doping site and concentration on piezoelectric, ferroelectric, and optical properties of ferroelectric $\text{Na}_{0.5}\text{Bi}_{0.5}\text{TiO}_3$ ”, J. Appl. Phys. 114 (2013), 124104e124111-6. doi.org/10.1063/1.4823812.

29. J. Li, E. Sun, L. Tang, Y. Zhou, L. Li, J. Miao, Z. Zhang, W. Cao, Non-contact localized probing of ferroelectric phase transitions in $\text{Li}^+/\text{Er}^{3+}:\text{BaTiO}_3$ ceramics using fluorescence abnormalities, Appl. Phys. Lett. 116 (4) (2020), <https://doi.org/10.1063/1.5129900>.

30. A. Shandilya, R.S. Yadav, A.K. Gupta and K. Sreenivas, Temperature-dependent light upconversion and thermometric properties of $\text{Er}^{3+}/\text{Yb}^{3+}$ -co-doped SrMoO_4 sintered ceramics, J. Mater. Sci. 56 (2021) 12716–12731, doi.org/10.1007/s10853-021-06078-8.

31. A. Banwal and R. Bokolia “Enhanced upconversion luminescence and optical temperature sensing performance in Er^{3+} doped $\text{BaBi}_2\text{Nb}_2\text{O}_9$ ferroelectric ceramics” Ceramic. Int 48(2022) 2230-2240 doi.org/10.1016/j.ceramint.2021.09.314.

32. R. Bokolia, M. Mondal, V.K. Rai and K. Sreenivas, “Enhanced infrared-to-visible upconversion emission and temperature sensitivity in (Er^{3+} , Yb^{3+} , and W^{6+}) tridoped $\text{Bi}_4\text{Ti}_3\text{O}_{12}$ ferroelectric oxide”, J. Appl. Phys. 121 (8) (2017), doi.org/10.1063/1.4977006.

33. C. Liu, Q. Wang, X. Wu, B. Sa, H. Sun, L. Luo, C. Lin, X. Zheng, T. Lin and Z. Sun, “Boosting upconversion photoluminescence and multielectrical properties via Er Doping-Modulated vacancy control in $\text{Ba}_{0.85}\text{Ca}_{0.15}\text{Ti}_{0.9}\text{Zr}_{0.1}\text{O}_3$ ”, ACS Omega 4 (2019) 11004–11013, doi.org/10.1021/acsomega.9b01391.

34. Y. Jiang, C. Chen, X. Jiang and N. Tu “Photoluminescence and electrical properties of Er^{3+} doped $\text{Na}_{0.5}\text{Bi}_{4.5}\text{Ti}_4\text{O}_{15}$ - $\text{Bi}_4\text{Ti}_3\text{O}_{12}$ inter-growth ferroelectric ceramics” Mater. Sci. 2017, 11(1): 51–58 doi 10.1007/s11706-017-0367-y.

35. S. Wang, H. Zhou, X. Wang and A. Pan “ Up-conversion luminescence and optical temperature sensing properties of Er³⁺ doped perv oskite Na_{0.5}Bi_{0.5}TiO₃ , J.Phys.Chem.Solids. 98 (2016) 28-31 doi.org/10.1016/j.jpcs.2016.06.002.
36. P. Du, L. Luo, W. Li, Q. Yue, “Upconversion emission in Er-doped and Er/Yb-codoped ferroelectric Na_{0.5}Bi_{0.5}TiO₃ and its temperature sensing application”, J. Appl. Phys. 116 (2014) doi.org/10.1063/1.4886575.
37. Peng Du, Jae Su Yu “Effect of molybdenum on upconversion emission and temperature sensing properties in Na_{0.5}Bi_{0.5}TiO₃:Er/Yb ceramics “Ceram. Int. 41 (2015) 6710–6714 doi.org/10.1016/j.ceramint.2015.01.113.
38. X.Jia, J. Zhang, Y. Gao, J. Wang, P. Zheng “Enhanced bipolar fatigue-resistance and optical temperature sensing in Er-modified 0.94(Bi_{0.5}Na_{0.5})TiO₃-0.06(K_{0.5}Na_{0.5})NbO₃ lead-free ceramics”, Mater. Sci.. 2017, 11(1): 51–58 doi.org/10.1016/j.materresbull.2016.12.051.
39. A. Bayart, F. Szczechanski, J.F. Blach, J. Rousseau, A. Katelnikovas, S. Saitzek, Upconversion luminescence properties and thermal quenching mechanisms in the layered perovskite La_{1.9}Er_{0.1}Ti₂O₇ towards an application as optical temperature sensor, J. Alloys Compd. 744 (2018) 516–527, <https://doi.org/10.1016/j.jallcom.2018.02.055>.
40. M.X. Façanha, J.P.C. doNascimento, M.A.S. Silva, M.C.C. Filho, A.N. LMarques, A. G. Pinheiro, A.S.B. Sombra, Up-conversion emission of Er³⁺/Yb³⁺-co-doped BaBi₂Nb₂O₉ (BBN) phosphors, J. Lumin. 183 (2017) 102–107, <https://doi.org/10.1016/j.jlumin.2016.08.011>.

CHAPTER - 4

Upconversion Luminescence and Temperature Sensing Properties of Er^{3+}/Yb^{3+} Co-Doped $Bi_{0.5}Na_{0.5}TiO_3$ Ferroelectric Ceramic

- ❖ This chapter discusses, a series of Er^{3+}/Yb^{3+} co-doped $Bi_{0.5-x-y}Er_xYb_yNa_{0.5}TiO_3$ ferroelectric ceramic is prepared using traditional solid-state technique to investigate the structural, optical and sensing properties.
- ❖ The photoluminescence spectra of all BNT ceramic compositions are measured under excitation wavelengths i.e. 489 nm and 980 nm. It has been noted that the two intense green and one visible red band were present at 530 nm, 549 nm, and 662 nm, respectively.
- ❖ The dependency of pump power on UCL spectra is observed with varying pump powers at 980 nm excitation. The two photons that are involved in the UCL process are confirmed by this investigation.
- ❖ The time-resolved fluorescence spectroscopy indicates that the efficiency of energy transfer between the dopant ions has increased for all co-doped BNT ceramic compositions. At 523 K and 303 K, the relative (S_r) and absolute (S_{ab}) sensitivity of the BE3Y3 ceramic composition are 1.24 % K^{-1} and 0.54 % K^{-1} , respectively. These findings suggest that the prepared ceramic has the capability to be used as multifunctional material.

*The results reported in this chapter have been published in Megha et. al. *Applied Physics A*.*

4.1 Introduction

Multifunctional materials represent a paradigm change in material science, offering unprecedented opportunities for innovation and advancement across various fields. Multifunctional materials can be well defined as the combination of optical, electrical, and mechanical properties [1-2]. These materials have drawn a lot of interest due to their potential for developing novel technologies. There are many applications of multifunctional materials such as actuators, transducers, accelerators, sensors, and non-volatile memories. Their preparation method, which included microwave processing, solid state reaction, and combustion reaction, also had a significant impact on their chemical and physical characteristics [3-4]. The need for environmental preservation on a worldwide scale has made lead-free materials more and more popular in recent years. New lead-free piezoelectric material needs to be improved due to growing environmental concerns. Lead-free ferroelectric material can be doped with rare earth ions exhibits various phenomena, like photoluminescence (PL), upconversion (UC) emission and it can enhance the piezoelectricity of the material [5-9]. To reduce the harmful effects of lead exposure on the environment and human health, ferroelectrics are a practical replacement for ceramics containing lead. Ferroelectrics are known to be superior alternative to lead-based materials in many applications since they don't harm the environment and perform better without sacrificing functionality [10-14]. Consequently, to substitute the lead-based materials, a new lead-free piezoelectric ceramic has to be developed. Bismuth sodium titanate (BNT), with the chemical formula $\text{Bi}_{0.5}\text{Na}_{0.5}\text{TiO}_3$ and a perovskite structure, is one of the most prevalent utilized lead-free piezoelectric materials. It was initially founded by Smolenskii *et al.* in 1960 [15-18]. BNT ceramic demonstrates good optical and luminescence properties. It is having strong Ferro electricity and high Curie temperature with large value of remnant polarization and coercive field that is $P_r = 38 \mu\text{C}/\text{cm}^2$, $E_c = 73 \text{ kV}/\text{cm}$, respectively so it has been considered as a good replacement for lead based materials like PZT [19-21]. However, BNT has a drawback due to its high conductivity, which possesses a problem during the poling process. Hence, in order to enhance the property of BNT ceramic, a small amount of rare-earth (RE) dopants can be incorporated, thereby improving its overall performance [22]. Rare-earth (RE) ion-doped materials have attracted a lot of

interest in ongoing research due to their many multifunctional applications. The integration of rare earth ions into ferroelectric materials at the nanoscale offers unique opportunities for tailoring their properties, which can be beneficial for various applications, including electronics, photonics, and sensing. Dopants like Er, Yb, Ce, Eu, La and Sm can improve piezoelectric properties and ferroelectric properties [23]. RE-doped ceramics have been the subject of extensive research because of their numerous uses in a variety of fields, such as optical sensors for temperature, bio imaging, and colour displays. [24]. Many properties like piezoelectric, ferroelectric and pyro electric properties can be enhanced by doping rare earth. RE ions such as Er^{3+} acts as an activator of UC luminescence in green and red emission under 980 nm [25]. The choice of a low-phonon-energy host material can optimize the energy transfer between dopant ions, leading to improved upconversion efficiency [26-27]. Er^{3+} is the most effective activator for producing upconversion luminescence. The crystal symmetry and crystal field of the matrix around Er^{3+} may alter when Er^{3+} is placed in an environment with a different matrix or ligand. This will therefore have an impact on the emission of photoluminescence. In most of the cases, Yb^{3+} ions, are indeed commonly used as sensitizers in various optical and optoelectronic applications, particularly in the field of rare-earth-doped materials. This is due to their favourable properties, including a high absorption cross-section at 980 nm and efficient energy transfer capabilities. When paired with erbium ions (Er^{3+}), which are well-known for their emission properties in the near-infrared region, Yb^{3+} ions can effectively transfer energy to Er ions, thereby enhancing the overall efficiency of the system. Yb^{3+} ions are commonly used dopant in upconversion materials due to its unique electronic structure and energy levels, which make it highly effective for enhancing upconversion processes. Yb^{3+} ions serve as sensitizer ions, absorbing lower-energy photons and transferring their energy to activator ions, which then emit higher-energy photons through upconversion processes. In our previous study, we saw that the UC emission intensity of Er-doped BNT ceramic reached its maximum value when the doping concentration was 0.03. So throughout this work, the concentration of Er^{3+} will be fixed to be 0.03. The maximum absolute optical temperature sensitivity (S_{ab}) is reported for same ceramic concentration, and is found to be 0.0047 K^{-1} at 523 K [28]. In this paper, we thoroughly studied the Er^{3+} and Yb^{3+} co doped BNT ceramic for optical and sensing performance.

4.2 Syntesis and Characterization Details

The initial precursors (Bi_2O_3 , Na_2CO_3 , Er_2O_3 , Yb_2O_3 , TiO_2) were purchased from Sigma Aldrich and possessed the highest purity level (99.99%) for the synthesis of $\text{Bi}_{0.5-x-y}\text{Er}_x\text{Yb}_y\text{Na}_{0.5}\text{TiO}_3$ ceramics by a traditional solid state conventional reaction technique. Er^{3+} and Yb^{3+} were employed as an additional rare earth agents during the preparation of the samples. All the powder with different concentrations was taken in the stoichiometric ratio and was mixed by using the ball mill technique using zirconia balls and ethanol for 12 hrs so that the powder gets mixed well, then this slurry was put in an oven for 24 hrs at 70°C to dry it out and after that we get the slurry in powder form, then this powder was calcined in high temperature furnace at 850°C for 3 hrs. The calcined powder was crushed using mortar pestle then this crushed powder was mixed thoroughly with a PVA binder for 2 hrs so that no granules were left over until fine powder was obtained. Then, using a hydraulic press machine, this calcined powder was pressurised at 50 MPa into a disc shape with a 10 mm diameter and 1 mm thickness to yield pellets. Then these pellets were sintered at 1050°C for 3 hours with the interval heat treatment at 500°C for 1 hour to remove the binder from the pellets. The synthesis technique is depicted in **Figure 4.1**.

The X-ray diffraction (XRD) patterns of the sintered pellet were recorded in step scan mode (step size $2\theta=10^\circ$ - 80° and scan rate 0.04 s/step) using an X-ray diffractometer (BRUKER, Model: D8 Advance-AXS) using $\text{Cu-K}\alpha$ radiation, to identify the crystal structure and the phase of the synthesized material. Scanning electron microscopy images were captured to understand the surface morphology of the pellet sample using ZEISS scanning electron microscope instrument with an airlock chamber. Sintered pellets were crushed to make powders for Fourier Transform Infrared (FTIR) Spectroscopy in ATR mode (Attenuated Total Reflectance) to analyze the formation of perovskite structure using the PerkinElmer spectrum-II instrument.

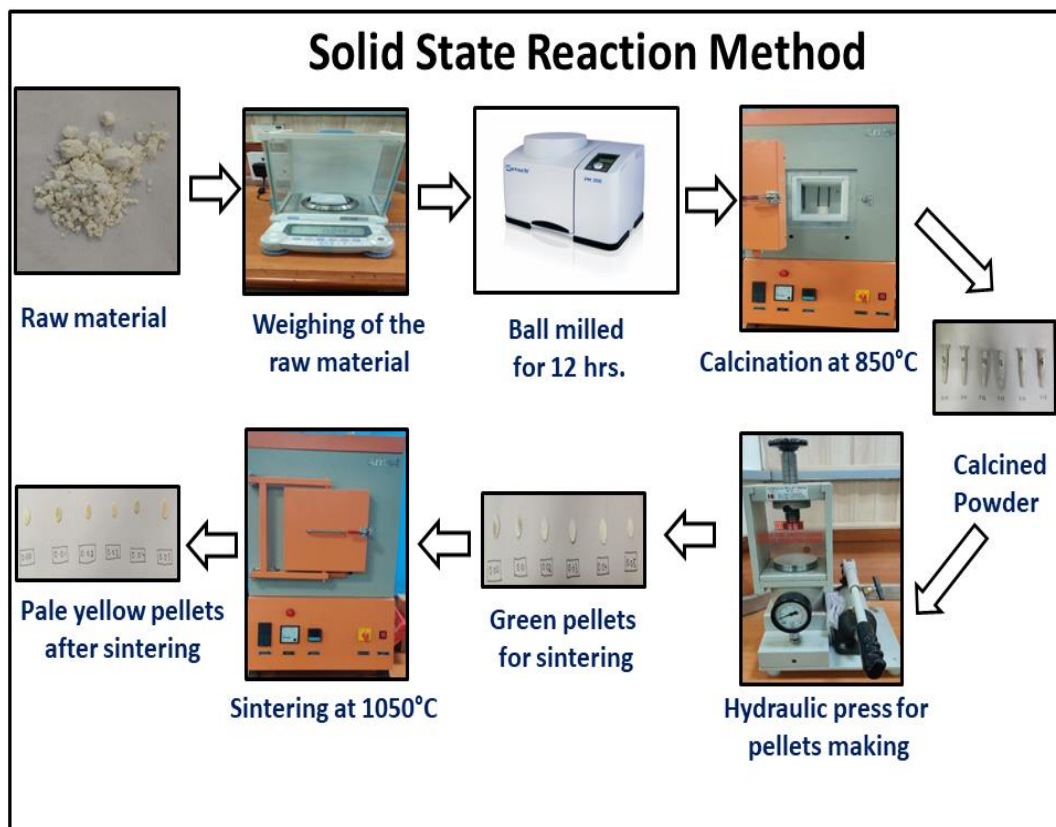


Figure 4.1: Pictorial depiction of synthesis process (solid-state method)

Using a xenon excitation source, a JASCO FP 8300 PC-spectrofluoro photometer was used to record the emission spectra. The HORIBA PTI Quanta-master device was used to record the upconversion luminescence spectra at ambient temperature. A continuous laser diode was used to excite the sample at 980 nm wavelength. A pulsed laser source with a 980 nm wavelength operating at ambient temperature was used to perform time-resolved fluorescence spectroscopy. To ascertain the role of photon count in the UC process, the pump power dependence on UC intensity was also examined. The cooled photo-multiplier tube was utilised to capture the temperature-dependent UC emission spectra for FIR analysis. The coding of samples is given in Table 4.1.

Table 4.1: Coding of prepared undoped and doped BNT compositions

Composition	Abbreviation	Er (x) content	Yb (y) content
$\text{Bi}_{0.5-x-y}\text{Er}_x\text{Yb}_y\text{Na}_{0.5}\text{TiO}_3$	BE0Y0	0.00	0.00
$\text{Bi}_{0.5-0.03-y}\text{Er}_{0.03}\text{Yb}_y\text{Na}_{0.5}\text{TiO}_3$	BE3Y0	0.03	0.00
$\text{Bi}_{0.5-0.03-0.01}\text{Er}_{0.03}\text{Yb}_{0.01}\text{Na}_{0.5}\text{TiO}_3$	BE3Y1	0.03	0.01
$\text{Bi}_{0.5-0.03-0.03}\text{Er}_{0.03}\text{Yb}_{0.03}\text{Na}_{0.5}\text{TiO}_3$	BE3Y3	0.03	0.03
$\text{Bi}_{0.5-0.03-0.05}\text{Er}_{0.03}\text{Yb}_{0.05}\text{Na}_{0.5}\text{TiO}_3$	BE3Y5	0.03	0.05
$\text{Bi}_{0.5-0.03-0.07}\text{Er}_{0.03}\text{Yb}_{0.07}\text{Na}_{0.5}\text{TiO}_3$	BE3Y7	0.03	0.07
$\text{Bi}_{0.5-0.03-0.09}\text{Er}_{0.03}\text{Yb}_{0.09}\text{Na}_{0.5}\text{TiO}_3$	BE3Y9	0.03	0.09
$\text{Bi}_{0.5-0.03-0.11}\text{Er}_{0.03}\text{Yb}_{0.11}\text{Na}_{0.5}\text{TiO}_3$	BE3Y11	0.03	0.11
$\text{Bi}_{0.5-0.03-0.13}\text{Er}_{0.03}\text{Yb}_{0.13}\text{Na}_{0.5}\text{TiO}_3$	BE3Y13	0.03	0.13

4.3 Results and Discussion

4.3.1 Structural and Microstructure Analysis

Figure 4.2(a) depicts the XRD patterns of all BNT ceramics with different concentrations of Er^{3+} ($x = 0.03$) and Yb^{3+} ($y = 0.00, 0.01, 0.03, 0.05, 0.07, 0.09, 0.11$, and 0.13). From XRD patterns, it was observed that each sample had a pure phase without any contaminants from the secondary phase. The absence of any apparent manifestations of undesired secondary phases validates the solubility and assimilation of Er^{3+} and Yb^{3+} ions into the host lattice BNT. Further, this is confirmed by JCPDS card no #00-036-0340. The result, as observed, suggests the presence of rhombohedral symmetry, space group R3c. From the magnification in **Figure 4.2(b)**, the reflection plane of greatest relative intensity (110) shifts to larger angles with the increases in the concentration of Yb^{3+} in the BNT structure. The shifting suggests that the host matrix BNT at the A-site of Bi^{3+} ions (1.32 \AA) has effectively substituted by the smaller Er^{3+} and Yb^{3+} ions (1.25 \AA , 1.22 \AA) [29]. They are bound to occupy A-sites in the crystal lattice, as evidenced by their efficient ionic radii match those of the A-site ions. The XRD profile fitting of BNT ceramic was carried by using TOPAS software employing Pawley refinement based on the least squares method. The XRD patterns were analyzed with initial parameters for the rhombohedral system of space group R3c to obtain the best fit between the observed and calculated values as tabulated in Table 4.2. The

refinement parameters and goodness of fit ($\chi \approx 1.5$) confirm the good fitting of experimental and theoretical. Using Archimedes' principle, the density of the sintered pellets is determined and is recorded in Table 4.2. An analysis of the data showed that with increasing $\text{Er}^{3+}/\text{Yb}^{3+}$ concentration in the host lattice, variation is seen in the density of the sintered pellets.

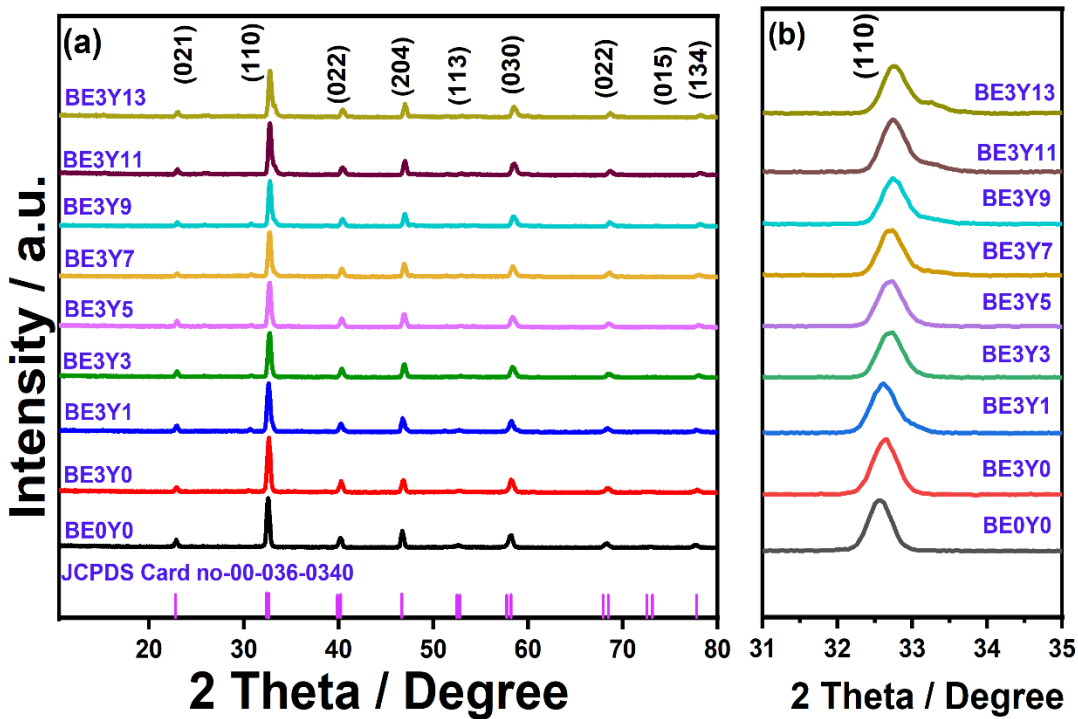


Figure 4.2: (a) XRD patterns showing rhombohedral symmetry in all BNT compositions (b) Peak shifting of (110) plane

For all the undoped, doped and co-doped BNT ceramic compositions, the typical surface morphology was obtained using SEM, depicted in **Figure 4.3 (a-f)**. All the samples are well-sintered, grain boundaries are well-delineated, and no porosity was observed. The grain size varies with the dopant concentrations, as in Table 4.2. It has been observed that the Yb^{3+} incorporation with Er^{3+} ions increases the grain size. The dense microstructure and well-defined grain boundaries could help improve electrical properties [30, 31].

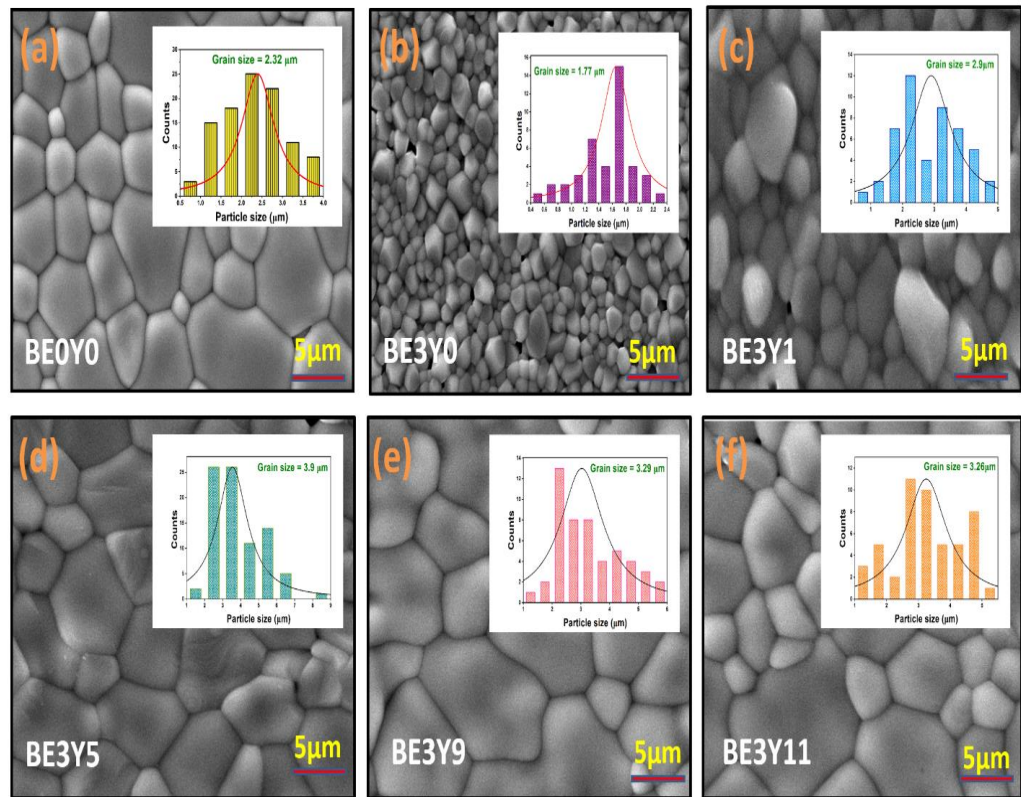


Figure 4.3: SEM images of BNT compositions (a) BE0Y0 (b) BE3Y0 (c) BE3Y1 (d) BE3Y5 (e) BE3Y9 and (f) BE3Y11. Inset: Histograms for grain size calculation

Table 4.2: Lattice and refinement parameters for all the BNT ceramic compositions

Parameters	$\text{Bi}_{0.5-x-y}\text{Er}_x\text{Y}_y\text{Na}_{0.5}\text{TiO}_3$								
	BE0 Y0	BE3 Y0	BE3 Y1	BE3 Y3	BE3 Y5	BE3 Y7	BE3 Y9	BE3 Y11	BE3 Y13
\mathbf{R}_{wp}	14.50	15.60	18.16	16.20	15.31	19.38	20.46	21.27	22.99
\mathbf{R}_{exp}	11.30	10.95	10.39	11.28	9.79	11.58	11.65	10.44	10.64
$\mathbf{R}_{\mathbf{P}}$	10.17	11.16	13.63	11.92	15.236	14.05	15.33	15.92	16.81
$\mathbf{GOF}(\chi)$	1.28	1.42	1.60	1.44	1.56	1.67	1.76	2.04	2.16
$\mathbf{a}(\text{\AA})$	5.4858	5.4718	5.4878	5.4632	5.4561	5.4845	5.4651	5.4632	5.4590
$\mathbf{b}(\text{\AA})$	5.4858	5.4718	5.4878	5.4632	5.4561	5.4845	5.4651	5.4632	5.4590
$\mathbf{c}(\text{\AA})$	6.7589	6.7399	6.7620	6.7240	6.7146	6.6801	6.7008	6.7016	6.7155
$\mathbf{V}(\text{\AA}^3)$	176.1558	174.76	176.3672	173.80	174.0439	174.0201	173.3256	173.2261	173.3210
$\mathbf{Density}$ (g/cm^3)	8.12	7.93	8.20	8.30	7.78	8.34	8.14	7.66	7.17
$\mathbf{Grain\,Size}$ (μm)	2.32	1.77	2.61	3.33	3.90	3.45	3.29	3.26	3.34

4.3.2 FTIR Spectroscopy

The Fourier-transform infrared (FTIR) spectra of all the BNT ceramics with different dopant concentrations is depicted in **Figure 4.4**. The FTIR spectra were recorded in the wavelength range of 400-900 cm⁻¹. In BNT, the intrinsic vibration band is represented by the bands observed at wavenumbers 550 and 820 cm⁻¹. The stretching of Ti-O bonds inside the octahedral groups seen in the perovskite structure is thought to be the cause of the absorption bands seen in this study. The FTIR bands at 820 and 550 cm⁻¹ show an obvious shift towards lower wavenumbers, which may be related to the host materials' sensitivity to foreign ions inside the host substrate [32-34].

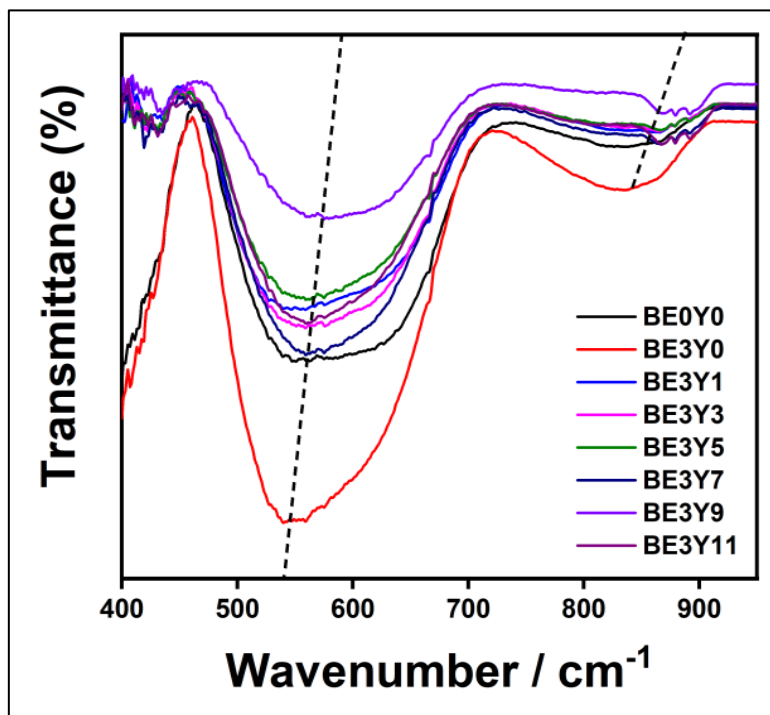


Figure 4.4. FTIR spectra of prepared BNT ceramic compositions

4.3.3 Diffuse Reflectance Spectroscopy

The reflectance spectra (DRS) of the sintered powders of ceramic with different compositions of BNT doped with Er³⁺ and Yb³⁺ is shown in **Figure 4.5(a)**. The various energy levels of Er³⁺ ions give rise to the absorption bands at about ~ 384, 488, 522, 545, 653, 795, 975 nm, which represents to various energy levels and are depicted as ⁴G_{11/2}, ⁴F_{7/2}, ²H_{11/2}, ⁴S_{3/2}, ⁴F_{9/2}, ⁴I_{9/2} and ⁴I_{11/2} respectively. Using Kubelka-Munk (K-M) relation the energy band gap of Er is calculated which is represented in Eq 4.1 [35]:

$$F(R_\infty) = \frac{(1 - R_\infty)^2}{2R_\infty} = \frac{K}{S} \quad (4.1)$$

where S denotes the scattering coefficient, K indicates the absorption coefficient, R_∞ represents the ratio between the diffuse reflectance from the sample and reference material. Furthermore, it can be used for diffused scattered light, where we can assume as S as constant value with respect to the wavelength. Additionally, by using Tauc expression we can calculate $F(R)$ and can be written as Eq. (4.2) [36]:

$$(F(R_\infty)hv)^n = B(hv - E_g) \quad (4.2)$$

In this formula, E_g denotes the optical energy band gap of the materials, B indicates the constant proportionality, ν stands for the vibrational frequency, h denotes the Planck's constant, and n is the electron transition.

The value of energy band gap is determined by the linear extrapolation of the data at the inflection point in $[F(R)hv]^2$ versus hv plot is depicted in **Figure 4.5(b-f)**. The measured values are consistent with the reported literature about the optical energy band gap of $\text{Bi}_{0.5-x}\text{Er}_x\text{Y}_y\text{Na}_{0.5}\text{TiO}_3$ ($E_g = 2.9$ eV) [37]. The band gap value is not varying much as the concentration is increasing. This little variation in the E_g value is due to the addition of Yb ions which introduces the new electronic level in the band gap and it reduces the energy band gap. There is a red shift in the energy band gap which is related to the oxygen vacancies and either defects due to the synthesis process involved on the reaction and one of the main reason for this is the large difference the Yb^{3+} and Bi^{3+} ionic radii [37].

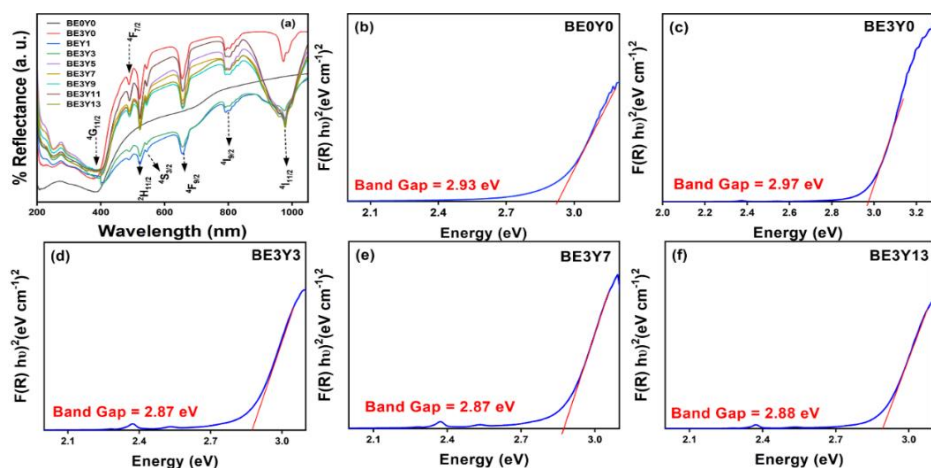


Figure 4.5: (a) Diffuse reflectance spectra of all the prepared BNT ceramic compositions, the Energy band gap of (b) BE0Y0 (c) BE3Y0 (d) BE3Y3 (e) BE3Y7 and (f) BE3Y13

4.3.4 Downshifting Photoluminescence spectroscopy

The photoluminescence excitation (under 549 nm emission) and PL emission (under 489 nm excitation) spectra of BNT ceramic with changing Yb^{3+} concentration is depicted in **Figure 4.6(a, b)**. **Figure 4.6(a)** shows excitation peaks of Er^{3+} resulting from ${}^4\text{F}_{5/2}$ and ${}^4\text{F}_{7/2}$ energy levels to different higher energy levels and observed at 450 nm and 489 nm [38-40]. The most intense peak was observed at 489 nm and was used as an excitation wavelength (λ_{exc}) to record the PL emission spectra. In **Figure 4.6(a)**, it can be seen that the doped BNT samples shows a broad band of low intensity around 310 nm which can only be attributed to the charge transfer from ligand to metal [41]. The lower intensity of charge transfer band than f-f transition ascertains the differential sensitization of erbium and ytterbium via host. Under excitation of 489 nm, the green emission at 530 nm and 549 nm contribute to the excited state to ground state from ${}^2\text{H}_{11/2}$ and ${}^4\text{S}_{3/2}$ to ${}^4\text{I}_{15/2}$. The weak red band transition is from ${}^4\text{F}_{9/2}$ to ${}^4\text{I}_{15/2}$ attributed at 662 nm. It can be seen from the **Figure 4.6 (b)**, the relative emission intensity of the green and red band decreases after the optimized concentration (BE3Y3) of the material. The occurrence of non- radiative transitions due to concentration quenching leads to a reduction in the emission intensity. These results are also consistent with the study of the upconversion luminescence spectra [38-40]. This is because, in the downshifting photoluminescence spectra under the excitation 489 nm, the electrons immediately acquire the energy state ${}^4\text{F}_{9/2}$. At this level, the non-radiative transition occurs due to the multiphonon relaxation, which eventually reduces the intensity of the emission band [28].

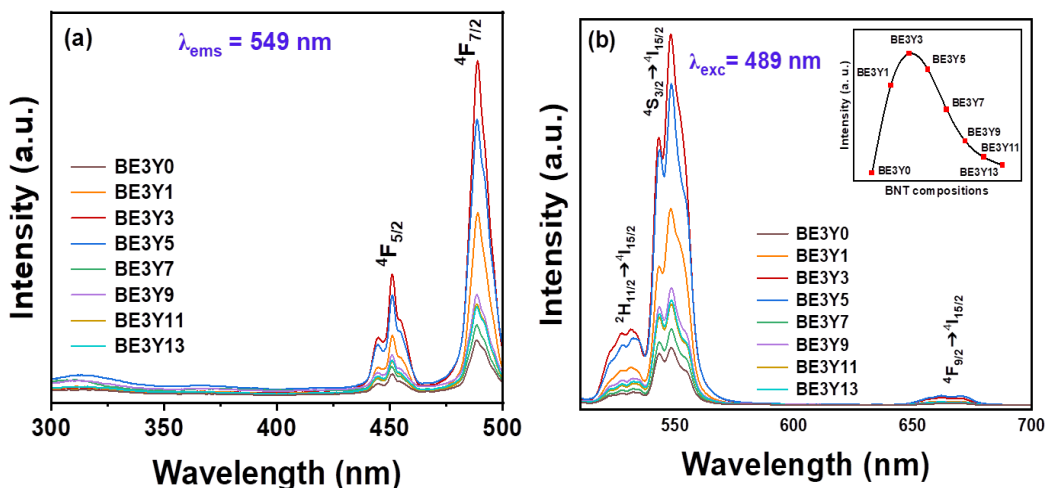


Figure 4.6: Downshifting photoluminescence (a) excitation spectra (b) emission spectra of prepared BNT ceramic compositions

4.3.5 Upconversion Luminescence (UCL) Spectroscopy

The upconversion luminescence (UCL) spectra traced at 980 nm excitation wavelength with the pumping power of 50 mW with excitation source density of 3.25 W/cm^2 for Er^{3+} -doped and series of $\text{Er}^{3+}/\text{Yb}^{3+}$ co-doped BNT ceramic composition is given in **Figure 4.7(a)**. Two green and one red emission band are observed in UCL spectra. The one green band at 530 nm is ascribed to the transitions from the $^2\text{H}_{11/2}$ to $^4\text{I}_{15/2}$, and the other intense green band at 549 nm is due to the transition from $^4\text{S}_{3/2}$ to $^4\text{I}_{15/2}$ level. The detectable red emission band is obtained at 662 nm due to the transition of the $^4\text{F}_{9/2}$ to the $^4\text{I}_{15/2}$ level. It has been observed that the incorporation of Yb^{3+} in the host lattice along with fixed Er^{3+} content can significantly increase the UCL emission intensity. This is because of the larger cross-sectional area provided by the Yb ions for the energy transfer process, which further increases the UC mechanism. The variation of UCL emission intensity with dopant concentration is given in **Figure 4.7(b)**. The highest emission intensity is obtained for BE3Y3 BNT composition. The fall in UCL intensity after this composition is because of the concentration-quenching effect, which occurs owing to easy energy transfer between the dopant ions when they get closer at higher dopant concentrations, leading to non-radiative transitions. It can also be seen that the UCL emission intensity is still maintained at higher dopant concentrations due to the various cross-relaxation process occurring at higher dopant concentrations. The distance between the dopant ions can be measured by Blasse Eq. 4.3 [42]:

$$R_c \approx 2 \left[\frac{3V}{4\pi x_c Z} \right]^{\frac{1}{3}} \quad (4.3)$$

where V denotes unit cell volume, Z represents the number of host cations, and X_c is the critical dopant concentration (BE3Y3). After substituting all the values, R_c is 15.56 Å. The energy level diagram for possible UCL mechanism is given in **Figure 4.7(c)**. The ions from $^4\text{I}_{15/2}$ are excited to a higher energy level $^4\text{I}_{11/2}$ via GSA (ground state absorption). Another ion from the $^4\text{F}_{9/2}$ level of Yb ions is excited to a higher energy level $^4\text{F}_{5/2}$. The levels $^4\text{F}_{5/2}$ and $^4\text{I}_{11/2}$ are at the same level, making easy energy transfer between the Er and Yb ions. Now, the ions at the $^4\text{I}_{11/2}$ level jump to $^4\text{F}_{7/2}$ through ESA (excited state absorption). Also, ions from level $^4\text{F}_{5/2}$ reached the $^4\text{F}_{7/2}$ via ET (energy transfer), thus populating this level. From the $^4\text{F}_{7/2}$ level, the ions fall non-radiatively in

the energy levels $^2\text{H}_{11/2}$, $^4\text{S}_{3/2}$, and $^4\text{F}_{9/2}$ via MPR (multiphonon relaxation). Lastly, from these levels, the ions make their transition to the lower energy level and result in three UCL emission bands at 530 nm, 549 nm, and 662 nm through transitions $^2\text{H}_{11/2}$, $^4\text{S}_{3/2}$, $^4\text{F}_{9/2}$ to $^4\text{I}_{15/2}$ level, respectively.

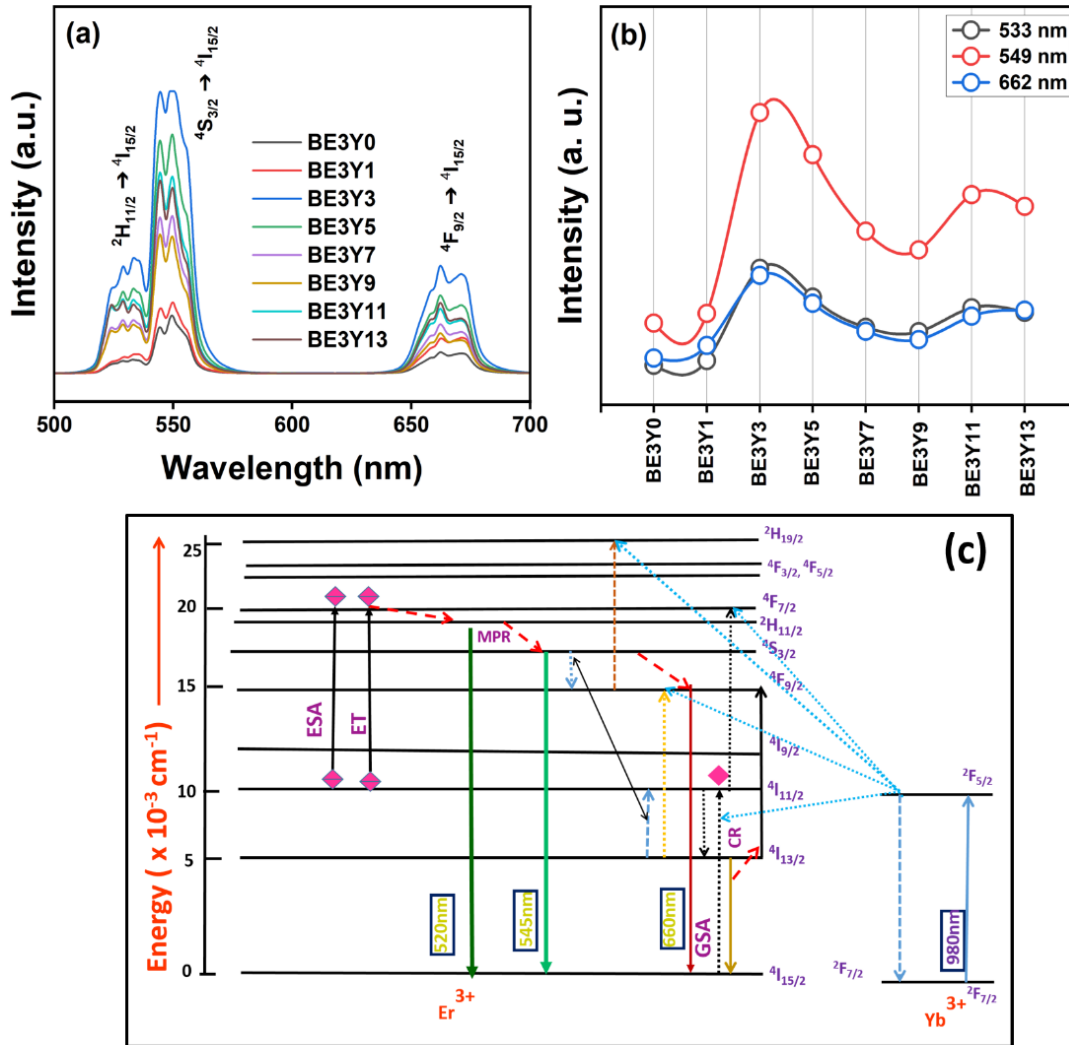


Figure 4.7: (a) UCL spectra of Er^{3+} -doped and series of $\text{Er}^{3+}/\text{Yb}^{3+}$ co-doped BNT ceramic compositions (b) UC emission versus dopant concentration (c) Energy level diagram showing possible pathways for UCL emission

4.3.6 Time decay analysis

The decay curve is obtained under the excitation at 980 nm and the emission under 549 nm with the transition of $^4\text{S}_{3/2} \rightarrow ^4\text{I}_{15/2}$ for BNT ceramics compositions is depicted in Figure 4.8(a-e). Using tri-exponential function the decay time was measured which is given by the Eq. (4.4):

$$I(t) = I_0 + A_1 \exp\left(-\frac{t}{\tau_1}\right) + A_2 \exp\left(-\frac{t}{\tau_2}\right) + A_3 \exp\left(-\frac{t}{\tau_3}\right) \quad (4.4)$$

where A_1, A_2, A_3 are the fitting parameters, I_0 is the intensity at $t = 0$ s, is $I(t)$ is the intensity at time t , and τ is decay time. The average time is calculated by Eq. 4.5:

$$\langle \tau \rangle = \frac{A_1 \tau_1^2 + A_2 \tau_2^2 + A_3 \tau_3^2}{A_1 \tau_1 + A_2 \tau_2 + A_3 \tau_3} \quad (4.5)$$

The average decay time of BNT ceramic compositions varies with dopant concentration. It can be seen that the average decay time decreases from 133.53 μ s to 9.31 μ s. This might be due to the rapid energy exchange between the Er^{3+} and Yb^{3+} ions, resulting in a non-radiative transition [43-44]. The efficiency in energy transfer by the incorporation of Yb^{3+} ions can be measured using Eq. 4.6 [45]:

$$\eta = 1 - \frac{\tau_2}{\tau_1} \quad (4.6)$$

τ_1 is mean decay time for single Er^{3+} -doped BNT and τ_2 is the mean decay time for $\text{Er}^{3+}/\text{Yb}^{3+}$ BNT ceramic.

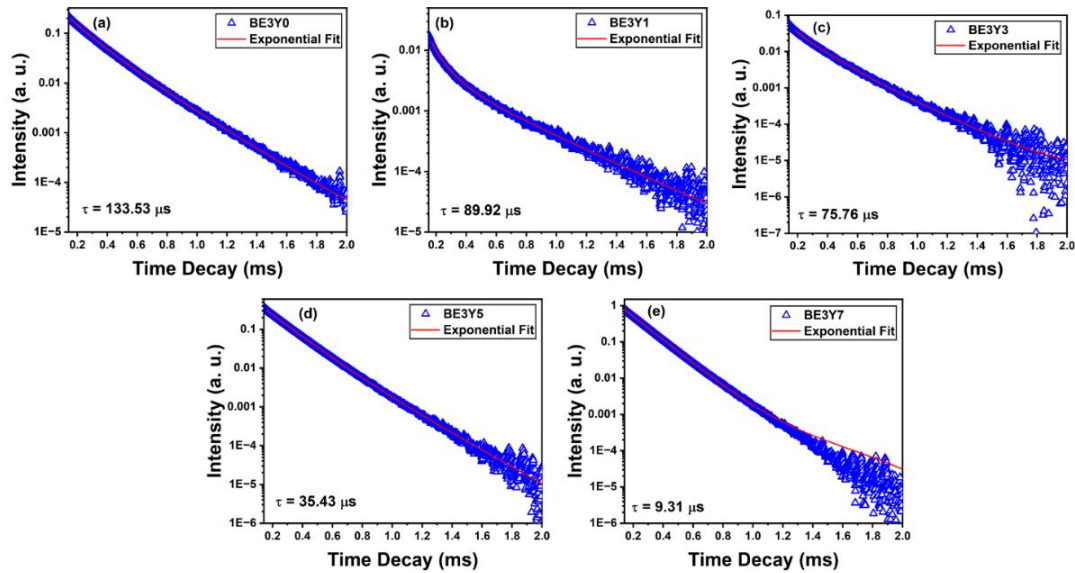


Figure 4.8: Time decay profile of BNT compositions (a) BE3Y0 (b) BE3Y1 (c) BE3Y3 (d) BE3Y5 (e) BE3Y7

It has been observed that the efficiency in energy transfer between the dopant ions is increased for all the co-doped BNT ceramic compositions and ranges from 32% to 93% for BE3Y1 to BE3Y7 ceramic.

4.3.7 Pump power dependency

An essential investigation to ascertain the quantity of photons engaged in the UC process is the dependence of pump power on upconversion luminescence. Luminescence spectra demonstrating upconversion under various pump powers density that lie in the range 29.41- 62.09 W/cm² is depicted in **Figure 4.9(a)**. Pump power appears to be correlated with the intensity of UCL. In this study we see that the UCL appears to intensify as pump power is increased and this can be calculated using the Eq. 4.7 [46]:

$$I_{UCL} \propto P^n \quad (4.7)$$

The variables P, n, and I_{UCL} represent the pumping power, photon count, and UCL intensity, respectively, required for the upconversion process. Plot of intensity versus excitation pump power log is shown in **Figure 4.9(b)**. The logarithmic plot's slope is used to calculate the value of n for the green and red emission bands. The n values are 2.31, 1.69 for the green bands and 2.14 for the red band. This validates the contribution of two photons to the intensity of the UC emission. Multiple mechanisms (non-radiative transitions, ET, and ESA) have an impact on the emission spectra, which accounts for the disparity [47].

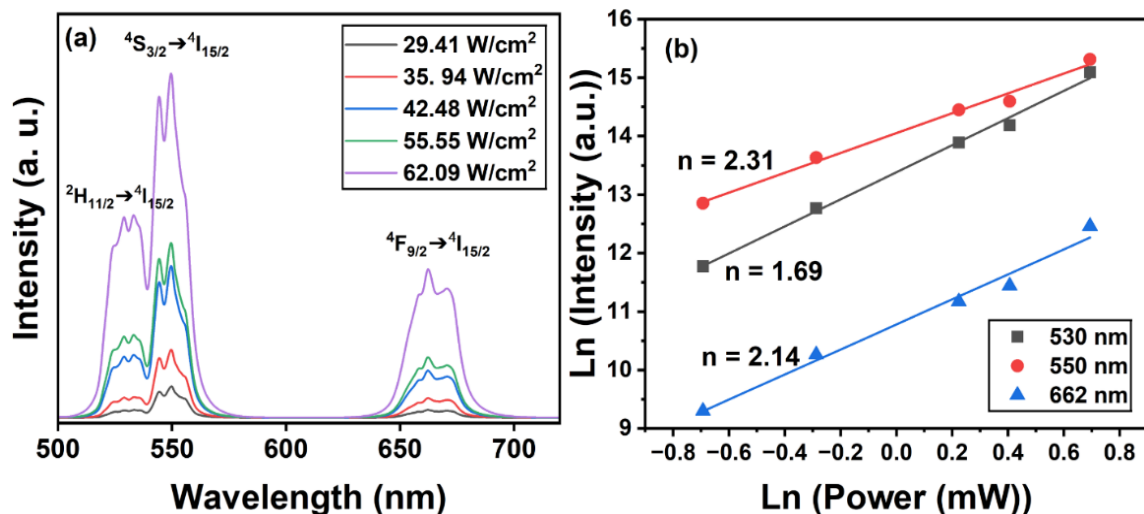


Figure 4.9: (a) Pump power dependency on UCL spectra of BE3Y3 ceramic compositions
 (b) Ln (intensity) versus Ln (power) plot

4.3.8 Optical temperature sensitivity

The optical temperature sensing of BE3Y3 ceramic was examined utilizing the FIR method. It has been widely employed to investigate the temperature sensitivity of numerous host materials doped with RE [48-49]. **Figure 4.10(a)** illustrates the temperature-dependent UCL spectra, which span a temperature range of 303 K to 523 K. The intensity of the UCL diminishes as the temperature rises as a consequence of thermal equilibrium in the TCLs. The FIR is represented by Eq. 4.8 [50-51]:

$$FIR = \frac{I_H}{I_S} = C \exp\left(-\frac{\Delta E}{K_B T}\right) \quad (4.8)$$

where I_H represent the intensity of the green bands at 530 nm and I_S represent the intensity of the green bands at 550 nm, C is the exponential coefficient, and ΔE is the energy difference. The FIR values are depicted in **Figure 4.10(b)**. The linear form of Eq. 4.7 is presented in Eq. 4.9:

$$\ln(FIR) = -\left(\frac{\Delta E}{K_B}\right)\left(\frac{1}{T}\right) + \ln C \quad (4.9)$$

Figure 4.10(c) shows the $\ln(FIR)$ against the inverse of temperature. The slope of this graph gives the value of $\Delta E/K_B$ value and intercept $\ln C$, which is used for calculating the absolute (S_{ab}) and relative (S_r) sensitivity of the materials established using Eq. 4.10, 11, respectively:

$$S_{ab} = \frac{d(FIR)}{dT} = \frac{d\left(C \exp\left(-\frac{\Delta E}{K_B T}\right)\right)}{dT} = C \exp\left(-\frac{\Delta E}{K_B T}\right) \left(\frac{\Delta E}{K_B T^2}\right) \quad (4.10)$$

$$S_r = \frac{1}{FIR} * S_{ab} = \left(\frac{\Delta E}{K_B T^2}\right) \quad (4.11)$$

The plot of S_r and S_{ab} is denoted in **Figure 4.10(d)**. The S_{ab} and S_r of BE3Y3 ceramic composition are 0.54 % K⁻¹ and 1.24 % K⁻¹ at 523 K and 303 K, respectively. For a practical sensor, the repeatability and resolution should be checked. The FIR values are varied between two temperatures (303 K and 523 K) and it was observed that the FIR value does not change abruptly confirming the

good repeatability of the sample as shown in **Figure 10(e)**. Taking specific (Δ_{sp}) and mean values (Δ_m) of FIR and δ_Δ/Δ being the accuracy of the instrument, the mathematical expression for repeatability (R) and resolution (δT) is given in the Eq. 4.12, 4.13, respectively [51]:

$$R = 1 - \frac{(\Delta_m - \Delta_{sp})}{\Delta_{Av}} \quad (4.12)$$

$$\delta T = \frac{1}{S_r} \times \frac{\delta_\Delta}{\Delta} \quad (4.13)$$

Figure 4.10(f) shows that the temperature resolution increases with increasing temperature. The comparison Table 4.3 is given for the sensitivity of various host materials co-doped with $\text{Er}^{3+}/\text{Yb}^{3+}$ ions.

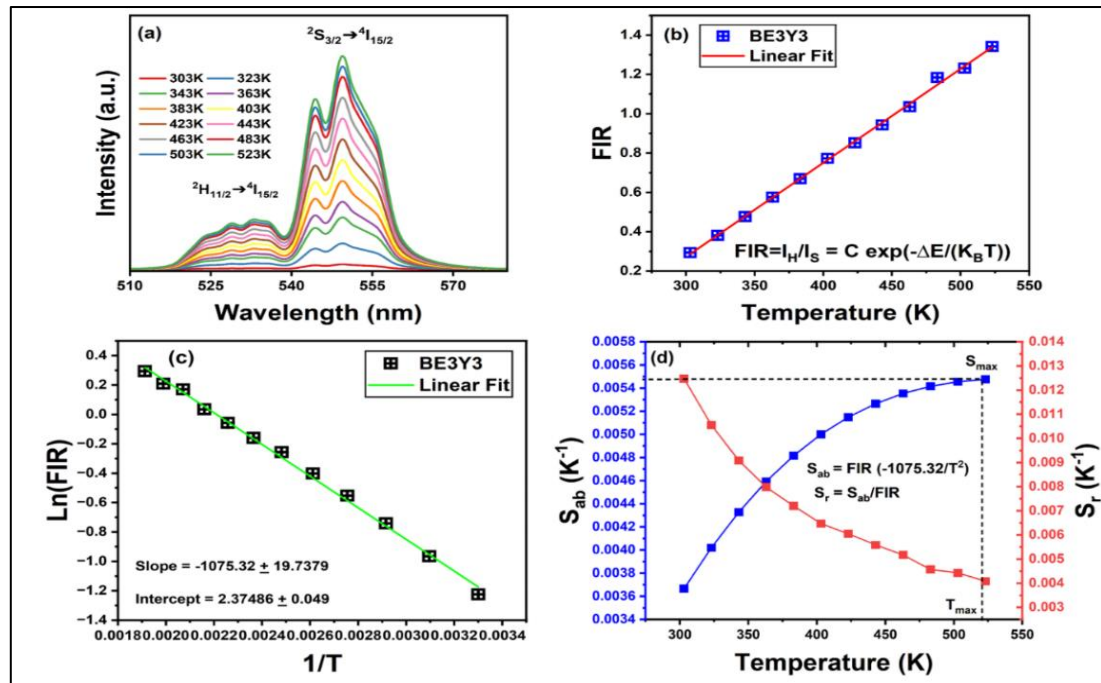


Figure 4.10: (a) Temperature dependent UCL spectra (b) Plot of FIR and temperature (c) $\text{Ln}(\text{FIR})$ vs T^{-1} , (d) Plot of S_{ab} and S_r

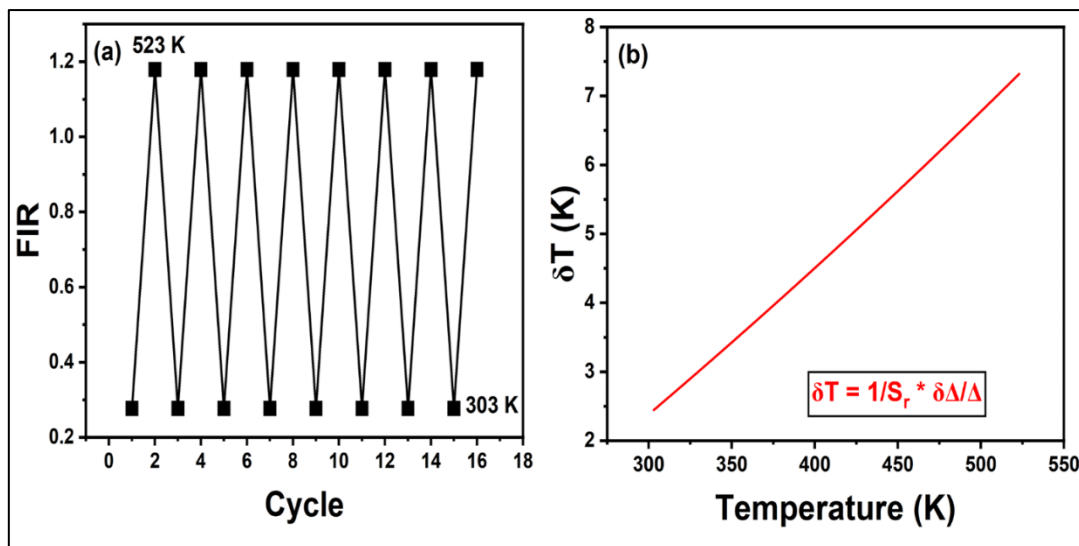


Figure 4.10: (e) Repeatability test between 303 K and 523 K (f) Plot of δT vs temperature

Table 4.3: Absolute sensitivity values of various Er/Yb co-doped ferroelectric ceramic

S. No.	Host material	Temp range (K)	Max sensitivity temp, T_{\max} (K)	Max sensitivity, S_{ab} (K^{-1})	Ref
1.	BNT: Er	175-500	380	0.0017	[13]
2.	BNT: Er/Yb	175-553	493	0.0035	[52]
3.	BNTO: Er/Yb	153-483	483	0.0078	[41]
4.	NBT: Er	80-480	-	0.053	[53]
5	BNT: Er/Yb	163-613	-	0.0031	[54]
6	BBN: Er	300-623	483	0.00996	[42]
7	BNT: Er	303-523	523	0.0047	[28]
8.	BNT: Er/Yb	303-523	523	0.0054	[This work]

4.4 Summary

The structural, upconversion luminescence, and sensing properties of a series of Er^{3+}/Yb^{3+} co-doped $Bi_{0.5-x-y}Er_xYb_yNa_{0.5}TiO_3$ ferroelectric ceramics are investigated. The rhombohedral geometry is confirmed by the XRD analysis, and the solubility of the dopant ions is demonstrated by the absence of any additional peaks. The dense microstructure with well-defined boundaries were evident in the SEM images. The typical characteristics of perovskite structure are illustrated by the FTIR vibrational

bands at 550 cm^{-1} and 820 cm^{-1} , which are the result of the elongation of Ti-O bonds in octahedral groups. The Tauc plot displays the energy band gaps (E_g) in a range of 2.93 eV to 2.88 eV as a function of the dopant concentration. The photoluminescence spectra of all BNT ceramic compositions are measured under excitation wavelengths i.e. 489 nm and 980 nm. It has been noted that the two intense green and one visible red bands were present at 530 nm, 549 nm, and 662 nm, respectively. When excited at 980 nm, the UCL spectra vary with different pumping powers, indicating that the process involves two photons. The time-resolved fluorescence spectroscopy indicates that the efficiency of energy transfer between the dopant ions has increased for all co-doped BNT ceramic compositions. At 523 K and 303 K, the relative (S_r) and absolute (S_{ab}) sensitivity of the BE3Y3 ceramic composition are 1.24 \% K^{-1} and 0.54 \% K^{-1} , respectively. These findings suggest that the prepared ceramic has the capability to be used as multifunctional material.

A detailed examination of the upconversion luminescence and optical temperature-sensing characteristics of the $\text{Er}^{3+}/\text{Yb}^{3+}$ co-doped BNT ferroelectric system revealed that the incorporation of $\text{Er}^{3+}/\text{Yb}^{3+}$ ions has a pronounced influence on the resulting ceramic. In addition to $\text{Er}^{3+}/\text{Yb}^{3+}$ incorporation, Ho^{3+} ions were also introduced into the $\text{Bi}_{0.5}\text{Na}_{0.5}\text{TiO}_3$ lattice to further tailor its optical response in the next chapter.

4.5 References

1. S. Makishima, H. Yamamoto, T. Tomotsu, S. Shionoya, Luminescence spectra of Sm^{3+} in BaTiO_3 host lattice, *J. Phys. Soc. Jpn.* 20 (1965) 2147–2151.
2. D.D. Dung, N.B. Doan, N.Q. Dung, L.H. Bac, N.H. Linh, L.T.H. Thanh, D.V. Thiet, N.N. Trung, N.C. Khang, T.V. Trung, N.V. Duc, Role of Co dopants on the structural, optical and magnetic properties of lead-free ferroelectric $\text{Na}_{0.5}\text{Bi}_{0.5}\text{TiO}_3$ materials, *J. Sci. Adv. Mater. Devices* 4 (2019) 584–590, <https://doi.org/10.1016/j.jsamd.2019.08.007>.
3. P. Julphunthong, T. Bongkarn, S. Maensiri, The effect of firing temperatures on phase formation, microstructure and via the combustion route, *Ceram. Int.* 41 (2015) S143–S151, <https://doi.org/10.1016/j.ceramint.2015.03.229>.
4. M. Bengisu, Production of Ceramic Bodies, *Engineering Ceramics, Engineering Materials*, Springer, Berlin, Heidelberg, 2001, https://doi.org/10.1007/978-3-662-04350-9_3.
5. R.D. Shannon, Revised effective ionic radii and systematic studies of interatomic distances in halides and chalcogenides, *J. Acta Cryst. A* 32 (2016) 751–767, <https://doi.org/10.1107/S0567739476001551>.
6. C. Kornphom, K. Saenkam, T. Bongkarn, Enhanced energy storage properties of BNT–ST–AN relaxor ferroelectric ceramics fabrication by the solid-state combustion technique, *Phys. Status Solidi A* (2022), 2200240, <https://doi.org/10.1002/pssa.202200240>.
7. O. Mitsuhiro, O. Masashi, B. Teruo, M. Mamoru, Temperature dependence of the fatigue and mechanical properties of lead zirconate titanate piezoelectric ceramics, *Int. J. Fatigue* 31 (2009) 1254–1261, <https://doi.org/10.1016/j.ijfatigue.2009.01.008>.
8. J.G. Hao, R.Q. Chu, Z.J. Xu, G.Z. Zang, G.R. Li, Structure and electrical properties of (Li, Sr, Sb)-modified $\text{K}_{0.5}\text{Na}_{0.5}\text{NbO}_3$ lead-free piezoelectric ceramic, *J. Alloy. Compd.* 479 (2009) 376 – 380, <https://doi.org/10.1016/j.jallcom.2008.12.069>.
9. C.G. Xu, D.M. Lin, K.W. Kwok, Structure, electrical properties and depolarization

temperature of $(\text{Bi}_{0.5}\text{Na}_{0.5})\text{TiO}_3 - \text{BaTiO}_3$ lead-free piezoelectric ceramics, Solid. State Sci. 10 (2008) 934–940, <https://doi.org/10.1016/j.solidstatesciences.2007.11.003>.

10. A. Gallegos-Melgar, D.G. Espinosa-Arbelaez, F.J. Flores-Ruiz, A. Lahmar, J.-L. Dellis, N. Lem'ee, F.J. Espinoza-Beltran, J. Munoz-Saldana, “ Ferroelectric properties of manganese doped $(\text{Bi}_{1/2}\text{Na}_{1/2})\text{TiO}_3$ and $(\text{Bi}_{1/2}\text{Na}_{1/2})\text{TiO}_3 - \text{BaTiO}_3$ epitaxial thin films”, Appl. Surf. Sci. 359 (2015) 923–930, <https://doi.org/10.1016/j.apsusc.2015.09.175>.
11. C.Peng, J.-F. Li, W. Gong, Preparation and properties of $(\text{Bi}_{1/2}\text{Na}_{1/2})\text{TiO}_3 - \text{Ba}(\text{Ti},\text{Zr})\text{O}_3$ lead-free piezoelectric ceramics, Mater. Lett. 59 (2005) 1576–1580, <https://doi.org/10.1016/j.matlet.2005.01.026>.
12. R. Sahu, P. Kumar, Microstructural, dielectric and ferroelectric properties of $\text{Sr}_{0.8}\text{Bi}_{2.15}\text{Ta}_2\text{O}_9$ ceramics synthesized by microwave processing technique, Phase Transitions 93 (1) (2020) 91–99, <https://doi.org/10.1080/01411594.2019.1702190>.
13. X. Hui, D. Peng, H. Zou, J. Li, Q. Cao, Y. Li, X. Wang, X. Yao, A new multifunctional Aurivillius oxide $\text{Na}_{0.5}\text{Er}_{0.5}\text{Bi}_4\text{Ti}_4\text{O}_{15}$: up-conversion luminescent, dielectric, and piezoelectric properties, Ceram. Int. 40(4A)(2014)12477–12483, <https://doi.org/10.1016/j.ceramint.2014.04.102>.
14. H. Yabuta, H. Tanaka, T. Furuta, T. Watanabe, M. Kubota, T. Matsuda, T. Ifuku, Y. Yoneda, Enhancement of tetragonal anisotropy and stabilisation of the tetragonal phase by Bi/Mn-double-doping in BaTiO_3 ferroelectric ceramics, Sci. Rep. 7 (2017) 45842, DOI: 10.1038/srep45842
15. T.Rojac, A.Bencan, G.Drazic, N.Sakamoto, H.Ursic, B.Jancar, G.Tavcar, M.Makarovic, J. Walker, B.Malic, D.Damjanovic, Domain-wall conduction in ferroelectric BiFeO_3 controlled by accumulation of charged defects, Nat. Mater. 16(2017)322–327, <https://doi.org/10.1038/nmat4799>
16. M. Li, M.J. Pietrowski, R.A.D. Souza, H. Zhang, I.M. Reaney, S.N. Cook, J.A. Kilner, D.C. Sinclair, A family of oxide ion conductors based on the ferroelectric perovskite $\text{Na}_{0.5}\text{Bi}_{0.5}\text{TiO}_3$, Nat. Mater. 13 (2014) 31–35, <https://doi.org/10.1038/nmat3782>

17. Y. Li, Y. Jiao, S. Zhang, Z. Li, C. Song, J. Dong, G. Liu, Y. Yan, Improved electric energy storage properties of BT-SBT lead-free ceramics incorporating with A-site substitution with Na & Bi ions and liquid sintering generated by $\text{Na}_{0.5}\text{Bi}_{0.5}\text{TiO}_3$, *J. Alloy. Compd.* 856 (2021) 156708, <https://doi.org/10.1016/j.jallcom.2020.156708>.
18. X.Y. Tong, H.L. Li, J.J. Zhou, H. Liu, J.Z. Fang, Giant electrostrain under low driving field in $\text{Bi}_{1/2}\text{Na}_{1/2}\text{TiO}_3\text{-SrTiO}_3$ ceramics for actuator applications, *Ceram. Int.* 42 (2016) 16153–16159, <https://doi.org/10.1016/j.ceramint.2016.07.133>
19. C. Cui, Y. Pu, Z. Gao, J. Wan, Y. Guo, C. Hui, Y. Wang, Y. Cui, Structure, dielectric and relaxor properties in lead-free ST-NBT ceramics for high energy storage applications, *J. Alloy. Compd.* 711 (2017) 319–326, <https://doi.org/10.1016/j.jallcom.2017.04.023>
20. Y.C. Guo, H.Q. Fan, C.B. Long, J. Shi, L. Yang, S.H. Lei, Electromechanical and electrical properties of $\text{Bi}_{0.5}\text{Na}_{0.5}\text{TiO}_{1-x}\text{Mn}_x\text{O}_{3-\delta}$ ceramics with high remnant polarization, *J. Alloy. Compd.* 610 (2014), <https://doi.org/10.1016/j.jallcom.2014.04.038>
21. N. Lei, M. Zhu, P. Yang, L. Wang, L. Wang, Y. Hou, H. Yan, Effect of lattice occupation behavior of Li^+ cations on microstructure and electrical properties of $(\text{Bi}_{1/2}\text{Na}_{1/2})\text{TiO}_3$ -based lead-free piezoceramics, *J. Appl. Phys.* 109 (2011), 054102, <https://doi.org/10.1063/1.3555598>.
22. G. Viola, H. Ning, X. Wei, M. Deluca, A. Adomkevicius, J. Khalil, M. John Reece, H. Yan, Dielectric relaxation, lattice dynamics and polarization mechanisms in $\text{Bi}_{0.5}\text{Na}_{0.5}\text{TiO}_3$ -based lead-free ceramics, *J. Appl. Phys.* 114 (2013), 014107, <https://doi.org/10.1063/1.4812383>.
23. A. Hussin, A. Maqbool, R.A. Malik, M. Su Kim, T.K. Song, M.H. Kim, Structural and electrical properties of $\text{Bi}_{0.5}\text{Na}_{0.5}\text{TiO}_3$ templates produced by topochemical microcrystal conversion method, *New Physics:Sae Mulli* 65 (No. 8) (2015) 715–720, <https://doi.org/10.3938/NPSM.65.715>.
24. Y. Hiruma, H. Nagata, T. Takenaka, Thermal depoling process and

piezoelectric properties bismuth sodium titanate ceramics,
J.Appl.Phys.105(2009),084112,<https://doi.org/10.1063/1.3115409>.

25. G.A. Smolenskii, V.A. Isupov, A.I. Agranovskaya, S.N. Popov, Ferroelectrics with diffuse phase transitions, Sov. Phys. Solid State 2 (1961) 2584–2594.

26. D. Lin, K.W. Kwok, Dielectric and piezoelectric properties of $(Bi_{1-x-y}Nd_xNa_{1-y})_{0.5}BaTiO_3$ lead-free ceramics, Curr.Appl.Phys.10 (2010) 422–427, <https://doi.org/10.1016/j.cap.2009.06.044>.

27. Y. Li, W. Chen, Q. Xu, J. Zhou, X. Gu, Piezoelectric and ferroelectric properties of $Na_{0.5}Bi_{0.5}TiO_3-K_{0.5}Bi_{0.5}TiO_3-BaTiO_3$ piezoelectric ceramics, Mater. Lett. 59 (2005) 1361–1364, <https://doi.org/10.1016/j.matlet.2004.12.041>.

28. M. Narwan, A. Banwal, R. Sharma, R. Bokolia, Non-invasive thermal sensing and improved recoverable energy storage density of $Bi_{0.5}Na_{0.5}TiO_3$: Er^{3+} doped multifunctional ferroelectric ceramic, J.Lumin 265 (2024)<https://doi.org/10.1016/j.jlumin.2023.120236>

29. Z. Chen, J. Hu, Piezoelectric and dielectric properties of $(Bi_{0.5}Na_{0.5})_{0.94}Ba_{0.06}TiO_3-Ba(Zr_{0.04}Ti_{0.96})O_3$ lead-free piezoelectric ceramics, Ceram. Int. 35 (2009) 111–115, <https://doi.org/10.1016/j.ceramint.2007.09.110>.

30. A. Mishra, B. Majumdar, R. Ranjan, A complex lead-free $(Na, Bi, Ba)(Ti, Fe)O_3$ single phase perovskite ceramic with a high energy-density and high discharge efficiency for solid state capacitor applications, J. Eur. Ceram. Soc. 37 (2017) 2379–2384, <https://doi.org/10.1016/j.jeurceramsoc.2017.01.036>.

31. H. Yang, F. Yan, Y. Lin, T. Wang, F. Wang, High energy storage density over a broad temperature range in sodium bismuth titanate-based lead-free ceramics, Sci. Rep. 7 (2017) 8726, <https://doi.org/10.1038/s41598-017-06966-7>.

32. B. Liu, B. Lu, X. Chen, X. Wu, S. Shi, L. Xu, Y. Liu, F. Wang, X. Zhao, W. Shi, A high performance flexible piezoelectric energy harvester based on lead-free $(Na_{0.5}Bi_{0.5})TiO_3-BaTiO_3$ piezoelectric nanofibers, J. Mater. Chem. A. 5 (2017) 23634–23640, <https://doi.org/10.1039/C7TA07570G>.

33. M. Zannen, M. Dietze, H. Khemakhem, A. Kabadou, M. Es-Souni, The erbium's amphoteric behavior effects on sodium bismuth titanate properties, *Ceram. Int.* 40 (2014) 13461–13469, <https://doi.org/10.1016/j.ceramint.2014.05.069>.
34. A. Zeb, S.J. Milne, High temperature dielectric ceramics: a review of temperature stable high-permittivity perovskites, *J. Mater. Sci. Mater. Electron.* 26 (2015) 9243–9255, <https://doi.org/10.1007/s10854-015-3707-7>.
35. M. Zannen, A. Lahmar, M. Dietze, H. Khemakhem, A. Kabadou, M. Es-Souni, Structural, optical, and electrical properties of Nd-doped $\text{Na}_{0.5}\text{Bi}_{0.5}\text{TiO}_3$, *Mater. Chem. Phys.* 134 (2–3) (2012) 829–833, <https://doi.org/10.1016/j.matchemphys.2012.03.076>.
36. PA. Franco, P. Banerjee, P.L. Romanholo, Effect of composition induced transition in the optical band-gap, dielectric and magnetic properties of Gd doped $\text{Na}_{0.5}\text{Bi}_{0.5}\text{TiO}_3$ complex perovskite, *J. Alloys compd.* 764 (2018) 122e127, <https://doi.org/10.1016/j.jallcom.2018.06.007>.
37. L.T.H. Thanh, N.B. Doan, N.Q. Dung, L.V. Cuong, L.H. Bac, N.A. Duc, P.Q. Bao, D.D. Dung, Origin of room temperature ferromagnetism in Cr-doped lead-free ferroelectric $\text{Bi}_{0.5}\text{Na}_{0.5}\text{TiO}_3$ materials, *J. Electron. Mater.* 46 (2017) 3367–3372, <https://doi.org/10.1007/s11664-016-5248-0>
38. L. Mukhopadhyay, V.K. Rai, R. Bokolia, K. Sreenivas, 980 nm excited $\text{Er}^{3+}/\text{Yb}^{3+}/\text{Li}^+/\text{Ba}^{2+}$: NaZnPO_4 upconverting phosphors in optical thermometry, *J. Lumin.* 187 (October) (2017) 368–377, <https://doi.org/10.1016/j.jlumin.2017.03.035>.
39. R. Bokolia, O.P. Thakur, V.K. Rai, S.K. Sharma, K. Sreenivas, Dielectric, ferroelectric and photoluminescence properties of Er^{3+} doped $\text{Bi}_4\text{Ti}_3\text{O}_{12}$ ferroelectric ceramics, *Ceram. Int.* 41 (4) (2015) 6055–6066, <https://doi.org/10.1016/j.ceramint.2015.01.062>.
40. R. Bokolia, V.K. Rai, L. Chauhan, K. Sreenivas, Structural and light upconversion luminescence properties of Er^{3+} - Yb^{3+} - W^{6+} substituted $\text{Bi}_4\text{Ti}_3\text{O}_{12}$, *AIP Conf. Proc.* 1731 (2016) 4–7, <https://doi.org/10.1063/1.4948208>
41. L. Jacob, S. Sisira, K. P.Mani, K. Thomas, D. Alexander, P.R.Biju,

N.V.Unnikrishnan, C. Joseph, A new potential green-emitting erbium –activated α -Na₃Y(VO₄)₂ nanocrystals for UV-excit able single phase pc-WLED applications 6, SN applied Science, <https://doi.org/10.1007/s42452-020-2873-2>

42. A. Banwal, R. Bokolia, Enhanced upconversion luminescence and optical temperature sensing performance in Er³⁺ doped BaBi₂Nb₂O₉ ferroelectric ceramic, Ceram.Int. 48 (2) (2022) 2230–2240, <https://doi.org/10.1016/j.ceramint.2021.09.314>.

43. A. Shandilya, R.S. Yadav, A.K. Gupta, K. Sreenivas, Temperature-dependent light upconversion and thermometric properties of Er³⁺/Yb³⁺co-doped SrMoO₄ sintered ceramics, J. Mater. Sci. 56 (2021) 12716–12731, <https://doi.org/10.1007/s10853-021-06078-8>.

44. Z. Zhang, J. Li, L. Liu, J. Sun, J. Hao, W. Li, Upconversion luminescence and electrical properties of (K, Er) co-modified Na_{0.5}Bi_{4.5}Ti₄O₁₅ high-temperature piezoceramics, Phys. B Condens. Matter 580 (2020), 411920, <https://doi.org/10.1016/j.physb.2019.411920>, 09.

45. W. Qi, Y. Wang, J. Wu, Z. Hu, C. Jia, G. Viola, H. Zhang, H. Yan, Relaxor behavior and photocatalytic properties of BaBi₂Nb₂O₉, J. Am. Ceram. Soc. 103 (1) (2020) 28–34, <https://doi.org/10.1111/jace.16730>.

46. Y. Zhang, T. Xu, H. Yu, R. Chu, G. Li, C. Zhang, Z. Xu, Sm-modified bismuth layerstructured SrBi₂Nb₂O₉ multifunctional ceramics with enhanced electrical properties and good photoluminescence properties, Ceram. Int. 48 (2022) <https://doi.org/10.1016/j.ceramint.2022.03.182>.

47. Z. Liu, D. Chen, Upconversion photoluminescence and dual-mode temperature sensing properties of PIN-PMN-PT:Er³⁺ ceramic, J. Alloys Compd. 770 (2019) 214–221, <https://doi.org/10.1016/j.jallcom.2018.08.019>

48. C. Liu, Q. Wang, X. Wu, B. Sa, H. Sun, L. Luo, C. Lin, X. Zheng, T. Lin, Z. Sun, “Boosting upconversion photoluminescence and multielectrical properties via Er Doping-Modulated vacancy control in Ba_{0.85}Ca_{0.15}Ti_{0.9}Zr_{0.1}O₃”, ACS Omega 4 (2019) 11004–1101, <https://doi.org/10.1021/acsomega.9b01391>.

49. Z. Guan, X. Li, R. Shen, Z. Tian, H. Yu, Y. Cao, Y. Wang, J. Zhang, S. Xu, B. Chen, Intense red up-conversion luminescence and temperature sensing property of $\text{Yb}^{3+}/\text{Er}^{3+}$ co-doped BaGd_2O_4 phosphors, *Spectrochim. Acta Mol. Biomol. Spectrosc.* 284 (2023), 121805 <https://doi.org/10.1016/j.saa.2022.121805>
50. J. Xing, F. Shang, G. Chen, Upconversion luminescence of $\text{Yb}^{3+}/\text{Er}^{3+}$ co-doped NaSrPO_4 glass ceramic for optical thermometry, *Ceram. Int.* 147 (2021) 8330–8337, <https://doi.org/10.1016/j.ceramint.2020.11.195>.
51. A. Banwal, R. Bokolia, “Thermometric sensing performance in Erbium modified $\text{SrBi}_{2-x}\text{Nb}_2\text{Er}_x\text{O}_9$ ferroelectric ceramics for optoelectronics devices” *Ceram. Int.* 48 (2022) 34405–34414, [10/1016/j.ceramint.2022.08.019](https://doi.org/10.1016/j.ceramint.2022.08.019).
52. Du Peng, Jae Su Yu, “Effect of molybdenum on upconversion emission and temperature sensing properties in $\text{Na}_{0.5}\text{Bi}_{0.5}\text{TiO}_3:\text{Er}/\text{Yb}$ ceramics, *Ceram. Int.* 41 (2015) 6710–6714, <https://doi.org/10.1016/j.ceramint.2015.01.113>.
53. S. Wang, H. Zhou, X. Wang, A. Pan, Up-conversion luminescence and optical temperature sensing properties of Er^{3+} doped perovskite $\text{Na}_{0.5}\text{Bi}_{0.5}\text{TiO}_3$, *J. Phys. Chem. Solids.* 98 (2016) 28–31, <https://doi.org/10.1016/j.jpcs.2016.06.002>.
54. P. Du, L. Luo, W. Li, Q. Yue, Upconversion emission in Er-doped and Er/Yb codoped ferroelectric $\text{Na}_{0.5}\text{Bi}_{0.5}\text{TiO}_3$ and its temperature sensing application, *J. Appl. Phys.* 116 (2014), <https://doi.org/10.1063/1.4886575>

CHAPTER – 5

Upconversion Luminescence and Temperature Sensing Properties of Ho^{3+} Doped $Bi_{0.5}Na_{0.5}TiO_3$ Ferroelectric Ceramic

- ❖ The motivation behind this study is to estimate the prepared ceramic's energy storage device and multifunctional optoelectronic device potential in terms of its effectiveness and practical applications.
- ❖ This work presents a new method by adding Ho^{3+} ions to lead-free $Bi_{0.5}Na_{0.5}TiO_3$ (BNT) ceramics without any sensitizer, resulting in an multiphonon and previously unreported orange emission.
- ❖ In host matrix, Ho^{3+} usually shows green or red luminescence, however the appearance of orange emission in the BNT matrix reveals a special site symmetry and energy level interaction in the host lattice.
- ❖ This work is especially important because, by using a ferroelectric composition free of lead, it not only investigates novel luminous behaviour in rare-earth-doped BNT systems but also responds to the increasing need for environmentally friendly materials.
- ❖ Additionally, the study shows that Ho^{3+} doping greatly improves the ceramics' capacity for energy storage. Overall, this investigation provides new insights into rare-earth ion engineering in lead-free ceramics, offering a promising route for the development of advanced functional materials.

The results reported in this chapter have been published in **Megha et. al. in Ceramics International**.

5.1 Introduction

In this chapter, the Ho^{3+} ions are systematically inserted on the A-site of $\text{Bi}_{0.5-x}\text{Ho}_x\text{Na}_{0.5}\text{TiO}_3$ lead-free ferroelectric ceramic via solid-state method. The x-ray diffraction spectra (XRD) shows the rhombohedral structure of $\text{Bi}_{0.5-x}\text{Ho}_x\text{Na}_{0.5}\text{TiO}_3$. Fourier transform infrared (FTIR) spectroscopy shows two vibrational bands at 537 cm^{-1} and 832 cm^{-1} , due to the stretching vibrations of Ti-O bonds in the octahedral units of the perovskite structure. The diffuse reflectance spectra (DRS) showed three bands at 454, 542, and 646 nm transit from $^5\text{I}_8 \rightarrow ^5\text{G}_6$, $^5\text{I}_8 \rightarrow ^5\text{F}_4/ ^5\text{S}_2$, and $^5\text{I}_8 \rightarrow ^5\text{F}_5$, respectively. The band gap varies and maximum for 0.03 concentration due to the local structural instability within the lattice by Ho^{3+} ions. The photoluminescence (PL) emission spectra are traced under 452 nm, and one intense green band at 548 nm and two at 655 (orange) and 750 nm (red) were observed. In upconversion luminescence (UCL) spectra, four emission wavelengths were obtained at 490, 525, 552, and 660 nm. The orange emission band is highly intense, whereas other color bands are relatively weak. Pump power dependence on UCL spectra is analyzed using concentration ($x=0.03$). The decay profile for green and orange bands showed an average lifetime of $12.99\text{ }\mu\text{s}$ and $9.43\text{ }\mu\text{s}$, respectively. The PE loops become slimmer, and P_r values decrease with increasing concentration. The energy storage efficiency ($\eta\%$) of the ceramic is increasing with dopant concentration and comes out to be 90%. The maximum absolute and relative sensitivity observed for the BNT ($x = 0.03$) is 0.29 \% K^{-1} and 0.22 \% K^{-1} at 303 K, respectively. This study demonstrates the novel observation of orange emission in Ho^{3+} doped $\text{Bi}_{0.5}\text{Na}_{0.5}\text{TiO}_3$ ceramics without any sensitizers which is not usual behaviour as Ho^{3+} typically exhibits green or red emission. This unusual luminescence highlights distinct site symmetry and energy level interactions within the lead-free BNT matrix, validating the uniqueness of the work.

The remarkable piezoelectric performance of lead-based piezoelectric ceramics, such as $\text{Pb}(\text{Zr, Ti})\text{O}_3$ (PZT), makes them indispensable for use in transducers, actuators, etc. [1-3]. Despite their superior piezoelectric properties, lead-based

piezoelectric materials have lead toxicity. Exposure to lead and the chemicals that are derived from it is toxic to both the environment and human health. Because of this, lead-free ferroelectric and multifunctional materials have drawn more and more attention as environmental preservation and sustainable development gain in popularity [4,5]. Ferroelectric materials are well known for their multifunctional applications. The combination of magnetic, electrical, optical, and mechanical properties is characterized by multifunctional materials. There are different preparation methods, which include solid-state reactions, combustion reactions, and microwave processing, which also have a substantial impact on their chemical and physical properties. The current research focuses on lead-free titanate-based perovskites ferroelectric and piezoelectric ceramics such as $K_{0.5}Bi_{0.5}TiO_3$, $BaTiO_3$, $Bi_{0.5}Na_{0.5}TiO_3$, $BaZr_{0.08}Ti_{0.92}O_3$, bismuth ferrite ($BiFeO_3$), and alkaline niobate perovskites ($KNbO_3$, $NaNbO_3$, $((K, Na)NbO_3)$, as well as bismuth oxide layer structure ferroelectric materials ($SrBi_4Ti_4O_{15}$, $Bi_4Ti_3O_{12}$, Bi_3TiTaO_9) [6-10]. Among these, we chose sodium bismuth titanate $Bi_{0.5}Na_{0.5}TiO_3$ (abbreviated as BNT) lead-free piezoelectric material discovered in 1961 by Smolenskii et al. [11]. BNT has a rhombohedral perovskite ABO_3 structure and has high curie temperature ($T_c \sim 320^\circ C$) and strong remnant polarization ($P_r \sim 371 \text{ C/cm}^2$) [12,13]. One of the drawbacks of pure BNT is that it has a coercive field too large to be polarized and has a low piezoelectric coefficient; as a result, its practical application is severely limited. The primary cause of this problem is that, during the materials fabrication process, oxygen vacancies are created to compensate for the volatile bismuth ion (Bi^{3+}), which results in high leakage current and large conductivity [14-16]. This issue can be effectively resolved by using the site substitution technique to partially replace the Bi^{3+} ion. Rare earth ions are considered the ideal substitute for Bi^{3+} due to their identical valency and size, as well as their high melting temperature. According to the literature studied, it has been revealed that the substitution of a low amount of rare earth ions at the Bi^{3+} site of the host BNT-based ceramic frequently improves the ferroelectric and piezoelectric properties [17-20]. Furthermore, the BNT has a comparatively low phonon energy, which increases the

activator's upconversion emission intensity and decreases the possibility of non-radiative transitions caused by phonon vibration. BNT is, therefore, a perfect host material for photoluminescence properties [21-23].

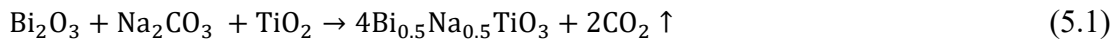
For the past couple of years, rare earth (RE)-doped ferroelectric materials have gained popularity due to their multifunctional properties, including photoluminescence, ferro/piezoelectric properties, and multiple coupling functions. Additionally, it has been seen that the BNT-BT-based lead-free ferroelectric triggered by the rare earth ions not only show good fluorescence capabilities with enhanced piezoelectric properties but their photoluminescence properties can be enhanced with electric field [24-28]. In addition, rare earth-doped BNT lead-free ferroelectric exhibits intense upconversion emission. Up-conversion luminescence (UCL) is a common nonlinear phenomenon that can combine two or more long-wavelength, absorbed lower-energy photons into a single, short-wavelength, higher-energy photon that is released [29-30]. UCL materials have an important role in optoelectronic systems, optical temperature sensors, fingerprint detection, and solar cells. Furthermore, temperature-sensing materials could be used in thermal sensors and luminescent probes. Rare-earth ions are typically employed as activators in upconversion luminescence materials due to the abundance of excited states [31-38]. Furthermore, apart from improving the ferroelectric properties and upconversion emission [39]. Ho^{3+} doped lead-free BNT ferroelectric ceramic can be used to provide good optical temperature sensitivity via the fluorescence intensity ratio (FIR) approach; we can also see good optical temperature sensing in the BNT host lattice doped with Ho^{3+} rare earth ion [40-43]. Thus, it can be considered that Ho^{3+} doped BNT can be a decent optical sensing material. Thus, we have synthesized BNT doped with Ho^{3+} with varying concentrations. The impact of Ho^{3+} dopant in BNT host lattice with different compositions on crystal structure and phase formation was methodically examined using XRD and FTIR. The emission spectra of the prepared ceramic were collected using the laser source of 980 nm excitation; using this, the photoluminescence behavior of Ho^{3+} doped BNT ceramic was studied. In order to investigate the photons involved in the process, the pump

power dependence on upconversion luminescence was also investigated. At a wavelength of 980 nm, time-decay was conducted at ambient temperature. The objective of this work is to investigate in detail how different Ho^{3+} concentrations affect the structural, microstructural, and upconversion photoluminescence characteristics of the ceramic $\text{Bi}_{0.5-x}\text{Ho}_x\text{Na}_{0.5}\text{TiO}_3$. The motivation behind this study is to estimate the prepared ceramic's energy storage device and multifunctional optoelectronic device potential in terms of its effectiveness and practical applications. This work presents a new method by adding Ho^{3+} ions to lead-free $\text{Bi}_{0.5}\text{Na}_{0.5}\text{TiO}_3$ (BNT) ceramics without any sensitizer, resulting in an multiphonon and previously unreported orange emission. In host matrix, Ho^{3+} usually shows green or red luminescence, however the appearance of orange emission in the BNT matrix reveals a special site symmetry and energy level interaction in the host lattice. This work is especially important because, by using a ferroelectric composition free of lead, it not only investigates novel luminous behaviour in rare-earth-doped BNT systems but also responds to the increasing need for environmentally friendly materials. Additionally, the study shows that Ho^{3+} doping greatly improves the ceramics' capacity for energy storage. Overall, this investigation provides new insights into rare-earth ion engineering in lead-free ceramics, offering a promising route for the development of advanced functional materials.

5.2 Synthesis and Characterization Details

The acquisition of highly pure level (99.99%) raw materials was carried out through Sigma Aldrich for the synthesis process. Bi_2O_3 , Na_2CO_3 , TiO_2 , and Ho_2O_3 were used as initial precursors to synthesize lead-free $\text{Bi}_{0.5-x}\text{Ho}_x\text{Na}_{0.5}\text{TiO}_3$ ($x = 0 - 0.07$) material. The solid-state technique was used to obtain the final product; it is also illustrated in **Figure. 5.1**. Firstly, the precursors were mixed in a stoichiometric amount given by **Eq. 5.1**, and subsequently, the dopant Ho^{3+} was mixed with different concentrations using **Eq. 5.2**:

For undoped BNT-



For Ho^{3+} doped BNT-



The initial unprocessed powder was weighed in accordance with the stoichiometric ratio and mixed for 12h by zirconia balls in a high-energy ball mill to guarantee that all precursors were fully homogenized. The mixture was left over and dry for 24 hours at 80°C in an oven, and lastly, calcined for 3 hours at 850°C in the hot air muffle furnace. The binder polyvinyl alcohol (PVA) was added to the powder to make pellets using a hydraulic press machine at 50 MPa. The compacted pellets were then sintered for 3 hours at a temperature of 1050°C in the same furnace.

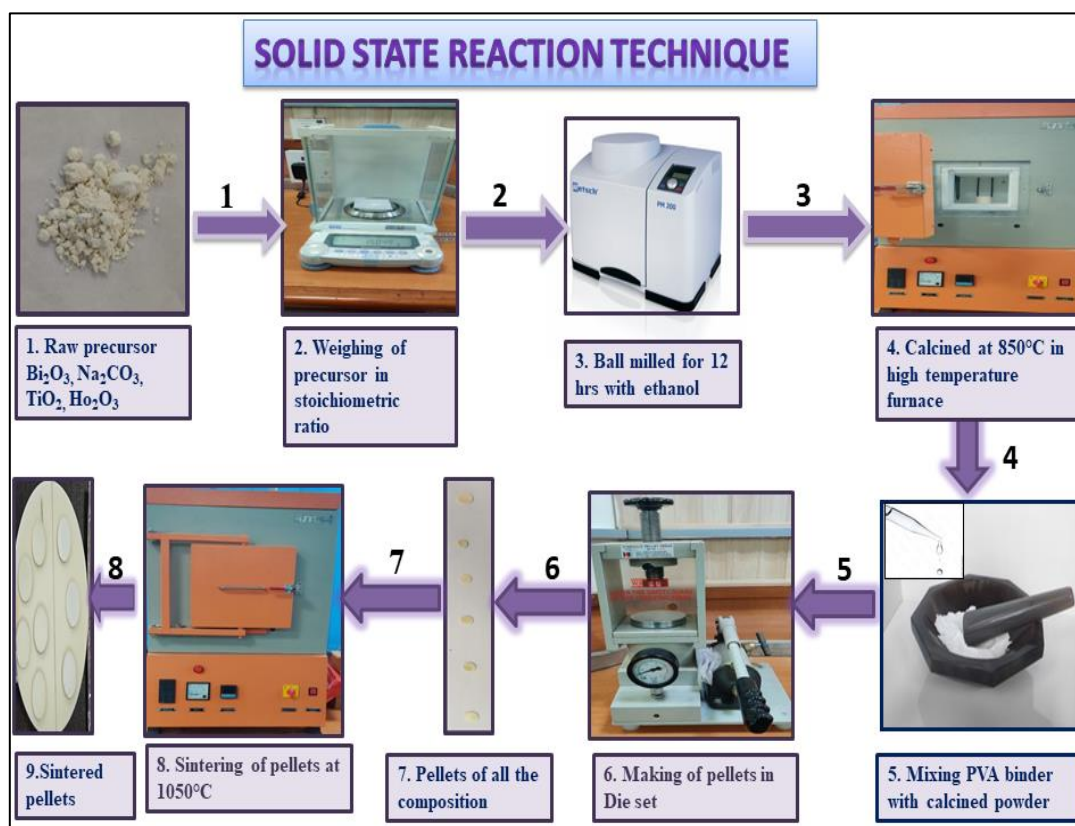


Figure 5.1: Pictorial depiction of the synthesis process

The structural properties were analyzed by XRD spectra using Cu-K α radiation, using a Bruker D-8 Advance X-ray diffractometer. The unit cell characteristics of the ceramic were optimized using TOPAZ software. Scanning electron microscopy was utilized to investigate the microstructure and increase of grain size of the unpolished ceramic surface. ATR mode is used in the Perkin Elmer spectrum-II instrument to analyze the FTIR spectra. The HORIBA PTI Quanta-master was employed to obtain the UCL spectra at 980 nm. Time decay was carried out at room temperature using a 980 nm pulsed laser source. The photoluminescence (PL) emission spectra were measured using a JASCO FP-8300 PC-spectrofluorophotometer set to 488 nm.

5.3 Results and Discussion

5.3.1 XRD and SEM

The X-ray diffraction (XRD) plot of pure $\text{Bi}_{0.5}\text{Na}_{0.5}\text{TiO}_3$ and Ho^{3+} modified $\text{Bi}_{0.5-x}\text{Ho}_x\text{Na}_{0.5}\text{TiO}_3$ ceramic with various dopant concentrations is illustrated in **Figure 5.2(a)**. It is noted that the peaks closely match the reported diffraction data with JCPDS card no. #00-036-0340, indicating that for all the different dopant compositions, a single phase of rhombohedral crystal structure of $\text{Bi}_{0.5-x}\text{Ho}_x\text{Na}_{0.5}\text{TiO}_3$ ($x = 0.00 - 0.07$) with an R3c space group has fully formed [44]. The lack of a secondary phase indicates the effective incorporation of Ho^{3+} ions onto the host cell structure at $x = 0.00 - 0.05$. A minor defect phase (* mark) is present in $x = 0.07$; this could be the result of secondary phase development caused by an impurity produced during the procedure of synthesis. **Figure 5.2(b)** shows an expanded view of the most prominent peak migrating towards higher 2 theta angles corresponding to the Braggs plane (110). This shift in the peak indicates the possibility of incorporation of smaller Ho^{3+} ions (1.18 Å with coordination number 12) within the host matrix $\text{Bi}_{0.5}\text{Na}_{0.5}\text{TiO}_3$ at the Bi^{3+} site (1.32 Å with coordination number 12) [45]. The XRD profile fit of all the dopant concentrations was calculated using TOPAS software implementing Pawley refinement based on the method of least squares. By using this software, **Figure 5.2(c)** displayed the best match among the measured and expected XRD of the lattice parameter and

profile parameter deduced from the profile fit and tabulated in Table 5.1. The fit of goodness is approximately near one, indicating that the refining results are reliable. Table 5.1 shows that when the concentration of Ho^{3+} increases, the unit cell volume decreases due to size differences. This is consistent with the trend of the (110) plane towards larger 2 theta values. The density for all the prepared samples is estimated using Archimedes' principle. The density of the samples increases with the increasing dopant content, and there is good agreement in experimentally calculated density with the theoretical density (5.99 g/cm^3) that has been published [46].

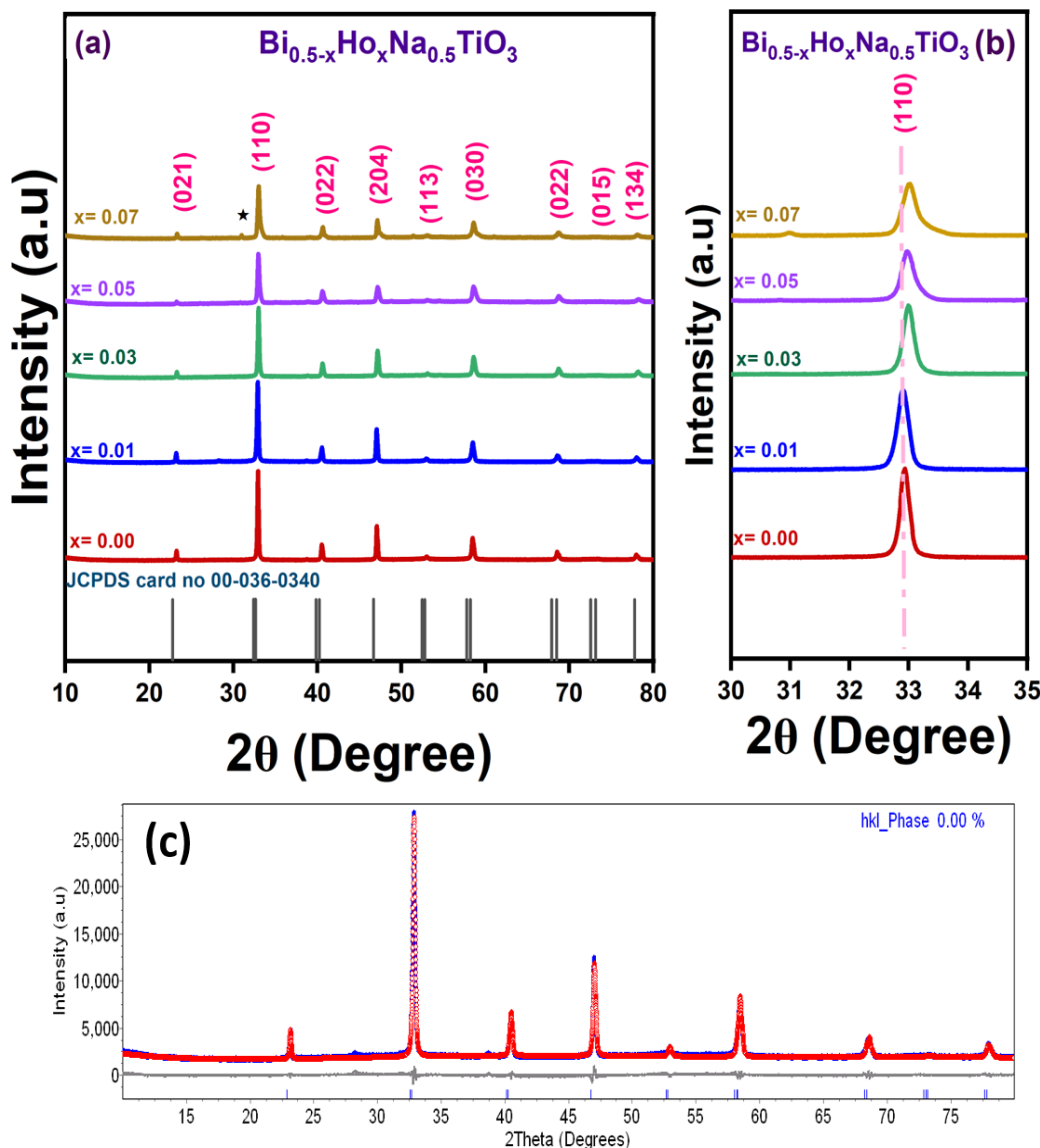


Figure 5.2: (a) XRD plot of undoped and Ho^{3+} doped BNT, (b) peak shifting of (110) plane, (c) profile fitting using topaz software

The microstructure and grain size of the sintered pellets surface of $\text{Bi}_{0.5-x}\text{Na}_0.5\text{TiO}_3$ doped with Ho^{3+} were recorded by scanning electron microscopy (SEM). **Figure 5.3(a-e)** reveals the microstructure details having a non-uniform distribution of grain size. Using Image J software, the histogram was plotted using the Lorentz fit plot to get the average grain size, which is depicted in the insets of **Figure. 5.3(a-e)**. The mean size of the grain has increased from a lower dopant concentration ($x = 0.00$) to a higher dopant concentration (0.07), illustrated in **Figure. 5.3(f)**. This grain growth behavior is due to the enhanced diffusion of foreign ions within the host during the sintering process. The foreign ions may facilitate mass transport by either forming point defects (such as oxygen vacancies) or altering the local lattice structure, which in turn promotes grain boundary mobility. As a result, the grains are able to grow more easily at higher dopant concentrations, leading to an overall increase in grain size [46].

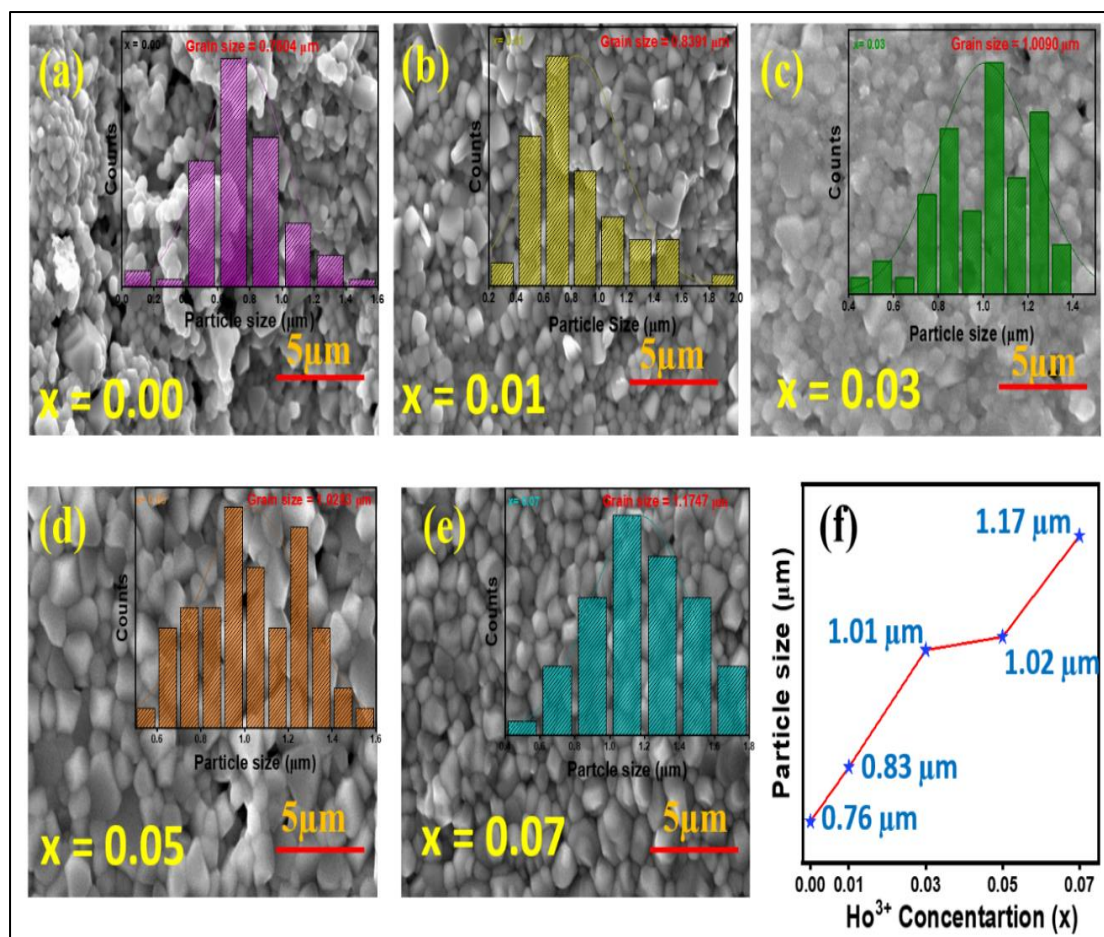


Figure. 5.3: (a-e) SEM of $\text{Bi}_{0.5-x}\text{H}_{0.0x}\text{Na}_0.5\text{TiO}_3$ ($x = 0.00 - 0.07$). Inset: Histograms for grain size calculation (f) variation of an average size of particles with dopant concentrations

Table 5.1: Parameters of XRD pattern for $\text{Bi}_{0.5-x}\text{Ho}_x\text{Na}_{0.5}\text{TiO}_3$ with different concentrations

Parameters	$\text{Bi}_{0.5-x}\text{Ho}_x\text{Na}_{0.5}\text{TiO}_3$				
	$x = 0.00$	$x = 0.01$	$x = 0.03$	$x = 0.05$	$x = 0.07$
R_{wp}	7.37	7.65	6.23	9.74	8.70
R_{exp}	3.62	3.52	3.50	4.39	3.01
$\text{GoF}(\chi)$	1.04	1.17	1.78	1.22	1.89
$a = b (\text{\AA})$	5.4967	5.4856	5.4963	54878	5.4620
$c (\text{\AA})$	6.7180	6.7411	6.7130	6.7054	6.7151
$V (\text{\AA}^3)$	175.7844	175.6820	175.6321	174.8899	173.4991
Density (g/cm³)	5.3050	5.3178	5.3221	5.5431	5.7301
Crystallite Size (nm)	131.6	118.8	102.2	70.5	49.0
Strain	0.2020	0.2249	0.2409	0.2511	0.2689

5.3.2 FTIR Spectroscopy

The IR bands for BNT ceramics were plotted in **Figure. 5.4(a)**. Four selected compositions of $\text{Bi}_{0.5-x}\text{Ho}_x\text{Na}_{0.5}\text{TiO}_3$ comprising undoped $\text{Bi}_{0.5}\text{Na}_{0.5}\text{TiO}_3$ (BNT), singly doped with Ho^{3+} dopant containing different contents ($x = 0.01 - 0.05$) were analyzed. The $400-2000 \text{ cm}^{-1}$ range was used to record the FTIR spectra. The vibrational bands detected at wave numbers 537 and 832 cm^{-1} correspond to the vibration band of $\text{Bi}_{0.5}\text{Na}_{0.5}\text{TiO}_3$. This study suggests that the absorption bands seen are caused by the stretching of Ti-O bonds inside the octahedral units present in the perovskite structure [47]. The shift in the FTIR bands at 832 cm^{-1} and 537 cm^{-1} is due to the Ho^{3+} ions in the host lattice is depicted in **Figure. 5.4(b)** [48].

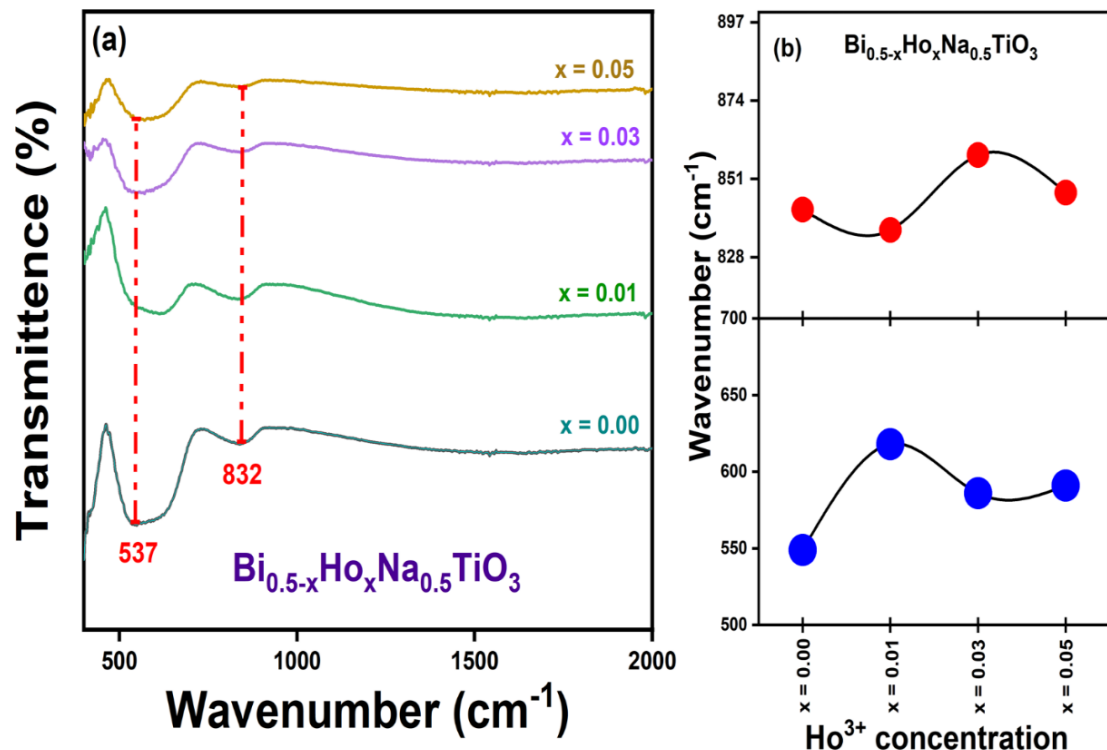


Figure 5.4: (a) FTIR spectra of pure and Ho³⁺ doped BNT ferroelectric ceramic, (b) shift in the FTIR bands

5.3.3 Diffuse Reflectance Spectra and Optical Band Gap

The UV-Vis DRS of Ho³⁺ doped in Bi_{0.5-x}Ho_xNa_{0.5}TiO₃ (x = 0.00, 0.03, 0.05, 0.07) noted in the range 200-1000 nm is depicted in Figure. 5.5(a). The ceramic has a high reflectivity in the visible light spectrum, ranging from 450-800 nm. The bands at 454, 542, and 646 nm appear via transition from ⁵I₈ → ⁵G₆, ⁵I₈ → ⁵F₄ / ⁵S₂, and ⁵I₈ → ⁵F₅, respectively. The optical band gap (E_g in eV) was calculated using the Kubelka-Munk (K-M) function by Eq. 5.3 [49]:

$$F(R) = \frac{(1-R)^2}{2R} = \frac{K}{S} \quad (5.3)$$

The absorption coefficient is denoted by K, the scattering coefficient by S, and the total reflectance of a specimen by R. Additionally, we assume S is constant to wavelength for diffused light. The Tauc plot equation can be related to F(R) and can be represented by the following Eq. 5.4 [50]:

$$(F(R)hv) = B(hv - E_g)^n \quad (5.4)$$

where B is the energy-independent constant of proportionality, ν is the vibrational frequency of incoming light, and h stands for Planck's constant. E_g represents the band gap, while n indicates the electronic transition. The value of n can be $1/2$ and 2 for direct and indirect allowed transition, respectively. In **Figure. 5.5(b-e)**, the band gap values from a plot of $[F(R)h\nu]^2$ vs $h\nu$ are displayed. According to the published literature, the results obtained for the band gap of BNT ($E_g = 3.00$ eV) are consistent [51]. The optical band gap value for the ceramics varies as we increase the Ho^{3+} content from ($x = 0.00$ to 0.07) and it can be seen maximum at 0.03 concentration. The fluctuations in the band gap are because of the produced oxygen vacancies and the local structural instability within the lattice, which develops when smaller Ho^{3+} ions are added to the Bi^{3+} sites and modify the electron density [52]. The intensity of photoluminescence is increased when there is a reduced band gap value because more ions are excited.

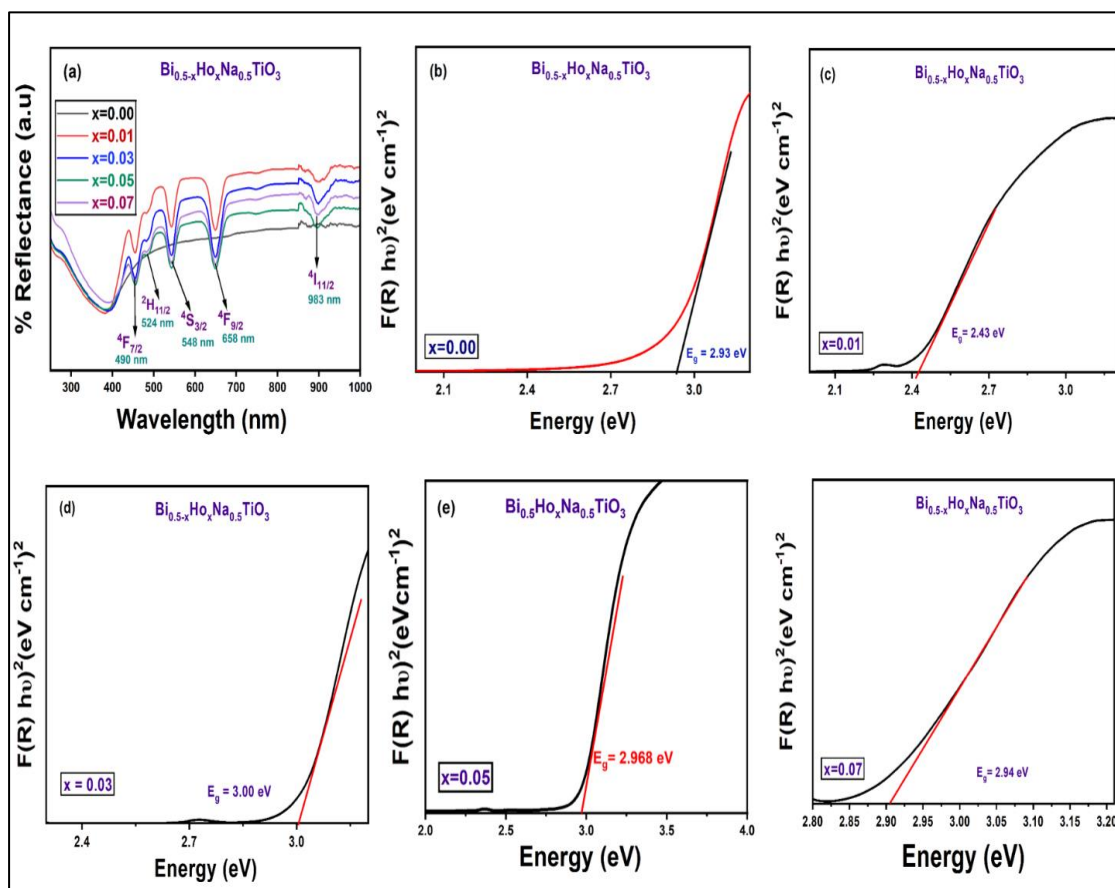


Figure 5.5: (a) DRS of pure and Ho^{3+} doped BNT, (b-e) energy band gap of $\text{Bi}_{0.5-x}\text{H}_{\text{x}}\text{Na}_{0.5}\text{TiO}_3$ ($x = 0.00, 0.01, 0.03, 0.05, 0.07$)

5.3.4 Photoluminescence Spectra

At 550 nm emission, the excitation spectra are recorded for all the Ho^{3+} doped BNT ceramics, as displayed in **Figure 5.6(a)**. The spectra showed four distinct excitation peaks attributed to the 4f-4f transition of the Ho^{3+} ions. The excitation peaks at 418 nm, 452 nm, 469 nm, 476 nm, and 489 nm are transit from the ground state ${}^5\text{I}_8$ to various energy states such as ${}^5\text{G}_5$, ${}^5\text{G}_6$, ${}^3\text{K}_8$, ${}^5\text{F}_2$, and ${}^5\text{F}_3$, respectively [53,54]. It has been observed from the excitation spectra that the 452 nm has the strongest intensity, so this excitation wavelength is considered for the evaluation of emission spectra of Ho^{3+} doped BNT ceramic, which is given in **Figure 5.6(b)**. A strong green band is visible at 548 nm via the transition of Ho^{3+} ions from ${}^5\text{F}_4 / {}^5\text{S}_2$ to ground state ${}^5\text{I}_8$. There are two relatively weak bands at 655 nm and 755 nm, which are observed via the transition of ions from levels ${}^5\text{F}_5$ to ${}^5\text{I}_8$ and ${}^5\text{S}_2$ to ${}^5\text{I}_7$. The onset of **Figure 5.6(b)** displayed the highest emission intensity corresponding to Ho^{3+} concentration $x = 0.03$; after this concentration of Ho^{3+} , the intensity decreases because of the non-radiative transition due to concentration quenching [55]. **Figure 5.6(c)** depicts the CIE graph of Ho^{3+} doped BNT ceramic. It can be seen that the samples exhibit a green color when excited with 452 nm.

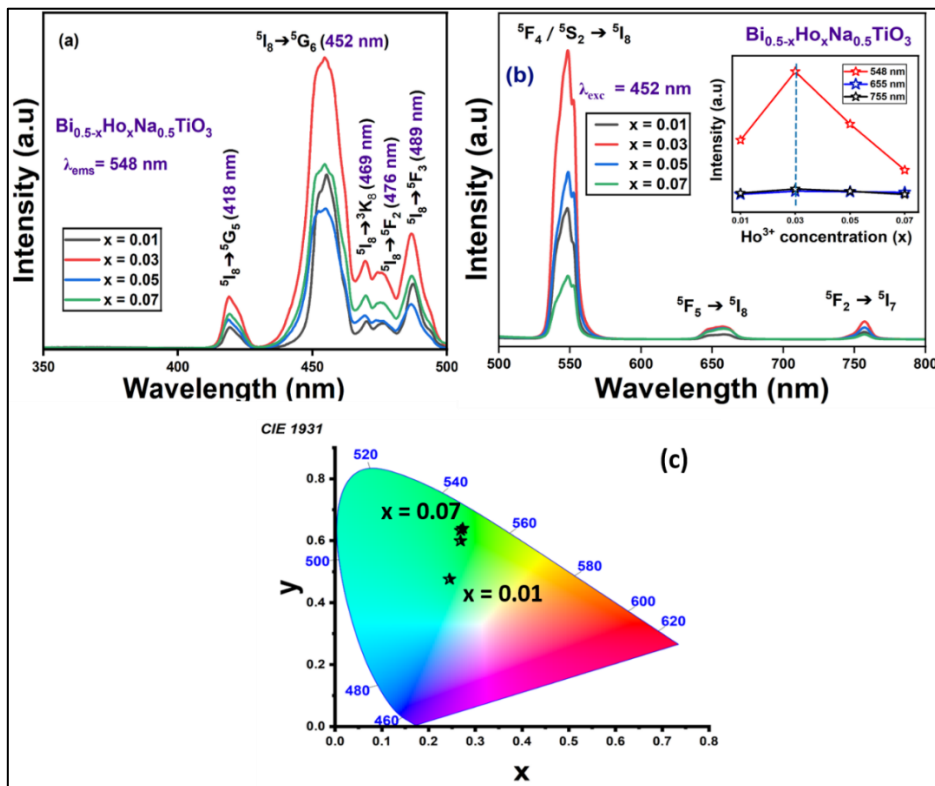


Figure 5.6: (a) Excitation spectra of Ho^{3+} doped BNT at 550 nm emission wavelength, (b) emission spectra of Ho^{3+} doped BNT at 452 nm excitation wavelength, (c) CIE plot

5.3.5 Upconversion Luminescence Spectra

The upconversion luminescence (UCL) plot for $\text{Bi}_{0.5-x}\text{Ho}_x\text{Na}_{0.5}\text{TiO}_3$ ceramic is detected under the excitation of 980 nm and is given in **Figure. 5.7(a)**. The four emission wavelengths were obtained at 490 nm, 525 nm, 551 nm, and 660 nm via transition through energy levels $^5\text{F}_3$, $^5\text{F}_4$, $^5\text{S}_2$, and $^5\text{F}_5$ to the lower energy level $^5\text{I}_8$, respectively [56]. One weak blue emission band via the $^5\text{F}_3$ to $^5\text{I}_8$ level, two visible green bands via $^5\text{F}_4/^5\text{S}_2$ to $^5\text{I}_8$, and one highly intense orange band via the transition of ions from the $^5\text{F}_5$ to $^5\text{I}_8$ level. From PL spectra, the green emission band has higher intensity, whereas, in the case of UCL spectra, the orange emission band dominates. This is because of the various UCL mechanisms taking place during the UCL process, such as ground state absorption (GSA), excited state absorption (ESA), energy transfer process (ET), multiple phonon relaxations (MPR), and cross-relaxation (CR) which increase the efficacy of the UCL. **Figure. 5.7(b)** demonstrates that the highest peak intensity for various Ho^{3+} doping is maximum for $x = 0.03$. After this concentration, the UCL intensity decreases because the dopant ions become so close to each other that they start exchanging energy between them without any discomfort. This ease in energy transfer between the dopant ions leads to non-radiative radiation, hence decreasing the UCL intensity. This effect is called concentration quenching [57]. Reduction in the emission intensity is due to the non-radiative transitions. The Blasse equation, represented as Eq. 5.5, is commonly employed to estimate the critical distance between dopant ions [58]:

$$R_c \approx 2 \left[\frac{3V}{4\pi x_c Z} \right]^{\frac{1}{3}} \quad (5.5)$$

here, $V = 175.632 \text{ \AA}^3$ (unit cell volume), $Z = 3$ (host cation), and $x_c = 0.03$ (quenched concentration). Putting these values, R_c comes to be 9.7686 \AA . The expected UCL pathway is given where the ions in the ground state $^5\text{I}_8$ absorb photons from the 980 nm illuminating wavelength and reach the higher energy level $^5\text{I}_5$ via GSA, as shown in **Figure. 5.7(c)**. From level $^5\text{I}_5$, it goes to higher level $^5\text{F}_3$, and some of the ions transit back to $^5\text{I}_6$ and $^5\text{I}_7$ and reach higher levels by ESA. The CR processes are taking place to pollute the higher energy levels. From higher energy level $^5\text{F}_3$, the ions non-radiatively fall to the levels $^5\text{F}_4$, $^5\text{S}_2$, and $^5\text{F}_5$ through the MPR process. The ions from level $^5\text{F}_3$ to $^5\text{I}_8$ emit a blue band, and ions from $^5\text{F}_4/^5\text{S}_2$ levels to ground state $^5\text{I}_8$ emit

two green emission bands. The ions from 5F_5 to 5I_8 result in an orange UCL band, and ions from 5S_2 to 5I_7 result in a red emission band. **Figure. 5.7(d)** depicts the CIE plot of Ho^{3+} doped BNT. It has been observed that the Ho^{3+} doped BNT ceramic showed orange emission intensity when excited through 980 nm wavelength. The difference in emission color between PL and UCL primarily arises from the nature of the excitation and the resulting energy transfer mechanisms involved in each process. In PL, a single high-energy photon excites the ion directly to a higher energy level. This leads to efficient green emission because these transitions have high quantum efficiency and fewer energy losses. Whereas in UCL, multiple photon absorption takes place and often leads to non-radiative relaxations and follows different cross relaxation paths to populate the higher excited states resulting in orange or red emission instead of green.

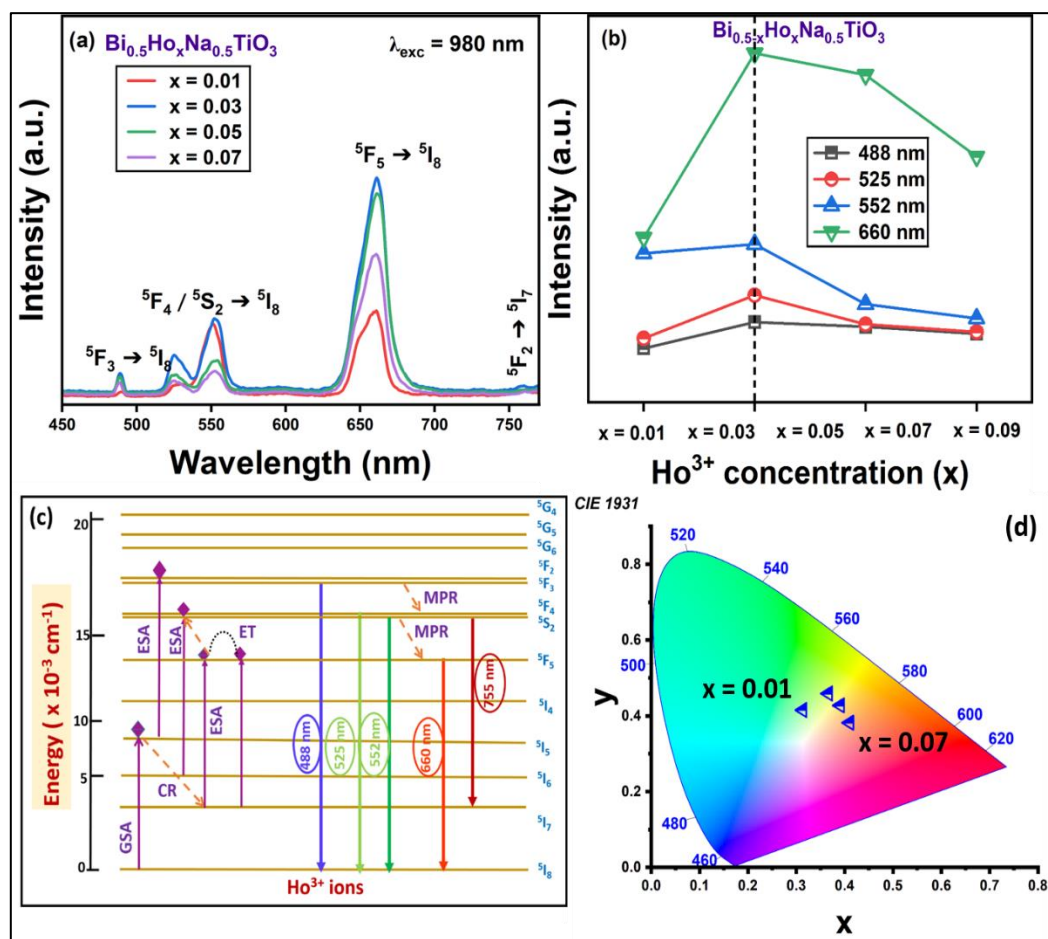


Figure 5.7: (a) UCL spectra of Ho^{3+} doped BNT ceramic at 550 nm emission wavelength, (b) comparison of UCL intensity of various Ho^{3+} doped BNT ceramic, (c) energy levels of Ho^{3+} ions for possible UC process, (d) CIE plot

5.3.6 Time Decay Measurements

The time-dependent UCL spectra are traced by a pulsed laser source under 980 nm. The time decay profile for Ho^{3+} doped BNT ceramic for green and orange emission bands is given in **Figure. 5.8(a-e)** and **Figure. 5.9(a-e)**, respectively. A tri-exponential fit is used to calculate the decay time of the doped samples, given by **Eq. 5.6**, where A_1 , A_2 , and A_3 are the variables, τ is decay time, I_0 is the intensity at $t = 0\text{s}$, and $I(t)$ is the intensity at t , and. **Eq. 5.7** gives the average lifetime [50, 57]:

$$I(t) = I_0 + A_1 \exp\left(-\frac{t}{\tau_1}\right) + A_2 \exp\left(-\frac{t}{\tau_2}\right) + A_3 \exp\left(-\frac{t}{\tau_3}\right) \quad (5.6)$$

$$\langle \tau \rangle = \frac{A_1 \tau_1^2 + A_2 \tau_2^2 + A_3 \tau_3^2}{A_1 \tau_1 + A_2 \tau_2 + A_3 \tau_3} \quad (5.7)$$

The lifetime of green bands of Ho^{3+} doped BNT ceramic ranges from $15.60\text{ }\mu\text{s}$ to $10.30\text{ }\mu\text{s}$, whereas, for orange emission bands, it varies from $6.21\text{ }\mu\text{s}$ to $12.65\text{ }\mu\text{s}$. This implies that in the orange emission bands, the dopant ions are quickly transferring their energy to the neighboring ions, which results in an intense orange UCL band as compared to green UC emission bands.

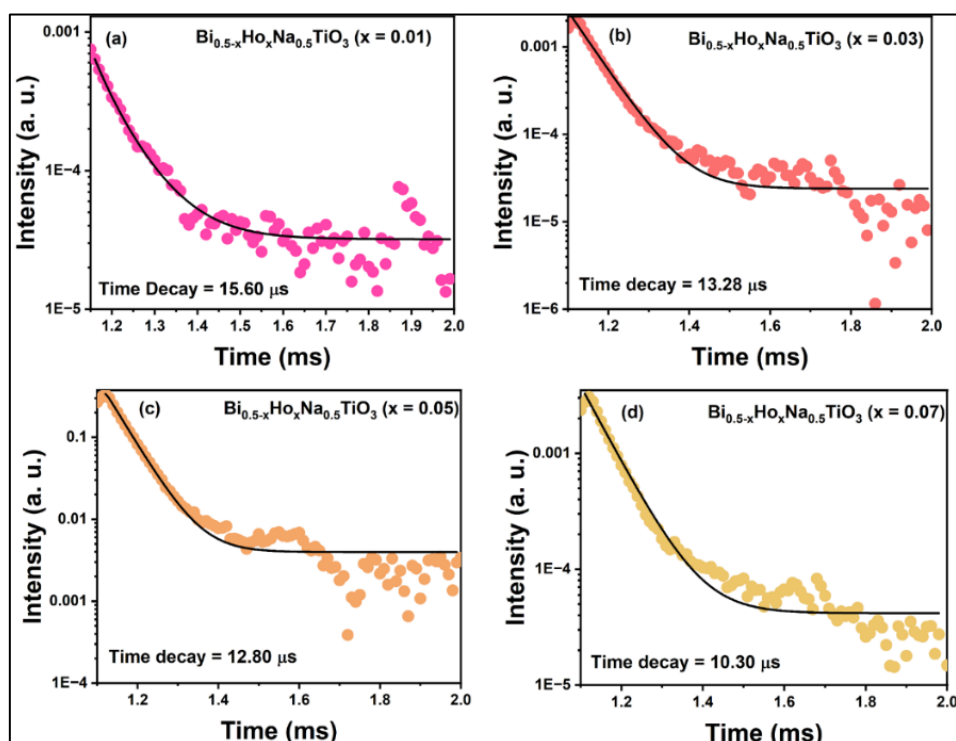


Figure 5.8: (a-e) Time decay of green band for Ho^{3+} doped BNT ceramics

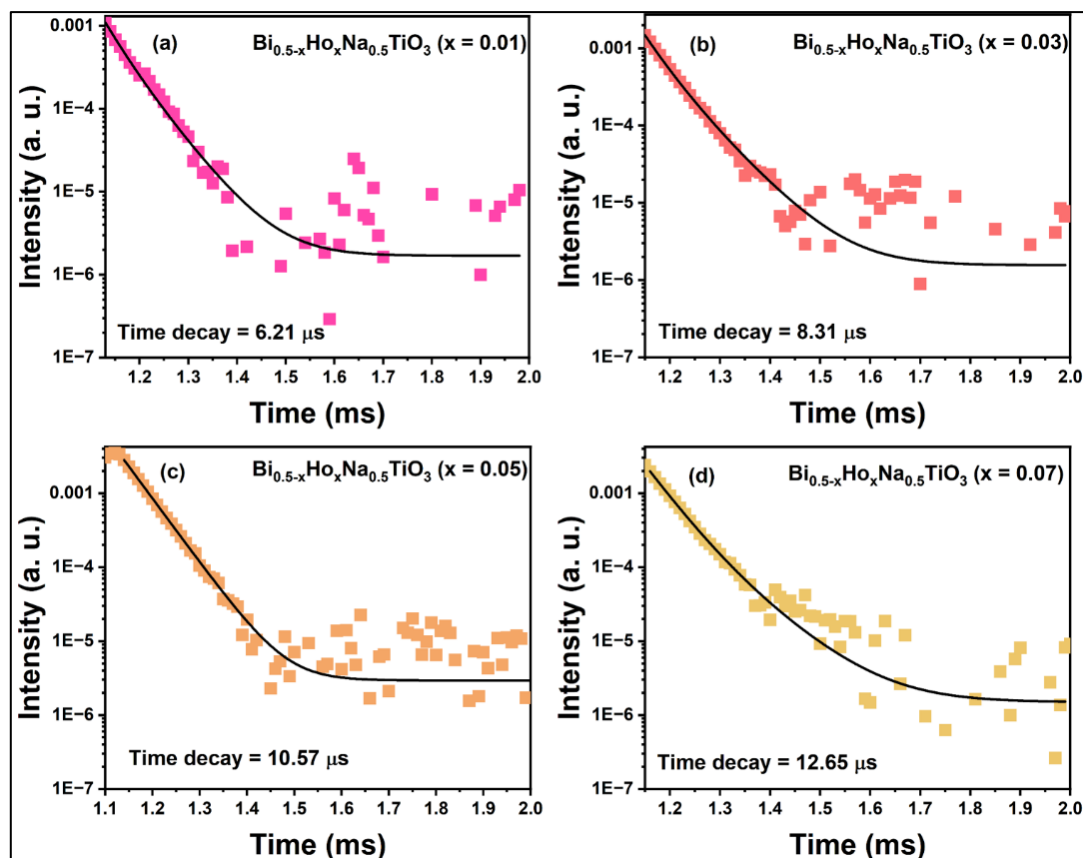


Figure 5.9: (a-e) Time decay of orange band for Ho^{3+} doped BNT ceramics

5.3.7 Pump Power Analysis

The UCL spectra for Ho^{3+} doped $\text{Bi}_{0.5-x}\text{H}_{ox}\text{Na}_{0.5}\text{TiO}_3$ ($x = 0.03$) ceramic is tested for various pump powers ranging from 0.30 mW to 0.81 mW. The pump power-dependent UCL spectra are displayed in **Figure. 5.10**. It has been seen that with the rising power of pumping, the intensity of UCL spectra is increasing, which agrees with the verified **Eq. 5.8** [59]:

$$I_{\text{UCL}} \propto P^n \quad (5.8)$$

In the above equation, the symbol P (pump power), n (no. of photons), and I_{UCL} is the emission intensity. This process helps to measure the total number of photons involved in the UCL mechanism. The log-log plot of intensity versus the pumping power is given in the inset of **Figure. 5.10**. For green bands (524 and 552 nm) and orange band (660 nm), n is approximately 2.17, 2.74, and 2.98. This confirms the involvement of two photons or more than two photons in the UC emission intensity [60].

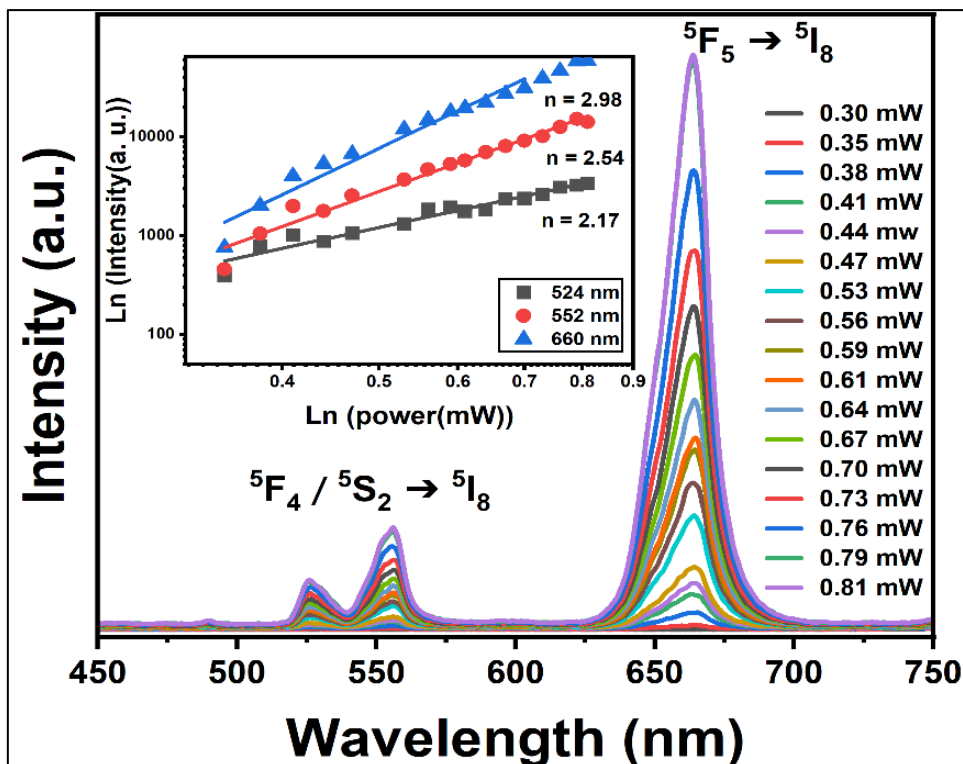


Figure. 5.10: Pump power dependency on UCL spectra and log-log plot (Inset)

5.3.8 Ferroelectric Curve and Energy Storage Density

The ferroelectric behavior of Ho^{3+} doped and undoped BNT ceramics is illustrated in Figure. 5.11(a). The polarization electric field (P-E) curves were recorded at room temperature under an applied electric field of 50 kV/cm. The undoped BNT ceramic exhibits a typical ferroelectric hysteresis loop, which is characteristic of conventional ferroelectric materials. However, with increasing Ho^{3+} doping concentration, the shape of the hysteresis loops begins to evolve, displaying features consistent with relaxor ferroelectric behavior with slimmer loops and reduced remanent polarization (P_r) values. This transformation can be attributed to the formation of oxygen vacancies induced by the incorporation of Ho^{3+} ions into the BNT lattice. Under an applied electric field, these oxygen vacancies migrate toward the domain walls, inhibiting domain switching and thereby reducing the remanent polarization. This behavior is further corroborated by XRD patterns and SEM micrographs, which reveal an increase in average grain size with higher Ho^{3+} content. The increase in grain size may also contribute to the observed reduction in

P_r values [61]. The measured P_r and P_m (maximum polarization) values were further utilized to evaluate the energy storage performance of the ceramics using the following equations [62].

$$W = \int_0^{P_m} EdP \quad (5.9)$$

$$W_{rec} = \int_{P_r}^{P_m} EdP \quad (5.10)$$

$$\eta = \frac{W_{rec}}{W} \times 100\% \quad (5.11)$$

Figure. 5.11(b) presents the variation in energy storage performance among the various Ho^{3+} doped BNT samples compared to the undoped BNT ceramic under the same electric field (50 kV/cm). The undoped BNT exhibits the highest energy density but the lowest efficiency. With increasing Ho^{3+} doping, a significant improvement in energy storage efficiency is observed, reaching a maximum of 89%. These findings suggest that achieving a lower P_r and a higher P_m is crucial for enhanced energy storage performance. Consequently, Ho^{3+} doping in BNT ceramics emerges as a promising strategy for optimizing materials for energy storage applications. The performance of the PE loop and energy storage density parameters has been summarized in Table 5.2.

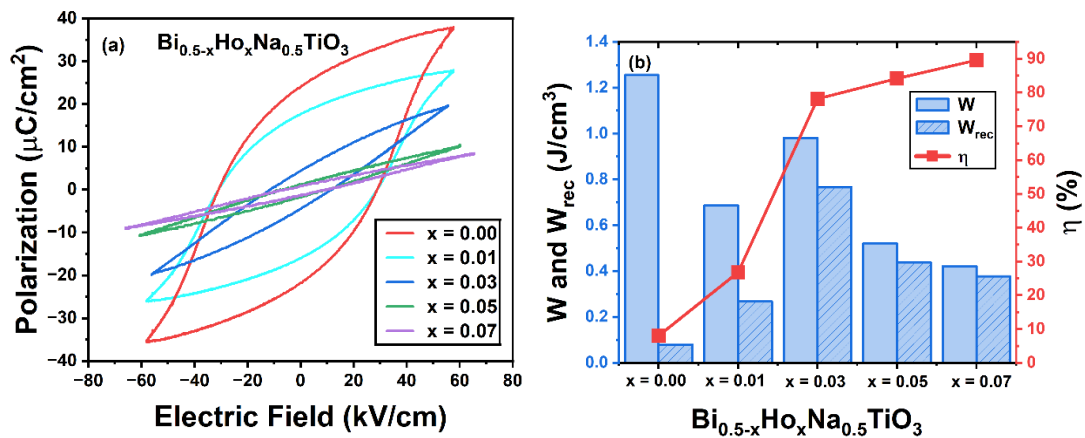
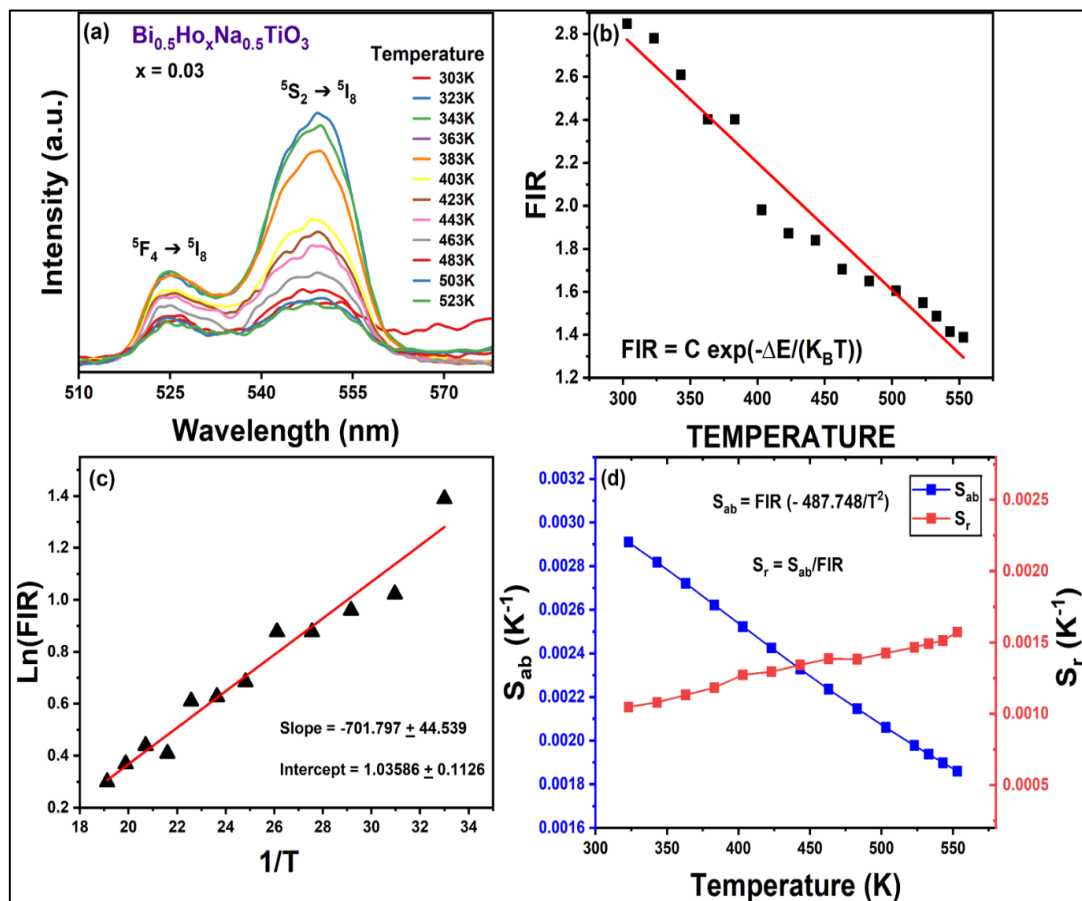


Figure 5.11: (a) PE loops for undoped and doped BNT, (b) variation of energy storage density parameters

Table 5.2: Summary of PE loop parameters ($2P_r$, $2E_c$) and energy storage density parameters (W , W_{rec} , $\eta\%$)

$\text{Bi}_{0.5-x}\text{Ho}_x\text{Na}_{0.5}\text{TiO}_3$	$2P_r$ ($\mu\text{C}/\text{cm}^2$)	$2E_c$ (kV/cm)	W (J/cm 3)	W_{rec} (J/cm 3)	η (%)
$x = 0.00$	46.19	50.22	1.255	0.101	8.01
$x = 0.01$	33.54	45.80	0.687	0.184	26.77
$x = 0.03$	8.58	39.24	0.981	0.767	78.13
$x = 0.05$	3.30	20.84	0.521	0.439	84.17
$x = 0.07$	1.76	16.86	0.421	0.378	89.56

5.3.9 Optical Temperature Sensing

**Figure 5.12: (a) Variation of UCL spectra with T, (b) FIR vs. temperature plot, (c) plot of $\text{Ln}(\text{FIR})$ against T^{-1} , (d) variation of S_{ab} and S_r with T**

The sensing behavior of the BNT ($x = 0.03$) ceramic was analyzed using the fluorescence intensity ratio (FIR) technique, which is a widely adopted approach for assessing temperature sensitivity in various rare-earth (RE) ion-doped host materials.

Figure. 5.12(a) presents the upconversion luminescence (UCL) spectra recorded between 303-553 K. The UCL strength decreases as the temperature increases due to thermal population redistribution between thermally coupled levels (TCLs). The FIR is expressed by Eq 5.12:

$$\text{FIR} = \frac{I_1}{I_2} = C \exp\left(-\frac{\Delta E}{K_B T}\right) \quad (5.12)$$

Here, I_1 and I_2 represent the emission intensities at 525 and 550 nm, respectively. ΔE signifies the energy gap between the TCLs, C is a pre-exponential factor, and k_B is Boltzmann's constant. The variation of FIR with temperature is illustrated in **Figure. 5.12(b)**. The logarithmic form of Eq. 5.12 is provided in Eq. 5.13:

$$\ln(\text{FIR}) = -\left(\frac{\Delta E}{K_B}\right)\left(\frac{1}{T}\right) + \ln C \quad (5.13)$$

This linear relationship is demonstrated in **Figure. 5.12(c)**, where the slope and intercept of the plot correspond to $\Delta E/K_B$ and $\ln C$, respectively. These values are crucial for evaluating both absolute sensitivity (S_{ab}) and relative sensitivity (S_r) of the material, as defined by Eq. 5.14 and 5.15:

$$S_{ab} = \frac{d(\text{FIR})}{dT} = \frac{d\left(C \exp\left(-\frac{\Delta E}{K_B T}\right)\right)}{dT} = C \exp\left(-\frac{\Delta E}{K_B T}\right) \left(\frac{\Delta E}{K_B T^2}\right) \quad (5.14)$$

$$S_r = \frac{1}{\text{FIR}} * S_{ab} = \left(\frac{\Delta E}{K_B T^2}\right) \quad (5.15)$$

Figure. 5.12(d) illustrates the variation of S_{ab} and S_r with temperature. The maximum absolute sensitivity observed for the BNT ($x = 0.03$) ceramic composition is $0.29\% \text{ K}^{-1}$ at 303 K, while the peak relative sensitivity reaches $0.22\% \text{ K}^{-1}$ at 303 K. To assess the practical applicability of a sensor, it is essential to evaluate its repeatability and resolution. The FIR values of the BNT ($x = 0.03$) ceramic were measured between 303-553 K. As presented in **Figure. 5.13(a)**, the FIR values exhibited a smooth and consistent variation across the temperature range without any abrupt fluctuations, indicating the good repeatability of the material. The repeatability (R) and temperature resolution (δT) of the sensor can be quantitatively evaluated using the specific FIR

value (Δ_{sp}), mean FIR value (Δ_m), average FIR value (Δ_{Av}), and the instrumental accuracy (δ_Δ/Δ). The corresponding expressions are provided in Eq. 5.16 and 5.17:

$$R = 1 - \frac{(\Delta_m - \Delta_{sp})}{\Delta_{Av}} \quad (5.16)$$

$$\delta T = \frac{1}{S_r} \times \frac{\delta_\Delta}{\Delta} \quad (5.17)$$

Figure. 5.13(b) demonstrates that the temperature resolution decreases with rising temperature, suggesting enhanced performance near room temperatures.

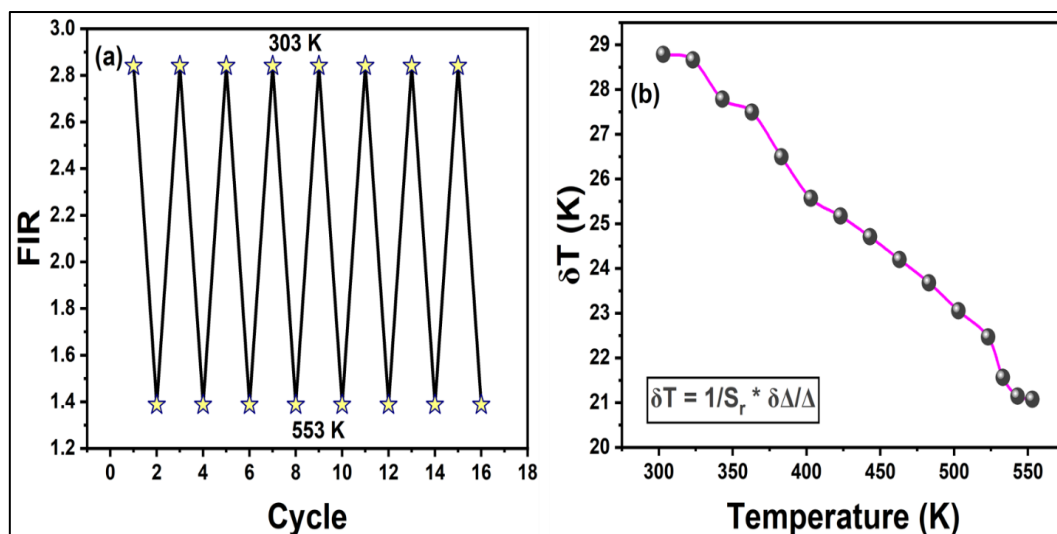


Figure. 5.13: (a) Repeatability test between 303K and 553K, (b) plot of δT vs temperature

5.4 Summary

In this study, Ho^{3+} ions were successfully incorporated into the A-site of $\text{Bi}_{0.5-x}\text{Ho}_x\text{Na}_{0.5}\text{TiO}_3$ ceramics using the solid-state method. Structural characterization through XRD confirmed the formation of a pure rhombohedral perovskite phase with an R3c space group without the presence of secondary phases. FTIR analysis supported the integrity of the perovskite structure by revealing characteristic Ti–O bond vibrations. The optical absorption study using DRS indicated strong f–f transitions of Ho^{3+} ions and a slight reduction in bandgap energy, attributed to the creation of oxygen vacancies and local structural distortions caused by Ho^{3+} doping. Photoluminescence measurements under 452 nm excitation revealed a prominent green emission at 548 nm, along with weaker red emissions at 655 nm and 750 nm. The UCL spectra under 980

nm excitation exhibited multiple emission bands, with the emission at 660 nm being significantly more intense than the green and blue emissions. The optimized composition ($x = 0.03$) showed strong pump power-dependent behavior and demonstrated efficient energy transfer processes, as evident from the calculated average lifetimes of $12.99 \mu\text{s}$ for green and $9.43 \mu\text{s}$ for orange emissions. The PE loops become slimmer, and P_r values decrease with increasing concentration. The energy storage efficiency ($\eta\%$) of the prepared ceramic is increasing with dopant concentration and comes out to be around 90%. The maximum absolute sensitivity and relative sensitivity observed for the BNT ($x = 0.03$) is $0.29\% \text{ K}^{-1}$ and $0.22\% \text{ K}^{-1}$ at 303 K, respectively. These findings suggest that Ho^{3+} doped BNT ceramics possess favorable structural and optical properties, making them promising candidates for use in optoelectronic and photonic applications, particularly in visible light-emitting devices and upconversion-based technologies.

In conclusion, this chapter demonstrates that the incorporation of Ho^{3+} ions into the $\text{Bi}_{0.5-x}\text{Ho}_x\text{Na}_{0.5}\text{TiO}_3$ lattice resulted in notable improvements in luminescence, sensing capability, and energy storage efficiency, reflecting a balanced multifunctional response. These findings provide a clear basis for the next chapter, which will examine the role of thin-film processing in further tailoring the structural and functional attributes of $\text{Bi}_{0.5-x}\text{Na}_{0.5}\text{TiO}_3$ ceramics for potential use in advanced device applications.

5.5 References

- [1] M. Li, M.J. Pietrowski, R.A.D Souza, H. Zhang, I.M. Reaney, S.N. Cook, J. A. Kilner, D.C. Sinclair, A family of oxide ion conductors based on the ferroelectric perovskite $\text{Na}_{0.5}\text{Bi}_{0.5}\text{TiO}_3$, *Nat. Mater.* 13 (2014) 31-35, <https://doi.org/10.1038/NMAT3782>
- [2] M.H. Lee, D.J. Kim, J.S. Park, S.W. Kim, T.K. Song, M.-H. Kim, W.-J. Kim, D. Do, I.- K. Jeong, High-performance lead-free piezoceramics with high curie temperatures, *Adv. Mater.* 27 (2015) 6976–6982, <https://doi.org/10.1002/adma.201502424>
- [3] D.K. Khatua, A. Kalaskar, R. Ranjan, Tuning photoluminescence response by electric field in electrically soft ferroelectrics, *Phys. Rev. Lett.* 116 (2016) 117601, <https://doi.org/10.1103/physrevlett.116.117601>
- [4] J-K. Lee, A. Nande, A. A. Bhat, S. Watanabe, T.K. G. Rao, V. Singh, Synthesis, structural, photoluminescence, and EPR analysis of far red emitting $\text{Ca}_3\text{La}_2\text{W}_2\text{O}_{12}:\text{Mn}^{4+}$ inorganic phosphor for applications in plant-growth LEDs, *Ceram. Int.* 50 (10) (2024) 17063-17074, <https://doi.org/10.1016/j.ceramint.2024.02.183>
- [5] M. Varshney, S. Soni, A. Banwal, M. Narwan, M. Verma, R. Bokolia, Effect of Er^{3+} ion incorporation on the structural, photoluminescence, and ferroelectric properties of $\text{K}_{0.5}\text{Na}_{0.5}\text{NbO}_3$ ceramic for optoelectronic applications, *Appl. Phys. A* 130 (2024) 267. <https://doi.org/10.1007/s00339-024-07447-1>
- [6] D.K. Khatua, A. Agarwal, R. Ranjan, Investigating the electrical conduction and relaxation phenomena in rare earth erbium doped lead free $0.94\text{Na}_{0.5}\text{Bi}_{0.5}\text{TiO}_3-0.06\text{BaTiO}_3$ by impedance spectroscopy, *J. Appl. Phys.* 123 (2018) 07410, <http://doi.org/10.1063/1.4999032>
- [7] A. Gallegos-Melgar, D.G. Espinosa-Arbelaez, F.J. Flores-Ruiz, A. Lahmar, J.-L. Dellis, N. Lemée, F.J. Espinoza-Beltran, J. Munoz-Saldana, Ferroelectric properties of manganese doped $(\text{Bi}_{1/2}\text{Na}_{1/2})\text{TiO}_3$ and $(\text{Bi}_{1/2}\text{Na}_{1/2})\text{TiO}_3-\text{BaTiO}_3$ epitaxial thin films, *Appl. Surf. Sci.* 359 (2015) 923-930, <https://doi.org/10.1016/j.apsusc.2015.09.175>

[8] A.B. Kounga, S.-T. Zhang, W. Jo, T. Granzow, J. R'' Model, Morphotropic phase boundary in $(1-x)Bi_{0.5}Na_{0.5}TiO_3-xK_{0.5}Na_{0.5}NbO_3$ lead-free piezoceramics, *Appl. Phys. Lett.* 92 (2008) 222902. <https://doi.org/10.1063/1.2938064>

[9] J. Yao, N. Monsegue, M. Murayama, W. Leng, W.T. Reynolds, Q. Zhang, H. Luo, J. Li, W. Ge, D. Viehland, Role of coexisting tetragonal regions in the rhombohedral phase of $Na_{0.5}Bi_{0.5}TiO_3$ -xat.% $BaTiO_3$ crystals on enhanced piezoelectric properties on approaching the morphotropic phase boundary, *Appl. Phys. Lett.* 100 (2012), 012901, <https://doi.org/10.1063/1.3673832>

[10] R. Roukos, S.A. Dargham, J. Romanos, F. Barakat, D. Chaumont, Complex structural contribution of the morphotropic phase boundary in $Na_{0.5}Bi_{0.5}TiO_3$ - $CaTiO_3$ system, *Ceram. Int.* 45 (2019) 4467-4473, <https://doi.org/10.1016/j.ceramint.2018.11.126>

[11] L.T.H. Thanh, N.B. Doan, N.Q. Dung, L.V. Cuong, L.H. Bac, N.A. Duc, P.Q. Bao, D.D. Dung, Origin of room temperature ferromagnetism in Cr-doped lead-free ferroelectric $Bi_{0.5}Na_{0.5}TiO_3$ materials, *J. Electron. Mater.* 46 (2017) 3367-3372. <https://doi.org/10.1007/s11664-016-5248-0>

[12] M. Zannen, A. Lahmar, M. Dietze, H. Khemakhem, A. Kabadou, M. Es-Souni, Structural, optical, and electrical properties of Nd-doped $Na_{0.5}Bi_{0.5}TiO_3$, *Mater. Chem. Phys.* 134 (2-3) (2012) 829-833. <https://doi.org/10.1016/j.matchemphys.2012.03.076>

[13] A. Mishra, B. Majumdar, R. Ranjan, A complex lead-free $(Na, Bi, Ba)(Ti, Fe)O_3$ single phase perovskite ceramic with a high energy-density and high discharge efficiency for solid state capacitor applications, *J. Eur. Ceram. Soc.* 37 (2017) 2379-2384, <http://doi.org/10.1016/j.jeurceramsoc.2017.01.036>

[14] A. A. Bhat, W. Bi, A. S. Ganie, S. A. Sofi, R. Tomar, H. S. M. Abd-Rabboh, and I. S. Syed, Europium Doped $SrSnO_3$ Perovskite: Structural, Spectroscopic, and Luminescent Characterization for Advanced Lighting Technologies and Beyond, *Energy & Fuels*, 38 (2024), 23726-23740, <https://doi.org/10.1021/acs.energyfuels.4c04141>

[15] T. Mearaj, A. Farooq, A. K. Hafiz, M. Khanuja, R. A. Zargar, and A. A. Bhat, Hydrothermal Synthesis and Characterization of WSe₂ Nanosheets: A Promising Approach for Wearable Photodetector Applications, *ACS Appl. Bio Mater.* 7, 2024, 3483-3495, <https://doi.org/10.1021/acsabm.4c00384>

[16] J-K. Lee, A. A. Bhat, A. Nande, S. Watanabe, T.K. Gundu Rao, V. Singh, Optimized Mn⁴⁺ doped Sr₉Y₂W₄O₂₄ perovskite for enhanced far-red-emitting luminescent material, *J.Ceram. Int.*, 50 (18) A (2024) 32978-32988, <https://doi.org/10.1016/j.ceramint.2024.06.112>

[17] E. Heumann, S. Bär, K. Rademaker, G. Huber, S. Butterworth, A. Diening, W. Seelert, Semiconductor-laser-pumped high-power upconversion laser, *Appl. Phys. Lett.* 88 (2006) 061108. <https://doi.org/10.1063/1.2172293>

[18] C.S. Devi, G.S. Kumar, G. Prasad, Control of ferroelectric phase transition in nanoparticulate NBT-BT based ceramics, *Mater. Sci. Eng. B Solid-State Mater. Adv. Technol.* 178 (2013) 283-292, <https://doi.org/10.1016/j.mseb.2012.12.001>

[19] M. Muneeswaran, B.C. Choi, S.H. Chang, J.H. Jung, Effect of dysprosium doping on structural and vibrational properties of lead-free (Na_{0.7}K_{0.3})_{0.5}Bi_{0.5}TiO₃ ferroelectric ceramics, *Ceram. Int.* 43 (2017) 13696-13701, <https://doi.org/10.1016/j.ceramint.2017.07.081>

[20] V. Singh, A. A. Bhat, M. Radha, M. Seshadri, S. H. Nandyalad and J. B. Joo, Investigation on structure and photoluminescence properties of Ho³⁺ doped Ca₃(VO₄)₂ phosphors for luminescent devices, *RSC Adv.*, 14, 2024, 18777, <https://doi.org/10.1039/D4RA03178D>

[21] Y. Hiruma, Y. Watanabe, H. Nagata, T. Takenaka, Phase transition temperatures of divalent and trivalent ion substituted (Bi_{1/2}Na_{1/2})TiO₃ ceramics, *Key. Eng. Mater.* 350 (2007) 93-96, <https://doi.org/10.4028/0-87849-449-9.93>

[22] C. Xu, D. Lin, K.W. Kwok, Structure, electrical properties and depolarization temperature of (Bi_{0.5}Na_{0.5})TiO₃-BaTiO₃ lead-free piezoelectric ceramics, *Solid State Sci.* 10 (2008) 934-940, <https://doi.org/10.1016/j.solidstatesciences.2007.11.003>

[23] S. Chen, M. Wu, L. An, Y. Li, S. Wang, Strong green and red upconversion

emission in Er^{3+} -doped $\text{Na}_{1/2}\text{Bi}_{1/2}\text{TiO}_3$ Ceramics, *J. Am. Ceram. Soc.* 90 (2) (2007) 664-666. <https://doi.org/10.1111/j.1551-2916.2006.01457.x>

[24] P. Du, L. Luo, W. Li, Q. Yue, H. Chen, Optical temperature sensor based on upconversion emission in Er-doped ferroelectric $0.5\text{Ba}(\text{Zr}_{0.2}\text{Ti}_{0.8})\text{O}_3$ - $0.5(\text{Ba}_{0.7}\text{Ca}_{0.3})\text{TiO}_3$ ceramic, *Appl. Phys. Lett.* 104 (2014) 152902, <https://doi.org/10.1063/1.4871378>

[25] Y. Zhao, Y. Ge, X. Zhang, Y. Zhao, H. Zhou, J. Li, H. Jin, “Comprehensive investigation of Er_2O_3 doped $(\text{Li}, \text{K}, \text{Na})\text{NbO}_3$ ceramics rendering potential application in novel multifunctional devices”, *J. Alloys Compd.* 683 (2016) 171-177, <https://doi.org/10.1016/j.jallcom.2016.05.084>

[26] A. Banwal, R. Bokolia, Enhanced upconversion luminescence and optical temperature sensing performance in Er^{3+} doped $\text{BaBi}_2\text{Nb}_2\text{O}_9$ ferroelectric ceramic, *Ceram. Int.* 42 (2021) 2230-2240, <https://doi.org/10.1007/s00339-024-07475-x>

[27] Q. Yao, F. Wang, F. Xu, C. Leung, T. Wang, Y. Tang, X. Ye, Y. Xie, D. Sun, W. Shi, Electric field-induced giant strain and photoluminescence-enhancement effect in rare-earth modified lead-free piezoelectric ceramics, *ACS Appl. Mater. Interfaces* 7 (2015) 5066-5075. <https://doi.org/10.1021/acsami.5b00420>

[28] X. Wang, C.N. Xu, H. Yamada, K. Nishikubo, X.G. Zheng, Electro-mechano-optical conversions in Pr^{3+} -doped BaTiO_3 - CaTiO_3 ceramics”, *Adv. Mater.* 17 (2005) 1254-1258. <https://doi.org/10.1002/adma.200401406>

[29] V. Singh, A. A. Bhat, C. M. Mehare, and S.J. Dhoble, Green-Emitting Perovskite $\text{BaTiO}_3:\text{Ho}^{3+}$ Phosphors for Solid-State Lighting, *J. Electron. Mater.*, 53, (2024) 4857-4868. <https://doi.org/10.1007/s11664-024-11183-w>

[30] V. Singh, A. A. Bhat, A. R. Kadam, S. Saravanakumar, P. K. Tripathi, S.J. Dhoble, and J. B. Joo1, Optimal Doping of Ho^{3+} in CaTiO_3 Perovskite for Enhanced Photoluminescence and Sustainable Green Emission, *Small, J. Electron. Mater.*, 53, (2024) 6384-6394. <https://doi.org/10.1007/s11664-024-11345-w>

[31] M. Rüdiger, S. Fischer, J. Frank, A. Ivaturi, B.S. Richards, K.W. Krämer, M.

Hermle, J.C. Goldschmidt, Bifacial n-type silicon solar cells for upconversion applications, *Sol. Energy Mater. Sol. Cells* 128 (2014) 57-68. <https://doi.org/10.1016/j.solmat.2014.05.014>

[32] F. Wang, X. Liu, Recent advances in the chemistry of lanthanide-doped upconversion nanocrystals, *Chem. Soc. Rev.* 38 (4) (2009) 976-989. <https://doi.org/10.1039/b809132n>

[33] Z. Liu, H. Deng, D. Chen, Temperature dependent upconversion properties of Yb^{3+} : Ho^{3+} co-doped Gd_2O_3 nanoparticles prepared by pulsed laser ablation in water, *Ceram. Int.* 45 (2019) 13235-13241. <https://doi.org/10.1016/j.ceramint.2019.04.009>

[34] M. Narwan, R. Sharma, R. Bokolia, Optical temperature sensing and upconversion luminescence in $\text{Er}^{3+}/\text{Yb}^{3+}$ co-doped BN ferroelectric ceramic, *Appl. Phys. A* 130 (2024) 854, <http://dx.doi.org/10.1007/s00339-024-08000-w>

[35] Y. Zhang, J. Hao, Color-tunable upconversion luminescence of Yb^{3+} , Er^{3+} , and Tm^{3+} tri-doped ferroelectric BaTiO_3 materials, *J. Appl. Phys.* 113 (2013) 184112. <https://doi.org/10.1063/1.4805050>

[36] A. Roy, A. Dwivedi, H. Mishra, D. Kumar, S.B. Rai, Dual mode (upconversion and downshifting) behavior of $\text{Ho}^{3+}/\text{Yb}^{3+}/\text{Bi}^{3+}$ co-doped YTaO_4 phosphor and its application as a security ink, *J. Alloys Compd.* 821 (2020) 153202 <https://doi.org/10.1016/j.jallcom.2019.153202>

[37] A. Basith, S. Singh, A. Banwal, M. Narwan, M. Verma, R. Bokolia, Regulating novel tunable green to red upconversion luminescence in $\text{Er}^{3+}/\text{Yb}^{3+}$ co-doped $\text{SrBi}_2\text{Nb}_2\text{O}_9$ ferroelectric ceramic, *Ceram. Int.* 50 (2024) 52344-52355. <https://doi.org/10.1016/j.ceramint.2024.10.086>

[38] P. Xiao, Y. Guo, M. Tian, Q. Zheng, N. Jiang, X. Wu, Z. Xia, D. Lin, Improved ferroelectric/piezoelectric properties and bright green/UC red emission in (Li, Ho)- doped $\text{CaBi}_4\text{Ti}_4\text{O}_{15}$ multifunctional ceramics with excellent temperature stability and superior water-resistance performance, *Dalton Trans.* 44 (2015) 17366-17380. <https://doi.org/10.1039/c5dt02728d>

[39] Y. Zhang, J. Liu, H. Sun, D. Peng, R. Li, C. Bulin, X. Wang, Q. Zhang, X. Hao,

Reversible luminescence modulation of Ho-doped $K_{0.5}Na_{0.5}NbO_3$ piezoelectrics with high luminescence contrast, *J. Am. Ceram. Soc.* 101 (2018) 2305-2312. <https://doi.org/10.1111/jace.15389>

[40] Y. Jiang, Y. Tong, S. Chen, W. Zhang, F. Hu, R. Wei, H. Guo, A three-mode self-referenced optical thermometry based on up-conversion luminescence of Ca_2MgWO_6 : Er^{3+} , Yb^{3+} phosphors, *Chem. Eng. J.* 413 (2021) 127470. <https://doi.org/10.1016/j.cej.2020.127470>

[41] Z. Zheng, J. Zhang, X. Liu, R. Wei, F. Hu, H. Guo, Luminescence and self-referenced optical temperature sensing performance in $Ca_2YZr_2Al_3O_{12}$: Bi^{3+} , Eu^{3+} phosphors, *Ceram. Int.* 46 (2020) 6154-6159. <https://doi.org/10.1016/j.ceramint.2019.11.081>

[42] S. Chen, W. Song, J. Cao, F. Hu, H. Guo, Highly sensitive optical thermometer based on FIR technique of transparent NaY_2F_7 : Tm^{3+}/Yb^{3+} glass ceramic, *J. Alloys Compd.* 825 (2020) 154011. <https://doi.org/10.1016/j.jallcom.2020.154011>

[43] S.F. Collins, S.A. Wade, G.W. Baxter, Fluorescence intensity ratio technique for optical fiber point temperature sensing, *J. Appl. Phys.* 94 (2003) 4743-4756. <https://doi.org/10.1063/1.1606526>

[44] R. Roy, A. Dutta, Microstructure correlated ion transport mechanism of sol-gel derived sodium bismuth titanate oxide ion conductors, *Appl. Physics Lett. Solid State Sciences* 102 (2020) 106174, <https://doi.org/10.1016/j.solidstatesciences.2020.106174>

[45] A. Banwal, M. Verma, B. Singh, R. Bokolia, Temperature stability and improved energy storage efficiency of $BaBi_2Nb_2O_9$: Er^{3+}/Yb^{3+} relaxor ferroelectric ceramic under moderate electric fields, *Appl. Phys. A* 130 (2024) 334, <https://doi.org/10.1007/s00339-024-07475-x>

[46] R.D. Shannon, Revised effective ionic radii and systematic studies of interatomic distances in halides and chalcogenides, *Acta Crystallogr. A* 32 (1976) 751-767, <https://doi.org/10.1107/S0567739476001551>

[47] A. Li, D. Xu, Y. Zhang, H. Lin, S. Yang, Z. Chen, Y. Shao, Upconversion luminescence and energy-transfer mechanism of $\text{NaGd}(\text{MoO}_4)_2$: $\text{Yb}^{3+}/\text{Er}^{3+}$ Microcrystals”, *J. Am. Ceram. Soc.* 99 (2016) 1657-1663. <https://doi.org/10.1111/jace.14141>

[48] L. Li, J. Zhang, W. Zi, S. Gan, G. Ji, H. Zou, X. Xu, Synthesis and luminescent properties of high brightness $\text{MRE}(\text{MoO}_4)_2:\text{Eu}^{3+}$ ($\text{M} = \text{Li, Na, K}$; $\text{RE} = \text{Gd, Y, Lu}$) red phosphors for white LEDs, *Solid State Sci.* 29 (2014) 58-65. <https://doi.org/10.1016/j.solidstatesciences.2014.01.003>

[49] M. Mondal, V.K. Rai, C. Srivastava, S. Sarkar, R. Akash, Enhanced frequency upconversion in $\text{Ho}^{3+}/\text{Yb}^{3+}/\text{Li}^+:\text{YMoO}_4$ nanophosphors for photonic and security ink applications, *J. Appl. Phys.* 120 (23) (2016) 233101. <https://doi.org/10.1063/1.4971966>

[50] M. Narwan, A. Banwal, R. Sharma, R. Bokolia, Non-thermal sensing and improved recoverable energy storage density of $\text{Bi}_{0.5}\text{Na}_{0.5}\text{TiO}_3$: Er^{3+} doped multifunctional ferroelectric ceramic, *J. Lumin.* 265 (2) (2024) 120236. <https://doi.org/10.1016/j.jlumin.2023.120236>

[51] B.K. Das, S.J. Bora, M. Chakrabortty, L. Kalita, R. Chakrabarty, R. Barman, Structural, thermal and spectroscopic properties of supramolecular coordination solids, *J. Chem. Sci.* 118 (2006) 487-494. <https://doi.org/10.1007/BF02703945>

[52] A.E. Morales, E.S. Mora, U. Pal, Use of diffuse reflectance spectroscopy for optical characterization of un-supported nanostructures, *Rev. Mexic. Fisica* 53 (2007) 18-22.

[53] S. Wang, H. Zhou, X. Wang, A. Pan, Up-conversion luminescence and optical temperature sensing properties of Er^{3+} doped perovskite $\text{Na}_{0.5}\text{Bi}_{0.5}\text{TiO}_3$, *J. Phys. Chem. Solids* 98 (2016) 28-31. <https://doi.org/10.1016/j.jpcs.2016.06.002>

[54] S. Kumari, A. Prasad, A.S. Rao, R.K. Sinha, Up-conversion luminescence in $\text{Sr}_9\text{Y}_2\text{W}_4\text{O}_{24}:\text{Ho}^{3+}, \text{Yb}^{3+}$ phosphors for applications in temperature sensing and w-LEDs, *Emergent Mater.* 7 (2024) 2957-2972, <https://doi.org/10.1007/s42247-024-00755-5>

[55] J. Divya, N.J. Shivaramu, E. Coetsee, R.E. Kroon, W. Purcell, H.C. Swart, Enhanced luminescence and photocatalytic activity of Bi_2O_3 : Ho^{3+} needles, *J. Alloys Compd.* 842 (2020) 155641. <https://doi.org/10.1016/j.jallcom.2020.155641>

[56] A. Marimuthu, R.N. Perumal, Investigations on structural, optical and electrical properties of holmium doped rubidium titanyl phosphate single crystals, *J. Alloys Compd.* 895 (2022) 162568. <https://doi.org/10.1016/j.jallcom.2021.162568>

[57] A. Banwal, R. Bokolia, Efficient tunable temperature sensitivity in thermally coupled levels of $\text{Er}^{3+}/\text{Yb}^{3+}$ co-doped $\text{BaBi}_2\text{Nb}_2\text{O}_9$ ferroelectric ceramic, *J. Lumin.* 263 (2023) 120071. <https://doi.org/10.1016/j.jlumin.2023.120071>

[58] Z. Mu, Y. Hu, G. Ju, Luminescence properties of Eu^{3+} and Ho^{3+} in Sr_2TiO_4 , *J. Rare Earths* 30 (2012) 744-747. [https://doi.org/10.1016/S1002-0721\(12\)60122-7](https://doi.org/10.1016/S1002-0721(12)60122-7)

[59] A. Dubey, A.K. Soni, A. Kumari, R. Dey, V.K. Rai, Enhanced green upconversion emission in NaYF_4 : $\text{Er}^{3+}/\text{Yb}^{3+}/\text{Li}^+$ phosphors for optical thermometry, *J. Alloys Compd.* 693 (2017) 194-200. <https://doi.org/10.1016/j.jallcom.2016.09.154>

[60] C. Micale, R.M. Almeida, Structure and properties of Er and Er/Yb-doped YF_3 up-conversion phosphors compared with oxide hosts through an internal standard, *Mater. Today Commun.* 31 (2022) 103239. <https://doi.org/10.1016/j.mtcomm.2022.103239>

[61] R. Bokolia, M. Mondal, V.K. Rai, K. Sreenivas, Enhanced infrared-to-visible upconversion emission and temperature sensitivity in (Er^{3+} , Yb^{3+} , and W^{6+}) tridoped $\text{Bi}_4\text{Ti}_3\text{O}_{12}$ ferroelectric oxide, *J. Appl. Phys.* 121 (8) (2017).

[62] A. Banwal, B. Kumar, M. Verma, A. Shandilya, B. Singh, R. Bokolia, Improved optical characteristics in $\text{BaBi}_2\text{Nb}_2\text{O}_9$ ferroelectric ceramic infused with transition metal ion (W^{6+}) and rare earth ions ($\text{Er}^{3+}/\text{Yb}^{3+}$) *J. Lumin.* 275 (2024) 120809, <https://doi.org/10.1016/j.jlumin.2024.120809>

CHAPTER – 6

Flexible BNT-PVDF Thin Films with Tunable Composition for Energy Harvesting Application

- ❖ This chapter presents the development and characterization of flexible piezoelectric nanocomposite films based on bismuth sodium titanate (BNT) embedded in a polyvinylidene fluoride (PVDF) matrix for efficient mechanical energy harvesting.
- ❖ BNT ceramic powder was synthesized via a conventional solid-state reaction route and subsequently incorporated into PVDF at varying concentrations (0 – 25 wt% BNT) using a drop casting method
- ❖ Structural analyses confirmed the successful formation of phase-pure rhombohedral BNT and enhancement of the electroactive β -phase in PVDF upon BNT addition.
- ❖ FTIR and XRD studies substantiated the β -phase promotion in the composites, while polarization–electric field (P–E) loop measurements demonstrated improved ferroelectric behavior with increasing BNT content, peaking at 20 wt% BNT.
- ❖ A practical demonstration using the composite film to power LEDs confirmed its potential as a flexible nanogenerator. These findings highlight the suitability of BNT/PVDF composites as promising candidates for next-generation, lead-free, wearable energy harvesting devices.

The results reported in this chapter have been published in Megha et. al. Ceramics International.

6.1 Introduction

Chapter 6 presents the development and characterization of flexible piezoelectric nanocomposite films based on bismuth sodium titanate (BNT) embedded in a polyvinylidene fluoride (PVDF) matrix for efficient mechanical energy harvesting. BNT ceramic powder was synthesized via a conventional solid-state reaction route and subsequently incorporated into PVDF at varying concentrations (0 – 25 wt% BNT) using a drop casting method. Structural analyses confirmed the successful formation of phase-pure rhombohedral BNT and enhancement of the electroactive β -phase in PVDF upon BNT addition. Morphological evaluation using FESEM revealed uniform dispersion of BNT up to 20 wt% BNT, beyond which agglomeration was observed. FTIR and XRD studies substantiated the β -phase promotion in the composites, while polarization–electric field (P–E) loop measurements demonstrated improved ferroelectric behavior with increasing BNT content, peaking at 20 wt% BNT. Notably, the piezoelectric voltage and current outputs were maximized at 20 wt% BNT, registering 25V and 12 μ A, respectively, under mechanical excitation. A practical demonstration using the composite film to power LEDs confirmed its potential as a flexible nanogenerator. These findings highlight the suitability of BNT/PVDF composites as promising candidates for next-generation, lead-free, wearable energy harvesting devices.

The ever-growing demand for sustainable and decentralized power sources has catalyzed significant research into energy harvesting technologies, particularly those capable of converting ambient mechanical energy into usable electrical energy [1-2]. In an era characterized by rapid advancements in microelectronics, the proliferation of wearable sensors, implantable devices, and Internet-of-Things (IoT) systems has led to a pressing need for compact, autonomous power sources that eliminate or minimize dependence on conventional batteries [3-4]. Conventional power storage units not only suffer from limited life spans and high maintenance costs but also contribute significantly to environmental degradation due to the use of toxic materials and challenges associated with large-scale disposal. Consequently, self-powered systems based on mechanical energy scavenging have emerged as a promising solution [5-7].

Among the various energy harvesting technologies, piezoelectric nanogenerator stands out to be promising due to its ability to convert mechanical deformation, such as pressure, strain, or vibration, into electrical charge via piezoelectric material—a property that has found application in diverse fields including structural health monitoring, biomedical implants, smart textiles, and portable electronics [8-9]. The piezoelectric materials are particularly well-suited for environments where continuous motion, such as walking, engine vibration, or acoustic energy, can be harnessed to generate consistent power [10-11].

Commercial piezoelectric devices are predominantly fabricated using lead-based ceramics, especially lead zirconate titanate ($\text{Pb}(\text{Zr},\text{Ti})\text{O}_3$, PZT), owing to their excellent electromechanical coupling and high piezoelectric coefficients [12-15]. However, the widespread use of lead-based materials has become increasingly controversial due to their toxicity and environmental hazards [16-17]. Regulations such as the Restriction of Hazardous Substances (RoHS) directive and the Waste Electrical and Electronic Equipment (WEEE) directive have further driven the research community to identify and develop lead-free alternatives that can match or exceed the performance of their toxic counterparts [18-20].

In this pursuit, sodium bismuth titanate ($\text{Bi}_{0.5}\text{Na}_{0.5}\text{TiO}_3$, BNT) have emerged as a promising lead free ferroelectric and piezoceramic material having numerous advantages such as high piezoelectric coefficient (~ 75 pC/N), elevated Curie temperature, strong ferroelectric polarization, a wide operational frequency range, a high electromechanical coupling coefficient, and low dielectric loss making it suitable candidate to fabricate PNG [21-23]. However, despite these advantages the practical implementation of BNT ceramic still faces challenges including high leakage currents, elevated coercive fields, and difficulties in domain orientation, which collectively complicate the poling process necessary to realize their full potential in flexible and high-performance devices. To address these limitations and enhance mechanical flexibility, recent efforts have shifted toward the development of flexible piezoelectric composites, where ceramic particles are embedded within polymer matrices such as polyvinylidene fluoride (PVDF), polydimethylsiloxane (PDMS), or thermoplastic polyurethanes (TPU) [24-26]. Such composites combine the superior piezoelectric

performance of ceramics with the flexibility, low density, and ease of processing of polymers. Moreover, polymer-ceramic composites are highly compatible with low-temperature fabrication techniques, enabling their integration into unconventional substrates and wearable form factors [27-28].

These flexible systems have shown great promise in next-generation self-powered wearable electronics, with the potential for integration into clothing, footwear, sports gear, medical patches, and structural materials. Notably, their non-toxicity and biocompatibility make them ideal for biomedical applications [29].

Despite the considerable progress made in recent years, key research questions remain regarding the optimization of material composition, filler morphology, dispersion quality, and interface engineering to enhance energy conversion efficiency and mechanical robustness [30-32]. This paper aims to explore these aspects, focusing on the development of high-performance, environmentally benign piezoelectric composites based on BNT embedded within flexible polymer matrices. Through a comprehensive review of recent advancements, fabrication methodologies, and performance metrics, we seek to illuminate the path toward viable alternatives to conventional lead-based piezoelectric generators.

In this study, BNT powder with the chemical formula $\text{Bi}_{0.5}\text{Na}_{0.5}\text{TiO}_3$, is synthesised by traditional solid state reaction method. PVDF nanocomposite films were prepared by incorporating BNT at different weight percentages (Weight percentages of 0%, 5%, 10%, 15%, and 20% and 25% BNT). These films were subsequently used to fabricate piezoelectric nano generator (PNG) devices. The fabricated PNG exhibited enhanced output performance, primarily due to the increased β -phase content in the PVDF film upon the addition of BNT nanofillers which is confirmed by FTIR and P-E loop measurements. Finally, to evaluate its practical applicability, the developed PNG was tested for energy harvesting activities. These findings indicate that BNT-PVDF nanocomposites can serve as promising materials for high-performance PNGs, paving the way for their integration into next-generation flexible and wearable energy harvesting systems.

6.2 Experimental Details

6.2.1 Preparation of BNT Ceramic Powder

High-grade powders were obtained from Sigma-Aldrich, and lead-free $\text{Bi}_{0.5}\text{Na}_{0.5}\text{TiO}_3$ ceramics were prepared using Bi_2O_3 , Na_2CO_3 , and TiO_2 as raw materials. Solid state reaction method is used to synthesize the pure BNT ceramic powder as depicted in **Figure 6.1**. A stoichiometric mixture of the powders was obtained based on the synthesis reaction provided in Eq. 6.1.



A high-energy ball milling process, using zirconia balls as the grinding medium, was employed to mix the raw powder for 12 hours. Following the ball milling process, the mixture was dried in an oven at 70 °C for 24 hours and subsequently calcined at 850 °C for 3 hours. Finally, this calcined material was grinded again to get the fine powder and further this powder is used to make the fabrication of the films.

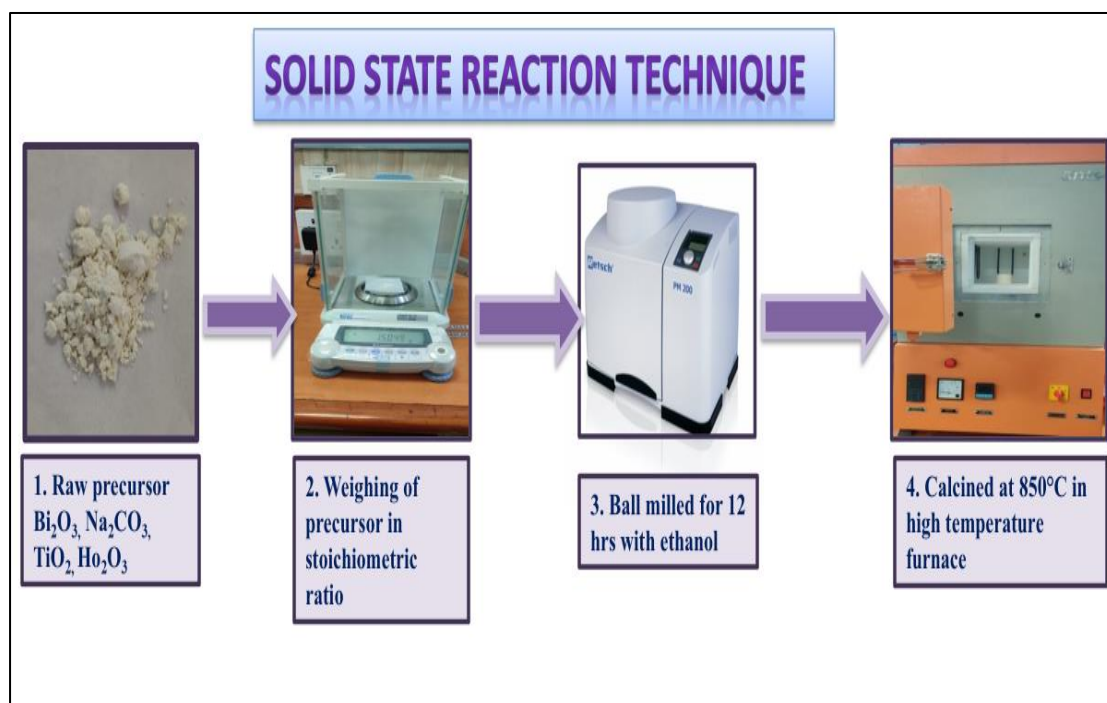


Figure 6.1: Schematic diagram outlining the preparation process of BNT ceramic

6.2.2 Fabrication of PVDF- BNT Flexible Composite Films

N, N-Dimethylformamides (DMF) and Polyvinylidene fluoride (PVDF) were procured from Alfa Aesar. Initially, 1g of PVDF powder was dispersed and dissolved in DMF under stirring conditions at 50° C for a duration of one hour, resulting in a homogenous clear solution. Meanwhile, varying concentrations of calcined BNT powder (Weight percentages of 0%, 5%, 10%, 15%, and 20% and 25% BNT) were dispersed in DMF and subjected to ultrasonication for 30 minutes at room temperature to ensure uniform dispersion. Subsequently, the BNT solutions with different weight percentages were gradually added to the PVDF solution and stirred magnetically at 50°C for 4 hours. To further minimize particle agglomeration, the resulting mixture was ultrasonically treated for an additional 10 minutes. The prepared homogeneous composite mixture was deposited onto a glass substrate and dried at 90 °C for one hour to form flexible BNT/PVDF films. Following the drying process, the films were soaked in deionized (DI) water to release the standalone films. The complete synthesis of the composite films was performed under ambient atmospheric conditions. The BNT/PVDF film fabrication process is schematically represented in **Figure. 6.2**, along with pictorial representation of the composite films that were created using varying weight percentages of BNT ceramic powder in PVDF.

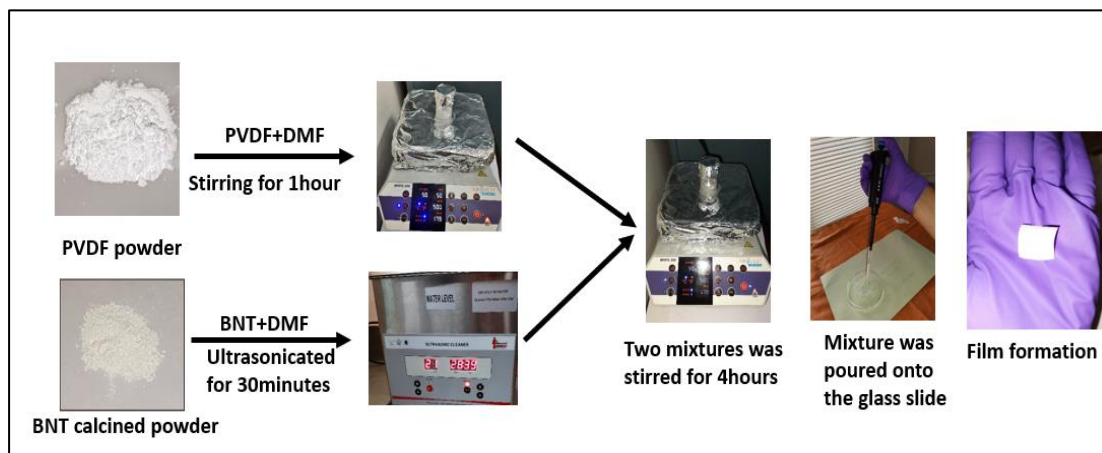


Figure 6.2: Schematic diagram showing the preparation of flexible BNT/PVDF composite films

6.2.3 Fabrication of a Piezoelectric Generator Based on BNT/PVDF Composite

The flexible BNT/PVDF films synthesized via the drop-casting method were cut into a square area of 1.5 by 1.5 centimetres pieces, both surfaces of the films were coated with aluminium tape to act as the top and bottom electrodes during piezoelectric generator (PEG) fabrication. Thereafter, to establish the required electrical connections for measuring the device performance, Copper wires were subsequently connected to the aluminium tape using silver paste. The schematic of the fabricated PEG device is shown in **Figure 6.3**.

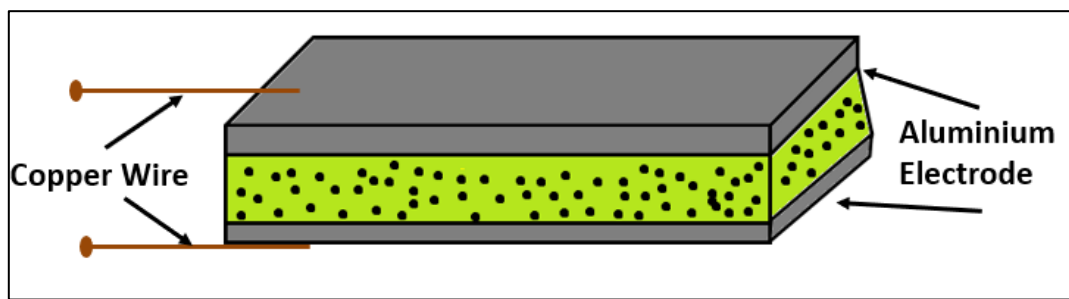


Figure 6.3: A schematic illustration of the PEG device with its key components

6.2.4 Characterizations

Using a Bruker D8 Advance X-ray diffractometer with a Cu-K α source ($\lambda = 1.54 \text{ \AA}$), the phase purity and crystalline structure of the ceramic calcined at 850 °C and the prepared BNT composite films at different weight percentages were analyzed. The XRD pattern of the calcined ceramic and films were scanned in the 2θ range 10° -80°. The surface morphology of the powder and fabricated films with different weight percentage were analyzed using Field Emission Scanning Morphology (FESEM) using Zeiss GeminiSEM 500 Thermal field emission type. Fourier Transform Infrared (FTIR) spectroscopy was done on the powder as well as the fabricated films with different weight percentage to assess the presence of the β -phase in BNT/PVDF composites utilizing the PerkinElmer Spectrum II spectrometer. The generated voltage and current signals from the PEG devices were analyzed using a Keithley DMM7510 digital multimeter and a Tektronix MDO500 digital storage oscilloscope.

6.3 Analysis of Results

6.3.1 Study of Structural and Surface Morphological Properties of BNT Ceramic Powder

Figure 6.4 represents the X-Ray Diffraction (XRD) pattern of pure BNT powder at room temperature synthesised using solid state reaction technique calcined at 850°C. The obtained XRD pattern in the range from $2\theta = 20^\circ - 80^\circ$, perfectly matches with the reported standard data with JCPDS card no #00-036-0340, indicating the pure perovskite structure with no secondary peak emphasis the phase purity of the ceramic, indicating that the BNT was successfully synthesized with rhombohedral with R3c space group [33]. The synthesized BNT ceramic powder was characterized for its surface morphology via SEM, and the micrographs are illustrated in **Figure 6.5(a)**. Using Image J software, the average particle size of the manufactured BNT ceramic powder was determined to be 188 nm. The average particle size calculation is shown in **Figure 6.5(b)**.

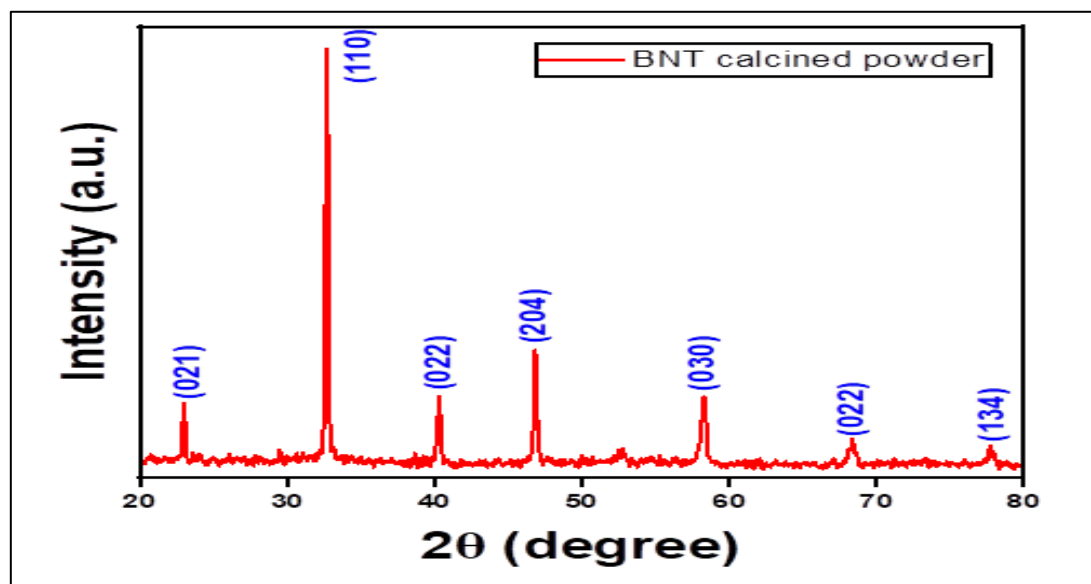


Figure 6.4: XRD plot representing the calcined BNT ceramic sample

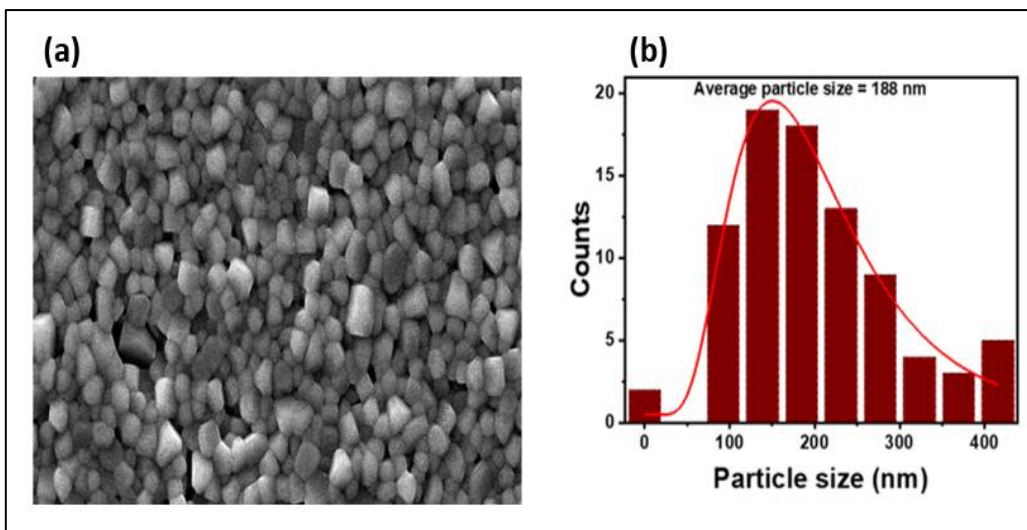


Figure 6.5: (a) Micrograph obtained by SEM illustrating the morphology of the calcined BNT ceramic powder (b) the corresponding size distribution of particles

6.3.2 Investigation of the Structural Behavior of PVDF and BNT/PVDF Composite Materials

The crystallographic properties of the pure PVDF film and the BNT/PVDF composite films were examined using X-ray diffraction (XRD), and the corresponding diffraction patterns are presented in **Figure 6.6(a)**. The XRD profile of pure PVDF exhibits characteristic peaks corresponding to both the polar β -phase and the non-polar α -phase. Specifically, the β -phase is indicated by a distinct diffraction peak at approximately 20.1° , whereas a broad and comparatively weaker peak near 18.6° corresponds to the α -phase [34]. These observations are consistent across all composite samples. In the composite films, additional diffraction peaks attributed to the BNT ceramic phase are also observed and are denoted in the diffraction patterns by asterisks (\blacklozenge , \blacklozenge), confirming the successful incorporation of BNT particles into the PVDF matrix.

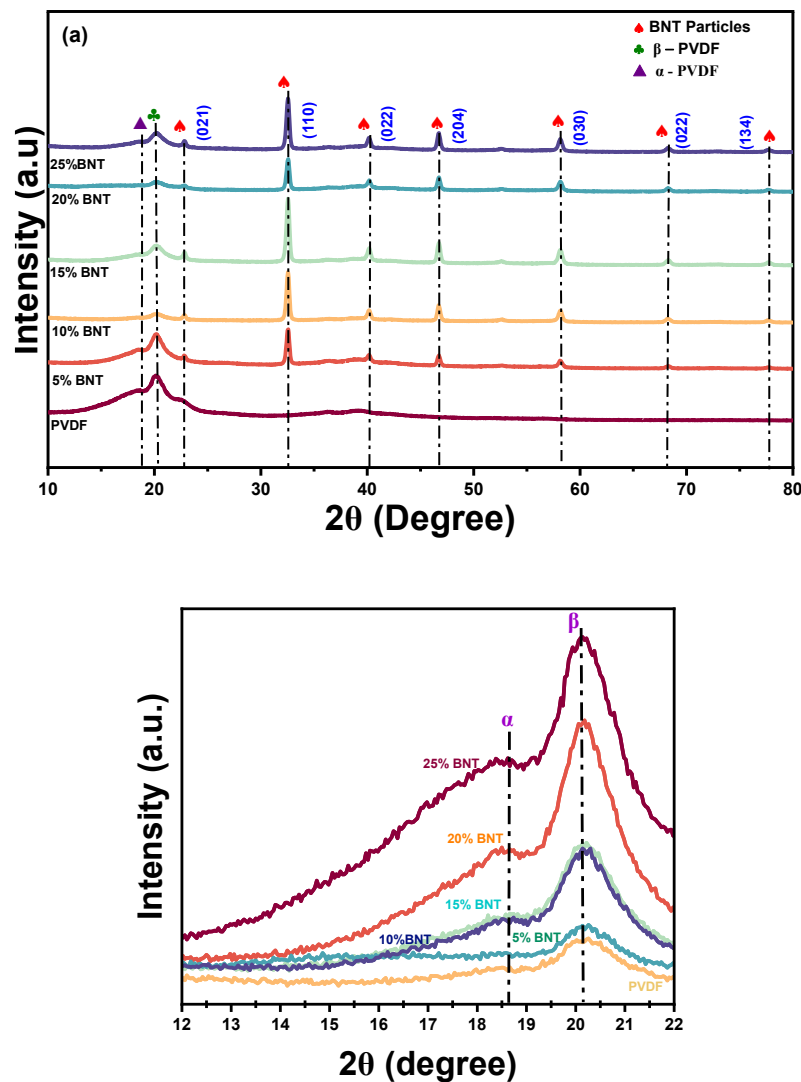


Figure 6.6: (a) XRD spectra of PVDF and PVDF composites films containing different amounts of BNT ceramic powder and (b) a magnified section of Fig. 6(a) with 2θ ranging from 12° to 22° .

Figure 6.6(b) highlights a comparative view of the β - and α -phase intensities across the different compositions. With increasing BNT content from 0 to 20 wt%, the β -phase peak intensity exhibits significant enhancement, highlighting the role of BNT in promoting electroactive β -phase formation in PVDF. A subsequent drop in intensity is evident at 25 wt% BNT. However, when the BNT content is increased to 25 wt% BNT, a decline in the β -phase peak intensity is observed. This reduction may be attributed to the agglomeration of BNT particles at higher loadings, which can disrupt the uniform distribution of the filler and hinder effective polymer–filler interaction. Such agglomeration leads to the

formation of non-uniform domains and interfacial defects, which may restrict the chain mobility of PVDF, thereby suppressing further transformation into the β -phase [35]. Additionally, excessive ceramic content can lead to increased rigidity of the composite, reducing the ability of the polymer chains to reorient under internal fields generated during film processing. Overall, the XRD results demonstrate a synergistic enhancement of the β -phase with BNT incorporation up to an optimal filler concentration (20 wt% BNT), beyond which the structural integrity and phase development are adversely affected due to filler aggregation and phase separation.

6.3.3 Comparative Analysis of the Surface Morphology of BNT, PVDF, and BNT/PVDF Films

The surface morphology of pure PVDF and BNT/PVDF composite films containing varying concentrations of BNT was examined using field emission scanning electron microscopy (FESEM), and the corresponding micrographs are shown in **Figure. 6.7(a-f)**. The pure PVDF film exhibits a relatively smooth and homogeneous surface, characteristic of semi-crystalline polymer structures formed under controlled processing conditions.

In contrast, the composite films containing BNT reveal a distinct microstructural evolution with increasing ceramic content. The presence of BNT particles is clearly seen within the PVDF matrix in all composite samples. At lower filler concentrations, the ceramic particles appear to be well-dispersed throughout the polymer matrix, indicating effective filler–matrix interaction and uniform distribution. This uniformity is essential for consistent mechanical and functional performance of the composites. As the BNT content increases, a gradual increase in surface roughness is observed, which is attributed to the higher density of embedded ceramic particles [36]. Despite the increase in particle loading, no significant agglomeration is evident up to 20 wt% BNT, suggesting good compatibility between the ceramic phase and the polymer matrix. At 25 wt% BNT, however, localized clusters begin to form, indicating the onset of particle aggregation at higher filler concentrations. Such clustering may affect the homogeneity of the composite and could potentially impact its piezoelectric and mechanical behavior. Overall, the FESEM analysis confirms the successful incorporation and distribution of BNT within the PVDF matrix, supporting the

phase, in agreement with the XRD results. The relative enhancement of the β -phase is particularly notable in the composite containing 20 wt% BNT, aligning with the observed optimal concentration for structural and morphological uniformity. Furthermore, the β -phase content of the prepared samples was quantitatively evaluated using the Lambert–Beer law given by the following equation

$$F(\beta) = \frac{A_\beta}{\left(\frac{k_\beta}{k_\alpha}\right)A_\alpha + A_\beta} \times 100\%$$

where A_α and A_β are absorbance at 762 cm^{-1} and 840 cm^{-1} , $k_\alpha = 6.1 \times 10^4\text{ cm}^2/\text{mol}$ and $k_\beta = 7.7 \times 10^4\text{ cm}^2/\text{mol}$ represents absorption coefficients at corresponding wavenumber. The calculated β -phase contents for pristine PVDF and PVDF/BNT composites containing 5, 10, 15, 20, and 25 wt% BNT were found to be 60.4%, 80.1%, 81.2%, 88.0%, 95.2%, and 90.6%, respectively.

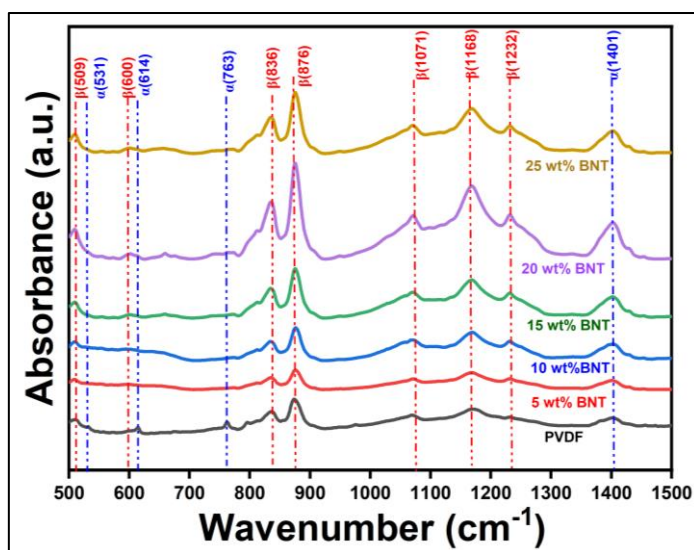


Figure 6.8: FTIR spectra of pure PVDF and BNT/PVDF composite films containing varying amounts of BNT ceramic

As evident from the results, the β -phase fraction in PVDF increases progressively with the incorporation of BNT ceramic powder, reaching a maximum at 20 wt% BNT, followed by a slight decline at 25 wt% BNT. This trend is also reflected in the FTIR spectra shown in **Figure 6.8**, where the characteristic absorption peak corresponding to the β -phase at approximately 836 cm^{-1} becomes more prominent with increasing BNT content up to 20 wt% BNT. Compared to the pure PVDF film, all BNT/PVDF composite films exhibit

enhanced β -phase absorption, suggesting a significant improvement in the electroactive crystalline phase of PVDF upon BNT addition. These observations are consistent with the XRD results, which similarly show intensified β -phase features in the composite structures. The enhancement in β -phase content upon the addition of BNT can be attributed to several interrelated mechanisms. Firstly, BNT particles act as effective nucleating agents due to their high surface energy, which promotes the transformation of PVDF chains from the non-polar α -phase to the all-trans β -phase configuration during film formation. The interfacial interactions between the BNT ceramic surface and PVDF molecular chains induce localized dipole alignment, facilitating β -phase crystallization. Moreover, the inclusion of ceramic fillers introduces internal stress and microstructural confinement within the polymer matrix, which further favors the formation of the thermodynamically less stable but electroactive β -phase. The incorporation of BNT not only enhances the β -phase content of PVDF through nucleation and interfacial polarization effects but also highlights an optimal filler threshold beyond which structural uniformity and phase conversion efficiency begin to deteriorate. This result underlines the critical role of ceramic–polymer interactions in tailoring the crystalline behavior of PVDF for advanced functional applications.

6.3.5 Polarization–Electric Field (P–E) Hysteresis Characterization

The ferroelectric properties of the fabricated films were evaluated by recording the P–E hysteresis loops of pure PVDF and BNT/PVDF nanocomposites with varying BNT concentrations. These measurements were carried out under room temperature conditions at a constant frequency of 50 Hz, and the applied electric field of 400 kV/cm, with the results graphically presented in Figure 6.9. For these measurements, the PVDF and BNT/PVDF composite films were sandwiched between two conducting electrodes with an area of approximately 35 mm and a thickness of about 1 mm to perform the P–E measurements.

As observed, pure PVDF exhibits a narrow, linear-like hysteresis loop, characteristic of its relatively weak ferroelectric response due to the dominance of the non-polar α -phase [40]. Upon the incorporation of BNT ceramic into the PVDF matrix, a notable broadening of the hysteresis loops is observed, indicating enhanced polarization behavior in the nanocomposite films [41]. An increase in remnant polarization is

observed for PVDF and nanocomposite films as the BNT content rises, reaching a maximum at 20 wt% BNT, after which a slight drop occurs. The data are summarized in Table 6.1. This trend suggests that moderate BNT incorporation facilitates better alignment of dipoles and promotes β -phase formation in PVDF, thus enhancing its ferroelectric properties. The optimal enhancement at 20 wt% BNT is likely due to an effective interfacial interaction between the polymer matrix and ceramic particles, which aids in dipolar ordering and acts as nucleation sites for β -phase crystallization. However, further increase in BNT content beyond the optimal level appears to introduce particle agglomeration and phase separation effects, which may disrupt the homogeneity of the dipole alignment, thereby reducing the remnant polarization. This decline is indicative of an upper threshold in filler content, beyond which the ferroelectric benefit is diminished due to microstructural heterogeneity.

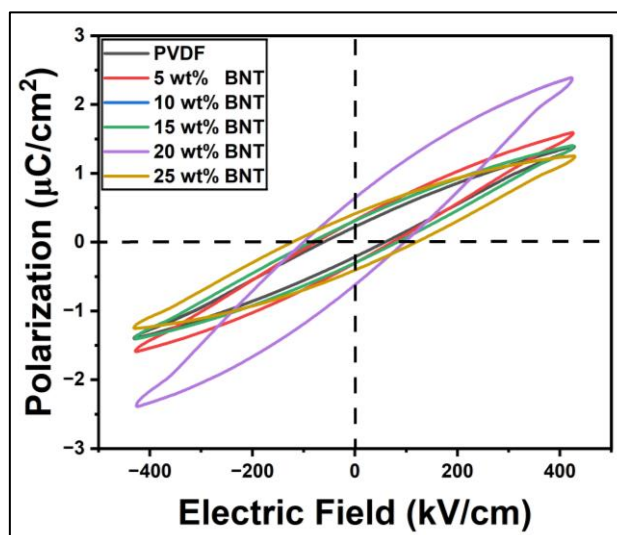


Figure 6.9: P–E loops of pristine PVDF and composite films incorporating various concentrations of BNT ceramics in the PVDF matrix

Table 6.1: Remnant Polarization value of PVDF and its composite films with different concentrations of BNT

Concentration	Remnant Polarization (P_r) ($\mu\text{C}/\text{cm}^2$)
PVDF	0.231
5 wt % BNT	0.301
10 wt% BNT	0.320
15 wt% BNT	0.340
20 wt% BNT	0.628
25 wt% BNT	0.408

6.3.6 Piezoelectric Voltage Response of PVDF and BNT/PVDF Nanocomposite Films

The piezoelectric performance of the pristine PVDF and its nanocomposites with varying BNT concentrations was evaluated by monitoring the voltage output under periodic mechanical tapping at 7 Hz frequency, and 10 N force under ambient laboratory conditions, as illustrated in **Figure. 6.10**. The recorded output signals demonstrate the dynamic response of the samples over a time span of 5 seconds [42]. The pristine PVDF film **Figure. 6.10 (a)** exhibits relatively low and irregular voltage output, with peak amplitudes fluctuating between approximately ± 5.3 V. This limited response is attributed to the inherently low content of electroactive β -phase in PVDF, which governs the material's piezoelectric efficiency [43]. Upon the incorporation of BNT into the PVDF matrix, a significant enhancement in output voltage is observed. For the nanocomposite with 5 wt% BNT **Figure. 6.10 (b)**, the peak voltage reaches approximately ± 8.84 V, indicating improved dipole alignment due to the nucleating effect of BNT. The enhancement becomes more pronounced at 10 wt% BNT **Figure. 6.10 (c)**, where the output reaches peaks around ± 12.2 V, suggesting an optimal increase in the polar phase content and efficient stress transfer at the polymer–ceramic interface. The composite with 15 wt% BNT **Figure. 6.10 (d)** shows a consistent and symmetric voltage profile with peak amplitudes near ± 13 V, supporting the formation of a stable piezoelectric network. Interestingly, the 20 wt% BNT film **Figure. 6.10 (e)** exhibits the highest output, with sharp peaks exceeding ± 25 V, confirming that at this concentration, the ceramic particles are well dispersed and interact effectively with the polymer chains to maximize the piezoelectric response. However, further increase in BNT content to 25 wt% BNT **Figure. 6.10 (f)** results in a reduction in the output voltage ± 12.8 V, with irregular and less intense peaks. This decline can be attributed to the agglomeration of ceramic particles at higher loadings, which hinders dipole alignment and reduces the mechanical-to-electrical energy conversion efficiency [44]. Overall, the voltage output behavior demonstrates a strong correlation between BNT concentration and piezoelectric performance, with 20 wt% BNT emerging as the optimum composition for maximum energy harvesting output. The value of voltage vs time is given in Table 6.2 and the comparative study of voltage is tabulated in Table 6.3.

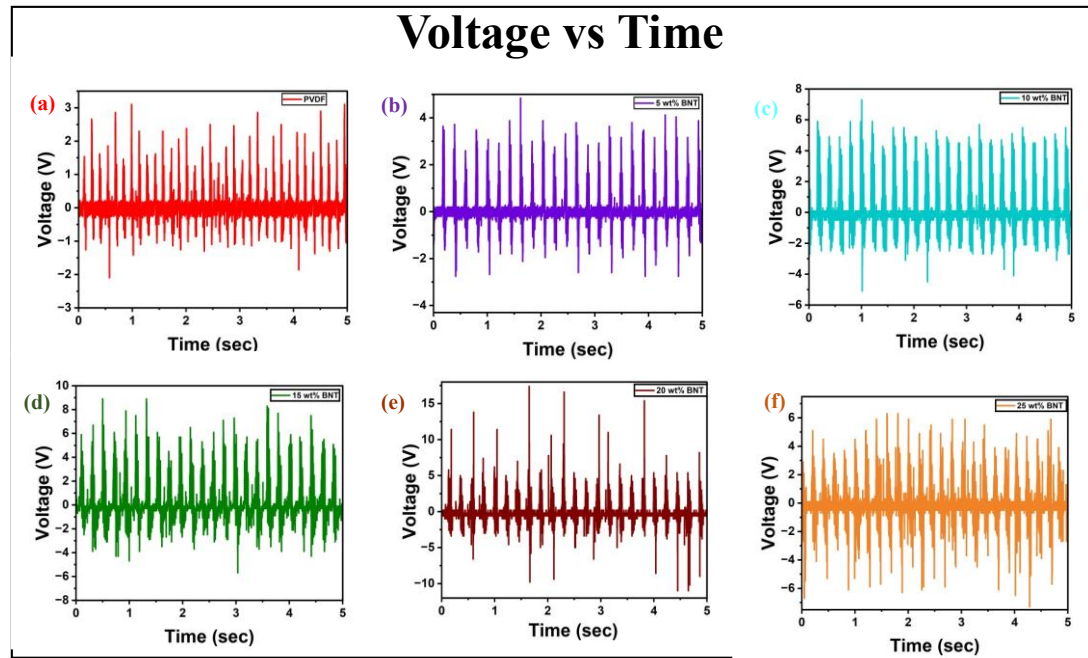


Figure 6.10: (a-f) Output voltage response of PVDF and BNT/PVDF Nanocomposite films at 7 Hz frequency

Table 6.2: Value of Voltage vs Time with different concentrations

Concentration	Voltage
PVDF	5.3 V
5 wt% BNT	8.84 V
10 wt% BNT	12.2 V
15 wt% BNT	13 V
20 wt% BNT	25 V
25 wt% BNT	12.8 V

Table 6.3: Tabulated Performance of Various Energy Harvesting Materials

S.No	Piezoelectric and filler material	Output Voltage (V)	Ref
1.	PVDF / Ag_2CO_3	2.7	[45]
2.	Poly (vinylidene fluoride-hexafluoropropylene) (PVDF-HFP) / BCZT	10	[46]
3.	PVDF / $\text{BiFe}_{0.9}\text{Co}_{0.1}\text{O}_3$ (BFCO)- doped KNN	0.713	[47]
4.	PVDF / $(\text{Na}_{0.5}, \text{K}_{0.5})\text{NbO}_3$	0.98	[48]
5.	PVDF / ZnO	2	[49]
6.	PVDF / MAPbBr	5	[50]
7.	PVDF / BNT	25	This work

6.3.7 Piezoelectric Current Output from PVDF and BNT/PVDF Nanocomposites

The piezoelectric current responses of pristine PVDF and BNT-loaded PVDF nanocomposite films were recorded under periodic mechanical stimuli, as illustrated in **Figure. 6.11**. The transient current output was monitored over a time duration of 10 seconds for all samples to evaluate their piezoelectric energy conversion performance [51]. The pristine PVDF sample **Figure. 6.11 (a)** exhibited a relatively weak and symmetric alternating current signal, with a peak output of 5.5 μ A. This low magnitude can be attributed to the limited alignment of dipolar domains and low β -phase content in the unmodified PVDF matrix [52]. Upon the addition of BNT ceramic filler, a gradual improvement in current output was observed. The composite containing 5 wt% BNT **Figure. 6.11 (b)** generated a current of 7.5 μ A, indicating enhanced polar phase development and improved interfacial polarization. The 10 wt% BNT film **Figure. 6.11 (c)** showed a further increase, reaching a peak of 8 μ A, suggesting effective stress transfer at the polymer–ceramic interface and improved piezoelectric response. With 15 wt% BNT loading **Figure. 6.11 (d)**, the current output increased slightly to 8.5 μ A, accompanied by a higher signal frequency and stability. A significant enhancement was noted at 20 wt% BNT **Figure. 6.11(e)**, where the composite demonstrated the highest current output of 12 μ A. This performance peak can be attributed to the optimum filler dispersion and strong dipolar interactions within the hybrid matrix, resulting in enhanced charge mobility and piezoelectric activity [53]. However, further increasing the BNT content to 25 wt% BNT **Figure. 6.11(f)** led to a reduction in current to 9.5 μ A. This decline is likely due to ceramic agglomeration at higher filler concentrations, which impedes the homogeneous distribution of stress and restricts effective domain alignment, leading to charge carrier recombination losses. Overall, the trend indicates that the incorporation of BNT enhances the piezoelectric current response of PVDF, with 20 wt% BNT identified as the optimum composition for maximizing current generation in the fabricated nanocomposites. The value of Current corresponding to Time is collaborated in Table 6.3.

Load matching studies have been carried out across different load resistance and maximum power of device achieved is around $17\mu\text{W}/\text{cm}^2$ at $8\text{ M}\Omega$. The corresponding results have been presented in **Figure. 6.12(a) and (b)** for better illustration.

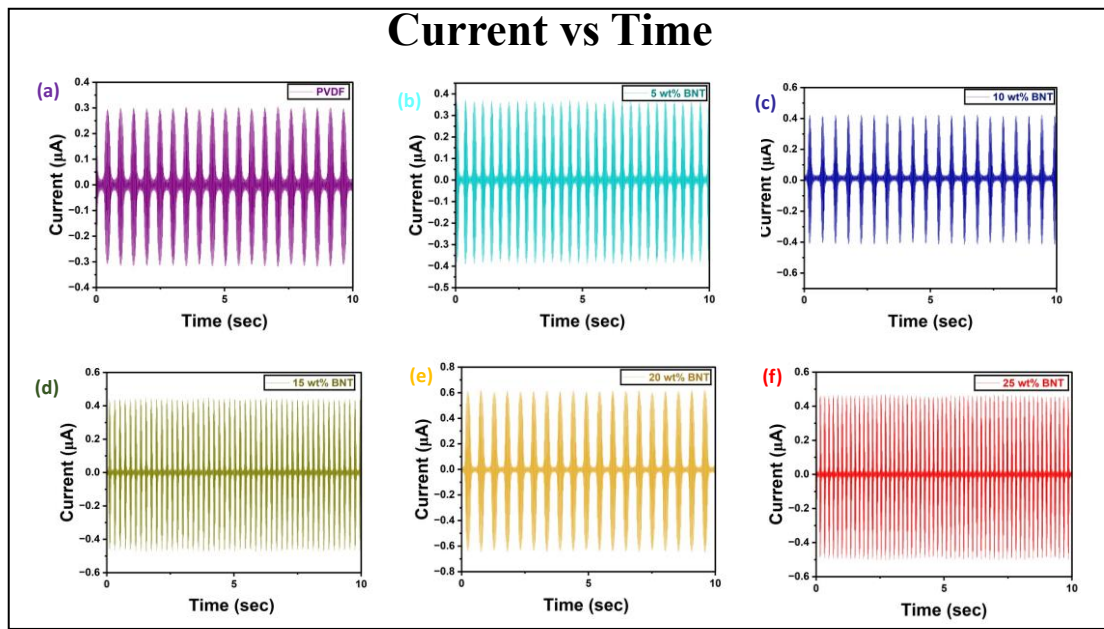


Figure 6.11: Output Current obtained for PVDF and BNT/PVDF Nanocomposites Films at 7 Hz frequency

Table 6.4: Value of Current vs Time with different concentrations

Concentration	Current
PVDF	5.5 μ A
5 wt% BNT	7.5 μ A
10 wt% BNT	8 μ A
15 wt% BNT	8.5 μ A
20 wt% BNT	12 μ A
25 wt% BNT	9.5 μ A

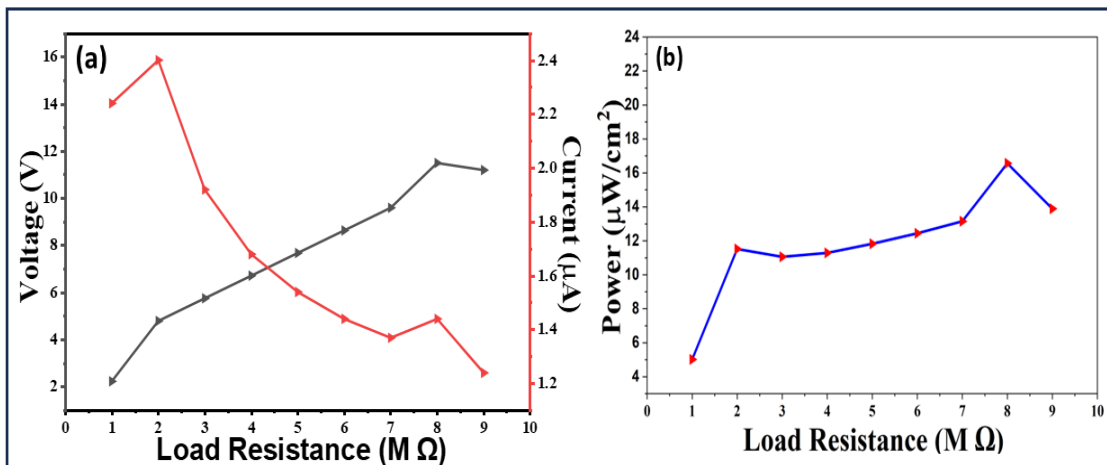


Figure 6.12: (a) Output voltage and current measurements of PNG devices with different load resistance and (b) power measurement of PNG device with different load resistance

6.3.8 Validation of Output Characteristics Using LED Illumination

To demonstrate the practical applicability of PVDF/BNT nanocomposite films based nanogenerator, the power generated by the nanogenerator is utilized to illuminate the LEDs. Figure 13 displays the experimental setup and corresponding circuit diagram, demonstrating the ability of the device to power light-emitting diodes (LEDs). In this configuration, the alternating current (AC) output from the PNG was converted into direct current (DC) through a bridge rectifier, and the rectified output was stored in a capacitor before being discharged to illuminate the LEDs. Upon repeated mechanical impact, the generated voltage was sufficient to power multiple LEDs (green, blue, and white) without any external energy source, confirming the strong piezoelectric output of the optimized 20 wt% BNT/PVDF composite.

The clear and consistent illumination of the LEDs indicates the capability of the nanocomposite film based PNG to deliver stable electrical output under cyclic mechanical stress, validating its effectiveness for energy conversion in self-powered systems. The enhanced electrical output and stability of the BNT/PVDF-based PNG suggest its strong potential for next-generation flexible electronics, particularly where conventional batteries are impractical or unsustainable.

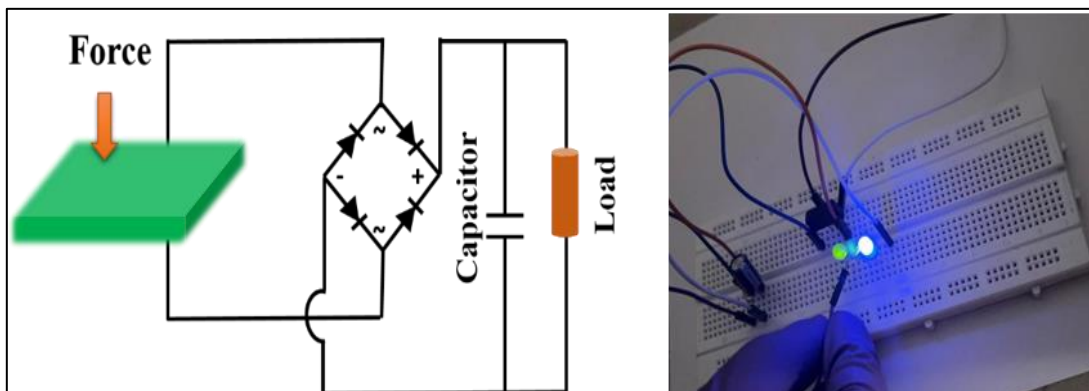


Figure 6.13: A schematic showing the circuit diagram of PNG device used to illuminate the LEDs with photographic image of LEDs illumination

6.4 Summary

In summary, flexible and lead-free piezoelectric nanocomposite films were fabricated by embedding BNT ceramic particles into a PVDF matrix using a drop-casting technique. Structural characterization confirmed the coexistence of α - and β -phases in PVDF, with BNT addition promoting a substantial increase in the electroactive β -phase content, as evidenced by both XRD and FTIR analyses. The enhancement in polar phase fraction, combined with uniform ceramic dispersion up to the optimal filler loading, significantly improved the ferroelectric and piezoelectric responses of the composites. The composition containing 20 wt% BNT displayed the best performance, yielding an open-circuit voltage of 25 V and a short-circuit current of 12 μ A when subjected to mechanical excitation. The practical capability of the optimized film was demonstrated through the successful illumination of multiple LEDs without any auxiliary power source, confirming its suitability for real-time energy harvesting. The findings underscore the potential of BNT/PVDF nanocomposites as high-performance, environmentally benign materials for next-generation self-powered and wearable electronics.

6.5 References

- [1] M. Li, M.J. Pietrowski, R.A.D. Souza, H. Zhang, I.M. Reaney, S.N. Cook, J.A. Kilner, D.C. Sinclair, A family of oxide ion conductors based on the ferroelectric perovskite $\text{Na}_0.5\text{Bi}_0.5\text{TiO}_3$, *Nat. Mater.* 13 (2014) 31–35, <https://doi.org/10.1038/nmat3782>
- [2] S. Makishima, H. Yamamoto, T. Tomotsu, S. Shionoya, Luminescence spectra of Sm^{3+} in BaTiO_3 host lattice. *J. Phys. Soc. Jpn.* 20, 2147–2151 (1965), <https://doi.org/10.1143/JPSJ.20.2147>
- [3] D.D. Dung, N.B. Doan, N.Q. Dung, L.H. Bac, N.H. Linh, L.T.H. Thanh, D.V. Thiet, N.N. Trung, N.C. Khang, T.V. Trung, N.V. Duc, Role of Co dopants on the structural, optical and magnetic properties of lead-free ferroelectric $\text{Na}_0.5\text{Bi}_0.5\text{TiO}_3$ materials. *J. Sci. Adv. Mater. Dev.* 4, 584–590 (2019), <https://doi.org/10.1016/j.jsamrd.2019.08.007>
- [4] Z. Tianmin, Z. Yanqiu, W. Zhongli, C. Baojiu, Concentration effect and temperature quenching of upconversion luminescence in $\text{BaGd}_2\text{ZnO}_5:\text{Er}^{3+}/\text{Yb}^{3+}$ phosphor, *J. Rare Earths* 33 (7) (2015) 686, [https://doi.org/10.1016/S1002-0721\(14\)60471-3](https://doi.org/10.1016/S1002-0721(14)60471-3).
- [5] M.K. Mahata, T. Koppe, T. Mondal, C.B. Sewitz, K. Kumar, V.K. Rai, H. Hofsass, U. Vetter, Incorporation of Zn^{2+} ions into $\text{BaTiO}_3:\text{Er}^{+}/\text{Yb}^{3+}$ nanophosphor: an effective way to enhance upconversion, defect luminescence, and temperature sensing, *Phys. Chem. Chem. Phys.* 17 (2015) 20741–20753, <https://doi.org/10.1039/c5cp01874a>.
- [6] K. Zhang, S. Wang, Y. Yang, A one-structure-based piezo-tribo-pyrophotoelectric effects coupled nanogenerator for simultaneously scavenging mechanical, thermal, and solar energies, *Adv. Energy Mater.* 7 (2017) 1601852, <https://doi.org/10.1002/aenm.201601852>
- [7] Q. Zhou, J.G. Park, K.N. Kim, A.K. Thokchom, J. Bae, J.M. Baik, T. Kim, Transparent-flexible-multimodal triboelectric nanogenerators for mechanical energy harvesting and self-powered sensor applications, *Nano Energy* 48 (2018) 471–480, <https://doi.org/10.1016/j.nanoen.2018.03.074>
- [8] M. Sharma, V. Srinivas, G. Madras, S. Bose, Outstanding dielectric constant and

piezoelectric coefficient in electrospun nanofiber mats of PVDF containing silver decorated multiwall carbon nanotubes: assessing through piezoresponse force microscopy, RSC Adv. 6 (2016) 6251–6258. <https://doi.org/10.1039/D5TC02231B>

[9] V. Vivekananthan, N.R. Alluri, Y. Purusothaman, A. Chandrasekhar, S. Selvarajan, S.-J. Kim, Biocompatible collagen nanofibrils: an approach for sustainable energy harvesting and battery-free humidity sensor applications, ACS Appl. Mater. Interfaces 10 (22) (2018) 18650–18656, <https://doi.org/10.1021/acsami.8b02915>

[10] W. Jin, Z. Wang, H. Huang, X. Hu, Y. He, Li Meng, L. Li, Y. Gao, Y. Hu, H. Gu, High-performance piezoelectric energy harvesting of vertically aligned Pb(Zr,Ti) O₃ nanorod arrays, RSC Adv. 8 (2018) 7422–7427, <https://doi.org/10.1039/C7RA13506H>.

[11] G.-T. Hwang, D. Im, S.E. Lee, J. Lee, M. Koo, S.Y. Park, S. Kim, K. Yang, S.J. Kim, K. Lee, K.J. Lee, In vivo silicon-based flexible radio frequency integrated circuits monolithically encapsulated with biocompatible liquid crystal polymers, ACS Nano 7 (2013) 4545–4553, <https://doi.org/10.1021/nn401246y>.

[12] H. Katzke, M. Dietze, A. Lahmar, M. Es-Souni, N. Neumann, S.-G. Lee, Dielectric, ultraviolet/visible, and Raman spectroscopic investigations of the phase transition sequence in 0.71Pb(Mg_{1/3}Nb_{2/3})O₃-0.29PbTiO₃ crystals, Phys. Rev. B 83 (2011), 174115, <https://doi.org/10.1103/PhysRevB.83.174115>.

[13] J.-H. Lee, K. Heo, K. Schulz-Schönhagen, J.H. Lee, M.S. Desai, H.-E. Jin, S.-W. Lee, Diphenylalanine peptide nanotube energy harvesters, ACS Nano 12 (2018) 8138–8144, <https://doi.org/10.1021/acsnano.8b03118>.

[14] A.R. Jeyaraman, S.K. Balasingam, C. Lee, H. Lee, B. Balakrishnan, S. Manickam, M. Yi, H.-J. Kim, K. Sivalingam Nallathambi, Y. Jun, H. Kuzhandaivel, Enhanced solar to electrical energy conversion of titania nanoparticles and nanotubes based combined photoanodes for dye-sensitized solar cells, Mater. Lett. 243 (2019) 180–182, <https://doi.org/10.1016/j.matlet.2019.02.006>

[15] H. Kawai, The piezoelectricity of poly (vinylidene fluoride) related content

piezoelectricity of poly (vinylidene fluoride) under high pressure, *Jpn. J. Appl. Phys.* 8(1969) 975, <https://doi.org/10.1143/JJAP.8.975>

[16] S. Garain, S. Jana, T.K. Sinha, D. Mandal, Design of in situ poled Ce 3+-doped electrospun PVDF/graphene composite nano fibers for fabrication of nanopressure sensor and ultrasensitive acoustic nanogenerator, *ACS Appl. Mater. Interfaces* 8 (2016) 4532–4540, <https://doi.org/10.1021/acsami.5b11356>.

[17] A. Salimi, A.A. Yousefi, FTIR studies of β -phase crystal formation in stretched PVDF films, *Polym. Test.* 22 (2003) 699–704, [https://doi.org/10.1016/S0142-9418\(03\)00003-5](https://doi.org/10.1016/S0142-9418(03)00003-5).

[18] C.W. Lim, L.H. He, Exact solution of a compositionally graded piezoelectric layer under uniform stretch, bending and twisting, *Int. J. Mech. Sci.* 43 (2001) 2479–2492, [https://doi.org/10.1016/S0020-7403\(01\)00059-5](https://doi.org/10.1016/S0020-7403(01)00059-5)

[19] J. Gomes, J.S. Nunes, V. Sencadas, S. Lanceros-Méndez, Influence of the β -phase content and degree of crystallinity on the piezo-and ferroelectric properties of poly (vinylidene fluoride), *Smart Mater. Struct.* 19 (2010) 065010 <https://doi.org/10.1088/0964-1726/19/6/065010>.

[20] Y. Hiruma, H. Nagata, T. Takenaka, Thermal depoling process and piezoelectric properties of bismuth sodium titanate ceramics. *J. Appl. Phys.* 105, 084112 (2009). <https://doi.org/10.1063/1.3115409>

[21] S.R. Platt, S. Farritor, K. Garvin, H. Haider, The use of piezoelectric ceramics for electric power generation within orthopedic implants, *IEEE/ASME Trans. Mechatron.* 10 (2005) 455–461, <https://doi.org/10.1109/TMECH.2005.852482>.

[22] D. Vatansever, R.L. Hadimani, T. Shah, E. Siores, Characterisation of energy generating PolyVinylidene Fluoride (PVDF) based piezoelectric filament, *Adv. Mater. Res.* 410 (2011) 366–369, <https://doi.org/10.4028/www.scientific.net/amr.410.366>.

[23] X. Ni, F. Wang, A. Lin, Q. Xu, Z. Yang, Y. Qin, Flexible nanogenerator based on single BaTiO₃ nanowire, *Sci. Adv. Mater.* 5 (2013) 1781–1787, <https://doi.org/10.1166/sam.2013.1629>

[24] J. Cheng, S. Wang, S. Chen, J. Zhang, X. Wang, Properties and crystallization behavior of poly (vinylidene fluoride) (PVDF)/thermoplastic polyurethane

elastomer (TPU) blends, Desalination and Water Treatment, 34, 1–3, 2011, 184–189, <https://doi.org/10.5004/dwt.2011.2791>.

[25] D. Nawrocka, “Environmental supply chain management, ISO 14001 and RoHS. How are small companies in the electronics sector managing” Corp, Soc. Responsib. Environ. Manag. 15 (2008) 349–360, <https://doi.org/10.1002/csr.176>.

[26] S.R. Anton, H.A. Sodano, A review of power harvesting using piezoelectric materials, Smart Mater. Struct. 16 (2007) R1–R21, <https://doi.org/10.1088/0964-1726/16/3/R01>.

[27] M. Narwan, A. Banwal, R. Sharma, R. Bokolia, Non-thermal sensing and improved recoverable energy storage density of $\text{Bi}_{0.5}\text{Na}_{0.5}\text{TiO}_3$: Er^{3+} doped multifunctional ferroelectric ceramic, J. Lumin. 265 (2) (2024) 120236, <https://doi.org/10.1016/j.jlumin.2023.120236>

[28] A. Hussin, A. Maqbool, R.A. Malik, M. Su Kim, T.K. Song, M.H. Kim, Structural and electrical properties of $\text{Bi}_{0.5}\text{Na}_{0.5}\text{TiO}_3$ tem plates produced by topochemical microcrystal conversion method. New Phys. Sae Mulli 65(8), 715–720 (2015). <https://doi.org/10.3938/NPSM.65.715>

[29] R. Roy, A. Dutta, Microstructure correlated ion transport mechanism of sol-gel derived sodium bismuth titanate oxide ion conductors, Appl. Physics lett solid state sciences 102 (2020), 106174, <https://doi.org/10.1016/j.solidstatesciences.2020.106174>.

[30] C.K. Jeong, C. Baek, A.I. Kingon, K.I. Park, S.H. Kim, Lead-free perovskite nano wire-employed piezopolymer for highly efficient flexible nanocomposite energy harvester, Small 14 (2018) 1704022, <https://doi.org/10.1002/smll.201704022>.

[31] A. Marin, S. Bressers, S. Priya, Multiple cell configuration electromagnetic vibration energy harvester, J. Phys. D Appl. Phys. 44 (2011) 295501, <https://doi.org/10.1088/0022-3727/44/29/295501>.

[32] A. Talbourdet, F. Rault, G. Lemort, C. Cochrane, E. Devaux, C. Campagne, 3D interlock design 100% PVDF piezoelectric to improve energy harvesting, Smart Mater. Struct. 27 (2018) 075010 (075017pp), <https://doi.org/10.1088/1361-665X/aab865>.

[33] J. Yao, N. Monsegue, M. Murayama, W. Leng, W.T. Reynolds, Q. Zhang, H. Luo, J. Li, W. Ge, D. Viehland, Role of coexisting tetragonal regions in the rhombohedral phase of $\text{Na}_{0.5}\text{Bi}_{0.5}\text{TiO}_3$ -xat.% BaTiO_3 crystals on enhanced piezoelectric properties on approaching the morphotropic phase boundary, *Appl. Phys. Lett.* 100 (2012), 012901, <https://doi.org/10.1063/1.3673832>

[34] B. Dutta, E. Kar, N. Bose, S. Mukherjee, Significant enhancement of the electro active β -phase of PVDF by incorporating hydrothermally synthesized copper oxide nanoparticles, *RSC Adv.* 5 (2015) 105422–105434, <https://doi.org/10.1039/C5RA21903E>.

[35] D. Rouxel, B. Vincent, L. Badie, F.D. Dos Santos, E. Lamouroux, Y. Fort, Influence of cluster size and surface functionalization of ZnO nanoparticles on the morphology, thermomechanical and piezoelectric properties of P (VDF-TrFE) nano composite films, *Appl. Surf. Sci.* 279 (2013) 204–211, <https://doi.org/10.1016/j.apsusc.2013.04.070>.

[36] B. Liu, B. Lu, X. Chen, X. Wu, S. Shi, L. Xu, Y. Liu, F. Wang, X. Zhao, W. Shi, A high performance flexible piezoelectric energy harvester based on lead-free $(\text{Na}_{0.5}\text{Bi}_{0.5})\text{TiO}_3$ – BaTiO_3 piezoelectric nanofibers. *J. Mater. Chem. A.* 5, 23634–23640 (2017), <https://doi.org/10.1039/C7TA07570G>

[37] F. Khatun, N.A. Hoque, P. Thakur, N. Sepay, S. Roy, B. Bagchi, A. Kool, S. Das, 4' Chlorochalcone-assisted electroactive polyvinylidene fluoride film-based energy storage system capable of self-charging under light, *Energy Technol.* 5 (2017) 2205–2215, <https://doi.org/10.1002/ente.201700265>.

[38] P. Martins, A.C. Lopes, S. Lanceros-Mendez, Electroactive phases of poly(vinylidene fluoride): determination, processing and applications, *Prog. Polym. Sci.* 39 (2014) 683–706, <https://doi.org/10.1016/j.progpolymsci.2013.07.006>.

[39] D. Mandal, A. Tamang, S.K. Ghosh, Md.S. Garain, M. Alam, J. Haeberle, K. Henkel, D. Schmeisser, DNA-assisted β phase nucleation and alignment of molecular dipoles in PVDF film: a realization of self-poled bioinspired flexible polymer nanogenerator for portable electronic devices, *ACS Appl. Mater. Interfaces* 7 (2015) 16143–16147, <https://doi.org/10.1021/acsami.5b04161>

[40] M. Muneeswaran, B.C. Choi, S.H. Chang, J.H. Jung, Effect of dysprosium doping on structural and vibrational properties of lead-free (Na_{0.7}K_{0.3})_{0.5}Bi_{0.5}TiO₃ ferroelectric ceramics, *Ceram. Int.* 43 (2017) 13696–13701, <https://doi.org/10.1016/j.ceramint.2017.07.081>.

[41] W. Qiu, H.H. Hng, Effects of dopants on the microstructure and properties of PZT ceramics, *Mater. Chem. Phys.* 75 (2002) 151–156, [https://doi.org/10.1016/S0254-0584\(02\)00045-7](https://doi.org/10.1016/S0254-0584(02)00045-7).

[42] Y. He, Z. Wang, X. Hu, Y. Cai, L. Li, Y. Gao, X. Zhang, Z. Huang, Y. Hu, H. Gu, Orientation-dependent piezoresponse and high-performance energy harvesting of lead-free (K,Na)NbO₃ nanorod arrays, *RSC Adv.* 7 (2017) 16908–16915, <https://doi.org/10.1039/C7RA01359K>.

[43] M.K. Gupta, S.-W. Kim, B. Kumar, Flexible high-performance lead-free Na_{0.47}K_{0.47}Li_{0.06}NbO₃ microcube-structure-based piezoelectric energy harvester, *ACS Appl. Mater. Interfaces* 8 (2016) 1766–1773, <https://doi.org/10.1021/acsami.5b09485>.

[44] C. Zhang, Y. Fan, H. Li, Y. Li, L. Zhang, S. Cao, S. Kuang, Y. Zhao, A. Chen, G. Zhu, Z.L. Wang, Fully rollable lead-free poly(vinylidene fluoride)-niobate-based nano generator with ultra-flexible nano-network electrodes, *ACS Nano* 12 (2018) 4803–4811, <https://doi.org/10.1021/acsnano.8b0153>.

[45] H.K. Mishra, D. Sengupta, A. Babu, B.M. Pirzada, R. Sarkar, B.S. Naidu, T.K. Kundu, D. Mandal, PVDF/Ag₂CO₃ nanocomposites for efficient dye degradation and flexible piezoelectric mechanical energy harvester, *Sustain. Energy Fuels* 6 (2022) 1625–1640, <https://doi.org/10.1039/D1SE01889B>

[46] K.S. Chary, V. Kumar, C.D. Prasad, H.S. Panda, Dopamine-modified Ba_{0.85}Ca_{0.15}Zr_{0.1}Ti_{0.9}O₃ ultra-fine fibers/PVDF-HFP composite-based nanogen erator: synergistic effect on output electric signal, *J. Aust. Ceram. Soc.* 56 (2020) 1107–1117, <https://doi.org/10.1007/s41779-020-00458-0>

[47] J. Xing, H. Chen, L. Jiang, C. Zhao, Z. Tan, Y. Huang, B. Wu, Q. Chen, D. Xiao, J. Zhu, High performance BiFe_{0.9}Co_{0.1}O₃ doped KNN-based lead-free ceramics for acoustic energy harvesting, *Nano Energy* 84 (2021) 105900, <https://doi.org/10.1016/j.nanoen.2021.105900>

[48] H.B. Kang, C.S. Han, J.C. Pyun, W.H. Ryu, C.Y. Kang, S.C. Yong, (Na,K)NbO₃ nanoparticle-embedded piezoelectric nanofiber composites for flexible nanogenerators, *Compos. Sci. Technol.* 111 (2015) 1–8, <https://doi.org/10.1016/j.compscitech.2015.02.015>

[49] L. Z, Z. X, L. G, In situ ZnO nanowire growth to promote the PVDF piezo phase and the ZnO-PVDF hybrid self-rectified nanogenerator as a touch sensor, *Phys. Chem. Chem. Phys.* 16 (12) (2014) 5475–5479, <https://doi.org/10.1039/C3CP54083A>

[50] A. Sultana, M.M. Alam, P. Sadhukhan, U.K. Ghorai, S. Das, T.R. Middya, D. Mandal, Organo-lead halide perovskite regulated green light emitting poly(vinylidene fluoride) electrospun nanofiber mat and its potential utility for ambient mechanical energy harvesting application, *Nano Energy* 49 (2018) 380–392, <https://doi.org/10.1016/j.nanoen.2018.04.057>

[51] H.S. Lee, J. Chung, G.-T. Hwang, C.K. Jeong, Y. Jung, J.-H. Kwak, H. Kang, M. Byun, W.D. Kim, S. Hur, S.-H. Oh, K.J. Lee, Flexible inorganic piezoelectric acoustic nanosensors for biomimetic artificial hair cells, *Adv. Funct. Mater.* 24 (2014) 6914–6921, <https://doi.org/10.1002/adfm.201402270>.

[52] H. Shintaku, T. Kobayashi, K. Zusho, H. Kotera, S. Kawano, Wide-range frequency selectivity in an acoustic sensor fabricated using a microbeam array with non-uniform thickness, *J. Micromech. Microeng.* 23 (2013) 115014, <https://doi.org/10.1088/0960-1317/23/11/115014>.

[53] J.H. Han, J.-H. Kwak, D.J. Joe, S.K. Hong, H.S. Wang, J.H. Park, S. Hur, K.J. Lee, Basilar membrane-inspired self-powered acoustic sensor enabled by highly sensitive multi tunable frequency band, *Nano Energy* 53 (2018) 198–205, <https://doi.org/10.1016/j.nanoen.2018.08.053>.

CHAPTER - 7

Conclusion, Future Scope, and Social Impact

- ❖ *This chapter provides an overview of the research conducted in this thesis.*
- ❖ *It further presents a brief discussion of the key conclusions drawn from the results.*
- ❖ *Finally, it identifies possible avenues for future research and examines the societal impacts that could enhance and expand upon this study.*

7.1 Conclusion

In summary, this thesis has presented a comprehensive investigation into the effect of doping $\text{Bi}_{0.5}\text{Na}_{0.5}\text{TiO}_3$ ceramics with Er^{3+} , $\text{Er}^{3+}/\text{Yb}^{3+}$, and Ho^{3+} ions, with a particular focus on their structural, photoluminescence, sensing, and ferroelectric behaviors. The study has also extended to the fabrication of thin films aimed at energy-harvesting applications, thereby demonstrating the versatility of this material system in both bulk and thin-film forms. The results obtained from this work provide significant contributions to the broader understanding of how rare-earth and transition-metal ion incorporation can modify the intrinsic properties of perovskite ceramics. Through a systematic analysis of each doping scenario, the thesis highlights the role of ionic substitution in influencing crystallographic structure, enhancing luminescent efficiency, improving ferroelectric responses, and tailoring functional performance.

Furthermore, the findings emphasize the potential of $\text{Bi}_{0.5}\text{Na}_{0.5}\text{TiO}_3$ -based systems as multifunctional materials with promising applications across several emerging technologies. These include advanced optoelectronic devices, optical security instruments, non-contact sensing platforms, and self-powered energy-harvesting systems.

Chapter 1: Presents a detailed overview of photoluminescent and ferroelectric materials, examining their fundamental characteristics and intrinsic properties. The discussion highlights their distinctive features and outlines the wide range of potential applications associated with these materials. Particular emphasis is placed on the role of rare-earth ions in tuning the behavior of host lattices, where controlled doping strategies are shown to significantly influence structural and functional performance. The chapter also provides a brief account of the diverse applications of upconversion luminescent materials across different technological fields. In addition, it outlines the main objectives of the present research and offers a concise description of the overall organization of the thesis

Chapter 2: Addresses a detailed account of the synthesis methodology and the characterization approaches adopted in this study. The $\text{Bi}_{0.5}\text{Na}_{0.5}\text{TiO}_3$ ceramic was synthesized using the conventional solid-state reaction technique, in which high-purity raw powders were thoroughly weighed, mixed, and ground to achieve a homogeneous

composition. The mixed powders were subjected to calcination at elevated temperatures in a controlled furnace to promote solid-state diffusion and phase formation. Subsequently, the calcined powders were compacted into pellets and sintered at optimized conditions to obtain dense ceramic samples with well-defined microstructures. To evaluate the properties of the synthesized ceramics, a range of characterization techniques was employed. Structural information was obtained through X-ray diffraction (XRD), while the surface morphology and grain distribution were studied using scanning electron microscopy (SEM). Fourier-transform infrared spectroscopy (FTIR) was used to confirm bond vibrations and chemical stability. Optical properties were investigated through photoluminescence studies, which included upconversion (UCL) emission spectra, pump power-dependent behavior, and time-resolved fluorescence measurements. The fluorescence intensity ratio (FIR) method was applied to assess the temperature-sensing capability of the material. In addition, ferroelectric measurements were carried out at room temperature to examine the dielectric and polarization characteristics of the ceramics. Furthermore, the synthesized ceramic powders were incorporated into thin films with varying concentrations using appropriate deposition techniques, and these films were evaluated for their suitability in energy-harvesting applications. Collectively, this chapter provides a comprehensive explanation of the synthesis procedures and experimental strategies adopted to systematically analyze both the structural and functional properties of the prepared materials.

Chapter 3: Highlights the successful synthesis of $\text{Bi}_{0.5}\text{Na}_{0.5}\text{TiO}_3$ ceramics by the solid-state method and the effective incorporation of Er^{3+} ions at various concentrations without the formation of secondary phases. Structural investigations confirmed complete solubility of Er^{3+} in the host lattice along with slight lattice contraction. The ceramics exhibited stable ferroelectric behavior with saturated P–E loops, while the energy storage density and efficiency were notably enhanced, particularly at $x = 0.04$. Photoluminescence studies revealed intense green and weak red emissions under dual excitation, with maximum intensity observed at $x = 0.03$, accompanied by a reduction in lifetime due to non-radiative effects. The upconversion process was confirmed to be two-photon in nature, and a gradual decrease in band gap was noted with higher dopant

content. The composition with $x = 0.03$ further demonstrated promising thermal sensing capability in the 303–523 K range. Overall, these findings indicate that Er^{3+} -doped $\text{Bi}_{0.5}\text{Na}_{0.5}\text{TiO}_3$ ceramics are promising multifunctional materials for applications in optoelectronics and energy storage systems.

Chapter 4: Demonstrates that $\text{Er}^{3+}/\text{Yb}^{3+}$ co-doped $\text{Bi}_{0.5-x-y}\text{Er}_x\text{Yb}_y\text{Na}_{0.5}\text{TiO}_3$ ceramics exhibit stable rhombohedral structure with complete dopant solubility, as confirmed by XRD, SEM, and FTIR analyses. The energy band gap was found to decrease slightly with increasing dopant concentration. Photoluminescence studies under 489 nm and 980 nm excitation revealed two strong green emissions (530 nm, 549 nm) and one red emission (662 nm), with upconversion confirmed as a two-photon process. Time-resolved fluorescence measurements indicated efficient energy transfer between dopant ions. Thermal sensing evaluation showed relative and absolute sensitivities of 1.24 % K^{-1} and 0.54 % K^{-1} , respectively. These results suggest that the co-doped ceramics are promising multifunctional materials suitable for optoelectronic, sensing, and energy-related applications.

Chapter 5: Provides the successful incorporation of Ho^{3+} ions into $\text{Bi}_{0.5-x}\text{Ho}_x\text{Na}_{0.5}\text{TiO}_3$ ceramics via the solid-state method, resulting in a pure rhombohedral perovskite structure without secondary phases. FTIR and DRS analyses confirmed structural integrity and revealed f–f transitions of Ho^{3+} ions, along with a slight reduction in bandgap energy due to oxygen vacancies and local distortions. Photoluminescence studies under 452 nm excitation showed strong green emission at 548 nm and weaker red emissions at 655 nm and 750 nm, while upconversion under 980 nm excitation exhibited multiple bands with efficient energy transfer, particularly at $x = 0.03$. Ferroelectric measurements indicated slimmer P–E loops with increasing dopant content, and the energy storage efficiency reached ~90%. Thermal sensing evaluation showed maximum relative and absolute sensitivities of 0.22 % K^{-1} and 0.29 % K^{-1} , respectively. Overall, Ho^{3+} -doped BNT ceramics exhibit excellent structural, optical, and functional properties, making them promising candidates for optoelectronic and upconversion-based applications.

Chapter 6: Reports the fabrication of flexible, lead-free BNT/PVDF nanocomposite films via a drop-casting method. Structural analyses confirmed the coexistence of α - and β -phases in PVDF, with BNT incorporation enhancing the electroactive β -phase content. Uniform dispersion of ceramic particles up to 20 wt% significantly improved ferroelectric and piezoelectric properties. The optimized composition generated an open-circuit voltage of 25 V and a short-circuit current of 12 μ A under mechanical excitation, successfully powering multiple LEDs without external energy. These results highlight the potential of BNT/PVDF nanocomposites as environmentally friendly, high-performance materials for self-powered and wearable electronic applications.

7.2 Future Scope

The central aim of this thesis was to examine the structural, photoluminescence, sensing, and ferroelectric properties of Er^{3+} -doped, $\text{Er}^{3+}/\text{Yb}^{3+}$ co-doped, and Ho^{3+} -doped $\text{Bi}_{0.5}\text{Na}_{0.5}\text{TiO}_3$ ceramics. In addition, these ceramics were employed in the fabrication of thin films intended for energy-harvesting applications. Although the present work has made significant progress toward these objectives, several areas remain open for further work and may serve as valuable directions for future research:

1. **Dielectric characterization:** A more in-depth study of the dielectric properties is required to optimize BNT ceramic for use in energy-storage devices, capacitors, and sensing technologies.
2. **Mechanoluminescence studies:** Exploring stress-induced luminescence may provide new insights into their potential for sensing applications and advanced optoelectronic systems.
3. **Improved film fabrication:** The application of advanced deposition methods, such as spin coating or sputtering, could yield thin films with greater uniformity and enhanced quality.
4. **Nanogenerator development:** Further work on PVDF–BNT-based triboelectric and piezoelectric nanogenerators may enable their practical deployment in powering LEDs, wearable devices, and self-powered sensors.
5. **Flexible and transparent films:** The design and fabrication of

multifunctional nanocomposite films with flexibility and transparency could extend their use in next-generation energy-harvesting and optoelectronic devices.

6. **Complex dopant systems:** Investigation of quaternary dopant combinations may uncover synergistic effects, thereby providing opportunities to further tailor and enhance the functional properties of these materials.

7.3 Social Impact

Rare-earth ion-doped BNT ceramics have wide-ranging applications across various technological fields, offering notable advantages and benefits to society in multiple areas. Moreover, their innovative functionalities and eco-friendly nature align with and support several Sustainable Development Goals (SDG) as outlined below:-

1. Environmental Sustainability

Development of rare-earth ion-doped BNT sceramics and their PVDF composites promotes environmentally friendly, lead-free materials for next-generation electronics, reducing reliance on toxic lead-based systems.

2. Energy Efficiency and Carbon Reduction

Enhanced energy efficiency in optoelectronic devices, such as LEDs, lowers power consumption and reduces carbon emissions, supporting sustainable technology development.

3. Cost Reduction and Accessibility

The improved efficiency and long lifespan of these materials help reduce operational costs, making high-performance devices more affordable and accessible, particularly in resource-limited regions.

4. Biomedical Applications

These materials enable the fabrication of non-toxic, sustainable biomedical devices, including non-invasive temperature sensors and wearable health monitors, contributing to safer healthcare technologies.

5. Self-Powered and Remote Applications

Integration into flexible energy-harvesting systems facilitates self-powered devices, providing practical solutions for remote and rural areas where electricity access may be limited.

6. Advancement of Multifunctional Smart Devices

The multifunctional properties of these materials support the development of smart electronics, optoelectronic devices, and energy-harvesting technologies, aligning with global efforts toward green and sustainable innovations.



Full Length Article

Non-invasive thermal sensing and improved recoverable energy storage density of $\text{Bi}_{0.5}\text{Na}_{0.5}\text{TiO}_3$: Er^{3+} doped multifunctional ferroelectric ceramic

Megha Narwan, Ankita Banwal, Richa Sharma, Renuka Bokolia *

Department of Applied Physics, Delhi Technological University, Delhi, 110042, India

ARTICLE INFO

Keywords:
 Upconversion luminescence
 Ferroelectric ceramic
 Energy storage density
 Optical temperatures sensing
 Er^{3+} doping
 Diffuse reflectance spectroscopy

ABSTRACT

In this work, Er^{3+} substituted bismuth sodium titanate ceramics with the chemical composition $\text{Bi}_{0.5-x}\text{Er}_x\text{Na}_{0.5}\text{TiO}_3$ ($x = 0.00, 0.01, 0.02, 0.03, 0.04$, and 0.05) were synthesized using conventional solid state technique. The influence of Er^{3+} ions on structural, optical, ferroelectric, and temperature sensing properties have been investigated. The prepared ceramic powders were initially heated at a calcination temperature 850°C to form single phase $\text{Bi}_{0.5-x}\text{Er}_x\text{Na}_{0.5}\text{TiO}_3$ and finally sintered at temperature 1050°C . Formation of pure phase compositions with rhombohedral crystal structure is confirmed through X-ray diffraction studies. The typical FTIR bands near $540, 860, 910\text{ cm}^{-1}$ confirmed the presence of Ti–O stretching of octahedral groups in the perovskite structure. The decent squared shaped saturated P-E hysteresis are obtained under an electric field of $60 \leq E \leq 70\text{ kV/cm}$, and the loops become slimmer at higher Er^{3+} concentrations ($x = 0.04$). The efficiency of energy storage density increases with Er^{3+} doping and an improved recoverable energy storage ($W_r = 2.73\text{ J/cm}^3$) and a higher efficiency ($\eta = 70.77\%$) are obtained for Er content, $x = 0.04$. The photoluminescence spectra were recorded at two excitation wavelengths (488 nm and 980 nm). Two distinct green emission bands (529 nm and 550 nm) and one weak red emission band (670 nm) were observed at both excitation wavelengths. Increasing Er^{3+} content beyond ($x > 0.03$) leads to significant quenching of light emission due to cross relaxation process and non-radiative relaxations. The pump power dependency revealed that two photons were involved in the light upconversion process. The time-resolved fluorescence spectroscopy confirmed the decrease in lifetime with increasing Er^{3+} concentration. The absolute and relative sensitivity of the prepared ceramic at Er^{3+} concentration ($x = 0.03$) were found to be $0.47\% \text{ K}^{-1}$ at 523 K and $1.1\% \text{ K}^{-1}$ at 303 K , respectively. These optical and electrical properties open the possibility of realizing multifunctionality in the field of energy storage and optoelectronic applications.

1. Introduction

In order to keep pace with the rapid progress of contemporary technology in the present era, it is essential to incorporate and analyze materials. Multifunctional materials have attracted significant attention lately due to their inherent versatility. When considering multifunctional applications, it is necessary to select dielectric and ferroelectric materials that demonstrate an ideal combination of down and upconversion emissions. With the increasing prominence of environmental issues, there is a pressing need to explore alternative lead-free piezoelectric materials. The challenge arises due to environmental issues which limits the use of lead-based materials [1,2]. As a result, alternative lead-free ferroelectric materials based on $\text{Na}_0.5\text{Bi}_0.5\text{TiO}_3$ (NBT), $\text{K}_{0.5}\text{Na}_{0.5}\text{NbO}_3$ (KNN), and Bismuth layered ferroelectrics (BLSFs), etc.

are being investigated to replace the current lead-containing materials [3–5]. Bismuth sodium titanate, $\text{Bi}_{0.5}\text{Na}_{0.5}\text{TiO}_3$ (abbreviated as BNT) is among the most widely used lead-free piezoelectric materials. BNT is an important member of classical electrical functional materials known for its notable characteristics, including a high dielectric constant and curie temperature, along with a relatively large remnant polarization [6]. Hence, the utilisation of BNT can be extended to include multiple functionalities in the domains of luminescence and ferroelectricity. BNT ceramics exhibit a lowered vibrational energy, rendering them highly suitable for applications involving down conversion (PL) and upconversion (UC) luminescence. Numerous works confirmed the existence of ferroelectricity-enhanced function in rare-earth doped BNT ceramics [7]. The BNT material doped with rare earths (RE) exhibits exceptional photoluminescence characteristics. As an example, Wang et al.

* Corresponding author.

E-mail address: renukabokolia@dtu.ac.in (R. Bokolia).



Optical temperature sensing and upconversion luminescence in Er^{3+} / Yb^{3+} co-doped BNT ferroelectric ceramic

Megha Narwan¹ · Richa Sharma¹ · Renuka Bokolia¹

Received: 18 July 2024 / Accepted: 14 October 2024
© The Author(s), under exclusive licence to Springer-Verlag GmbH Germany, part of Springer Nature 2024

Abstract

In the present work, a series of $\text{Er}^{3+}/\text{Yb}^{3+}$ co-doped $\text{Bi}_{0.5-x-y}\text{Er}_x\text{Yb}_y\text{Na}_{0.5}\text{TiO}_3$ ferroelectric ceramic is prepared using traditional solid state technique to investigate the structural, optical and sensing properties. The XRD analysis confirms the rhombohedral geometry and no extra peaks shows the solubility of the dopant ions. SEM images exhibited a dense micro-structure with well-defined grain boundaries. The FTIR vibrational bands observed at 550 cm^{-1} and 820 cm^{-1} depict the typical characteristics of perovskite structure caused by the expansion of the octahedral group of Ti–O bonds. The Tauc plot displays the energy band gaps (E_g) in a range of 2.93 eV to 2.88 eV as a function of the Yb^{3+} concentration. The photoluminescence spectra were measured at two wavelengths of excitation at 489 nm and 980 nm for all the BNT ceramic compositions. It has been observed that the two intense green bands and one visible red band appeared at 530 nm , 549 nm and 662 nm , respectively. The dependency of pump power on UCL spectra is observed with varying pump powers at 980 nm excitation. The two photons that are involved in the UCL process are confirmed by this investigation. The time-resolved fluorescence spectroscopy reveals that the efficiency in energy transfer between the dopant ions increased for all the co-doped BNT ceramic compositions. The absolute (S_{ab}) and relative (S_r) sensitivity of BE3Y3 ceramic composition are $0.54\% \text{ K}^{-1}$ and $1.24\% \text{ K}^{-1}$ at 523 K and 303 K , respectively.

Keywords UCL · Sensing · Ceramic · Time decay · Diffuse reflectance spectroscopy · BNT

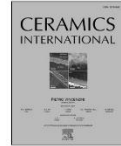
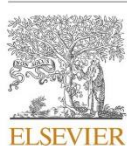
1 Introduction

Multifunctional materials represent a paradigm change in material science, offering unprecedented opportunities for innovation and advancement across various fields. Multifunctional materials can be well defined as the combination of optical, electrical, and mechanical properties [1, 2]. These materials have drawn a lot of interest due to their potential for developing novel technologies. There are many applications of multifunctional materials such as actuators, transducers, accelerators, sensors, and non-volatile memories. Their preparation method, which included microwave processing, solid state reaction, and combustion reaction, also had a significant impact on their chemical and physical characteristics [3, 4]. The need for environmental preservation on a worldwide scale has made lead-free materials more and

more popular in recent years. New lead-free piezoelectric material needs to be improved due to growing environmental concerns. Lead-free ferroelectric material can be doped with rare earth ions exhibits various phenomena, like photoluminescence (PL), upconversion (UC) emission and it can enhance the piezoelectricity of the material [5–9]. To reduce the harmful effects of lead exposure on the environment and human health, ferroelectrics are a practical replacement for ceramics containing lead. Ferroelectrics are known to be superior alternative to lead-based materials in many applications since they don't harm the environment and perform better without sacrificing functionality [10–14]. Consequently, to substitute the lead-based materials, a new lead-free piezoelectric ceramic has to be developed. Bismuth sodium titanate (BNT), with the chemical formula $\text{Bi}_{0.5}\text{Na}_{0.5}\text{TiO}_3$ and a perovskite structure, is one of the most prevalent utilized lead-free piezoelectric materials. It was initially founded by Smolenskii et al. in 1960 [15–18]. BNT ceramic demonstrates good optical and luminescence properties. It is having strong Ferro electricity and high Curie temperature with large value of remnant polarization and coercive field that is

✉ Renuka Bokolia
renukabokolia@dtu.ac.in

¹ FMRL Department of Applied Physics, Delhi Technological University, Delhi 110042, India



Ho³⁺-driven novel orange emission and enhanced energy storage in lead-free Bi_{0.5}Na_{0.5}TiO₃ ceramics



Megha Narwan^a, Ankita Banwal^a, Bhavya Kumar^{a,b}, Manoj Verma^c, Ankur Shandilya^c, Vineet Kumar Rai^d, Richa Sharma^a, Renuka Bokolia^a

^a Functional Material Research Laboratory, Department of Applied Physics, Delhi Technological University, Delhi, 110042, India

^b School of Engineering & Technology, Vivekananda Institute of Professional Studies-Technical Campus, AU-Block (Outer Ring Road), Pitampura, Delhi, 110034, India

^c Department of Physics, Hindu College, University of Delhi, 110007, India

^d Laser and Spectroscopy Laboratory, Department of Physics, Indian Institute of Technology (Indian School of Mines), Dhanbad, Jharkhand, 826004, India

ARTICLE INFO

Handling editor: Dr P. Vincenzini

Keywords:

Upconversion luminescence
Ferroelectric ceramic
Ho³⁺ doping
Diffuse reflectance spectroscopy
Band gap
Time decay

ABSTRACT

In this study, the Ho³⁺ ions are systematically inserted on the A-site of Bi_{0.5-x}Ho_xNa_{0.5}TiO₃ lead-free ferroelectric ceramic via solid-state method. The x-ray diffraction spectra (XRD) shows the rhombohedral structure of Bi_{0.5-x}Ho_xNa_{0.5}TiO₃. Fourier transform infrared (FTIR) spectroscopy shows two vibrational bands at 537 cm⁻¹ and 832 cm⁻¹, due to the stretching vibrations of Ti-O bonds in the octahedral units of the perovskite structure. The diffuse reflectance spectra (DRS) showed three bands at 454, 542, and 646 nm transit from ³I₈→³G₆, ³I₈→³F₄/³S₂, and ³I₈→³F₅, respectively. The band gap varies and maximum for 0.03 concentration due to the local structural instability within the lattice by Ho³⁺ ions. The photoluminescence (PL) emission spectra are traced under 452 nm, and one intense green band at 548 nm and two at 655 (orange) and 750 nm (red) were observed. In upconversion luminescence (UCL) spectra, four emission wavelengths were obtained at 490, 525, 552, and 660 nm. The orange emission band is highly intense, whereas other color bands are relatively weak. Pump power dependence on UCL spectra is analyzed using concentration (x = 0.03). The decay profile for green and orange bands showed an average lifetime of 12.99 μs and 9.43 μs, respectively. The PE loops become slimmer, and P_f values decrease with increasing concentration. The energy storage efficiency (η%) of the ceramic is increasing with dopant concentration and comes out to be 90 %. The maximum absolute and relative sensitivity observed for the BNT (x = 0.03) is 0.29 % K⁻¹ and 0.22 % K⁻¹ at 303 K, respectively. This study demonstrates the novel observation of orange emission in Ho³⁺ doped Bi_{0.5}Na_{0.5}TiO₃ ceramics without any sensitizers which is not usual behavior as Ho³⁺ typically exhibits green or red emission. This unusual luminescence highlights distinct site symmetry and energy level interactions within the lead-free BNT matrix, validating the uniqueness of the work.

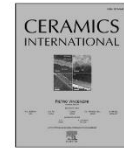
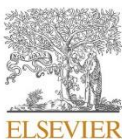
1. Introduction

The remarkable piezoelectric performance of lead-based piezoelectric ceramics, such as Pb(Zr, Ti)O₃ (PZT), makes them indispensable for use in transducers, actuators, etc. [1–3]. Despite their superior piezoelectric properties, lead-based piezoelectric materials have lead toxicity. Exposure to lead and the chemicals that are derived from it is toxic to both the environment and human health. Because of this, lead-free ferroelectric and multifunctional materials have drawn more and more attention as environmental preservation and sustainable development gain in popularity [4,5]. Ferroelectric materials are well known for their multifunctional applications. The combination of magnetic, electrical,

optical, and mechanical properties is characterized by multifunctional materials. There are different preparation methods, which include solid-state reactions, combustion reactions, and microwave processing, which also have a substantial impact on their chemical and physical properties. The current research focuses on lead-free titanate-based perovskites ferroelectric and piezoelectric ceramics such as K_{0.5}Bi_{0.5}TiO₃, BaTiO₃, Bi_{0.5}Na_{0.5}TiO₃, BaZr_{0.08}Ti_{0.92}O₃, bismuth ferrite (BiFeO₃), and alkaline niobate perovskites (KNbO₃, NaNbO₃, (K, Na)NbO₃), as well as bismuth oxide layer structure ferroelectric materials (SrBi₄Ti₃O₁₅, Bi₄Ti₃O₁₂, Bi₂TiTaO₉) [6–10]. Among these, we chose sodium bismuth titanate Bi_{0.5}Na_{0.5}TiO₃ (abbreviated as BNT) lead-free piezoelectric material discovered in 1961 by Smolenskii et al. [11].

* Corresponding author.

E-mail address: renukabokolia@dtu.ac.in (R. Bokolia).



Fabrication of flexible thin film for energy harvesting application based on $\text{Bi}_{0.5}\text{Na}_{0.5}\text{TiO}_3$ nano powders

Megha Narwan^a, Shilpa Rana^a , Bharti Singh^a, Manoj Verma^b, Manju Bala^b, Renuka Bokolia^{a,*}

^a Functional Material Research Laboratory, Department of Applied Physics, Delhi Technological University, Delhi, 110042, India

^b Department of Physics, Hindu College, University of Delhi, 110007, India



ARTICLE INFO

Handling editor: Dr P. Vincenzini

ABSTRACT

This study presents the development and characterization of flexible piezoelectric nanocomposite films based on bismuth sodium titanate (BNT) embedded in a polyvinylidene fluoride (PVDF) matrix for efficient mechanical energy harvesting. BNT ceramic powder was synthesized via a conventional solid-state reaction route and subsequently incorporated into PVDF at varying concentrations (0–25 wt% BNT) using a drop casting method. Structural analyses confirmed the successful formation of phase-pure rhombohedral BNT and enhancement of the electroactive β -phase in PVDF upon BNT addition. Morphological evaluation using FESEM revealed uniform dispersion of BNT up to 20 wt% BNT, beyond which agglomeration was observed. FTIR and XRD studies substantiated the β -phase promotion in the composites, while polarization–electric field (P–E) loop measurements demonstrated improved ferroelectric behavior with increasing BNT content, peaking at 20 wt% BNT. Notably, the piezoelectric voltage and current outputs were maximized at 20 wt% BNT, registering 25 V and 12 μA , respectively, under mechanical excitation. A practical demonstration using the composite film to power LEDs confirmed its potential as a flexible nanogenerator. These findings highlight the suitability of BNT/PVDF composites as promising candidates for next-generation, lead-free, wearable energy harvesting devices.

1. Introduction

The ever-growing demand for sustainable and decentralized power sources has catalyzed significant research into energy harvesting technologies, particularly those capable of converting ambient mechanical energy into useable electrical energy [1,2]. In an era characterized by rapid advancements in microelectronics, the proliferation of wearable sensors, implantable devices, and Internet-of-Things (IoT) systems has led to a pressing need for compact, autonomous power sources that eliminate or minimize dependence on conventional batteries [3,4]. Conventional power storage units not only suffer from limited life spans and high maintenance costs but also contribute significantly to environmental degradation due to the use of toxic materials and challenges associated with large-scale disposal. Consequently, self-powered systems based on mechanical energy scavenging have emerged as a promising solution [5–7].

Among the various energy harvesting technologies, piezoelectric nanogenerator stands out to be promising due to its ability to convert

mechanical deformation, such as pressure, strain, or vibration, into electrical charge via piezoelectric material—a property that has found application in diverse fields including structural health monitoring, biomedical implants, smart textiles, and portable electronics [8,9]. The piezoelectric materials are particularly well-suited for environments where continuous motion, such as walking, engine vibration, or acoustic energy, can be harnessed to generate consistent power [10,11].

Commercial piezoelectric devices are predominantly fabricated using lead-based ceramics, especially lead zirconate titanate (Pb(Zr,Ti) O₃, PZT), owing to their excellent electromechanical coupling and high piezoelectric coefficients [12–15]. However, the widespread use of lead-based materials has become increasingly controversial due to their toxicity and environmental hazards [16,17]. Regulations such as the Restriction of Hazardous Substances (RoHS) directive and the Waste Electrical and Electronic Equipment (WEEE) directive have further driven the research community to identify and develop lead-free alternatives that can match or exceed the performance of their toxic counterparts [18–20].

* Corresponding author.

E-mail address: renukabokolia@dtu.ac.in (R. Bokolia).

Bio-data of the Author

Megha Narwan



ADDRESS: -

165-A Pocket F, GTB Enclave, Dilshad Garden, New Delhi-110095

Mob-9810860857

Email Id: narwanmegha@gmail.com

ACADEMIC BACKGROUND

Aug 2019 -July 2025

Ph.D., Physics

Materials Science

Department of Applied Physics,

Delhi Technological University, Delhi-110042

Thesis Advisor: Dr. Renuka Bokolia & Dr. Richa Sharma

Thesis Title: **Structural and Optical Properties in Lanthanide (Ln³⁺ = Er³⁺/Yb³⁺/Ho³⁺) Doped Bi_{0.5}Na_{0.5}TiO₃ Ceramics**

2017

NET

Physical Science JRF & Lectureship

Rank-271

CSIR

2015-2017

M. Tech

Nano Science & Technology

CGPA-6.99

Department of Nano Science & Technology

Guru Gobind Singh Indraprastha University, Delhi-110078

2009-2014

B. Tech

Engineering Physics with Major in Electronics and
minor in material science & Technology

CPI- 52.65

Department of Applied Physics,

Delhi Technological University, Delhi-110042

2009	Senior Secondary Education Percentage 58.4 Holy Child Sr. Sec. School, Delhi-110027
2007	Secondary Education Percentage 63.8 Holy Child Sr. Sec. School, Delhi-110027

Publications

Publications in Peer-Reviewed Journals from This Thesis Work

1. **M. Narwan**, A. Banwal, R. Sharma, R. Bokolia, “Non-invasive thermal sensing and improved recoverable energy storage density of $\text{Bi}_{0.5}\text{Na}_{0.5}\text{TiO}_3$: Er^{3+} doped multifunctional ferroelectric ceramic”, in *Journal of Luminescence* [265](#), 2024, 120236. (I.F. 3.6)
2. **M. Narwan**, R. Sharma, R. Bokolia “Optical temperature sensing and upconversion luminescence in $\text{Er}^{3+}/\text{Yb}^{3+}$ co-doped BN ferroelectric ceramic” *Applied Physics A* 130, 2024 , 854. (I.F. 2.8)
3. **M. Narwan** , A. Banwal, B. Kumar, M. Verma, A. Shandilya, V.K. Rai, R. Sharma, R. Bokolia “ Ho^{3+} -driven novel orange emission and enhanced energy storage in lead-free $\text{Bi}_{0.5}\text{Na}_{0.5}\text{TiO}_3$ ceramics” *Ceramics International* (I.F. 5.6)
4. **M. Narwan**, S. Rana, B. Singh, M. Verma, M. Bala, R. Bokolia, “Fabrication of flexible Thin Film for Energy Harvesting application based on $\text{Bi}_{0.5}\text{Na}_{0.5}\text{TiO}_3$ Nano powders” *Ceramics International* (I.F. 5.6)

Publications in Peer-Reviewed Journals Other Than This Thesis Work

- 1) M. Varshney, S. Soni, A. Banwal, **M. Narwan**, M. Verma, R. Bokolia, “Effect of Er^{3+} ion incorporation on the structural, photoluminescence, and ferroelectric properties of KNN ceramic for optoelectronic applications”, *Applied Physics A* 130,2024, 267 (I.F. 2.8)
- 2) A. Basith, S. Singh, A. Banwal, **M. Narwan**, M. Verma, R. Bokolia “Regulating novel tunable green to red upconversion luminescence in $\text{Er}^{3+}/\text{Yb}^{3+}$ co-doped $\text{SrBi}_2\text{Nb}_2\text{O}_9$ ferroelectric ceramic” *Ceramics International* 50(2024) 52344-52355. (I.F 5.6)

3) V. Khare, D. Garg, S.P Singh, **M.Narwan**, M. Verma, R. Bokolia, "Multifunctional Er^{3+} -Doped $\text{SrBi}_2\text{Ta}_2\text{O}_9$ Ceramics: Optimized Energy Storage and Photoluminescence Properties for Advanced Electronic Applications" *Applied Physics A* (I.F. 2.8)

Research Work Presented at International Conferences

1. **M. Narwan**, R. Sharma, R Bokolia "Fabrication and Characterization of Piezoelectric Composite of BNT/PVDF for energy harvesting applications", in 2nd International Analytical Conference & Exhibition, (IAC-2022), organized by Graphic Era University, Dehradun, India.
2. **M. Narwan**, R. Sharma, R Bokolia "BNT/PVDF Flexible Composite Films for Energy Harvesting Application" in International Conference on Nanotechnology for Sustainable Living and Environment (ICON NSLE-2022), organized by BITS Pilani, Rajasthan, India.
3. **M. Narwan**, R. Sharma, R Bokolia "Enhanced output performance of a flexible piezoelectric energy harvester based on BNT/PVDF composite films" in 1st International conference on Recent Trends in Physical, Chemical, Biological Nanosciences-2022 organized by Lal Bahadur Shastri College of Arts, Science and Commerce Satara, Maharashtra, India.
4. **M. Narwan**, A. Banwal, R. Bokolia "Comparative study of structural, upconversion and ferroelectric properties in Er^{3+} doped and $\text{Er}^{3+}/\text{Yb}^{3+}$ co-doped BNT ceramic" in International Conference on Atomic, Molecular, Material, Nano and optical Physics with Applications (ICAMNOP-2023) organized by Delhi Technological University, Delhi, India.
5. A. Basith, S. Singh, A. Banwal, **M. Narwan**, M. Verma, and R. Bokolia, "Structural, photoluminescence, and ferroelectric behaviour of $\text{Er}^{3+}/\text{Yb}^{3+}$ co-doped $\text{SrBi}_2\text{Nb}_2\text{O}_9$ ferroelectric ceramic for multifunctional device", in International Conference on Atomic, Molecular, Material, Nano and optical Physics with Applications (ICAMNOP-2023) organized by Delhi Technological University, Delhi, India.

Conferences and workshops attended

1. Attended National Webinar on "IoT Based Health Monitoring & Control System" (NWIOTHM&CS-2021) organized by the Department of Electrical Engineering, Manda Institution of Technology, Bikaner on April 22nd,2021.
2. Participated in Workshop on "Zotero" A tool to collect, organized by SAVANT Association, Department of Physics, Faculty of Science on 18th May,2021 at SGT University Gurugram, Delhi-NCR.

3. Participated in the National Webinar on “Single Molecule Diodes as Components of Next Generation Electronic Devices” conducted on 27th May 2021 at the Institution of Electronics and Telecommunication Engineer (IETE), Jabalpur.
4. Participated in the National Webinar on “Electric Vehicle” conducted on 3rd June, 2021 at the Institution of Electronics and Telecommunication Engineer (IETE), Jabalpur.
5. Attended National Conference on Luminescence and its application (NCLA)-on (10-12th Feb 2020), National Institute of Technology Warangal, Telagana.
6. Attended National Webinar on Advances in Physics (June 25-26, 2020), GJU, Hisar, Haryana.
7. 1st International conference on Recent Trends in Physical, Chemical, Biological Nano science (ICRT-PCBNano-2022) on 17th & 18th May 2022 Department of Nano sciences, Lal Bahadur Shastri College of Arts, Science and Commerce, Satara.
8. 2nd International Analytical Conference and Exhibition Organized by Graphic Era University Poster presented on “Fabrication and characterization of piezoelectric composite of BNT/PVDF for multifunctional applications”
9. Attended International webinar on Empowering Diversity in Science, 16th Feb 2022, Kamla Nehru Mahavidyalaya ,Nagpur.
10. Oral Presentation on “BNT/PVDF Flexible Composite Films for Energy Harvesting Application)” in International Conference on Nanotechnology for Sustainable Living & Environment (ICON-NSLE 2022) (14-16th April 2022) Department of Chemical Engineering, BITS Pilani, Pilani Campus
11. Attended “Chemical & Allied Science and their Application’s” organized by Department of Applied Chemistry, Delhi Technological University on Friday, 20 January, 2023.
12. Attended one day national seminar on “Recent Advancements in semiconductor devices and materials(RASDM -2023)” organized by Department of Applied Physics ,DTU on January 30,2023
13. Attended one day national seminar on “Implementation of NEP-2020 in special reference to Innovation and Entrepreneurship” organized by Department of Applied Physics ,DTU on 24th February,2023.
14. Attended one day national seminar on National Science Day (NSD-2023) organized by HRDC in association with IIC and Department of Applied Physics ,DTU on 28th February,2023.

TRANING

- ❖ In B-Tech from DRDO 06 -06- 2012 to 31-07- 2012.
- ❖ In M-Tech from DRDO 01-06-2016 to 29-07-2016.

From NPL 16-01-2017 to 31-07-2017.

TEACHING EXPERINCE

- ❖ 6 months teaching experience in Meerabai Institute of Technology.
- ❖ 6 -8 months teaching experience in Bhagwan Parshuram Institute of Technology.
- ❖ Teaching Assistant (2019-2024), Delhi Technological University - Undergraduate and post- graduate labs.

PERSONAL INFORMATION

Date of birth : 05-01-1991
Nationality : Indian
Gender : Female
Marital Status : Married
Language : Hindi/English
Hobbies : Listening Music & Reading Book also cooking and Traveling

STRENGTH

- ❖ Enthusiastic and hardworking.
- ❖ Possess Positive attitude.
- ❖ Responsible towards work.
- ❖ Self-motivated and directed

DECLARATION:-

I do hereby declare that the particulars of information and facts stated herein above Are true, correct and Complete to the best of knowledge and belief

DATE: 28/01/2026

Place DELHI

Megha Narwan